Ultrahigh Vacuum Studies of the Reaction Kinetics and Mechanisms of Nitrate Radical with Model Organic Surfaces

Yafen Zhang

Dissertation submitted to the faculty of the Virginia Polytechnic Institute and State University in partial fulfillment of the requirements for the degree of

Doctor of Philosophy
In
Chemistry

John R. Morris, Chair
Diego Troya
James M. Tanko
Brian M. Tissue

August 12th, 2015
Blacksburg, Virginia

Keywords: Nitrate radicals, Organic surfaces, Self-assembled monolayers, Ultra-high vacuum, Reaction probability, Organic nitrates

Ultrahigh Vacuum Studies of the Reaction Kinetics and Mechanisms of Nitrate Radical with Model Organic Surfaces

Yafen Zhang

ABSTRACT

Detailed understanding of the kinetics and mechanisms of heterogeneous reactions between gas-phase nitrate radicals, a key nighttime atmospheric oxidant, and organic particles will enable scientists to predict the fate and lifetime of the particles in the atmosphere. In an effort to acquire knowledge of interfacial reactions of nitrate radical with organics, model surfaces are created by the spontaneous adsorption of methyl-/vinyl-/hydroxyl-terminated alkanethiols onto a polycrystalline gold substrate. The self-assembled monolayers provide a well-defined surface with the desired functional group (-CH_3, H_2C=CH-, or HO-) positioned precisely at the gas-surface interface. The experimental approach employs *in situ* reflection-absorption infrared spectroscopy (RAIRS) to monitor bond rupture and formation while a well-characterized flux of NO_3 impinges on the organic surface. Overall, the reaction kinetics and mechanisms were found to depend on the terminal functional group of the SAM and incident energy of the nitrate radical (NO_3). For reactions of the H_2C=CH-SAM with NO_3, the surface reaction kinetics obtained from RAIRS reveals that the consumption rate of the terminal vinyl groups is nearly identical to the formation rate of a surface-bound nitrate species and implies that the mechanism is one of direct addition to the vinyl group rather than hydrogen abstraction. Upon nitrate radical collisions with the surface, the initial reaction probability for consumption of carbon-carbon double bonds was determined to be $(2.3 \pm 0.5) \times 10^{-3}$. Studies of reactions of the HO-SAM with the effusive source of NO_3 suggest that the reaction between NO_3 and the HO-SAM is initiated by hydrogen abstraction at the terminal $-CH_2OH$ groups with an initial reaction probability of $(6 \pm 1) \times 10^{-3}$. An Arrhenius plot was obtained to determine the activation energy of H abstraction from the HO-SAM. Further, for reactions of the HO-SAM with the high incident energy of NO_3 molecules created by molecular beam, the reaction probability for H abstraction at the hydroxyl terminus was determined to be ~0.4. Overall, the reaction rates of NO_3 with the model organic surfaces that have been investigated are orders of magnitude greater than the rate of ozone reactions on the same surfaces, which suggests that oxidation of surface-bound organics by nighttime nitrate radicals may play an important role in atmospheric chemistry despite their relatively low concentration. X-ray photoelectron spectroscopic (XPS) data suggests that oxidation of the model organic surfaces by NO_3 leads to the production of organic nitrates, which are stable for a period time. The results presented in this thesis may help researchers to predict the fate and environmental impact of organic particulates with which nitrate radicals interact.

ACKNOWLEDGEMENT

The contents of this dissertation would not have been possible without the support of my family and friends. First, I would like to thank my mom and dad for their encouragement through my life. I would not be where I am today without their patience and guidance. I would also like to thank my husband, Fei. Your encouragement and appreciation have made my life enjoyable, even during those frustrated days.

I would like to thank my fellow group members who made the daily graduate research enjoyable. Erin, thank you for being a good and patient teacher. You have done a wonderful job in passing me on all skills of operating that ozone chamber. Jessica and Tommy, thank you for helping me create NO_3 and engaging discussions. Rob, thank you for so many things, as a collaborator and a friend! Steve, thank you for being my Doraemon (who can always produce gadgets and tools from his pocket). I would also like to thank Amanda Wilmsmeyer, Alec Wagner, Josh Abelard, Guanyu Wang, Chikki Chen, Angela Edwards, Cecilia Smith, Darren Driscoll, Conor Sharp, Tyler Grissom.

I would like to thank my committee members for their guidance and expertise over the last six years. In particular, I thank Dr. Troya, for his knowledge of reaction dynamics and for his help in all computational work presented in this work; Dr. Tanko, for helping me to understand organic reaction kinetics and mechanisms; Dr. Tissue, for his encouragement and patience on my graduate research.

Finally, I am extremely appreciative of my advisor Dr. John Morris for being a valuable role-model for me to follow. I am very grateful for his patience in mentoring me to be a better scientist and helping me to improve my presentation and scientific writing. His guidance, inspiration, and scientific expertise are always appreciated.

DEDICATIONS

Several colleagues and collaborators aided the author in the research and manuscript preparation in this dissertation. A brief description of their contributions is included here.

Prof. John R. Morris is the Primary Advisor. He provided guidance for the experimental aspects of the research and collaborated with the author in preparing the previously published manuscripts included within this dissertation.

Prof. Diego Troya collaborated with the author in performing the calculations and preparing the manuscript in Chapter 3.

Rob C. Chaplaski is a member of the Morris research group. He collaborated with the author in performing the calculations and preparing the manuscript in Chapter 3. He also helped the author perform the research presented in Chapter 5.

Dr. Jessica W. Lu was a member of the Morris research group. She helped the author perform the research presented in Chapter 3.

Tommy Rockhold was a member of the Morris research group. He helped the author perform the research presented in Chapter 3.

Tyler Grissom is a member of the Morris research group. He helped the author perform the research presented in Chapter 5.

Xi Geng is a graduate student in Prof. Tijana Grove's group. He helped the author perform the research presented in Chapter 5.

Candace Wall was a member of Prof. Alan Esker's group. She helped the author perform the research presented in Chapter 6 and Appendix.

Table of Contents

List of Figures

List of Tables

Chapter 1

Introduction and Motivation

Thesis Statement

The objectives of the research described here are to develop a fundamental understanding of gas-surface interactions and reactions between nitrate radicals and organic surfaces and to determine the effect of surface functionality and background gases on the overall reactions.

1.1 Background and Research Overview

Interfacial reactions between nitrate radicals (NO_3) and organic surfaces are important due to their significant role in atmospheric chemistry. Atmospheric organic particles with a variety of functional groups on their surfaces, such as carbon-carbon double bonds, aromatic rings, hydroxyl groups, and carbonyls, provide sites for important heterogeneous reactions with oxidative gases.[1-7] Reactions initiated by these oxidative gases, including NO_3, hydroxyl radicals (OH), ozone, and chloride radicals (Cl), have an impact on the size and optical properties of particles, which may further alter absorption and scattering of light by the particles and thus the global climate.[4,8] Although aspects of reactions involving NO_3 and organic surfaces have been explored previously,[3,9-12] the reaction mechanistic pathways and the reaction products have yet to be elucidated. The main goal of this study is to explore the reaction kinetics and mechanisms of NO_3 in collisions with organic surfaces. The first step toward this goal is to develop a deep understanding of atmospherically relevant interactions and reactions of NO_3 on model organic surfaces. The objectives of this dissertation and the research described herein focus on three aspects:

1. Determine the reaction probability for NO_3 collisions on model organic surfaces
2. Explore how surface structure and functionality affect the overall reaction
3. Elucidate the reaction pathways of NO_3 with model organic surfaces

By addressing these objectives, this research aims to further the knowledge of the atmospheric chemistry due to interfacial reactions of oxidative gases with organic surfaces and explore environmental impacts of these reactions.

1.2 Environmental Considerations

Organic compounds released into the atmosphere can negatively affect the environment through the formation of various organic particulates, which may decrease air quality, affect visibility, and alter the solar radiation balance.[13] The impact of air pollution on human health and the environment can be traced back to the last century.[14,15] For example, the smog (historically thought to be the combination of smoke and fog) generated from the widespread domestic use of high-sulfur coal, was discovered to cause thousands of deaths and severe respiratory problems in London in the 20th century.[16,17] Even now, smog, as well as haze and aerosols, are still an environmental problem all over the world, especially in developing countries including China, India, and Brazil.[18-21] In addition to causing health problems, organic particles, produced by anthropogenic emissions from automobiles and industrial plants in many urban areas and by biogenic emissions in remote areas, could reduce object contrast by scattering light out of the sight line to the observer's eyes in the daytime and by scattering light out of the visual path at night, and thereby decreasing the visual range.[8,22] Further, changes in optical properties of organic particulates would influence the balance between the incoming solar radiation and the outgoing infrared radiation and may contribute to global warming.[23]

1.2.1 Formation and Transformation of Organic Particles

The environmental concerns described above have motivated scientists in their studies of the formation mechanism and fate of atmospheric organic particulates. Atmospheric particulates arise from natural sources, including forest vegetation, volcanoes, windborne dust, and from anthropogenic activities, including combustion of fuels, solvent utilization, and even cigarette smoke.[13] These particles, often referred to as aerosols, generally range in size from a few nanometers (nm) to tens of micrometers (μm) in diameter.[24] The schematic illustration of pathways for the generation and transformation of organic particulates and the effect their reactions with oxidative gases on the environment is shown in Figure 1.1.

Particles composed of organic compounds can be directly derived from biogenic emission in remote areas with negligible contributions of combustion processes. Structurally complex and low vapor pressure organic compounds have been identified in airborne particles.[8] For example, n-Alkanes in the C_{26}-C_{35} range, which were attributed largely to epicuticular waxes of vascular plants by Simoneit et al., are commonly present in nonurban aerosols.[25] To differentiate biogenic from anthropogenic sources, the carbon preference index (CPI), which indicates the relative concentration of compounds with odd and even numbers of carbon atoms is typically used.[26] A CPI > 2 for C_{23}-C_{35} alkanes is indicative of biogenic emissions. For example, the CPI for C_{25}-C_{35} alkanes found in aerosols was close to 6, and the CPI of the C_{22}-C_{34} alkanoic acids from vascular plant wax was ~4.[25] In addition to alkanes and alkanoic acids, aldehydes and ketones were reported to be present both in the leaf wax and in airborne particles by Chen and Simoneit.[27]

Another major source of organic particulates comes from direct emission by anthropogenic activities, such as contributions from engines and vehicles, storage and transportation, and solvent utilization in factories.[13] It was reported that the annual anthropogenic VOC (volatile organic

compound) emissions in the United States was up to 17 Tg in 1990's.[28] VOCs, such as aromatic aldehydes and acids, polycyclic aromatic hydrocarbons (PAHs), oxidized PAH derivatives, pentacyclic triterpanes, and azanapthalenes are attributed to fuel combustion of automobile and heavy-duty diesel trucks and have been shown to be carcinogenic in animals.[13,29] The other component of carbonaceous particles generated from combustion processes is called graphitic, black, or elemental carbon. Graphitic carbon particles are considered to be the most abundant light-absorbing aerosol species in the atmosphere, which may result in the increase of the Earth's surface temperature.[30] Moreover, an interesting example of anthropogenic emissions of organic particles into urban areas is that from cigarette smoke. Rogge et al. estimated that cigarette smoke was responsible for ~1% of the fine particle concentrations in the Los Angeles area.[31]

In addition to direct emissions, organic particulates can be formed in the atmosphere by gas-to-particle conversion processes, which are referred to as secondary aerosol (SOA).[13] In the presence of oxidative gases, such as ozone (O_3), nitrate radicals (NO_3), and hydroxyl radicals (OH), VOCs in urban air can form a wide variety of multifunctional organics.[24] Satsumabayashi et al. showed that 30-50% of the total organic particulate matter were mostly formed by oxidation of precursors in air.[32] Multifunctional organic particles generated from the oxidation of cyclic alkenes, aromatic hydrocarbons, or cycloalkanes, such as R-(CH_2)-R (n=1-5) where R can be -COOH, -CHO, CH_2OH, -CH_2ONO, -COONO, or –$COONO_2$, have been observed in a number of studies in urban areas.[33-35] For example, a large fraction of particles collected in the east coast areas in the late 20th century was identified as nitro compounds, organic nitrates, or nitrites, which are the major products from oxidation of VOCs by NO_3.[8,36]

Beyond the contribution of direct gas-phase reactions on particulate formation, organic particles can be formed through coating of long-chain organics with one or more polar functional

groups (acting as surfactants) over the surface of the aerosol. For example, the surfaces of some elemental carbon particles are able to hold significant amounts of water, likely due to the adsorption of polar functional groups such as carboxylic acids.[37] It has been discovered that organic films may affect the uptake of water into particles or alter the rate of water evaporation from particles. For example, Xiong et al. found that one monolayer of the saturated straight-chain lauric and stearic acids significantly reduced the uptake of water into particles.[38] In addition, Chang and Hill exposed water drops to a stream of air containing nonanal and observed a decrease in the rate of water evaporation.[39]

As discussed above, organic particles can be airborne through environmental processes including condensation of vapor species, coagulating with other particles, or chemical reactions with oxidative gases. The resultant particles may be eventually removed from the atmosphere by deposition at the Earth's surface which could contribute to the formation of cloud droplets.[13] Therefore, motivated by the effects of reactions involving NO_3 and organic particles on human health and global climate,[8,40] our research objective is to develop a fundamental understanding of gas-surface interactions and reactions between nitrate radicals and organic surfaces, and ultimately, to understand the formation and transformation mechanisms of organic particles.

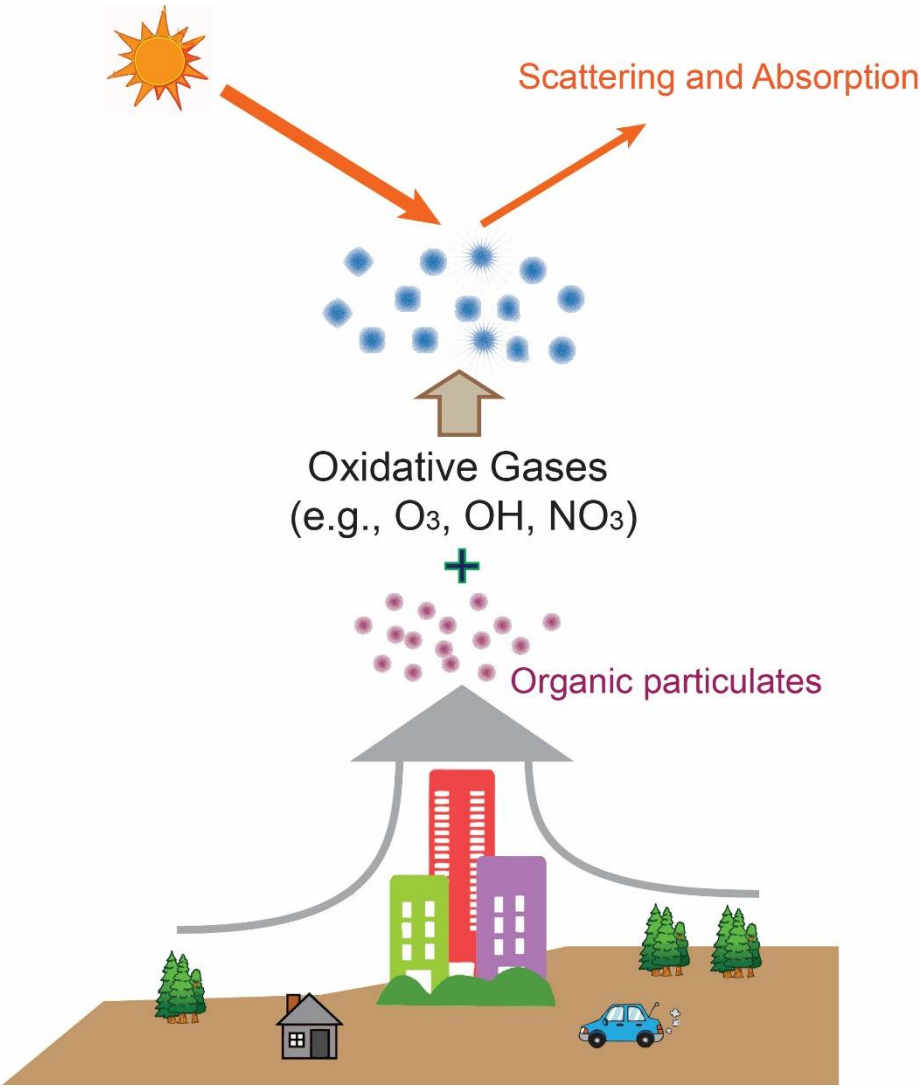

Figure 1.1. Schematic illustration of possible pathways for the generation and transformation of organic particulates in the atmosphere. Organic particles arose from natural sources and anthropogenic activities may undergo further oxidation by O_3, OH, or NO_3. Change in chemical composition and size of particles due to these reactions can affect the absorption and scattering of light in the atmosphere.

1.2.2 Nitrate Radicals in the Atmosphere (NO_3)

Though first observed in Los Angeles in the early 1980s, the importance of the nitrate radical in nocturnal chemistry was not recognized till the beginning of the 1990s.[41-44] The nocturnal chemistry of NO_3 affects a number of atmospheric chemical systems, such as those of sulfur, nitrogen, and halogens. Reactions between NO_3 and VOCs (including alkanes, alkenes, and

alcohols) initiate active radical chemistry which is responsible for the presence of OH, HO_2, and RO_2 radicals at night.[45] Reactions of NO_3 with biogenic hydrocarbons, such as isoprenes and terpenes, lead to the formation of SOA in high yields, and may even exceed SOA formation rate by day-time reactions involving OH.[46] NO_3 chemistry dominates the oxidation of dimethylsulfide (DMS) in coastal areas and thus impacts the formation of sulphate aerosols and CCN in the marine atmosphere.[47] In addition, noxious or even toxic compounds, such as peroxyacylnitrates (PAN) may be formed in the atmosphere.[48]

The largest source of nitrate radicals in the atmosphere is the reaction between NO_2 and ozone:[49,50]

$$NO_2 + O_3 \rightarrow NO_3 + O_2 \qquad (1.1)$$

Since the formation of NO_3 requires the presence of NO_2, the process is always accompanied by the generation and thermal decomposition of dinitrogen pentoxide, N_2O_5 (Reaction (1.2)).[45]

$$NO_3 + NO_2 \leftrightarrow N_2O_5 \qquad (1.2)$$

In addition to the loss by reaction with NO_2, NO_3 is photochemically unstable due to the rapid photolysis to $NO_2 + O$ or $NO + O_2$ during daylight hours.[49,51,52] As a result, the nitrate radicals are only accumulated at night and can reach concentrations ranging from 5×10^7 to 1×10^{10} molecules cm^{-3}.[41,53]

The formation and consumption of NO_3 during the nighttime are important and result in subsequent environmental processes including the production of other reactive species, such as O_3 and OH which are responsible for a great deal of day-time atmospheric chemistry.[48,54,55] The cycle of O_3, NO_3, and OH atmospheric reactions is provided in Figure 1.2. This figure shows that i) oxidation of NO_2 by O_3 generates NO_3; ii) O_3 is primarily generated from the reaction of atmospheric O_2 with ground-state $O(^3P)$ radicals that result from the photolytic dissociation of

ambient NO_2;[8,56] and iii) OH is formed through rapid reactions of water vapor with an electronically excited oxygen atom ($O(^1D)$) that is produced from photodissociation of O_3 by UV radiation.[57,58]

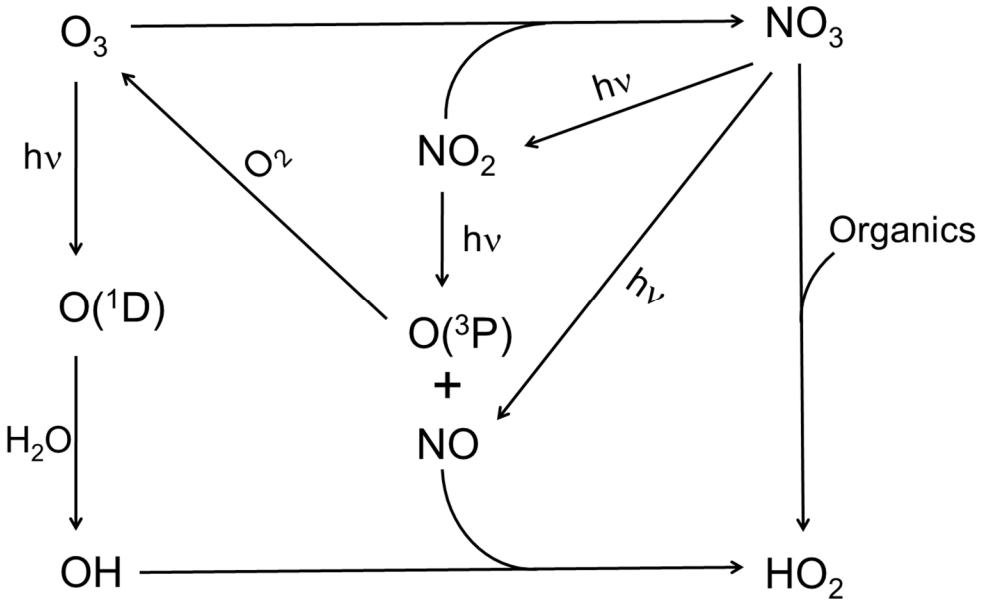

Figure 1.2. Cycling scheme of oxidative gases in the atmosphere. NO_3 is formed from oxidation of NO_2 by O_3. Photolysis and reactions of NO_3 contribute to the production of O_3 and OH in the daytime.

Reports show that the NO_3 reactions contribute to ~60% of organic nitrates present in the atmosphere.[59] The nitrate radical can undergo electrophilic addition to the carbon-carbon double bond or hydrogen abstraction from hydrocarbons.[45,48] Reactions of NO_3 with alkenes proceed by addition to the carbon-carbon double bond. As shown in Figure 1.3, the initial exothermic step forms an excited adduct (Product ①) that can be stabilized (Product ②) or decompose by breaking the CO-NO_2 bond to form the epoxide (Product ③).[8,60] However, Berndt and Boge reported epoxide yields of only 7, 12, and 18% from the reactions of isobutene, trans-2-butene, and 1-butene, respectively.[61] Further, the nitroxyalkyl radical (Product ②) can rapidly react with O_2 to form a nitroxyalkyl-peroxy radical (Product ④) under ambient condition.[62,63] Reactions of the peroxy radical with NO_2 lead to the formation of thermally unstable nitrooxy peroxynitrates

(Product ⑤).[64] Alternatively, the peroxy radical can further react with other peroxy radicals to produce nitroxy-alkoxy radicals (Product ⑥) that may yield dinitroxy hydrocarbons (Product⑦), aldehydes or ketones eventually.[65] In addition to alkene reactions, reactions of NO_3 with saturated hydrocarbons are initiated by H-atom abstraction to form an alkyl radical and nitric acid (HNO_3).[63] Once the alkyl radical is formed, the reaction can proceed in similar pathways to alkene reactions such that hydroperoxy-nitrates, hydroxyl-nitrates, nitroxy-aldehydes/-ketones would be generated.

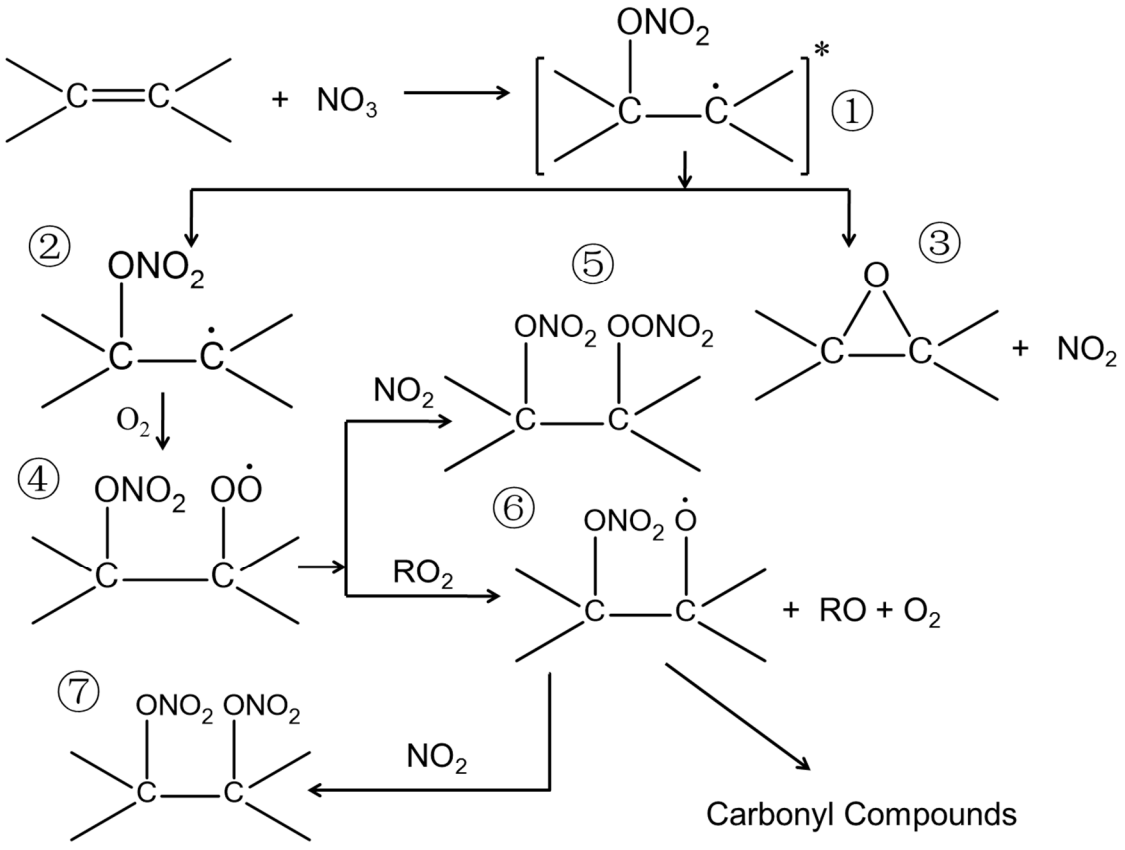

Figure 1.3. Schematic illustration of reactions between NO_3 and alkenes that lead to the formation of alkyl radicals, RO_2, and carbonyl compounds. Adapted from Ref. 8.

Reactions of NO_3 with alkenes are considered to be more significant than reactions with alkanes because of a much lower activation energy for NO_3 addition to the double bond compared to that of the H-atom abstraction.[8] In particular, the rate constants of reactions with biogenic VOCs

(which are speculated to occur via addition to the double bonds) were measured to be in the range of $10^{-13} – 10^{-10}$ cm^3 $molecule^{-1}$ s^{-1}, while the rate constants for hydrogen abstraction from alkanes were found to be up to 6 orders of magnitude smaller.[62,66] However, environmental scientists recently discovered that hydrogen abstraction could be a dominant mechanism for reactions involving saturated hydrocarbons with one or multifunctional groups, such as alcohols, aldehydes, and glycol ethers.[11,67,68]

1.3. NO_3 Reactions with Organic Surfaces

As discussed in the previous section, organic aerosols contribute largely (10-90%) to the total fine particulate matter in the atmosphere.[69] The emission of organic aerosols arise from natural sources and anthropogenic activities. For example, methoxyphenols, levoglucosans, and abietic acids are derived from wood smoke or biomass burning, which accounts for 10-50% of the total organic aerosols.[70] Fatty acids are among the most common components found in ambient fine particles originating from meat cooking, road dust, and tire wear.[71] Aromatic hydrocarbons from anthropogenic sources such as transportation, solvent utilization, and fuel combustion have yearly global emissions ranging from 18.7 to 25 Tg yr^{-1}.[72] These organic particles can be in the form of primary organic aerosols, or alternatively mixed with inorganic material to form organic coatings adsorbed on the surface of solid particles.[69] In addition, organic particles can be modified and contribute to the formation of SOA (50-910 Tg yr^{-1}) through reactions with oxidative gases such as O_3, OH, and NO_3.[8] Further, changes in the chemical and physical properties of organic particles impact air quality, public health, and climate.[13] For example, the occurrence of polycyclic aromatic hydrocarbons (PAHs) and their derivatives constitutes a health risk to the population due to their allergenic, mutagenic, and carcinogenic characters, while the oxidation of PAHs by NO_3 may either degrade the organic or generate even more toxic derivatives.[73] Because of the potential

importance of heterogeneous reactions involving NO_3 and organics, a number of laboratory and theoretical studies have investigated the interfacial reactions between NO_3 and atmospherically relevant organic surfaces which will be discussed in details below.

Fry and Sackinger used the Weather Research and Forecasting/Chemistry (WRF-Chem) model to investigate heterogeneous sink for organic aerosols in the presence of NO_3 in the western United States.[3] The model was run for the four individual months, representing the four seasons, of January, May, August, and October, to generate spatial maps of surface concentration of organic aerosols. The simulations for predicting SOA formation rates and organic aerosol loss rates due to heterogeneous reactions initiated by NO_3 were based on the assumption that oxidation occurred at the saturated sites via H-atom abstraction or at unsaturated sites via NO_3 addition. According to their results, the NO_3 reactions were found to be more important in producing SOA than in consuming existing organic aerosols.

Motivated by the role of NO_3 reactions in atmospheric chemistry, Yang et al. explored reactions between NO_3 and suspended carbaryl particles that are widely used for agricultural purposes.[74] An online vacuum ultraviolet photoionization aerosol time-of-flight mass spectrometer (VUV-ATOFMS) was used for the identification of reaction products and the determination of the apparent reaction rate. In their work, characteristic signal of the carbaryl in the MS was found to decrease with the reaction time concurrently with the increase of signal for formation of product. In addition, they observed the mass spacing between carbaryl and two products was 45 amu, which they attributed to the substitution of one hydrogen atom by one nitro group. However, they were unable to determine whether the substitution occurred in the benzene ring or at the carbamate functional group.

To differentiate the particle surface oxidation from the bulk reaction, Liu et al. measured the uptake coefficients (the ratio of the number of molecules lost to the surface to the number that collide with the surface) of NO_3 onto particulate syringaldehyde (SA, 0.33), vanillic acid (VA, 0.31), and coniferyl aldehyde (CA, 0.28) using the same technique, VUV-ATOFMS, combined with gas chromatography-mass spectrometry analysis (GC-MS).[70] According to their control experiments, the effect of N_2O_5 (formed by reactions of NO_3 with NO_2, see Reaction (1.2)) on the loss of methoxyphenol aerosols was not taken into account due to its much lower reactivity (3 orders of magnitude lower) than that of NO_3. Different from the conclusion made by Yang (who identified nitro-containing compounds as the primary product), they reported both nitrates and nitro-compounds as the reaction products, which may result from the NO_3 electrophilic addition followed by H-abstraction and nitro-substitution processes. The different observations for these two studies may be due to the fact that many products observed in GC-MS analysis were not detected by the VUV-ATOFMS because of the different detection limits of the two analytical methods.[75]

As discussed in Liu's work, the uptake coefficient is negatively correlated with the particle size, likely due to the elevated interfacial reactivity with increasing curvature of small particles.[76] To reduce the effect of non-homogeneous distributed particle size on reaction kinetics, Moise et al. studied the reactive uptake of NO_3 by liquid and frozen organics including alkanes, alkenes, alcohols and carboxylic acids in a rotating wall flow tube.[10] The measured uptake coefficients ranged from 1.4×10^{-3} to 1.5×10^{-2} for reactions of NO_3 with the liquid organics. The uptake coefficients were found to decrease dramatically (a factor of five) upon freezing for some organics (i.e., n-hexadecane and n-octanoic acid) and no change for others (e.g., 1-hexadecene, 2,2,4,4,6,8,8 heptamethyl nonane, and 10,12 octadecadienoic acid). For the reactions in which the coefficient

did not change upon freezing, evaporation or mobility of the surface molecules was thought to provide a constantly renewed surface. The authors related key differences in these surface mechanisms to the solubility constant and diffuso-reactive length (the approximate distance within the liquid over which reaction is taking place) of NO_3 in each liquid organic. Moreover, the estimated diffuso-reactive length indicated that the reaction only occurred within a few molecular layers. In addition, they proposed a reaction mechanism involving NO_3 addition to the double bonds, which was based on the observation that reactivity increases with the addition of this functional group. Further, Gross et al. measured uptake coefficients of NO_3 on alkenoic acid, alkanoate, and polyalcohol substrates.[77] The uptake coefficients on the liquid alkenoic acids including oleic acid (OA), linoleic acid (LA), and conjugated linoleic acid (CLA) were large (>0.07), likely due to the NO_3 loss pathways both at the surface and in the bulk. The uptake coefficients for reactions on the saturated organics were determined in the range of $(7.8 – 46) \times 10^{-4}$, and the low uptake coefficient of glycerol was attributed to its high viscosity.

To better understand the reactivity of unsaturated and saturated organics in multicomponent and multiphase atmospheric particles, Xiao et al. investigated the reactive uptake of NO_3 on binary mixtures containing methyl oleate and matrix molecules, such as diethyl sebacate (DES), dioctyl sebacate (DOS), and squalane.[78] The measured uptake coefficients on the binary mixtures were ordered in the same trend as the diffusion coefficients of the matrix molecules, DES > DOS > squalane, which suggested a bulk reaction mechanism. By assuming a 1:1 stoichiometric ratio and a surface density of 6×10^{14} molecule cm^{-2} for one monolayer, they approximated that 10 monolayers of organics were oxidized during 90 min of NO_3 exposure, which was consistent with only the top few monolayers of the material being available for reactions.

Since multiphase reactions with NO_3 are important chemical aging processes of organic aerosols, Shiraiwa recently explored reaction kinetics of NO_3 with levoglucosan and abietic acid, aerosol components from biomass burning, using a cylindrical flow tube.[9] They employed the kinetic double-layer model (K2-SURF) and the kinetic multilayer model (KM-SUB) to determine the uptake coefficients and bulk diffusion coefficients. The levoglucosan oxidation was found to be dominated by hydrogen abstraction from an alkyl group in the bulk, while the addition of NO_3 to the carbon-carbon bond in the abietic acid was mainly contributed by surface reactions instead of reactions in the bulk. In addition, they demonstrated that relative humidity played a role in the degradation of the two surrogates.

To further investigate the reaction mechanism of NO_3 with organic surfaces, Zhao et al. explored the effect of O_2 on reactions of NO_3 with four unsaturated fatty acids in a flow tube reactor coupled to a chemical ionization mass spectrometer (CIMS).[71] It was evident in CIMS that the primary products were alcohols and ketones in the presence of O_2, while the organonitrates were likely the major products in the absence of O_2. In addition to Zhao's work, the effect of O_2 on NO_3 oxidation was reported by Shu and co-workers, following studies of nitration of typical PAHs and their derivatives (nitro-, oxy-, and hydroxyl-PAHs) adsorbed on azelaic acid particles using a flow tube reactor coupled to a VUV-ATOFMS.[79] In their mass spectra, anthraquinone was observed and identified as one product that may be the result of O_2 involvement. Further, in a study of the reaction kinetics and mechanism of NO_3 with pyrene, Gross and Bertram identified HNO_3 and NO_2 as the major gas-phase products with CIMS.[73] The observation of these two gases was in agreement with their proposed mechanism: the reaction was initiated by NO_3 addition to the aromatic rings to form NO_3 – PAH adduct which may undergo oxidation by either NO_2 or O_2; the resultant products could decompose with the release of HNO_3 or NO_2.

The work reviewed above focused on interfacial reactions involving NO_3 and organic particles or organic compounds adsorbed on particulates in the liquid or solid phase. The uptake coefficients measured for those reactions were attributed to both surface and bulk contributions. Therefore, in an attempt to isolate the gas-surface component of the reaction, Knopf et al. employed a saturated hydrocarbon monolayer in a flow tube reactor coupled to CIMS for the investigation of heterogeneous reactions between NO_3 and organic surfaces.[80] Their uptake coefficient of NO_3 on the monolayer was lower than the reactivity of OH radicals,[81] but they suggested that, considering the atmospheric abundance of NO_3, the oxidation could be potentially competitive with OH. In addition, they used X-ray photoelectron spectroscopy (XPS) to monitor surface oxidation and found that C-O containing compounds, ketones or aldehydes, and carboxylic groups were the primary reaction products. To investigate how surface functionality affects NO_3 oxidation, Gross et al. employed both an alkanethiol and a terminal alkenethiol self-assembled monolayers and monitored the reaction (in the presence of NO_2 and O_2) with infrared spectroscopy (IRS) and time-of-flight secondary ion mass spectrometry (TOF-SIMS).[69] The IR and MS results indicated the formation of organic nitrates ($RONO_2$), but little nitrogen-containing surface species was observed in XPS which was likely due to the instability of $RONO_2$ under X-ray. The uptake coefficient of NO_3 on alkene monolayers was higher than the values obtained using liquid and solid alkene bulk films, which was attributed to the position of the double bond located at the interface.[10]

According to the results from previous studies, it was discovered that reactions of NO_3 with organics were initiated by H abstraction for alkanes or by NO_3 addition to the double bond for alkenes. The primary products of these reactions were found to be organic nitrates or carbonyl compounds under atmospheric conditions. However, the measured reaction rates from these

previous studies were determined based on the consumption rate of NO_3, as opposed to the removal rate of a particular functional group. As a result, the actual rate of NO_3 addition or H-abstraction have yet to be reported. In this thesis, self-assembled monolayers serve as model organic surfaces where functional groups are positioned precisely at the gas-solid interface. By employing an IR instrument, the functional groups consumption and product formation upon NO_3 exposure, instead of NO_3 loss, are used to determine the reaction probability.

1.4 Gas-Surface Reaction Dynamics

In an ambient environment, gas-phase atoms or molecules approach a surface and undergo collision dynamics involving three interactive components: energy transfer, diffusion, and reaction. When a gas-phase molecule, such as NO_3, encounters a solid surface with a specific translational energy and angle, it interacts with the surface by several channels, including i) recoiling back into the gas phase after one or a few collisions without much loss of the impinging translational energy, also known as impulsive scattering (IS); ii) reaction upon a single collision; iii) lacking sufficient perpendicular momentum to escape the gas-surface potential well during the initial collision and being temporarily trapped before desorbing back into the gas phase (thermal desorption, TD); iv) reaction after thermal accommodation.[82-84] The four channels described above are shown in Figure 1.4.

Molecules that undergo TD leave the surface with a Maxell-Boltzmann distribution of energies at the surface temperature.[85] For reactive scattering events, following thermal accommodation, the gas molecule can diffuse to available reactive sites where the enthalpic and entropic requirements could be achieved for reaction.[86] In such case, the impinging species loses memory of its incident trajectory in a very short time (~10^{-12} s), then dissipates its excess energy during the thermal accommodation, and eventually undergoes product desorption.[87,88] This

reaction channel is called Langmuir-Hinshelwood (L-H) mechanism in which the reaction rate depends on the surface temperature. For reactions described by the L-H mechanism, since gas-surface thermal accommodation is a necessary first step to product formation, the reaction probability is often limited by the accommodation coefficient, α, which is defined as the fraction of the total number of incident molecules that fully thermalized on a surface (α = number of molecules thermally accommodated/total collisions).[89] Therefore, the accommodation is critical to the overall reaction rates.

Alternative to the L-H pathway is the direct reaction pathway, as highlighted in Figure 1.4. The Eley-Rideal (E-R) mechanism involves production formation in a single impulsive collision in which the incident energy is critical to surmounting reaction barriers to form new chemical bonds at the gas-surface interface.[90] Interfacial reactions on organic surfaces are generally governed by L-H dynamics.[90] Notwithstanding, E-R reaction mechanisms have been observed for open-shell gases, such as radicals, reacting on organic surfaces.[91] The particular pathway for NO_3 on organic surfaces has yet to be elucidated.

A complete understanding of the reaction mechanism at the gas-surface interface is best achieved by investigating energy transfer of the individual steps (as outlined in Figure 1.4) during the interaction dynamics. Molecular beam techniques in ultrahigh vacuum (UHV) environments provide control over the energy, angle and flux of the incident gas while velocity and angular resolved detection of the scattered atoms or molecules offers information about the energy transfer. The principle ideas of gas-surface energy transfer could be described classical mechanical models, which provide guidelines and physical pictures to understand the dynamics of NO_3-surface collisions.

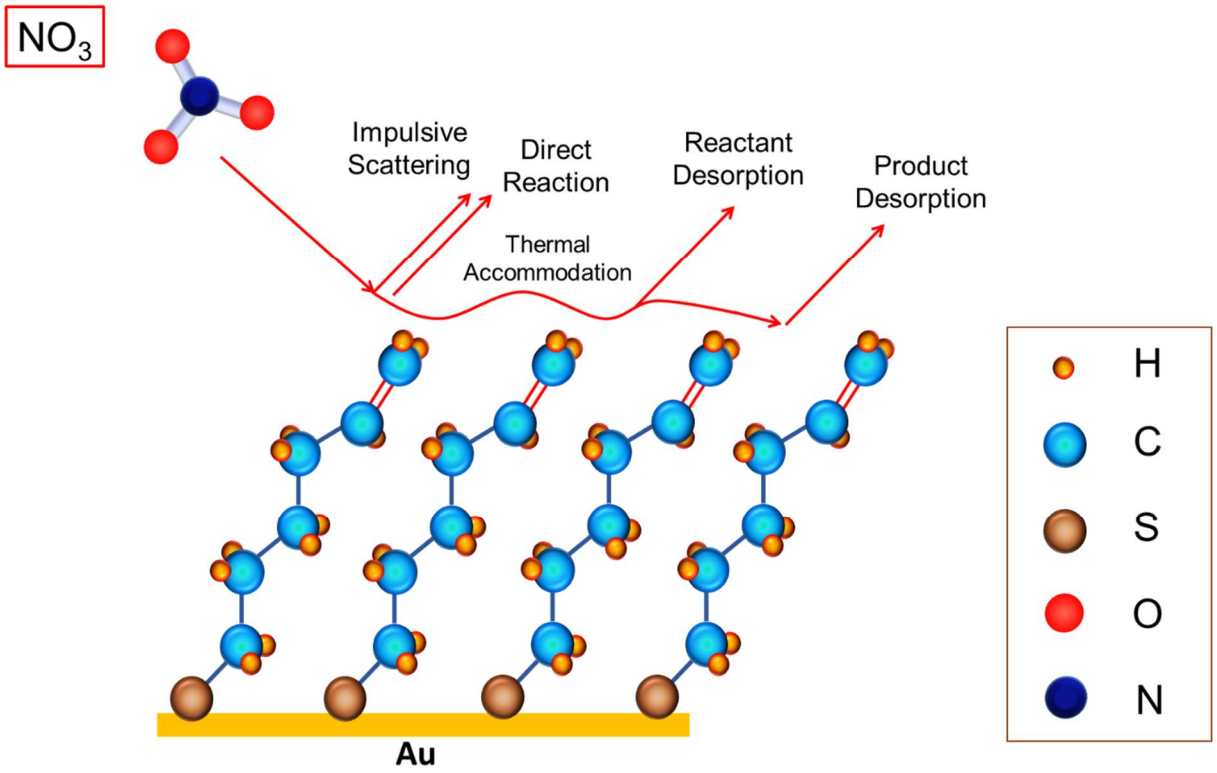

Figure 1.4. Schematic depicting interaction and reaction pathways in a gas-surface collision.

1.4.1 Classical Models for Gas-Surface Scattering

Gas-surface scattering models utilize projectile motion physics as the foundation for understanding complex gas-surface interactions in a qualitative way. These models, once validated through experimentally verifiable components, assist in determining the dynamics of momentum and energy exchange that govern the outcome of gas-surface collisions. Below, we outline four of these classical models that have been developed and used in gas-surface scattering dynamics studies, including the seminal work by Logan et al.[92,93] that provided the "hard-cubes" and the "soft-cubes" models, and the extended work by Tully et al.[83,94] that led to the "hard spheres" and the "washboard" models.

1.4.1.1 The Hard-Cube Model

To understand the momentum and energy transfer between a gas and a solid surface, a simple classical model was proposed by Logan and Stickney in the 1960's and has been used to qualitatively predict experimental results of gas atoms scattering from solid surfaces. Their model is commonly known as the hard-cube model.[92] A schematic of this model is illustrated in Figure 1.5, which shows a projectile of mass m_g, at a specific incident angle θ_i and velocity v_i, impinging on a surface of effective mass m_s (the mass corresponding to the part of a surface that responds to forces) and velocity v, and returning to the gas phase with v_f and θ_f after imparting part of the incident energy to the surface. In the hard-cube model, the interaction of a gas atom with a flat surface is impulsive with a uniform gas-surface intermolecular potential in the plane of the surface while each surface atom is represented by a square-well potential. The gas-surface collision does not affect the tangential momentum so that only the motions along the surface normal of the cube play a role in energy transfer. This simple model provides relationships between the scattering characteristics (such as final energy, final angle) and their dependence on the incident angle of the gas and the temperatures and masses of the gas and surface atoms. One important result of the hard-cube model is the relationship (as shown in Equation (1.1)) between energy transfer and the gas-to-surface mass ratio, μ ($\mu = m_g/m_s$).

$$\frac{\Delta E}{E_i} = \frac{4\mu}{(1+\mu)^2} \qquad (1.1)$$

Where ΔE is the change in energy of the gas atom, E_i is the incident gas energy and μ is the mass ratio. The model predicts that the maximum energy transfer achieves when μ is unity.

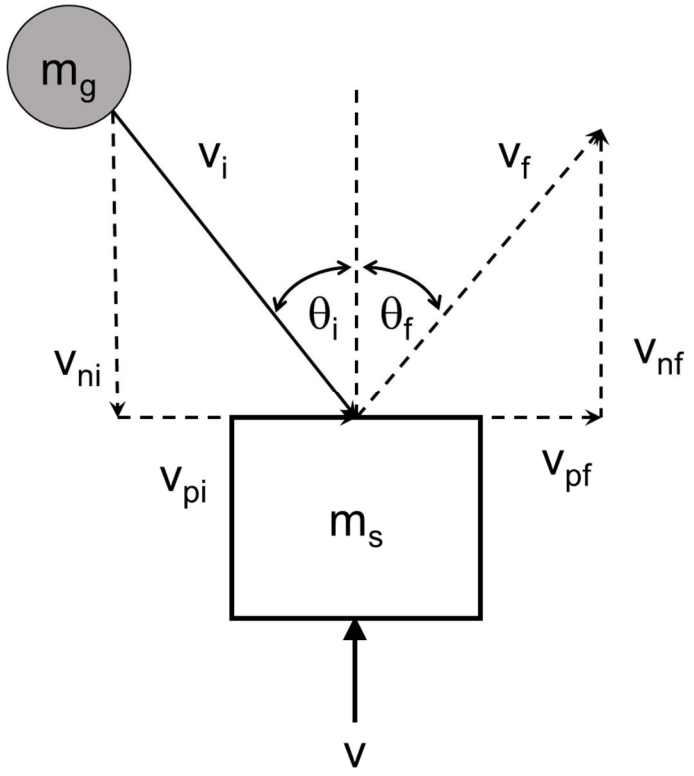

Figure 1.5. Schematic of the hard-cube model. Adapted from Ref. 90.

1.4.1.2 The Soft-Cube Model

Since atmospherically-relevant collisions are not impulsive and much more complex than the dynamics captured by the hard-cube model, a more sophisticated model is required. Logan and Keck proposed the soft-cube model in 1968 as an extension of the hard-cube model that accounts for trapping and sticking probabilities during gas-surface collisions.[93] In this model, the gas atoms are assumed to interact with the surface through a stationary square-well attractive potential and an exponential repulsive potential. In addition, the surface atom involved in the collision is attached by a single spring to the remainder of the lattice represented by a rigid wall, as illustrated in Figure 1.6. As a result, the surface oscillators represent an equilibrium energy distribution at the temperature of the surface and the tangential velocity component of the gas atom is conserved

because the surface is considered to be flat in the model. According to these assumptions, the energy loss of the gas atom may be written as:

$$\Delta E = \frac{m_g u_\infty^2}{2}\left(1 - \frac{\cot^2 \theta_f}{\cot^2 \theta_i}\right) \quad (1.2)$$

Here, m_g is the mass of the gas atom or molecule, u_∞ is the incident normal velocity outside the potential well, θ_i is the incident angle, and θ_f is the reflection angle of the gas.

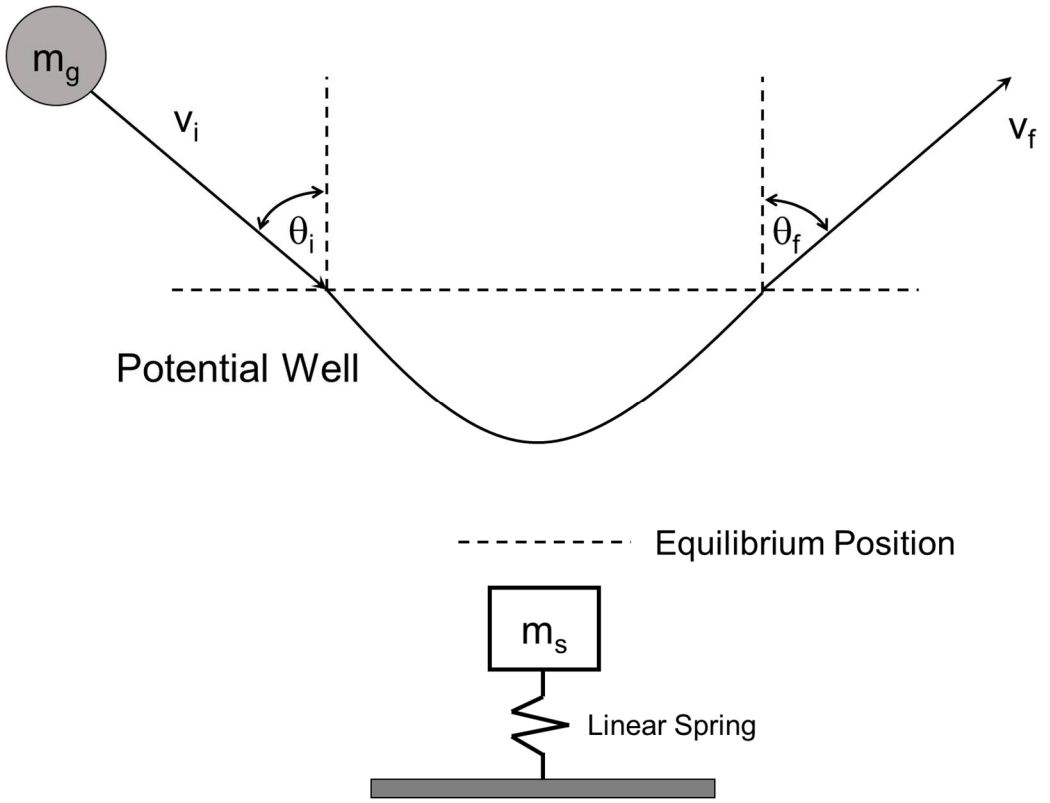

Figure 1.6. A schematic illustration of the soft-cube model. Adapted from Ref. 91.

Using this model, satisfactory agreement was obtained with available experimental data for the angular position of the maximum of the scattering distribution and for a heavier gas atom scattering from a lighter surface atom (Xe on Ag). However, the effects of surface roughness have been assumed small in this model, rendering it generally insufficient to describe energy transfer and reactivity.

1.4.1.3 The Hard Spheres Model

In gas-surface scattering where the interfacial region of the surface is not well-ordered, such as organic liquid with rough and bumpy landscapes or SAMs with many defects, collisions between gas and surface species is similar to two spheres colliding.[83] As exhibited in Figure 1.7, a gas molecule or atom of mass, m_g, strikes a surface of effective mass, m_s, with initial translational energy, E_i, at an incident angle θ_i with respect to the normal from the global surface plane. The deflection angle, χ, is either equal to $180° - \theta_i - \theta_f$ or $180° - \theta_{i\text{-}loc} - \theta_{f\text{-}loc}$. The $\theta_{i\text{-}loc}$ and $\theta_{f\text{-}loc}$ are the local approaching and final angles with respect to the axis that contains the line through the center of both gas and surface spheres. By assuming the attraction between the gas and surface molecules as a square well potential of depth V along the line of centers, the energy transfer can be shown to be:

$$\frac{\Delta E}{E_i} = \frac{2\mu}{(1+\mu)^2}\left(1 - \cos\chi\sqrt{1-\mu^2\sin^2\chi} + \mu\sin^2\chi\right)\left(1 + \frac{V-2RT_s}{E_i}\right) \qquad (1.3)$$

Where μ refers to the mass ratio m_g/m_s, and T_s is the surface temperature.

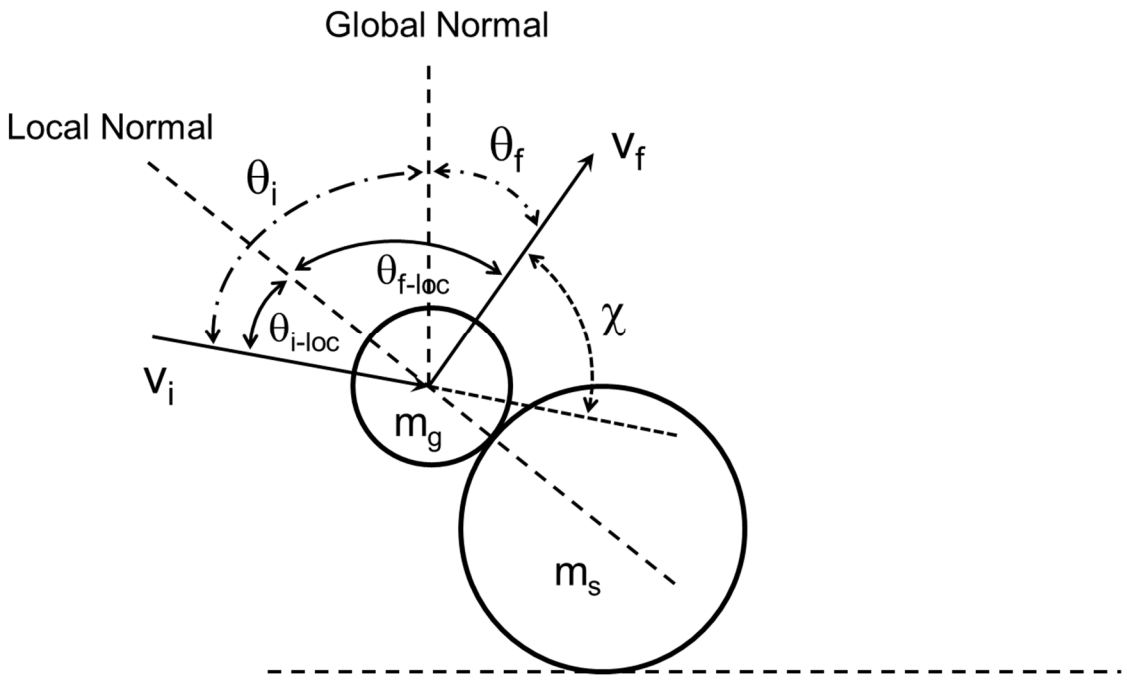

Figure 1.7. Diagram of the hard spheres model. Adapted from Ref. 81.

One important conclusion of the hard spheres models is that the energy transfer is most efficient in a head-on collision and least efficient for glancing collisions. This model has been successfully applied to the study of angular distribution of scattering in gas-liquid collisions by Nathanson and co-workers.[83] However, for solid surfaces such as metals, surface corrugation is generally well defined so that a model makes a reasonable physical attempt to incorporate that effect on scattering is required.[95]

1.4.1.4 The Washboard Model

Another extension of the hard cube model developed by Tully in 1989 is the washboard model that incorporates the effects of surface corrugation.[94] In this model, the gas-surface interaction is represented by a one-dimensional sinusoidally varying hard-wall repulsion that can be altered by adjusting two parameters, the amplitude, *A*, and the period ,*a*, of the surface, plus an

uncorrugated attractive square well of depth *W*. The cube surface is only tangent to the surface contour at the position of gas impact, offset by α with respect to the global surface, as illustrated in Figure 1.8. As a result, only the component of gas momentum normal to the local surface is affected by collision, while the local tangential momentum is conserved. After being refracted by the attractive well and scattering from the local corrugated surface, angular scattering distribution, the energy distribution, and the trapping probability can be determined through the following parameters: the mass ratio μ, the well depth *W*, the corrugation strength *A* and *a*, the incident kinetic energy E_i, the incident angle θ_i, and the surface temperature T_s. Good agreement with the trajectory results could be achieved by adjustment of the washboard parameters, but the model is too simple to expect quantitatively accurate prediction.

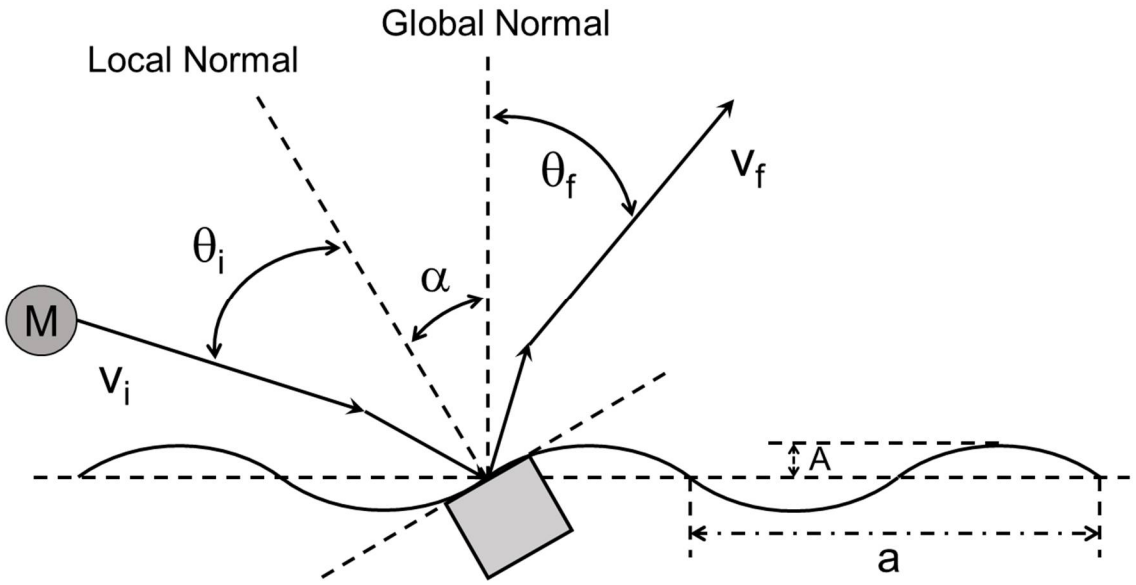

Figure 1.8. Schematic representation of the washboard model. Adapted from Ref. 92.

Although the four classical models discussed above do not afford an accurately quantitative description of gas-surface scattering, they do show promise as a useful tool for elucidating trends of energy exchange in the scattering events. First, surface dissipates more energy with unity mass

ratio (μ). Further, the energy transfer for gas-surface collisions maximizes with decreasing incident angle. Finally, the corrugation of solid surfaces (e.g., SAMs) affects the accommodation coefficient by providing multiple collisions.

1.4.2 Interactions and Reactions in Gas-Surface Collisions

Cohen, Naaman, and Sagiv were among the pioneers who reported their scattering work of molecular beams of rare gases, O_2 and NO colliding with organized organic monolayer surfaces.[96] Following their work, a vast number of gas-surface collision dynamics experiments conducted on self-assembled monolayers (SAMs) with which the chemical functionality at the interface can be altered through the end groups of the alkanethiols.[97-101] For example, Shuler et al. explored atomic Ar scattering from H_3C- and HO-SAMs to probe the dynamics of energy transfer and thermalization.[102] In both Cohen and Shuler's results, they discovered that the greater corrugation introduced by SAMs (compared to bare gold surfaces) increased energy transfer by providing opportunities for multiple collisions. Most importantly, the SAMs provide excellent energy sinks for absorbing collision energy. The transferred energy may be dissipated through end-group rotation as well as concerted waving motions.[102] In addition, Shuler et al. found that the atomic beam thermalized with the H_3C-SAM surface more efficiently than the HO-SAM, which was attributed to differences in the available energy modes and the structural rigidity of the two monolayers.

Inspired by the early studies, Day et al. scattered Ar atoms on ω-functionalized SAMs to investigate how the terminal group, chain length, and surface density affect energy transfer and thermalization.[101,103] Long-chain H_3C-SAMs were found to be the most effective at dissipating the translational energy of impinging atoms due to the role of the low-energy long-range motions

involving methylene groups along the chains. In contrast to H_3C-SAMs, monolayers composed of hydrogen-bonding terminal groups, HO-SAMs, COOH-SAMs, and NH_2-SAMs, exhibited decreased energy transfer efficiency resulting in more rigid surfaces. Beyond experiments, Hase and co-workers performed classical chemical dynamics simulations to compare energy transfer efficiency in collisions of Ar with H_3C- and HO-SAMs.[104] The results indicated that the surface of the HO-SAM was disordered arising from clustering of the hydrogen-bonded OH terminus, which played a role in decreasing thermalization efficiency of Ar with the surface. Moreover, the effect of the overall monolayer packing density on Ar scattering was explored in Day's work by employing silver and gold as substrates for SAMs.[103] It was discovered that the energy transfer and thermal accommodation efficiency were limited by the reduced number of low-energy bending and wagging modes of the denser H_3C-SAM on silver.

In addition to the effect of the surface structure, the mass ratio may affect the energy transfer according to the classical models discussed in the previous sections. The mass effect has been confirmed by studies of rare gases with various masses scattering from SAMs and triatomic gases scattering from different SAMs.[82,105] The results showed that heavier atoms transferred more energy to SAM surfaces and more massive SAMs dissipated less energy.

Previous studies of non-reactive collision dynamics suggest that the surface structure and properties of impinging gases play a role in gas-surface energy transfer. For reactive collisions, one may wonder if the energy transfer efficiency affects the reaction mechanism or products. D'Andrea et al. were among the ones who pioneered the exploration of the dynamics of hydroxyl radicals (OH) collision with organic surfaces.[106] They found that 60% of the H_3C-SAM monolayer was destroyed upon 10 min of OH exposure and only the terminal $-CH=CH_2$ groups underwent radical-induced polymerization at the interface following 5 min OH exposure. Further, Lu et al.

investigated the dynamics of O_3 molecules reaction with a long-chain vinyl-terminated SAM with different incident energies of the molecular beam and surface temperatures.[107] Measurements of reaction probability indicate that the room-temperature reaction of O_3 with H_2C=CH-SAM follows L-H mechanism that requires accommodation first, while elevated translational energies transition the dynamics to the E-R mechanism. For the purpose of the investigation of the reaction dynamics involving the adjustable incident energy of NO_3, in Chapter 6 of this thesis, we employed molecular beam techniques and investigated the dynamics of NO_3 molecules collisions with a hydroxyl-functionalized monolayer.

1.5 Summary and Research Outlook

The study of heterogeneous reaction kinetics and mechanisms at the gas-solid interface is extraordinarily important for its significant role in environmental processes, especially in the formation and transformation of organic particulates in the atmosphere. A comprehensive understanding of such processes requires the microscopic details of how the surface structure and functionality chemically alter the reaction dynamics. Previous studies of heterogeneous reactions between gas-phase NO_3 and organic surfaces suggest that the reactions are likely initiated through hydrogen abstraction or electrophilic addition to the C=C bonds and terminated by the formation of nitrogen- (nitrates or nitro compounds) or oxygen-containing (ketones or aldehydes) compounds. However, the detailed reaction mechanism and how the surface functionality affect the reaction kinetics have yet to be elucidated.

Building on the previous work, we employed an ultrahigh vacuum (UHV) system combined with surface analytical techniques including reflection-absorption infrared spectroscopy (RAIRS), X-ray photoelectron spectroscopy (XPS), and quadrupole mass spectroscopy (QMS) to investigate the reaction dynamics of NO_3 collision with model organic surfaces. Our primary goal

is to gain insights into the effects of surface structure and functionality as well as the incident energy of NO_3 molecules on the overall reaction kinetics and mechanisms. Ultimately, the fundamental study described in this dissertation is aiming to develop a deep understanding of atmospherically relevant interactions and reactions of NO_3 on organic surfaces, which enable scientists to predict the fate of organic particles and their effect on the environment.

REFERENCES

(1) Aschmann, S. M.; Atkinson, R., Effect of Structure on the Rate Constants for Reaction of NO_3 Radicals with a Series of Linear and Branched C_5−C_7 1-Alkenes at 296 ± 2 K. *J. Phys. Chem. A* **2011,** *115* (8), 1358-1363.

(2) Disselkamp, R. S.; Carpenter, M. A.; Cowin, J. P.; Berkowitz, C. M.; Chapman, E. G.; Zaveri, R. A.; Laulainen, N. S., Ozone Loss in Soot Aerosols. *J. Geophys. Res. Atmos.* **2000,** *105* (D8), 9767-9771.

(3) Fry, J. L.; Sackinger, K., Model Investigation of No_3 Secondary Organic Aerosol (SOA) Source and Heterogeneous Organic Aerosol (OA) Sink in the Western United States. *Atmos. Chem. Phys.* **2012,** *12* (18), 8797-8811.

(4) Gai, Y.; Wang, W.; Ge, M.; Kjaergaard, H. G.; Jørgensen, S.; Du, L., Methyl Chavicol Reactions with Ozone, OH and NO_3 Radicals: Rate Constants and Gas-Phase Products. *Atmos. Environ.* **2013,** *77* (0), 696-702.

(5) Goeschen, U. W. a. C., Oxidative Damage of Thymidines by the Atmospheric Free-Radical Oxidant NO_3. *Aust. J. Chem.* **2011,** *64* (6), 833-842.

(6) Jee, J.; Tao, F.-M., Reaction Mechanisms and Kinetics for the Oxidations of Dimethyl Sulfide, Dimethyl Disulfide, and Methyl Mercaptan by the Nitrate Radical. *J. Phys. Chem. A* **2006,** *110* (24), 7682-7689.

(7) Noda, J.; Hallquist, M.; Langer, S.; Ljungstrom, E., Products from the Gas-Phase Reaction of Some Unsaturated Alcohols with Nitrate Radicals. *Phys. Chem. Chem. Phys.* **2000,** *2*, 2555-2564.

(8) Finlayson-Pitts, B. J.; Pitts Jr, J. N., *Chemistry of the Upper and Lower Atmosphere: Theory, Experiments, and Applications*. Academic press: 1999.

(9) Shiraiwa, M.; Poschl, U.; Knopf, D. A., Multiphase Chamical Kinetics of NO_3 Radicals Reacting with Organic Aerosol Components from Biomass Burning. *Environ. Sci. Technol.* **2012,** *46*, 6630-6636.

(10) Moise, T.; Talukdar, R. K.; Frost, G. J.; Fox, R. W.; Rudich, Y., Reactive Uptake of NO_3 by Liquid and Frozen Organics. *J. Geophys. Res., [Atmos.]* **2002,** *107* (D2), AAC 6-1-AAC 6-9.
(11) Olariu, R. I.; Barnes, I.; Bejan, I.; Arsene, C.; Vione, D.; Klotz, B.; Becker, K. H., Ft-Ir Product Study of the Reactions of NO_3 Radicals with Ortho-, Meta-, and Para-Cresol. *Environ. Sci. Technol.* **2013,** *47* (14), 7729-7738.
(12) Jariyasopit, N.; McIntosh, M.; Zimmermann, K.; Arey, J.; Atkinson, R.; Cheong, P. H.-Y.; Carter, R. G.; Yu, T.-W.; Dashwood, R. H.; Massey Simonich, S. L., Novel Nitro-PAH Formation from Heterogeneous Reactions of Pahs with NO_2, NO_3/N_2O_5, and OH Radicals: Prediction, Laboratory Studies, and Mutagenicity. *Environ. Sci. Technol.* **2013,** *48* (1), 412-419.
(13) Seinfeld, J. H.; Pandis, S. N., *Atmospheric Chemistry and Physics: From Air Pollution to Climate Change*. John Wiley & Sons: 2012.
(14) Brimblecombe, P., Interest in Air Pollution among Early Fellows of the Royal Society. *Notes and records of the Royal Society of London* **1978**, 123-129.
(15) Mamane, Y., Air Pollution Control in Israel During the First and Second Century. *Atmos. Environ.* **1987,** *21* (8), 1861-1863.
(16) Brimblecombe, P., *The Big Smoke: A History of Air Pollution in London since Medieval Times*. Routledge: 2011.
(17) Wilkins, E. T. *Air Pollution and the London Fog of December 1952*; J. R. Sanit. Inst.; (United States): 1954; pp 1-15.
(18) Buran, B.; Butler, L.; Currano, A.; Smith, E.; Tung, W.; Cleveland, K.; Buxton, C.; Lam, D.; Obler, T.; Rais-Bahrami, S.; Stryker, M.; Herold, K., Environmental Benefits of Implementing Alternative Energy Technologies in Developing Countries. *Appl. Energy* **2003,** *76* (1–3), 89-100.
(19) Wilson, P., The Dilemma of a More Advanced Developing Country: Conflicting Views on the Development Strategy of Singapore. *Dev. Econ.* **2000,** *38* (1), 105-134.
(20) Gautam, R.; Hsu, N. C.; Kafatos, M.; Tsay, S.-C., Influences of Winter Haze on Fog/Low Cloud over the Indo-Gangetic Plains. *J. Geophys. Res., [Atmos.]* **2007,** *112* (D5), n/a-n/a.
(21) Reid, J. S.; Hobbs, P. V.; Ferek, R. J.; Blake, D. R.; Martins, J. V.; Dunlap, M. R.; Liousse, C., Physical, Chemical, and Optical Properties of Regional Hazes Dominated by Smoke in Brazil. *J. Geophys. Res., [Atmos.]* **1998,** *103* (D24), 32059-32080.
(22) Middleton, W. E. K., Vision through the Atmosphere. In *Geophysik Ii / Geophysics Ii*, Bartels, J., Ed. Springer Berlin Heidelberg: 1957; Vol. 10 / 48, pp 254-287.
(23) Stolarski, R. S.; Baughcum, S. L.; Brune, W. H.; Douglass, A. R.; Fahey, D. W.; Friedl, R. R.; Liu, S. C.; Plumb, R. A.; Poole, L. R.; Wesoky, H. L., The 1995 Scientific Assessment of the Atmospheric Effects of Stratospheric Aircraft. NASA; Washington, DC, United States, 1995.
(24) Ellison, G. B.; Tuck, A. F.; Vaida, V., Atmospheric Processing of Organic Aerosols. *J. Geophys. Res.* **1999,** *104* (D9), 11633-11641.
(25) Simoneit, B. R. T.; Cox, R. E.; Standley, L. J., Organic Matter of the Troposphere—Iv. Lipids in Harmattan Aerosols of Nigeria. *Atmos. Environ.* **1988,** *22* (5), 983-1004.
(26) Cooper, J. E.; Bray, E. E., A Postulated Role of Fatty Acids in Petroleum Formation. *Geochim. Cosmochim. Acta* **1963,** *27* (11), 1113-1127.

(27) Chen, X.; Simoneit, B. T., Epicuticular Waxes from Vascular Plants and Particles in the Lower Troposphere: Analysis of Lipid Classes by Iatroscan Thin-Layer Chromatography with Flame Ionization Detection. *J. Atmos. Chem.* **1994,** *18* (1), 17-31.
(28) EPA; Agency, U. S. E. P. *National Air Pollutant Emission Trends, 1900-1996*; December 1997, 1997.
(29) Rogge, W. F.; Hildemann, L. M.; Mazurek, M. A.; Cass, G. R.; Simoneit, B. R. T., Sources of Fine Organic Aerosol. 2. Noncatalyst and Catalyst-Equipped Automobiles and Heavy-Duty Diesel Trucks. *Environ. Sci. Technol.* **1993,** *27* (4), 636-651.
(30) Bond, T. C.; Bergstrom, R. W., Light Absorption by Carbonaceous Particles: An Investigative Review. *Aerosol Sci. Technol.* **2006,** *40* (1), 27-67.
(31) Rogge, W. F.; Hildemann, L. M.; Mazurek, M. A.; Cass, G. R.; Simoneit, B. R. T., Sources of Fine Organic Aerosol. 6. Cigaret Smoke in the Urban Atmosphere. *Environ. Sci. Technol.* **1994,** *28* (7), 1375-1388.
(32) Satsumabayashi, H.; Kurita, H.; Yokouchi, Y.; Ueda, H., Photochemical Formation of Particulate Dicarboxylic Acids under Long-Range Transport in Central Japan. *Atmos. Environ. A* **1990,** *24* (6), 1443-1450.
(33) Grosjean, D., In Situ Organic Aerosol Formation During a Smog Episode: Estimated Production and Chemical Functionality. *Atmos. Environ. A* **1992,** *26* (6), 953-963.
(34) Rogge, W. F.; Mazurek, M. A.; Hildemann, L. M.; Cass, G. R.; Simoneit, B. R. T., Quantification of Urban Organic Aerosols at a Molecular Level: Identification, Abundance and Seasonal Variation. *Atmos. Environ. A* **1993,** *27* (8), 1309-1330.
(35) Rogge, W. F.; Hildemann, L. M.; Mazurek, M. A.; Cass, G. R.; Simoneit, B. R. T., Mathematical Modeling of Atmospheric Fine Particle-Associated Primary Organic Compound Concentrations. *J. Geophys. Res., [Atmos.]* **1996,** *101* (D14), 19379-19394.
(36) Gundel, L. A.; Dalsey, J. M.; de Carvalho, L. R. F.; Kado, N. Y.; Schuetzle, D., Polar Organic Matter in Airborne Particles: Chemical Characterization and Mutagenic Activity. *Environ. Sci. Technol.* **1993,** *27* (10), 2112-2119.
(37) Chughtai, A. R.; Brooks, M. E.; Smith, D. M., Hydration of Black Carbon. *J. Geophys. Res., [Atmos.]* **1996,** *101* (D14), 19505-19514.
(38) Xiong, J. Q.; Zhong, M.; Fang, C.; Chen, L. C.; Lippmann, M., Influence of Organic Films on the Hygroscopicity of Ultrafine Sulfuric Acid Aerosol. *Environ. Sci. Technol.* **1998,** *32* (22), 3536-3541.
(39) Chang, D. P. Y.; Hill, R. C., Retardation of Aqueous Droplet Evaporation by Air Pollutants. *Atmos. Environ.* **1980,** *14* (7), 803-807.
(40) Dockery, D. W.; Pope, C. A.; Xu, X.; Spengler, J. D.; Ware, J. H.; Fay, M. E.; Ferris, B. G.; Speizer, F. E., An Association between Air Pollution and Mortality in Six U.S. Cities. *N. Engl. J. Med.* **1993,** *329* (24), 1753-1759.
(41) Platt, U. F.; Winer, A. M.; Biermann, H. W.; Atkinson, R.; Pitts, J. N., Measurement of Nitrate Radical Concentrations in Continental Air. *Environ. Sci. Technol.* **1984,** *18* (5), 365-369.
(42) Winer, A. M.; Atkinson, R.; Pitts, J. N., Gaseous Nitrate Radical - Possible Nighttime Atmospheric Sink for Biogenic Organic-Compounds. *Science* **1984,** *224* (4645), 156-159.
(43) Platt, U.; LeBras, G.; Poulet, G.; Burrows, J. P.; Moortgat, G., Peroxy Radicals from Night-Time Reaction of NO_3 with Organic Compounds. *Nature* **1990,** *348* (6297), 147-149.

(44) Solomon, S.; Miller, H. L.; Smith, J. P.; Sanders, R. W.; Mount, G. H.; Schmeltekopf, A. L.; Noxon, J. F., Atmospheric NO_3: 1. Measurement Technique and the Annual Cycle at 40°N. *J. Geophys. Res., [Atmos.]* **1989,** *94* (D8), 11041-11048.
(45) Brown, S. S.; Stutz, J., Nighttime Radical Observations and Chemistry. *Chem. Soc. Rev.* **2012,** *41* (19), 6405-6447.
(46) Hoyle, C. R.; Boy, M.; Donahue, N. M.; Fry, J. L.; Glasius, M.; Guenther, A.; Hallar, A. G.; Huff Hartz, K.; Petters, M. D.; Petäjä, T.; Rosenoern, T.; Sullivan, A. P., A Review of the Anthropogenic Influence on Biogenic Secondary Organic Aerosol. *Atmos. Chem. Phys.* **2011,** *11* (1), 321-343.
(47) Breider, T. J.; Chipperfield, M. P.; Richards, N. A. D.; Carslaw, K. S.; Mann, G. W.; Spracklen, D. V., Impact of BrO on Dimethylsulfide in the Remote Marine Boundary Layer. *Geophys. Res. Lett.* **2010,** *37* (2), L02807.
(48) Wayne, R. P.; Barnes, I.; Biggs, P.; Burrows, J. P.; Canosamas, C. E.; Hjorth, J.; Lebras, G.; Moortgat, G. K.; Perner, D.; Poulet, G.; Restelli, G.; Sidebottom, H., The Nitrate Radical - Physics, Chemistry, and the Atmosphere. *Atmos. Environ. A-Gen.* **1991,** *25* (1), 1-203.
(49) Geyer, A.; Alicke, B.; Konrad, S.; Schmitz, T.; Stutz, J.; Platt, U., Chemistry and Oxidation Capacity of the Nitrate Radical in the Continental Boundary Layer near Berlin. *J. Geophys. Res. Atmos.* **2001,** *106* (D8), 8013-8025.
(50) Platt, U.; Perner, D.; Winer, A. M.; Harris, G. W.; Pitts, J. N., Detection of NO_3 in the Polluted Troposphere by Differential Optical-Absorption. *Geophys. Res. Lett.* **1980,** *7* (1), 89-92.
(51) Magnotta, F.; Johnston, H. S., Photodissociation Quantum Yields for the NO_3 Free Radical. *Geophys. Res. Lett.* **1980,** *7* (10), 769-772.
(52) Orlando, J. J.; Tyndall, G. S.; Moortgat, G. K.; Calvert, J. G., Quantum Yields for Nitrate Radical Photolysis between 570 and 635 nm. *J. Phys. Chem.* **1993,** *97* (42), 10996-11000.
(53) Atkinson, R., Kinetics and Mechanisms of the Gas‐Phase Reactions of the NO_3 Radical with Organic Compounds. *J. Phys. Chem. Ref. Data* **1991,** *20* (3), 459-507.
(54) Okabe, H., *Photochemistry of Small Molecules*. Wiley: New York, 1978.
(55) Blacet, F. E., Photochemistry in the Lower Atmosphere. *Ind. Eng. Chem.* **1952,** *44*, 1339-1342.
(56) Blacet, F. E., Photochemistry in the Lower Atmosphere. *Ind. Eng. Chem.* **1952,** *44* (6), 1339-1342.
(57) Kurpius, M. R.; Goldstein, A. H., Gas-Phase Chemistry Dominates O_3 Loss to a Forest, Implying a Source of Aerosols and Hydroxyl Radicals to the Atmosphere. *Geophys. Res. Lett.* **2003,** *30* (7), 1371.
(58) Li, S.; Matthews, J.; Sinha, A., Atmospheric Hydroxyl Radical Production from Electronically Excited NO_2 and H_2O. *Science* **2008,** *319* (5870), 1657-1660.
(59) Tuazon, E. C.; Alvarado, A.; Aschmann, S. M.; Atkinson, R.; Arey, J., Products of the Gas-Phase Reactions of 1,3-Butadiene with OH and NO_3 Radicals. *Environ. Sci. Technol.* **1999,** *33* (20), 3586-3595.
(60) Oizmann, M.; Benter, T.; Liesner, M.; Schindler, R. N., On the Pressure Dependence of the NO_2 Product Yield in the Reaction of NO_3 Radicals with Selected Alkenes. *Atmos. Environ.* **1994,** *28* (16), 2677-2683.
(61) Berndt, T.; Böge, O., Products and Mechanism of the Reaction of NO_3 with Selected Acyclic Monoalkenes. *J. Atmos. Chem.* **1995,** *21* (3), 275-291.

(62) Atkinson, R.; Arey, J., Atmospheric Degradation of Volatile Organic Compounds. *Chem. Rev.* **2003,** *103* (12), 4605-4638.
(63) Brown, S. S.; Stutz, J., Nighttime Radical Observations and Chemistry. *Chem. Soc. Rev.* **2012,** *41*, 6405-6447.
(64) Gong, H.; Matsunaga, A.; Ziemann, P. J., Products and Mechanism of Secondary Organic Aerosol Formation from Reactions of Linear Alkenes with NO_3 Radicals. *J. Phys. Chem. A* **2005,** *109* (19), 4312-4324.
(65) Hjorth, J.; Lohse, C.; Nielsen, C. J.; Skov, H.; Restelli, G., Products and Mechanisms of the Gas-Phase Reactions between Nitrate Radical and a Series of Alkenes. *J. Phys. Chem.* **1990,** *94* (19), 7494-7500.
(66) Atkinson, R., Atmospheric Chemistry of VOCs and NO_x. *Atmos. Environ.* **2000,** *34* (12–14), 2063-2101.
(67) Moreno, A.; Salgado, M. S.; Martín, M. P.; Martínez, E.; Cabañas, B., Kinetic Study of the Gas Phase Reactions of a Series of Alcohols with the NO_3 Radical. *J. Phys. Chem. A* **2012,** *116* (42), 10383-10389.
(68) Chew, A. A.; Atkinson, R.; Aschmann, S. M., Kinetics of the Gas-Phase Reactions of NO_3 Radicals with a Series of Alcohols, Glycol Ethers, Ethers and Chloroalkenes. *J. Chem. Soc., Faraday Trans.* **1998,** *94* (8), 1083-1089.
(69) Gross, S.; Bertram, A. K., Products and Kinetics of the Reactions of an Alkane Monolayer and a Terminal Alkene Monolayer with NO_3 Radicals. *J. Geophys. Res., [Atmos.]* **2009,** *114* (D2), n/a-n/a.
(70) Liu, C.; Zhang, P.; Wang, Y.; Yang, B.; Shu, J., Heterogeneous Reactions of Particulate Methoxyphenols with No3 Radicals: Kinetics, Products, and Mechanisms. *Environ. Sci. Technol.* **2012,** *46* (24), 13262-13269.
(71) Zhao, Z.; Husainy, S.; Stoudemayer, C. T.; Smith, G. D., Reactive Uptake of NO_3 Radicals by Unsaturated Fatty Acid Particles. *Phys. Chem. Chem. Phys.* **2011,** *13* (39), 17809-17817.
(72) Hu, D.; Tolocka, M.; Li, Q.; Kamens, R. M., A Kinetic Mechanism for Predicting Secondary Organic Aerosol Formation from Toluene Oxidation in the Presence of NO_x and Natural Sunlight. *Atmos. Environ.* **2007,** *41* (31), 6478-6496.
(73) Gross, S.; Bertram, A. K., Reactive Uptake of NO_3, N_2O_5, NO_2, HNO_3, and O_3 on Three Types of Polycyclic Aromatic Hydrocarbon Surfaces. *J. Phys. Chem. A* **2008,** *112* (14), 3104-3113.
(74) Yang, B.; Meng, J.; Zhang, Y.; Liu, C.; Gan, J.; Shu, J., Experimental Studies on the Heterogeneous Reaction of NO_3 Radicals with Suspended Carbaryl Particles. *Atmos. Environ.* **2011,** *45* (12), 2074-2079.
(75) Gao, S.; Zhang, Y.; Li, Y.; Meng, J.; He, H.; Shu, J., A Comparison between the Vacuum Ultraviolet Photoionization Time-of-Flight Mass Spectra and the GC/MS Total Ion Chromatograms of Polycyclic Aromatic Hydrocarbons Contained in Coal Soot and Multi-Component Pah Particles. *Int. J. Mass Spectrom.* **2008,** *274* (1–3), 64-69.
(76) Smith, G. D.; Woods, E.; DeForest, C. L.; Baer, T.; Miller, R. E., Reactive Uptake of Ozone by Oleic Acid Aerosol Particles: Application of Single-Particle Mass Spectrometry to Heterogeneous Reaction Kinetics. *J. Phys. Chem. A* **2002,** *106* (35), 8085-8095.
(77) Gross, S.; Iannone, R.; Xiao, S.; Bertram, A. K., Reactive Uptake Studies of NO_3 and N_2O_5 on Alkenoic Acid, Alkanoate, and Polyalcohol Substrates to Probe Nighttime Aerosol Chemistry. *Phys. Chem. Chem. Phys.* **2009,** *11* (36), 7792-7803.

(78) Xiao, S.; Bertram, A. K., Reactive Uptake Kinetics of NO_3 on Multicomponent and Multiphase Organic Mixtures Containing Unsaturated and Saturated Organics. *Phys. Chem. Chem. Phys.* **2011,** *13* (14), 6628-6636.
(79) Zhang, Y.; Yang, B.; Gan, J.; Liu, C.; Shu, X.; Shu, J., Nitration of Particle-Associated Pahs and Their Derivatives (Nitro-, Oxy-, and Hydroxy-Pahs) with No_3 Radicals. *Atmos. Environ.* **2011,** *45* (15), 2515-2521.
(80) Knopf, D. A.; Mak, J.; Gross, S.; Bertram, A. K., Does Atmospheric Processing of Saturated Hydrocarbon Surfaces by NO_3 Lead to Volatilization? *Geophys. Res. Lett.* **2006,** *33* (17), L17816.
(81) Molina, M. J.; Ivanov, A. V.; Trakhtenberg, S.; Molina, L. T., Atmospheric Evolution of Organic Aerosol. *Geophys. Res. Lett.* **2004,** *31* (22), L22104.
(82) Lu, J. W.; Day, B. S.; Fiegland, L. R.; Davis, E. D.; Alexander, W. A.; Troya, D.; Morris, J. R., Interfacial Energy Exchange and Reaction Dynamics in Collisions of Gases on Model Organic Surfaces. *Prog. Surf. Sci.* **2012,** *87* (9–12), 221-252.
(83) Nathanson, G. M., Molecular Beam Studies of Gas-Liquid Interfaces. *Annu. Rev. Phys. Chem.* **2004,** *55* (1), 231-255.
(84) Levine, R. D., *Molecular Reaction Dynamics*. Cambridge University Press: 2005.
(85) Kleyn, A. W., Molecular Beams and Chemical Dynamics at Surfaces. *Chem. Soc. Rev.* **2003,** *32* (2), 87-95.
(86) Rettner, C. T.; Auerbach, D. J.; Tully, J. C.; Kleyn, A. W., Chemical Dynamics at the Gas−Surface Interface. *J. Phys. Chem.* **1996,** *100* (31), 13021-13033.
(87) Adamson, A. W.; Gast, A. P., Physical Chemistry of Surfaces. **1967**.
(88) Rettner, C. T.; Auerbach, D. J., Distinguishing the Direct and Indirect Products of a Gas-Surface Reaction. *Science* **1994,** *263* (5145), 365-367.
(89) King, D. A.; Wells, M. G., Molecular Beam Investigation of Adsorption Kinetics on Bulk Metal Targets: Nitrogen on Tungsten. *Surf. Sci.* **1972,** *29* (2), 454-482.
(90) Weinberg, W.; Rettner, C.; Ashfold, M., Dynamics of Gas Surface Interactions. Royal Society of Chemistry, London: 1991.
(91) Mhairi, A.; Paul, A. J. B.; Sven, P. K. K.; Stewart, K. R.; Robin, E. W.; Matthew, L. C.; Kenneth, G. M., Dynamics of Interfacial Reactions between $O(^3P)$ Atoms and Long-Chain Liquid Hydrocarbons. *Phys. Scr.* **2007,** *76* (3), C42.
(92) Logan, R. M.; Stickney, R. E., Simple Classical Model for the Scattering of Gas Atoms from a Solid Surface. *J. Chem. Phys.* **1966,** *44* (1), 195-201.
(93) Logan, R. M.; Keck, J. C., Classical Theory for the Interaction of Gas Atoms with Solid Surfaces. *J. Chem. Phys.* **1968,** *49* (2), 860-876.
(94) Yan, T.; Hase, W. L.; Tully, J. C., A Washboard with Moment of Inertia Model of Gas-Surface Scattering. *J. Chem. Phys.* **2004,** *120* (2), 1031-1043.
(95) Day, B. S., The Dynamics of Gas-Surface Energy Transfer in Collisions of Rare Gases with Organic Thin Films. **2005**.
(96) Cohen, S. R.; Naaman, R.; Sagiv, J., Translational Energy Transfer from Molecules and Atoms to Adsorbed Organic Monolayers of Long-Chain Amphiphiles. *Phys. Rev. Lett.* **1987,** *58* (20), 2153-2153.
(97) Isa, N.; Gibson, K. D.; Yan, T.; Hase, W.; Sibener, S. J., Experimental and Simulation Study of Neon Collision Dynamics with a 1-Decanethiol Monolayer. *J. Chem. Phys.* **2004,** *120* (5), 2417-2433.

(98) Gibson, K. D.; Isa, N.; Sibener, S. J., Experiments and Simulations of Ar Scattering from an Ordered 1-Decanethiol–Au(111) Monolayer. *J. Chem. Phys.* **2003,** *119* (24), 13083-13095.
(99) Camillone, N.; Chidsey, C. E. D.; Eisenberger, P.; Fenter, P.; Li, J.; Liang, K. S.; Liu, G. Y.; Scoles, G., Structural Defects in Self‐Assembled Organic Monolayers Via Combined Atomic Beam and X‐Ray Diffraction. *J. Chem. Phys.* **1993,** *99* (1), 744-747.
(100) Ferguson, M. K.; Lohr, J. R.; Day, B. S.; Morris, J. R., Influence of Buried Hydrogen-Bonding Groups within Monolayer Films on Gas-Surface Energy Exchange and Accommodation. *Phys. Rev. Lett.* **2004,** *92* (7), 073201.
(101) Day, B. S.; Shuler, S. F.; Ducre, A.; Morris, J. R., The Dynamics of Gas-Surface Energy Exchange in Collisions of Ar Atoms with ω-Functionalized Self-Assembled Monolayers. *J. Chem. Phys.* **2003,** *119* (15), 8084-8096.
(102) Shuler, S. F.; Davis, G. M.; Morris, J. R., Energy Transfer in Rare Gas Collisions with Hydroxyl- and Methyl-Terminated Self-Assembled Monolayers. *J. Chem. Phys.* **2002,** *116* (21), 9147-9150.
(103) Day, B. S.; Morris, J. R., Packing Density and Structure Effects on Energy-Transfer Dynamics in Argon Collisions with Organic Monolayers. *J. Chem. Phys.* **2005,** *122* (23), 234714.
(104) Tasić, U.; Day, B. S.; Yan, T.; Morris, J. R.; Hase, W. L., Chemical Dynamics Study of Intrasurface Hydrogen-Bonding Effects in Gas−Surface Energy Exchange and Accommodation. *J. Phys. Chem. C* **2007,** *112* (2), 476-490.
(105) Lu, J. W.; Morris, J. R., Gas–Surface Scattering Dynamics of CO_2, NO_2, and O_3 in Collisions with Model Organic Surfaces. *J. Phys. Chem. A* **2011,** *115* (23), 6194-6201.
(106) D'Andrea, T. M.; Zhang, X.; Jochnowitz, E. B.; Lindeman, T. G.; Simpson, C.; David, D. E.; Curtiss, T. J.; Morris, J. R.; Ellison, G. B., Oxidation of Organic Films by Beams of Hydroxyl Radicals. *J. Phys. Chem. B* **2008,** *112* (2), 535-544.
(107) Lu, J. W.; Fiegland, L. R.; Davis, E. D.; Alexander, W. A.; Wagner, A.; Gandour, R. D.; Morris, J. R., Initial Reaction Probability and Dynamics of Ozone Collisions with a Vinyl-Terminated Self-Assembled Monolayer. *J. Phys. Chem. C* **2011,** *115* (51), 25343-25350.

Chapter 2

Experimental Approach and Techniques

2.1 Background

Our research goal is to develop a fundamental understanding of gas-surface reactions between NO_3 and model organic surfaces. The interfacial reactions of NO_3 with organic particulates are important because the reactions have an effect on the scattering and absorption of light by those particles through changing their properties, such as particle size and chemical components (Chapter 1). In this chapter, a detailed description of the experimental approach for the investigation of interfacial reaction kinetics and mechanism will be given specifically for advanced ultrahigh vacuum (UHV) based instrumentation, self-assembled monolayers as model organic surfaces, and molecular beam techniques. In the ambient environment, gases are constantly colliding with organic surfaces that result in contamination and modification of surface-bound species through adsorption or reaction. The UHV system minimizes unwanted reactions of background gases with the sample surface to be studied by increasing the amount of time the surface remains clean. The minimal time for a clean surface to be fully covered with a monolayer can be estimated by assuming a unit sticking probability (S = 1). At atmospheric pressure, this time would be ~1 ns. At the pressure of 10^{-6} Torr, a monolayer of coverage would be obtained after 1 s. However, at UHV pressures (< 10^{-9} Torr) it takes up to ~ 3 hrs to form a complete monolayer (at unit sticking probability). In addition, at pressures within this range, the mean free path (MFP) of a molecule, defined as the average distance a gas-phase molecule traveling between collisions,[1] is as large as 500 km. The low-pressure environments began to draw interest for research in 1960's since they could reproduce conditions in outer space.[2] Moreover, metals that

are often used as substrates for the exploration of fundamental interactions between a gas and a solid surface are stable in UHV conditions.[2] Lednovich and Fenn,[3] Nathanson and co-workers,[4] and Sibener and co-workers[5] are among the ones who pioneered the study of collision dynamics of a gas with a liquid/solid surface under UHV conditions. In this thesis, the UHV system enables the implementation of surface analytical techniques, such as X-ray photoelectron spectroscopy (XPS) and mass spectroscopy (MS). Self-assembled monolayers serve as model organic surfaces due to their easy preparation and thermal stability.[6] Using these tools, along with molecular beam techniques, we have embarked on a study aimed at developing a deep understanding of the reaction dynamics for gas-phase NO_3 with model organic surfaces.

2.2 Self-Assembled Monolayers

Bare metal surfaces tend to adsorb organic compounds readily to lower the surface free energy.[7] However, such surfaces are not well defined and present poor reproducibility.[6] Self-assembled monolayers (SAMs) provide a convenient strategy to organic surfaces in this project for the following reasons: (i) they can be used to introduce functional groups at the gas-solid interface; (ii) they are well ordered; (iii) they show high stability and reproducibility.[6] SAMs can be formed by the adsorption of organic molecules from solution or the gas phase onto the surface of solids.[8,9] The adsorbates then organize spontaneously into crystalline or semicrystalline structures. SAMs created from adsorption of alkanethiols on metal surfaces generally contain four components: a terminal functional group located precisely at the gas-solid interface, an organic spacer (usually a long alkane chain) connecting the terminal group, a head group that links the spacer and a metal substrate with a chemical bond (e.g., Au-S),[10] as shown in Figure 2.1 (A). Among all metal substrates, gold is most commonly used because gold is easy to obtain and pattern; gold is straightforward to prepare thin films through chemical adsorption, physical vapor

deposition, sputtering, or electrodeposition; and gold is an inert metal that does not react with atmospheric oxygen (O_2) and most chemicals.[6] For SAMs formed on gold surfaces, the sulfur head group covalently bonds to the gold substrate (bond strength of ~44 kcal/mol), and hence the resultant monolayers are quite stable.[11,12] Typically, the monolayer forms a $(\sqrt{3} \times \sqrt{3})R30°$ overlayer structure (Figure 2.1 (B)) on Au(111) regions.[13] The sulfur atoms are bound to the three-fold hollow site on the gold substrate and spaced by 4.99 Å.[14] This distance is greater than the distance of closest approach of the alkyl chains (4.24 Å).[15,16] Therefore, to maximize their van der Waals interactions and increase the monolayer stability, the hydrocarbon chains tilt away from the surface normal and rotate about the long axis of a methylene chain. For methyl-terminated SAMs (H_3C-SAMs), optimum interactions are achieved by a tilt angle (a) of ~30° and a twist angle (b) of ~52° which is defined as the rotation angle of the terminal carbon from its initial configuration.[17] The chain-chain attractive interactions contribute 1.4 – 1.8 kcal/mol per methylene unit to the stabilization of the monolayer and the density of the chains is 4.67×10^{14} molecule cm^{-2}.[18]

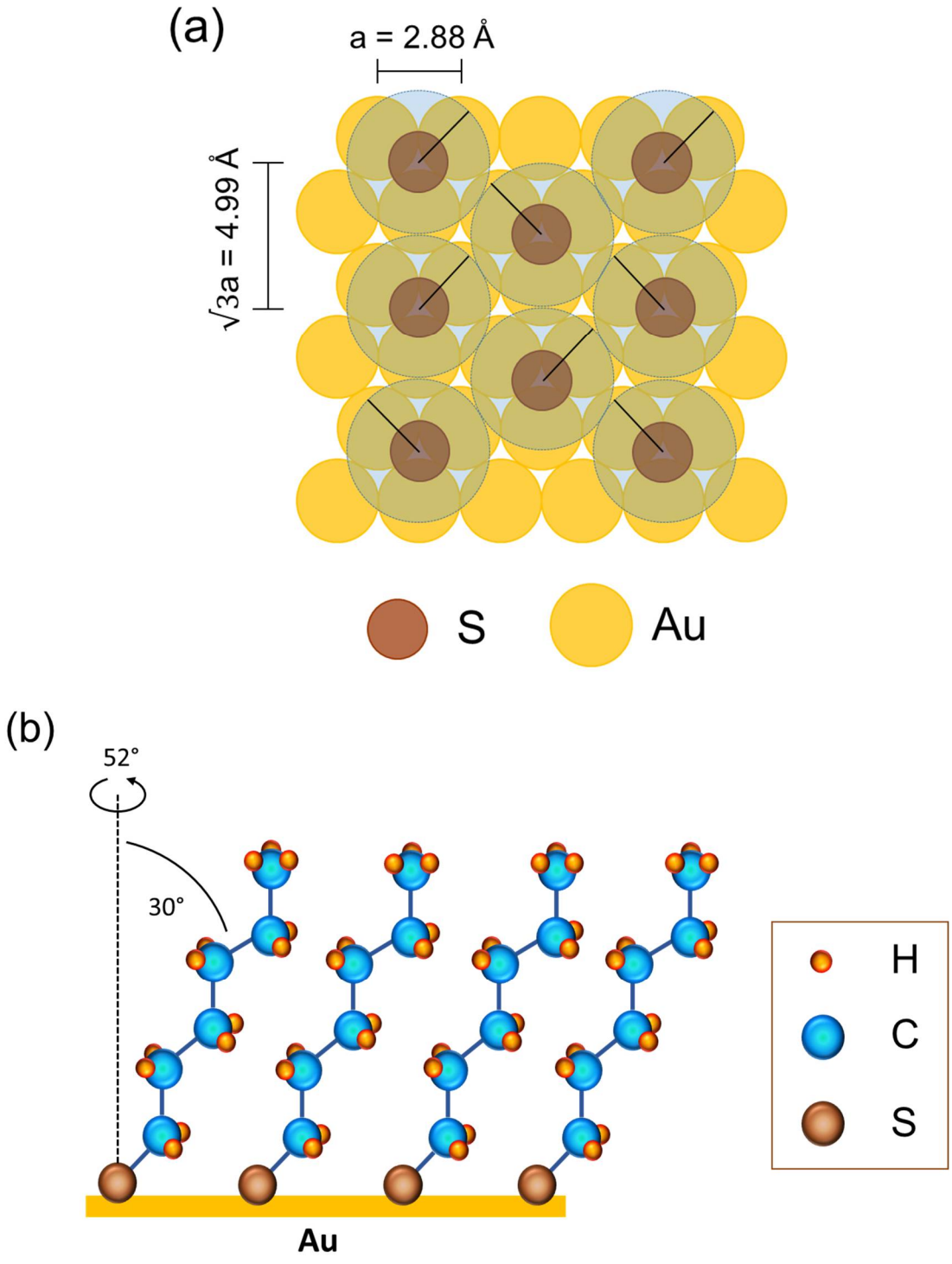

Figure 2.1. (a) Schematic diagram of alkanethiol adsorbed on Au(111) lattice depicting a ($\sqrt{\mathbf{3}} \times \sqrt{\mathbf{3}}$) R30° structure where the sulfur atoms are positioned in the 3-fold hollows of the gold lattice. The light blue circles with the dashed lines indicate the approximated projected surface area occupied by each alkane chain, and the solid black lines indicate the projection of the C-C-C plane of the alkane chain onto the surface. (b) The self-assembled monolayer, with CH_3-functionality, showing a tilt angle (α = 30°) and a twist angle (β = 52°).

2.3 Preparation of Model Organic Surfaces

The 1-decanethiol (96%) and 1-octadecanethiol (98.5%) used in this project were purchased from Sigma-Aldrich, Inc. The 17-octadecene-1-thiols were synthesized by members of the Morris research group according to procedures established by Hu and Fox.[19] The molecules were verified to be >99% pure by ^{1}H NMR measurements (see Chapter 2 of thesis written by Larry R. Fiegland).[20] The 16-mercapto-1-hexadecanol was purchased from Frontier Scientific, Inc. The ω-functionalized SAMs were formed by thermodynamically spontaneous chemisorption of alkanethiols onto polycrystalline gold slides. The gold slides employed in this study were commercially available (EMF Corp) and created by coating a thin layer (~50 nm) of chromium onto glass slides to strongly bind a 1000 Å layer of gold to the substrate. These gold substrates were immersed in a piranha solution (composed of 70% sulfuric acid and 30% hydrogen peroxide) for ~1 h to remove surface contamination. The Au surfaces were then taken out of the piranha solution and rinsed thoroughly with deionized water (Millipore Purification Systems, 18.2 MΩ). Each substrate was dried with a stream of ultrahigh purity nitrogen (UHP N_2) and immediately placed in a freshly prepared 1 mM solution of the corresponding thiol solution for at least 24 hours to achieve a well-ordered and tightly packed monolayer. The SAMs were then rinsed with the solvent of the thiol solution (ethanol or hexane) and dried under a stream of UHP N_2 before being placed into the UHV chamber through a sample transfer load-lock system.

2.4 UHV Main, Detector, and Load-Lock Chambers

All experiments were performed in an ultrahigh vacuum (UHV) surface science instrument designed by Larry R. Fiegland[20] for the study of the kinetics and mechanisms of reactions between nitrate radicals and model organic surfaces. The UHV main chamber is isolated from the load-lock

chamber by a manual gate valve so that the load lock chamber can be vented with ultrahigh purity (UHP) N_2 while switching samples. Once a SAM sample is prepared and put into the load-lock chamber, the chamber was then evacuated to high vacuum pressures (~10^{-5} - 10^{-7} Torr) by a LN_2-cooled sorption pump and a small turbo pump (Agilent, 700 L s^{-1}). A linear translator installed on the load lock allows horizontal transfer of samples onto the sample mount at the end of the manipulator in the main chamber, see Figure 2.2. With a resistive heater nestled inside the mount and a liquid nitrogen (LN_2) reservoir attached to the back, the sample mount can be utilized for kinetic studies over a wide range of surface temperatures. In addition, the surface temperature can be monitored during heating or cooling with a thermocouple attached to the sample mount.

The UHV main chamber has a base pressure of 10^{-9} Torr that eliminates reactions of background gases with the surface and enables the implementation of analytical instruments. The Extrel quadrupole mass spectrometer (QMS, ABB Extrel, model: MEXM 1000) attached to the main chamber via a doubly-differentially pumped detector chamber allows for the detection of gas-phase products. The QMS is housed in the second stage of the doubly-differentially pumped chamber. Differential pumping is required during the dosing experiments to maintain a low pressure in the detector chamber. An X-ray photoelectron spectrometer (XPS) enables elemental characterization of the surface before and after reaction. An all-glass capillary array doser was employed to provide an effusive source of NO_3 radicals that impinge on the surface. The surface-bound species were tracked *in situ* using reflection-absorption infrared spectroscopy (RAIRS) during exposure.

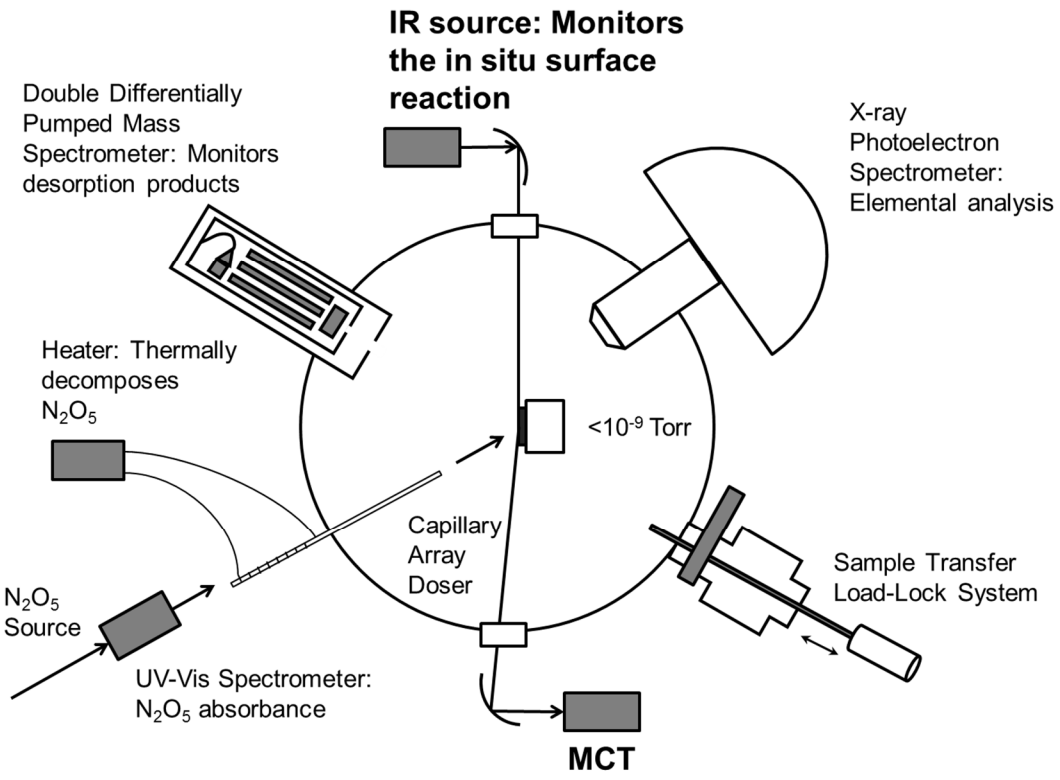

Figure 2.2. A schematic of the UHV system for surface analysis of NO_3 reactions with vinyl-terminated SAMs. All pre-exposure data were collected at a base pressure of $< 10^{-9}$ Torr. N_2O_5 gas molecules are characterized by UV-Vis spectroscopy prior to the thermal decomposition at the doser. In situ RAIRS is used to monitor the NO_3 reactions with the organic surface. Other aspects are described in the text.

2.5 Surface Characterization

Self-assembled monolayers formed from ω-functionalized alkanethiol adsorption onto gold substrates are a well-characterized system according to reported literature. To confirm that the SAMs used in our studies are reproducibly created and in agreement with published results, two surface-sensitive techniques were employed, reflection absorption infrared spectroscopy and X-ray photoelectron spectroscopy.

2.5.1 Reflection Absorption Infrared Spectroscopy (RAIRS)

The main technique used in our experiments, RAIRS, is non-destructive and can be performed without modification of the surface samples. Hence, the reaction between the model organic surfaces and the reactive gas could be monitored *in situ* as it progressed. Similar to the traditional FTIR spectroscopy, RAIRS utilizes a Michelson interferometer to make a full scan over the entire infrared region that has been studied. The interferometer outputs a time-domain interferogram which can be Fourier transformed into a frequency-domain spectrum.

The most important difference between traditional FTIR and RAIRS is the exploitation of reflection in RAIRS, which can give scientists information about chemical environment and the orientation of surface-bound molecules. In principle, the chemical compounds on the surface can absorb incoming light of specific frequencies in accordance with the surface-selection rule. The surface-selection rule was discovered by Greenler, who pioneered RAIRS measurements in 1960's.[21] Figure 2.3 shows a scheme of infrared radiation reflecting off a surface at a particular incident angle φ. Linearly polarized IR radiation reflected off a substrate surface can be resolved into two components: A P-polarized component (E_p), which is parallel to the incident plane, and an S-polarized component (E_s), which is perpendicular to the incident plane. Upon reflection, the S-polarized component undergoes a phase change of 180˚ at nearly all angles of incidence, which results in destructive interference and canceling out the amplitude of the S-polarized component at the surface.[21] In contrast, the P-polarized component undergoes an incident angle-dependent phase change. A grazing incidence of 88° induces a phase change of ~90° for the P-polarized component, which allows the P-component light to interfere constructively with itself. In addition to the behavior of light upon reflection, the other important phenomenon associated with RAIRS is related to the probability of a transition for a molecule on the surface, which depends on the

angle between the transition dipole moment and the electric field of the incident light, as illustrated in Equation (2.1):

$$P_T \propto |\boldsymbol{\mu}\, \boldsymbol{E}|^2 = |\mu|^2\, |E|^2 \cos^2\theta \qquad (2.1)$$

Where P_T is the probability of a transition, θ is the angle between the transition dipole moment ($\boldsymbol{\mu}$) and the incident light ($\boldsymbol{E}$). According to this relationship, the most probable transition from the ground state to the excited state of a particular vibration occurs when the surface active absorption modes have a component of their transition dipole moment perpendicular to the surface,.[21] This statement is known as the surface selection rule.

In our studies, reactions between NO_3 and SAMs were monitored using a Bruker IFS 66v/S spectrometer attached to the UHV chamber. Focused IR radiation from a SiC globar was reflected from the gold surface at ~86˚ relative to the surface normal through a differentially pumped KBr window. The reflected radiation was detected by a mid-range (750-4000 cm^{-1}) mercury cadmium telluride (MCT) detector, which was cooled by liquid nitrogen prior to each experiment.

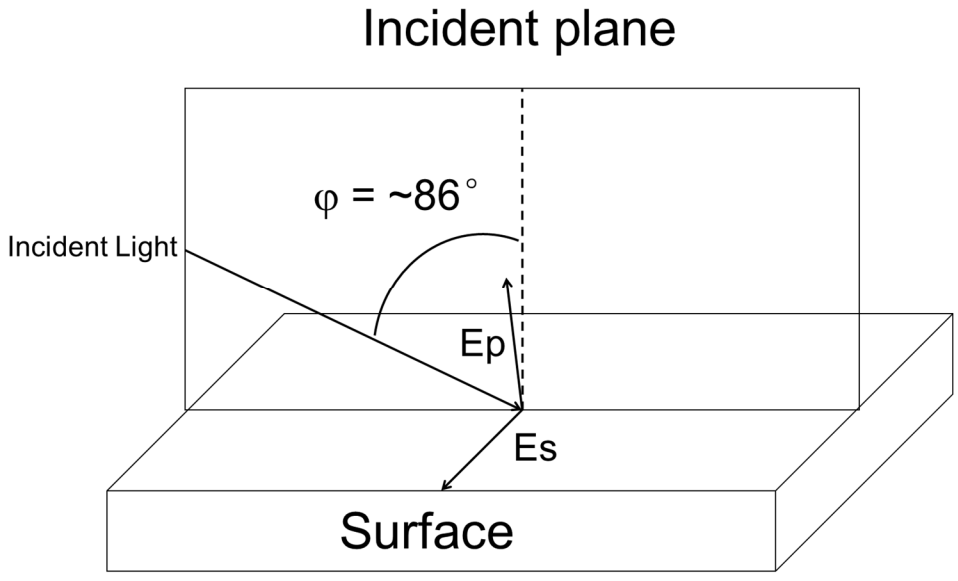

Figure 2.3. A Schematic depicting the two components of the electric field of light: E_s and E_p.

2.5.2 X-ray Photoelectron Spectroscopy (XPS)

X-ray photoelectron spectroscopy is another surface-sensitive technique that was employed in the experiments. XPS results provide information about the elemental composition and oxidation states of surface-bound molecules.[22,23] The theoretical basis behind XPS is Einstein's photoelectric effect, which states that electrons can be ejected from a metal surface by photons with sufficient energy.[24] Due to the different values of MFP (a measure of the average distance travelled by an ejected electron through a solid before it is inelastically scattered), electrons ejected from the bulk in the solid material do not efficiently escape the material while electrons at the surface are easily ejected. Therefore, the information gained from XPS is depth sensitive and can be controlled by the incident angle of the X-ray source relative to the sample orientation. Figure 2.4 demonstrates the one electron process that takes place during an XPS experiment, in which an electron is ejected from an inner shell orbital by an X-ray photon with a known energy, $h\nu$. The electron that escapes from the core-level orbital, with the binding energy, E_b, electronically excites the molecule, atom, or ions. The emitted electron that gains the kinetic energy, E_k, can be measured in the spectrometer. The elemental identity and local chemical environment can be determined by the binding energy. This binding energy is related to the energy of the incident photon ($h\nu$), the kinetic energy of the photoelectron (E_k), and the work function of the instrument (Φ), as shown in Equation (2.2):[25]

$$E_k = h\nu - \Phi - E_b \qquad (2.2)$$

Since the value of the work function depends on the surface material, the instrument should be recalibrated each time a new sample is introduced for XPS. Thus, the binding energy scales for all spectra were referenced to the Au ($4f_{7/2}$) peak at 83.8 eV.[26] In addition, the XPS data presented in this thesis was obtained by employing monochromatic radiation (Al Kα 1486.6 eV) from a

SPECS XR50 X-ray source operating at 250 W (12.5 kV and 20 mA). Ejected photoelectrons were detected using a 16.5” hemispherical energy analyzer (SPECS, Phoibos 100) operated at a take-off angle of 90º with respect to the surface.

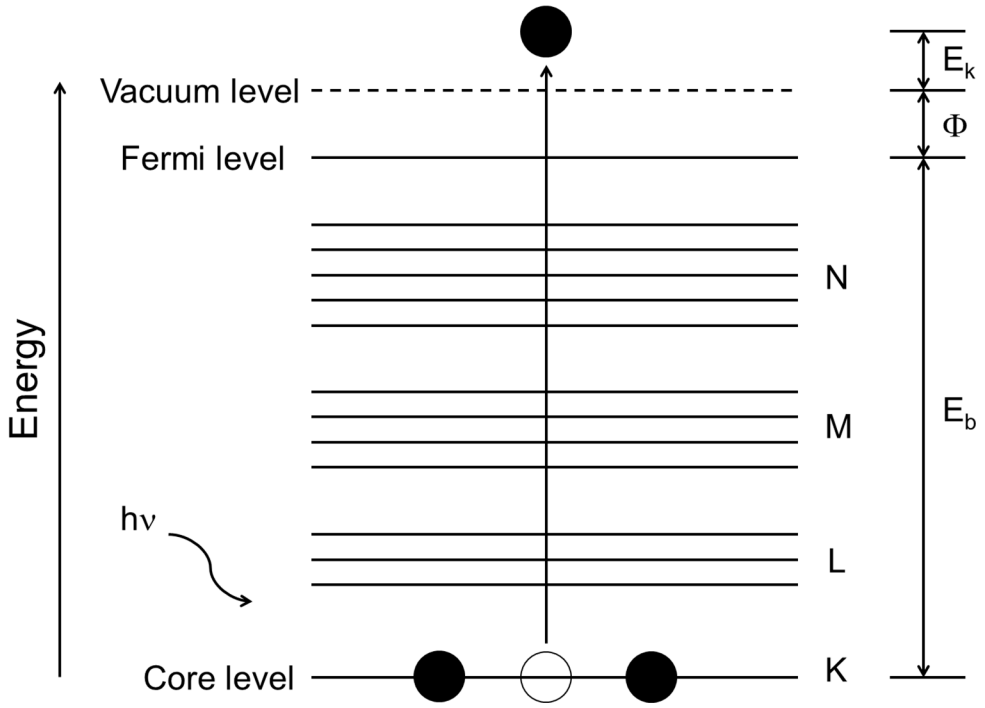

Figure 2.4. A depiction of the ejection of a core level electron upon X-ray illumination.

2.6 Generation of Nitrate Radicals (NO_3)

In order to work with high concentration of NO_3, the ability to synthesize and store large amounts for extended periods of time was required. Every time before any gas was introduced into the synthesis setup (Figure 2.5), the system was purged with UHP N_2 and then evacuated by a diaphragm pump (Pfeiffer Vacuum). After evacuation, the first step was the oxidation of nitrogen monoxide by an excess of ozone. This procedure initially formed N_2O_5 which was introduced into a glass trap submerged in a dry ice/ethanol bath, as shown in Figure 2.5. The entire setup was comprised of either glass or Teflon tubing considering the high reactivity of NO_3 on metal surfaces.

In addition, all valves used at junctions within the NO_3-generation setup were Swagelok® stainless steel Bellows-Sealed Valves (model: SS-4H).

During the dosing experiments, the trap was isolated from the dry ice/ethanol bath and warmed up with 0 °C ethanol. This step ensured that solid N_2O_5 was evaporated and delivered to the doser. Before NO_3 was produced, the storage system was evacuated to pressures below 1 Torr using a mechanical pump filled with Fomblin® oil. This step is to remove water, oxygen, ozone and other contaminants. NO_3 was then formed through thermal decomposition of N_2O_5 by heating the doser. The flux of N_2O_5 onto the surface was estimated from a calculation based on the pressure of N_2O_5 near the doser, the physical dimensions of the doser, and the kinetic theory of gases. The pressure of the N_2O_5 gas was measured by a full-range gauge (Pfeiffer Vacuum) and the temperature at the doser was monitored with a K-type thermocouple. While dosing with the capillary array doser, the high pressure side of the capillary was ~30 Torr, the pressures within the UHV chamber reached ~1×10^{-6} Torr, and the conductance of the capillary array doser was 4.1×10^{-4} cm^3 s^{-1}. The flux of N_2O_5 (2.3×10^{15} molecules s^{-1}) onto the surface was estimated from a calculation based on the kinetic theory of gases. According to the physical dimensions of the doser and the temperature-dependent equilibrium constant for $NO_3 + NO_2 \rightleftharpoons N_2O_5$ ($K_{eq} = 2.7 \times 10^{-27} \times \exp(11000/T)$ cm^3 $molecule^{-1}$),[27,28] the concentration of NO_3 adjacent to the surface for our doser temperature of 324 K, $[NO_3]_g$, was determined to be 2.8×10^{10} molecules cm^{-3}. The calculated flux was consistent with the pressure change in the vacuum chamber during NO_3 exposure to a clean gold surface.

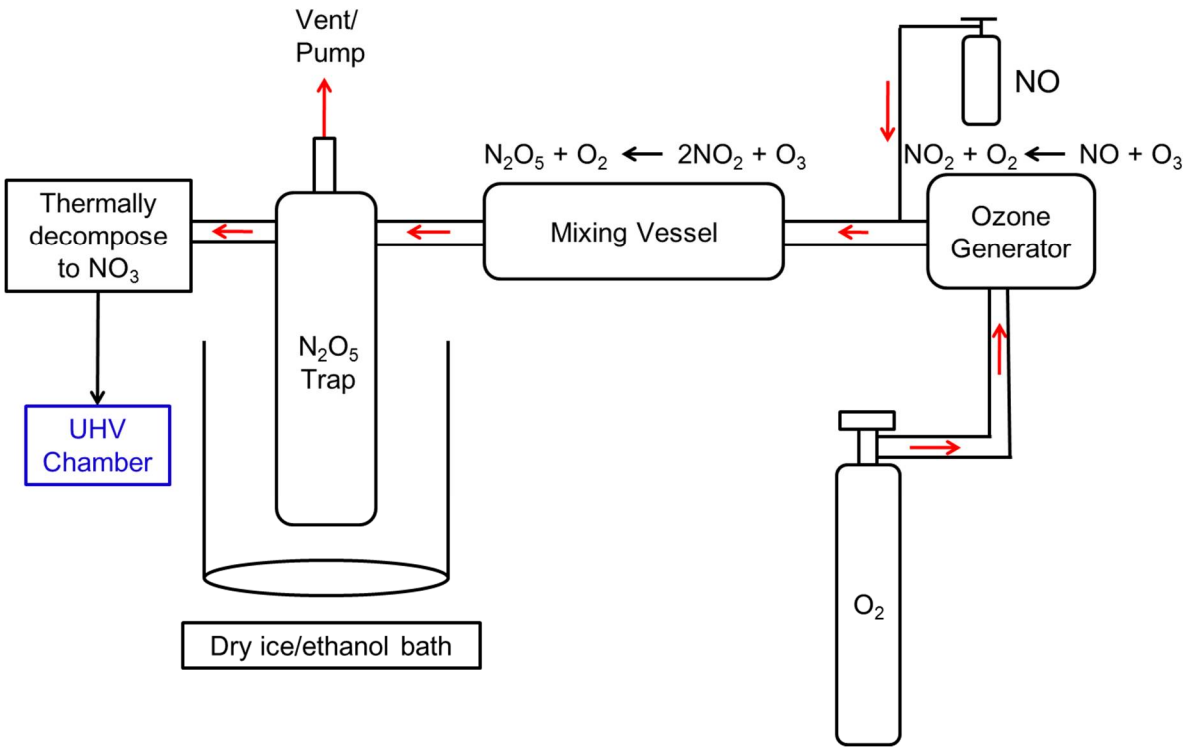

Figure 2.5. A schematic of NO_3 generation and storage system.

2.7 The Ultrahigh Vacuum Molecular Beam System

In addition to the study of reaction kinetics and mechanism of an effusive NO_3 beam (see Section 2.7.2) with ω-functionalized SAMs, the reaction dynamics have been explored by scattering a high-energy molecular beam of NO_3 from a hydroxyl-terminated SAM. All molecular beam scattering experiments were performed in a UHV chamber, designed similarly to the one shown in Figure 2.2. Three important features of the molecular beam chamber are the presence of a triply-differentially pumped source chamber that maintains the pressure of the main chamber $<2 \times 10^{-8}$ Torr even during beam exposure, the location of the detector chamber and that of the load-lock chamber relative to the source chamber. The load-lock chamber, which is located at the top tier of the main chamber is not horizontally aligned with the source chamber, while the detector

chamber and the source chamber share the same horizontal plane and both are located at the lower state of the main chamber.

2.7.1 The Source Chamber

To form molecular beams, gases at 700 Torr are introduced into the first differential stage of the source chamber through a 0.05 mm diameter nozzle (General Valve) which can be heated via current adjustment. After passing through a 0.40 mm diameter conical skimmer, the beam enters the second differential pumping stage where it collides with a doubly-slotted chopper wheel that rotates at 495 Hz for all experiments. The first differential chamber is constructed with a VHS Diffusion Pump (Varian Vacuum Technologies, 5000 L s^{-1}) to accommodate the large pressure load from the gas source. The second differential chamber utilizes a Diffstak® MK2 Diffusion Pump (BOC Edwards, 1500 L s^{-1}) to pump away background and effusive gases. The beam finally passes through a 1.5 mm collimating aperture to enter the third differential stage pumped by a Pfieffer TMU 261P turbo (250 L s^{-1}) prior to the access to the main chamber that is separated from the source chamber by a 2.2 mm diameter gate aperture. Figure 2.6 shows a schematic description of the source chamber used in our lab to create and collimate the molecular beams.

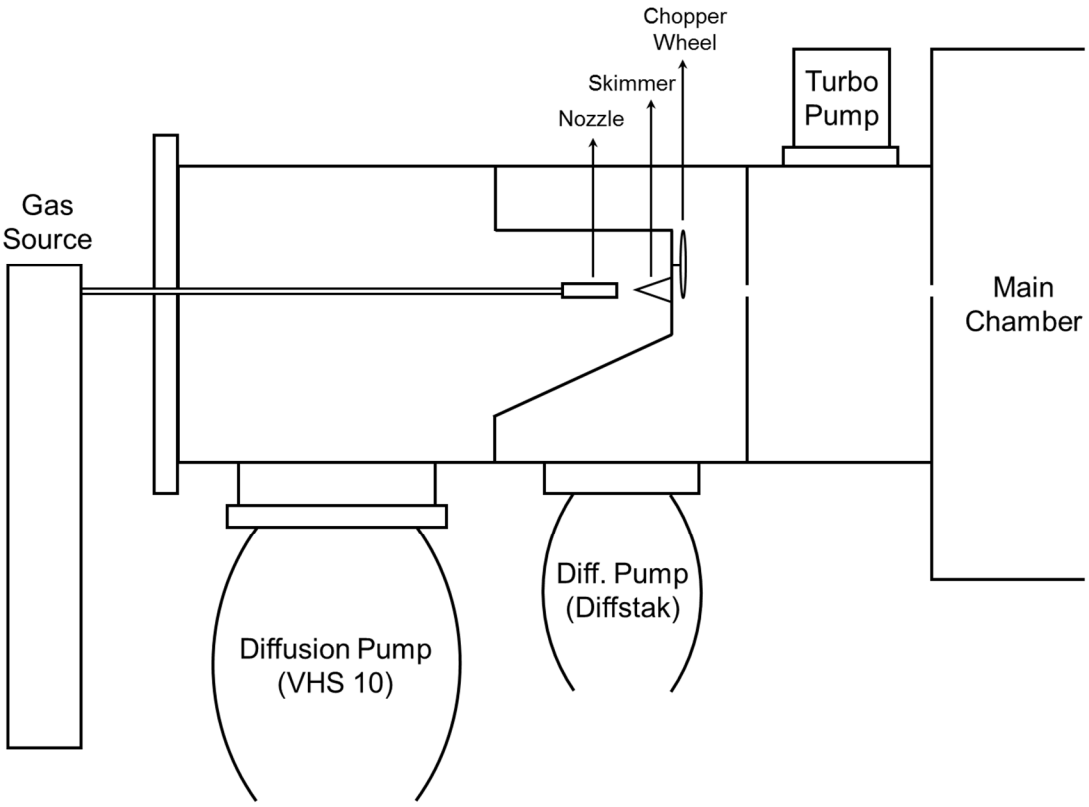

Figure 2.6. Side view of the source chamber.

2.7.2 Molecular Beams

Molecular-beam techniques are employed to investigate the reaction dynamics of gas-phase NO_3 collision with model organic surfaces in the UHV chamber because they provide an indirect method of probing the microscopic details of gas-surface interactions. A molecular beam is a source of molecules with a well-defined cross sectional area, mean velocity, and direction created by expanding a gas through a small orifice into a vacuum.[4,29] In principle, the molecular beam can be tuned to attain a range of average incident energies and angles. The change in the incident energy or direction of the scattered molecule is indicative of gas-surface interaction during

the collision.[30] There are two types of molecular beams commonly used in scattering techniques, effusive beams and supersonically expanded nozzle beams.

Molecules coming from effusive sources have mean free paths larger than the diameter of the orifice that they must travel through and flow into the vacuum chamber. The velocity distribution of the molecules emerging from the aperture is characterized by a flux-weighted Boltzmann distribution at the temperature of the stagnant beam source.[29] According to the kinetic theory of gases, the average energy of a gas in a volume is 3/2kT, while the average translational energy of the same system of the gas striking a surface is 2kT.[31] The angular distribution of a gas crossing a plane is weighted by $\cos(\theta)$, the angle relative to the surface normal.[32] As a result, the probability of molecules emerging from the aperture maximizes in the normal direction which is the basis for the directed motion of an effusive beam.[32]

A supersonically expanding nozzle beam is formed when the backing pressure of the gas is increased such that the mean free path of the gas is smaller than the diameter of the orifice. As the gas molecules are pushed through the nozzle, the beam expands into a region with much lower pressure where the molecules transition from a continuum flow to a molecular flow.[32] Following the adiabatic expansion at the nozzle exit, the gas molecules reach the local speed of sound and gases with random motion become a rotationally and vibrationally cold molecular beam with direction motion.[33] Molecular beams with a wide range of translational energies can be achieved by seeding a small percentage of the desired molecules into a light and inert carrier gas, such as Ar, He, or H_2. Upon expansion of the mixed gases, the heavier molecules are accelerated to the velocity of the lighter gases, resulting in the desired molecules gaining large quantities of translational energy. By changing the percentage of the seeded gas relative to the carrier gas, the

carrier gas identity, and the nozzle temperature, the translational energy of the beam can be adjusted.

2.7.3 Sample Alignment and Molecular Beam Scattering

Once a SAM sample is cleaned and transferred into the main chamber through the load-lock system, the sample is aligned to the scattering position via a HeNe laser shining through a small window in the center of the flange attached to the rear part of the mass spectrometer. The laser beam traverses through the two apertures of the detector chamber and strikes the center of the SAM surface in the main chamber. After adjusting the manipulator angle to be ~0° so that the SAM surface is exactly perpendicular to the axis containing the laser beam, the sample is rotated by 30° toward the source chamber. Following the rotation, the sample position needs to be readjusted in order to have the laser beam that is reflected off the surface center being directed into the source chamber through the source aperture. The alignment of the SAM sample is demonstrated in Figure 2.7.

After the sample has been aligned in scattering position, the molecular beam is introduced into the main chamber by opening the gate valve between the source and the main. For scattering experiments, the beam is generated from commercially available tanks with mixed gases (2% UHP Ar/H_2, Airgas) or laboratory-developed gases (5% NO_3/He). Further details on beam generation can be found in the corresponding section of Chapter 6. The molecular beam is scattering from the surface with 30° of incidence and the mass spectrometer detects scattered molecules at the final angle of 30°. The ionizer of the mass spectrometer is 29 cm from the SAM surface and views a 1 cm^2 spot size on the surface through two collimating apertures.

The time-of-flight (TOF) distributions of the scattered molecules are determined by monitoring the quadrupole mass spectrometer (QMS – Extrel) signal at the singly ionized parent

mass as a function of time. The TOF scan is initiated when a slit of the chopper wheel passes between an LED-photodiode pair. Then a voltage pulse is sent to the computer to trigger a multichannel scalar (Qrtec) that integrates signal from the spectrometer in 10 μs intervals for scans containing 298 bins. The electron energy is set to 70 eV and the filament that ionizes the scattered molecules is set to 2.00 mA. The electron multiplier that is employed to amplify the ion signal contains two components, the dynode (−4000 V) and channeltron (1800 V).

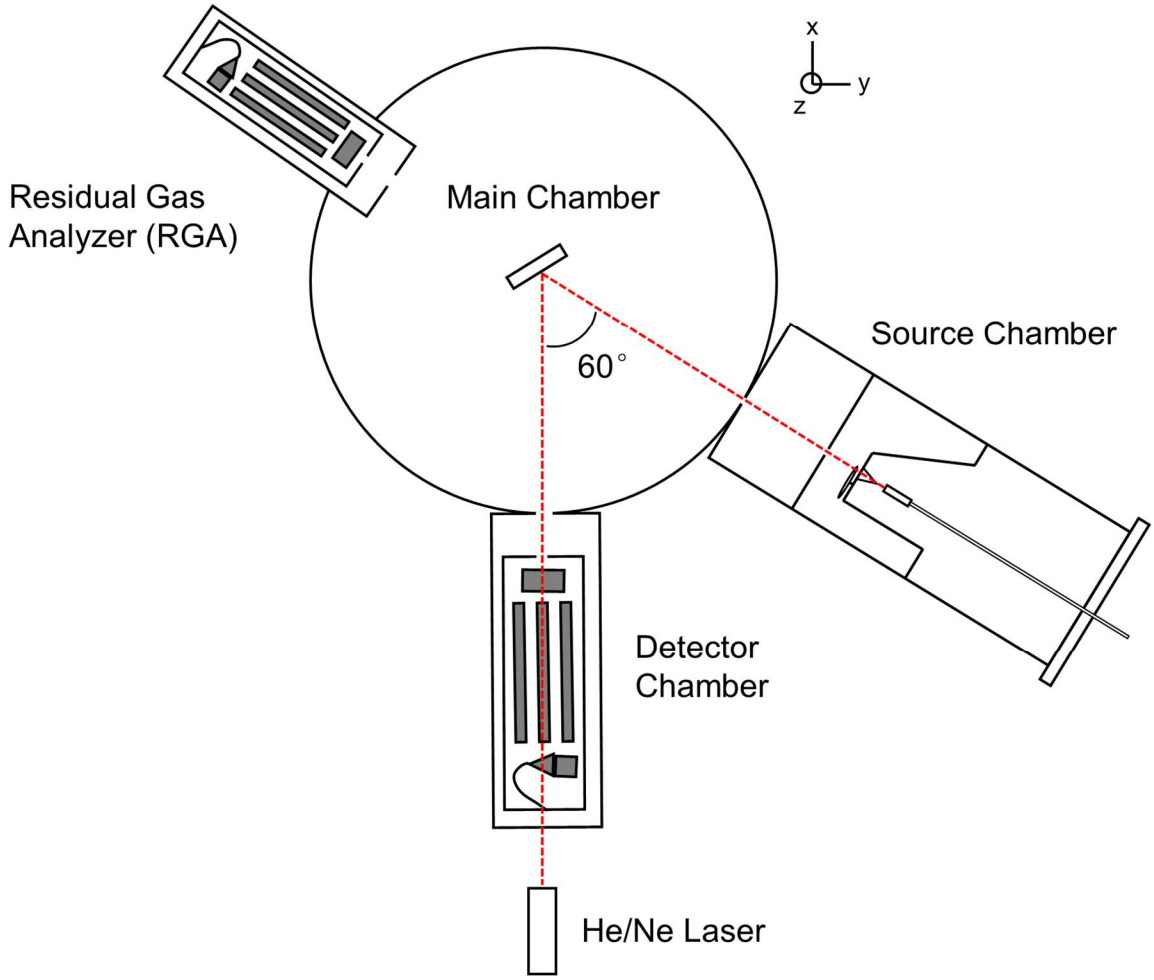

Figure 2.7. Schematic representation of sample alignment.

2.7.4 Timing Corrections

The raw data collected from the TOF measurements has several timing offsets and must be corrected prior to performing data analysis. The TOF distribution is recorded over a period of time that includes a response time of the LED-photodiode used in triggering apparatus, a lag time between the voltage pulse and the time the chopper slit passes in front of the aperture the source beam, the flight time of the incident gas from the chopper wheel to the sample, the time the gas molecules spends on the SAM surface, the flight time of the scattered molecules from the sample surface to the ionizer of the mass spectrometer, and the ion flight time in the quadrupoles. The equation below shows how the timing of the raw TOF spectra is corrected.

$$t_{\text{arr}} = t_{\text{total}} - t_{\text{electr}} - t_{\text{chopper-off}} - t_{\text{chopper-to-surface}} - t_{\text{mass-spec}} \qquad (2.2)$$

Where t_{arr} is the actual arrival time, t_{total} is the flight time measured by the mass spectrometer, t_{electr} is the electronic offset, $t_{\text{chopper-off}}$ is the front-back offset of the chopper wheel, $t_{\text{chopper-to-surface}}$ is the flight time from the chopper wheel to the surface, and $t_{\text{mass-spec}}$ is the time spent in the mass spectrometer.

The electronic timing offset, which is 2 μs, is estimated by measuring the time delay between exciting the photodiode with a laser pulse and the signal output on an oscilloscope. The chopper-offset time for the lag time between the photodiode trigger and the source aperture is shown in Figure 2.8. During the scattering experiments, the photodiode sends a pulse to the computer when the slit passes between the LED-photodiode pair, while the beam pulse occurs when the chopper slit passes in front of the source aperture. According to Figure 2.8, when the chopper wheel spins in the clockwise direction (CW), the beam pulse occurs prior to the trigger pulse. Conversely, when the chopper wheel rotates counterclockwise (CCW), the beam pulse

begins after the trigger pulse. The chopper-offset time is determined by measuring the difference in the peak arrival times of the incident beams with the chopper wheel spinning in both directions.

The rest timing offsets to consider are the chopper-to-surface offset and the time ions spent in the mass spectrometer. The chopper-to-surface flight time can be calculated directly based on the known distance between the chopper and the SAM surface (31 cm) and the gas velocity (calculated from measured translational energy). The flight time of ions in the mass spectrometer is obtained according to the following relationship:

$$t_q = (L_q \sqrt{\frac{1}{2E}}) \sqrt{m} = k \sqrt{m} \quad (2.3)$$

Here, t_q is the time spent in the quadrupoles, L_q is the flight path in the quadrupoles, E is the translational energy (together $L_q \sqrt{\frac{1}{2E}}$ can be considered as a constant k), and m is the mass to charge ratio. To determine the constant, k, the arrival times recorded from the TOF distribution for a gas that fragments into several ionic species (e.g., CO_2) are plotted as a function of the mass-to-charge ratio upon fragmentation in the QMS. As a result, the time spent in the quadrupoles for the corresponding fragments can be estimated using Equation (2.3). Once all the timing offsets have been corrected, the data is ready for analysis which will be further discussed in Chapter 7.

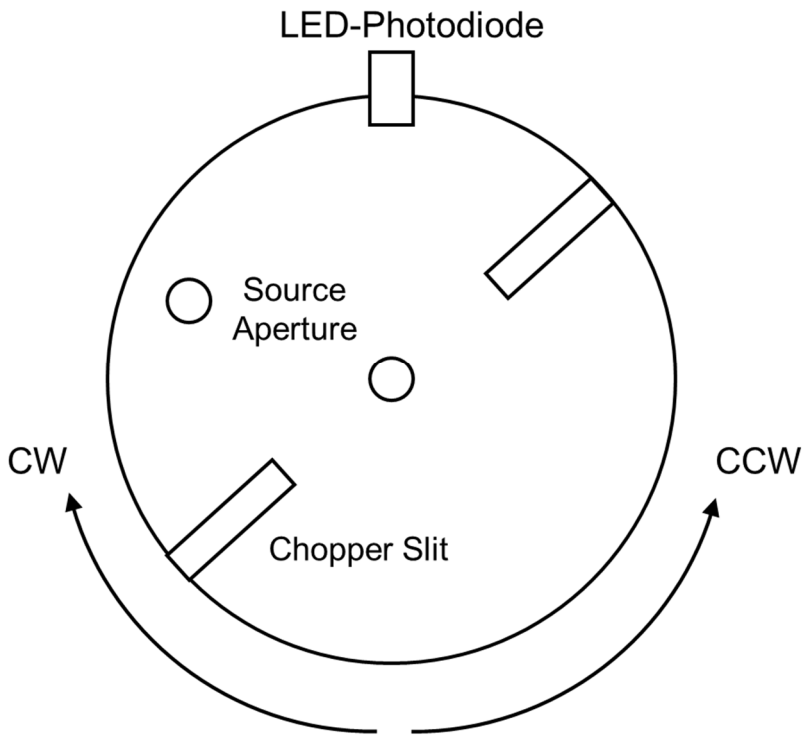

Figure 2.8. A front view of the chopper wheel to illustrate the time offset between the trigger pulse and the beam pulse.

2.8 Summary

To study the reaction kinetics and mechanism of NO_3 with model organic surfaces, precise characterization of the surface is of extreme importance. Various surface-sensitive techniques that require ultrahigh vacuum conditions can not only accurately characterize the organic surfaces, but also ensure that they remain uncompromised before, during, and after NO_3 exposure. In addition, molecular beam experiments provide the capability to explore the reaction dynamics of NO_3 with model organic surfaces.

REFERENCES

(1) Bird, G. A., Definition of Mean Free Path for Real Gases. *Phys. Fluids* **1983,** *26* (11), 3222-3223.

(2) Redhead, P. A.; Hobson, J. P.; Kornelsen, E. V., Physical Basis of Ultrahigh Vacuum. **1968**.

(3) Lednovich, S. L.; Fenn, J. B., Absolute Evaporation Rates for Some Polar and Nonpolar Liquids. *AIChE J.* **1977,** *23* (4), 454-459.

(4) Nathanson, G. M., Molecular Beam Studies of Gas-Liquid Interfaces. *Annu. Rev. Phys. Chem.* **2004,** *55* (1), 231-255.

(5) Yu, C.-f.; Whaley, K. B.; Hogg, C. S.; Sibener, S. J., Selective Adsorption Resonances in the Scattering of n-H_2 p-H_2 n-D_2 and o-D_2 from Ag(111). *Phys. Rev. Lett.* **1983,** *51* (24), 2210-2213.

(6) Love, J. C.; Estroff, L. A.; Kriebel, J. K.; Nuzzo, R. G.; Whitesides, G. M., Self-Assembled Monolayers of Thiolates on Metals as a Form of Nanotechnology. *Chem. Rev.* **2005,** *105* (4), 1103-1170.

(7) Adamson, A. W.; Gast, A. P., Physical Chemistry of Surfaces. 6th ed.; Wiley-Interscience New York, 1997.

(8) Walczak, M. M.; Chung, C.; Stole, S. M.; Widrig, C. A.; Porter, M. D., Structure and Interfacial Properties of Spontaneously Adsorbed N-Alkanethiolate Monolayers on Evaporated Silver Surfaces. *J. Am. Chem. Soc.* **1991,** *113* (7), 2370-2378.

(9) Maya Girón, J. V.; Zelaya, E.; Rubert, A.; Benítez, G.; Carro, P.; Salvarezza, R. C.; Vela, M. E., Surface Chemistry of 4-Mercaptobenzoic Acid Self-Assembled on Ag(111) and Ag Nanoparticles. *J. Phys. Chem. C* **2013,** *117* (47), 24967-24974.

(10) Laibinis, P. E.; Whitesides, G. M.; Allara, D. L.; Tao, Y. T.; Parikh, A. N.; Nuzzo, R. G., Comparison of the Structures and Wetting Properties of Self-Assembled Monolayers of N-Alkanethiols on the Coinage Metal Surfaces, Copper, Silver, and Gold. *J. Am. Chem. Soc.* **1991,** *113* (19), 7152-7167.

(11) Sellers, H.; Ulman, A.; Shnidman, Y.; Eilers, J. E., Structure and Binding of Alkanethiolates on Gold and Silver Surfaces: Implications for Self-Assembled Monolayers. *J. Am. Chem. Soc.* **1993,** *115* (21), 9389-9401.

(12) Dubois, L. H.; Nuzzo, R. G., Synthesis, Structure, and Properties of Model Organic-Surfaces. *Annu. Rev. Phys. Chem.* **1992,** *43*, 437-463.

(13) Strong, L.; Whitesides, G. M., Structures of Self-Assembled Monolayer Films of Organosulfur Compounds Adsorbed on Gold Single Crystals: Electron Diffraction Studies. *Langmuir* **1988,** *4* (3), 546-558.

(14) Widrig, C. A.; Alves, C. A.; Porter, M. D., Scanning Tunneling Microscopy of Ethanethiolate and N-Octadecanethiolate Monolayers Spontaneously Absorbed at Gold Surfaces. *J. Am. Chem. Soc.* **1991,** *113* (8), 2805-2810.

(15) Wunderlich, B., Crystalline Defects. In *Macromolecular Physics; Academic Press: New York*, 1973; Vol. 3, pp 439-499.

(16) Ulman, A.; Eilers, J. E.; Tillman, N., Packing and Molecular Orientation of Alkanethiol Monolayers on Gold Surfaces. *Langmuir* **1989,** *5* (5), 1147-1152.

(17) Nuzzo, R. G.; Dubois, L. H.; Allara, D. L., Fundamental Studies of Microscopic Wetting on Organic Surfaces. 1. Formation and Structural Characterization of a Self-Consistent Series of Polyfunctional Organic Monolayers. *J. Am. Chem. Soc.* **1990,** *112* (2), 558-569.
(18) Zhang, R.; Gellman, A. J., Straight-Chain Alcohol Adsorption of the Silver(110) Surface. *J. Phys. Chem.* **1991,** *95* (19), 7433-7437.
(19) Hu, J.; Fox, M. A., *J. Org. Chem.* **1999,** *64*, 4959-4961.
(20) Fiegland, L. R., Ultrahigh Vacuum Studies of the Reaction Mechanisms of Ozone with Saturated and Unsaturated Self-Assembled Monolayers. **2008**.
(21) Greenler, R. G., Infrared Study of Adsorbed Molecules on Metal Surfaces by Reflection Techniques. *J. Chem. Phys.* **1966,** *44* (1), 310-315.
(22) Baltrusaitis, J.; Jayaweera, P. M.; Grassian, V. H., Xps Study of Nitrogen Dioxide Adsorption on Metal Oxide Particle Surfaces under Different Environmental Conditions. *Phys. Chem. Chem. Phys.* **2009,** *11*, 8295-8305.
(23) Rosseler, O.; Sleiman, M.; Montesinos, V. N.; Shavorskiy, A.; Keller, V.; Keller, N.; Litter, M. I.; Bluhm, H.; Salmeron, M.; Destaillats, H., Chemistry of NO_x on TiO_2 Surfaces Studied by Ambient Pressure XPS: Products, Effect of UV Irradiation, Water, and Coadsorbed K^+. *J. Phys. Chem. Lett.* **2013,** *4*, 536-541.
(24) Einstein, A., *Annalen der Physik* **1905,** *17*, 132-148.
(25) Briggs, D.; Seah, M. P., *Practical Surface Analysis by Auger and X-Ray Photoelectron Spectroscopy*. John Wiley & Sons: 1983.
(26) Gorham, J.; Smith, B.; Fairbrother, D. H., Modification of Alkanethiolate Self-Assembled Monolayers by Atomic Hydrogen: Influence of Alkyl Chain Length. *J. Phys. Chem. C* **2007,** *111*, 374-382.
(27) Heintz, F.; Platt, U.; Flentje, H.; Dubois, R., Long-Term Observation of Nitrate Radicals at the Tor Station, Kap Arkona (Rügen). *J. Geophys. Res.* **1996,** *101* (D17), 22891-22910.
(28) DeMore, W. B.; Sander, S. P.; Golden, D.; Hampson, R.; Kurylo, M. J.; Howard, C.; Ravishankara, A.; Kolb, C.; Molina, M., *Chemical Kinetics and Photochemical Data for Use in Stratospheric Modeling*. JPL Pub.: 1994.
(29) Lu, J. W.; Day, B. S.; Fiegland, L. R.; Davis, E. D.; Alexander, W. A.; Troya, D.; Morris, J. R., Interfacial Energy Exchange and Reaction Dynamics in Collisions of Gases on Model Organic Surfaces. *Prog. Surf. Sci.* **2012,** *87* (9–12), 221-252.
(30) Levine, R. D., *Molecular Reaction Dynamics*. Cambridge University Press: 2005.
(31) Goodman, F.; Wachman, H., *Dynamics of Gas - Surface Scattering*. Academic: New York, 1976.
(32) Ceyer, S.; Gladstone, D.; McGonigal, M.; Schulberg, M., Physical Methods of Chemistry, Edited by Bw Rossiter and Rc Baetzold. Wiley, New York: 1993.
(33) Scoles, G.; Bassi, D.; Buck, U.; Lainé, D., *Atomic and Molecular Beam Methods*. Oxford university press New York: 1988; Vol. 1.

Chapter 3

Interfacial Reactions of Gas-phase Nitrate Radicals with Methyl- and Vinyl-terminated Self-Assembled Monolayers

3.1 Introduction

Following the first reported the presence of NO_3 in the troposphere,[1] several studies have focused on gas-phase reactions between nitrate radicals and organic compounds.[2-7] NO_3 generation for experimental studies has largely been accomplished by the thermal decomposition of dinitrogen pentoxide (N_2O_5) based on the $N_2O_5 \rightleftharpoons NO_3 + NO_2$ equilibrium.[8,9] Atkinson et al. were among the first to use this method to track the reaction rates of a series of selected organics (e.g. isobutene, benzene) with NO_3 relative to those of reference organics (e.g. ethane, propene) at room temperature.[10] Following these experiments, several other research groups have employed similar relative rate measurements in kinetic studies of gas-phase reactions between NO_3 and atmospheric hydrocarbons.[11-14] In the investigation of the reaction rates involving gas-phase NO_3 and a series of alkenes, Aschmann et al.[11] observed a positive correlation between the measured rate coefficient and the number of carbons within the alkene chain. They attributed this increase in reactivity with carbon content to the increase in inductive effects of longer alkyl substituent group chain length. That is, the rate of NO_3 addition to the alkene C=C bond increases with the donation of electron density to the C=C bond as provided by additional CH_2 groups.[15] However, for a given number of

carbon atoms, they also reported a decrease in reactivity with the extent of branching, which was attributed to steric effects.

Although gas-phase reactions of NO_3 with organics have been widely studied in the laboratory,[10,11,13,16,17] determining the overall atmospheric lifetime of NO_3 remains challenging due to difficulties in quantifying the contribution of heterogeneous processes. To help bridge this gap in understanding, Gross et al.[18] studied heterogeneous reactions of NO_3 and N_2O_5 with five different types of organic surfaces. They found the uptake coefficients of NO_3 to be about four orders of magnitude higher than those of N_2O_5. These important results suggest that reactions between NO_3 and organics play a larger role in atmospheric chemistry than reactions of N_2O_5. However, due to the lack of a well-defined surface, neither could be quantified with accuracy. To alleviate the challenges imposed by an ill-defined surface in the kinetics experiments involving NO_3 collisions, Knopf et al.[19] employed self-assembled monolayers (SAMs)[20-25] and measured uptake coefficient of NO_3 on a methyl-terminated alkane monolayer. They found that the reactivity of NO_3 on an alkane monolayer in the presence of O_2 was competitive with OH radicals (another important oxidative gas in the atmosphere) on the same surface. Later, Gross et al.[18] measured the uptake coefficient for NO_3 on vinyl-terminated SAMs and discovered that the uptake coefficient was higher than on liquid or amorphous solid films.[26] This trend likely reflects the differences in the location of the double bonds, which mediates their accessibility to the impinging gas-phase molecules. Interestingly, several expected products (reported in previous gas-phase studies[27,28]) were not observed in their infrared spectroscopic and X-ray photoelectron spectroscopic measurements, but this was attributed to the decomposition of products during XPS analysis and to the loss of the species of interest during sample transfer between instruments.[18] Hjorth et al.[29] and Barnes et al.[9] reported organic nitrates as the product of gas-phase reactions of NO_3 with a

series of alkenes by characterizing the reaction product with infrared spectroscopy. They found similarities between spectra recorded following their experiments and that of a reference compound, 3-nitrooxy-2-butanone; however, they did not assign these spectral features to specific vibrational modes of the molecules.

Although the studies summarized above revealed that NO_3 reacts efficiently with many types of organic compounds and that the reaction rates depend on the structure of the organic reactant,[18,26,30,31] many important questions remain. In particular, many fundamental aspects of the interfacial chemistry have yet to be investigated, including how surface structure and functionality affect NO_3 reactivity, the nature of major reaction products, and the overall reaction mechanisms. In this chapter, we aim to develop a deeper understanding of fundamental aspects, such as the kinetics and pathways, for reactions of NO_3 with methyl- and vinyl-terminated self-assembled monolayers on gold. SAM surfaces have a number of advantageous properties, including their ordered nature, high reproducibility, and they provide the capability of positioning the carbon-carbon double bond precisely at the gas-surface interface. *In situ* reflection-absorption infrared spectroscopy (RAIRS) was used to monitor NO_3 reactions with the organic surface. In addition to vibrational spectroscopic studies, X-ray photoelectron spectroscopy (XPS) was implemented to analyze the elemental composition of surface-bound molecules prior to and after reaction with NO_3. By tracking the rate of bond rupture and formation during the gas-surface collision, the initial reaction probability was determined and likely reaction pathways were identified for reactions of NO_3 with a vinyl-terminated SAM.

3.2 Experimental

The experiments were performed in an ultrahigh vacuum (UHV) surface science instrument designed for the study of the kinetics and mechanisms of reactions between nitrate

radicals and model organic surfaces. The UHV chamber (base pressure of 10^{-9} Torr) eliminates reactions of background gases with the surface and enables the implementation of XPS for elemental characterization of the surface before and after reaction. An all-glass capillary array doser was employed to provide an effusive source of NO_3 radicals that impinge on the surface. The surface-bound species were tracked *in situ* using reflection-absorption infrared spectroscopy (RAIRS), while products that desorb from the surface were monitored with a quadrupole mass spectrometer (QMS) during exposure.

3.2.1 Preparation of Vinyl-terminated Self-assembled Monolayers

Methyl- and vinyl-terminated SAMs were created on polycrystalline gold slides which were purchased from EMF Corp. These gold substrates were immersed in a piranha solution (7:3 ratio (v:v), 70% sulfuric acid/30% hydrogen peroxide) for ~1 h to remove surface contamination. The Au surfaces were then removed from the piranha solution and rinsed thoroughly with deionized water (Millipore Purification Systems, 18.2 MΩ). Each substrate was dried with a stream of ultrahigh purity nitrogen (UHP N_2) and immediately placed in a freshly prepared 1 mM solution of the corresponding thiol solution for at least 24 hours to achieve a well-ordered and tightly packed monolayer. The SAMs were then rinsed with the solvent the thiol solution (ethanol or hexane) and dried under a stream of UHP N_2 before being placed into the UHV chamber through a sample transfer load-lock system.

For benchmark measurements to help with spectral assignments, 2-ethylhexyl nitrate (97%) was obtained from Sigma-Aldrich and used without further purification. A thin film of 2-ethylhexyl nitrate was created by dropping the molecules onto a clean gold surface and then drying the surface under UHP N_2. Following bulk liquid evaporation, a RAIR spectrum was recorded.

3.2.2 Nitrate Radical Generation

To form NO_3, nitrogen monoxide was oxidized by an excess of ozone. This procedure initially formed N_2O_5 which was introduced into a glass trap submerged in a dry ice/ethanol bath. After isolating the trap from the dry ice/ethanol bath, N_2O_5 was volatilized and delivered to the doser. NO_3 was then formed through thermal decomposition of N_2O_5 by heating the doser. The flux of N_2O_5 (2.3×10^{15} molecules s^{-1}) onto the surface was estimated from a calculation based on the pressure of N_2O_5 near the doser, the conductance of the capillary array doser (4.1×10^{-4} cm^3 s^{-1}), and the kinetic theory of gases. According to the physical dimensions of the doser and the temperature-dependent equilibrium constant for $NO_3 + NO_2 \rightleftharpoons N_2O_5$ ($K_{eq} = 2.7 \times 10^{-27} \times \exp(11000/T)$ cm^3 $molecule^{-1}$),[32,33] the concentration of NO_3 adjacent to the surface for our doser temperature of 324 K, $[NO_3]_g$, was determined to be 2.8×10^{10} molecules cm^{-3}. The calculated flux was consistent with the pressure change in the vacuum chamber during NO_3 exposure to a clean gold surface.

3.2.3 Reflection-Absorption Infrared Spectroscopy

Reactions between NO_3 and SAMs were monitored using a Bruker IFS 66v/S spectrometer attached to the UHV chamber. Focused IR radiation from a SiC globar was reflected from the gold surface at ~86° relative to the surface normal through a differentially pumped KBr window. The reflected radiation was detected by a mid-range (750-4000 cm^{-1}) mercury cadmium telluride (MCT) detector, which was cooled by liquid nitrogen prior to each experiment. All spectra shown here were the average of 100 scans with a 2 cm^{-1} resolution.

3.2.4 X-ray Photoelectron Spectroscopy

The XPS data presented in this article was obtained by employing monochromatic radiation (Al Kα 1486.6 eV) from a SPECS XR50 X-ray source operating at 250 W (12.5 kV and 20 mA). Ejected photoelectrons were detected using a 16.5" hemispherical energy analyzer (SPECS, Phoibos 100) operated at a take-off angle of 90º with respect to the surface. All high-resolution spectra were acquired in the region of interest using the following experimental parameters: pass energy of 50 eV; step size of 0.1 eV and dwell time of 0.1 s. The binding energy scales for all spectra were referenced to the Au ($4f_{7/2}$) peak at 83.8 eV.[34] A Shirley background was subtracted from each spectrum to account for the inelastic scattering of electrons that contributes to the background broadening.[35,36] The peaks are fitted to symmetric curves containing a Gaussian/Lorentzian product with 70% Gaussian and 30% Lorentzian character.[37,38]

3.2.5 Computational Methods

Spectral interpretations and mechanistic insight into the reactions were further aided by a series of electronic structure calculations performed using the Gaussian09 code.[39] The geometries of nitrate-terminated linear alkyl radicals with varying carbon-chain length were optimized using both B3LYP/6-31G* and MP2/6-31G* levels of theory, and harmonic vibrational mode analyses were performed on each molecule using both methods. The calculated harmonic frequencies of the scissoring (δ), symmetric stretch (ν_s), and asymmetric stretch (ν_a) normal modes of the nitrate group were found to converge to a constant value with increasing chain length. The relevant vibrational frequencies calculated for each vibrational mode were found to vary by less than 10 cm^{-1} for chains with four or more carbon atoms; therefore, chains with eight carbon atoms were used for the remainder of the computational studies, which provides a balance between accuracy

and expense. All calculated vibrational frequencies reported in this work have been scaled by the recommended factors of 0.96 for B3LYP/6-31G* and 0.94 for MP2/6-31G*.[40]

3.3 Results and Discussion

3.3.1 Reactions of NO_3 with Methyl-terminated Self-Assembled Monolayers

Gas-phase NO_3 radicals impinging on a 10-C and an 18-C H_3C-SAM surface has been investigated by tracking bond rupture with infrared spectroscopy. During the exposure of the SAMs to NO_3, the NO_3 molecules could react with the terminal methyl groups, diffuse into the hydrocarbon chains and oxidized methylene groups, or simply desorb from the surface into the UHV chamber. For those surfaces that react, reaction products have been identified via XPS elemental analysis before and after NO_3 exposure.

3.3.1.1 Initial Characterization of 10-C and 18-C H_3C-SAMs by RAIRS

Reflection-absorption infrared spectra of a 10-C and an 18-C H_3C-SAM on a polycrystalline gold substrate, recorded prior to NO_3 exposure, are shown in Figure 3.1. In spectrum (a) of Figure 3.1, the most intense four bands at 2918 cm^{-1} and 2849 cm^{-1} are due to the asymmetric ($\nu_a(CH_2)$) and symmetric ($\nu_s(CH_2)$) stretching modes of -CH_2- groups along the backbone of the hydrocarbon chains.[41] Both the position and the width of the two peaks suggest that the chains reside in a crystalline-like environment and are organized in an all-trans configuration.[22,25] In addition to the methylene stretching modes, two bands associated with the terminal methyl group emerge in the spectrum (a). The features at 2965 cm^{-1} and 2878 cm^{-1} are assigned to the asymmetric ($\nu_a(CH_3)$) and symmetric ($\nu_s(CH_3)$) stretching modes of the -CH_3 group.[20] The other spectral feature that appears at the shoulder (2937 cm^{-1}) of the $\nu_a(CH_2)$ band is

attributed to the Fermi resonance of $\nu_s(CH_3)$ with the overtone of low frequency CH_2 deformation mode. Interestingly, it should be noted that intensities of both $\nu_a(CH_3)$ and $\nu_s(CH_3)$ are large compared to the intensities of bands assigned to the $\nu(CH_2)$ modes, despite the fact that there are 17 CH_2 groups for every CH_3-chain. According to the surface selection rule, only vibrational motions that produce a transition dipole moment perpendicular to the surface can be detected with RAIRS.[42] The relatively large intensities of the -CH_3 stretching modes most likely result from the more perpendicular (to the surface) transition dipole moments for those modes. Spectrum (b) in Figure 3.1 shows IR absorption of a 10-C H_3C-SAM on a gold surface. The four most intense bands have similar wavenumber to those for an 18-C H_3C-SAM, suggesting a well-ordered SAM formed on the surface. However, it should be noted that the band associated with the $\nu_a(CH_2)$ and the $\nu_s(CH_2)$ mode shift to a higher wavenumber compared with the one in spectrum (a). Typically, the asymmetric and symmetric CH_2 stretching modes in a tightly packed well-ordered monolayer absorb IR light at 2918 cm^{-1} and 2849 cm^{-1}, respectively.[22] Relatively disordered organic films exhibit stretching modes at higher vibrational energy.[33] Therefore, the blue shift of these two modes for methylene chains observed in Figure 3.1 indicates that the 10-C H_3C-SAM is less ordered than the 18-C H_3C-SAM.

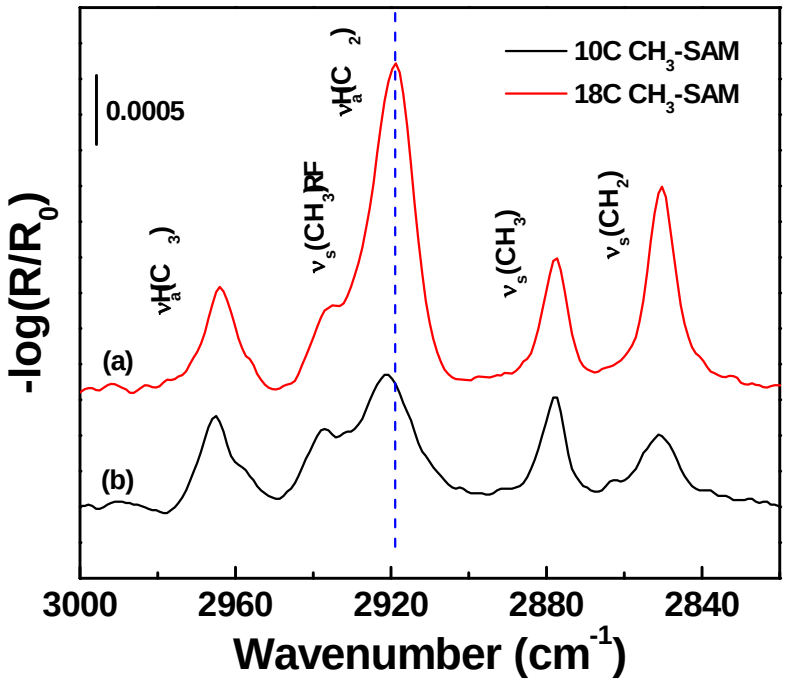

Figure 3.1. Reflection-absorption infrared spectrum of a 10-C H_3C-SAM (spectrum (a)) and an 18-C H_3C-SAM (spectrum (b)) on Au formed from methyl-terminated alkenethiols fabricated through solution immersion. The four most intense IR active modes are highlighted as $\nu_a(CH_3)$, $\nu_s(CH_3)$, Fermi Resonance, $\nu_a(CH_2)$, and $\nu_s(CH_2)$.

3.3.1.2 IR Characterization of H_3C-SAMs before and after NO_3 exposure

Figure 3.2 shows RAIRS of the 18-C H_3C-SAM and the 10-C H_3C-SAM on Au before (spectra (a) and (c)) and after reactions (spectra (b) and (d)) with NO_3 radicals. Following the initial characterization, the methyl-terminated SAMs were exposed to a continuous source of NO_3 gas. Spectra (a) and (c) in Figure 3.2 were used as the background such that negative features indicate the removal of modes from the surface. After exposing to 4000 L of NO_3, all modes associated with the terminal methyl groups and the methylene back bone completely disappear for the 10-C H_3C-SAM, suggesting that reactions between NO_3 and the surface consume all hydrocarbons of the SAM. However, even after 7000 L exposure of NO_3 to the 18-C H_3C-SAM,

the bands associated with the methylene chains of the SAM decrease in intensity by only ~10%. In addition, one can barely observe changes in bands associated with the terminal methyl groups, which suggests that reactions of NO_3 with the 18-C H_3C-SAM, if any, mainly take place at the methylene backbone instead of the terminal methyl groups. Since the 10-C H_3C-SAM is less ordered than the 18-C H_3C-SAM, the shorter chain-length SAM has more defects on the surface for NO_3 to attack which could result in the oxidation of methylene groups along the backbone of the chain or even the oxidation of sulfur attached to the gold substrate. Further, the oxidation of sulfur may cause the entire hydrocarbon chains to desorb from the surface, as exhibited by spectrum (d) of Figure 3.2.

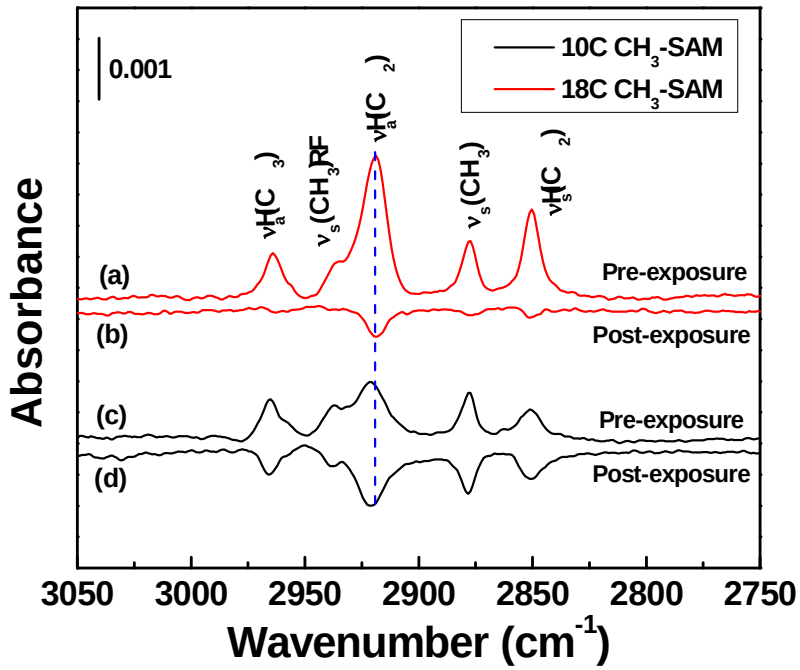

Figure 3.2. Reflection-absorption infrared spectrum of an 18-C H_3C-SAM and a 10-C H_3C-SAM on Au before (spectra (a) and (c)) and after reactions (spectra (b) and (d)) with NO_3 radicals. Spectra (a) and (c) use a clean gold slide as the background, while spectra (b) and (d) use the original SAM as the background.

3.3.1.3 XPS Characterization

While infrared spectral results suggest the oxidation of sulfur and the desorption of the entire methylene chains, XPS provides further evidence by effectively analyzing the elemental composition of the surface adsorbates before and after NO_3 exposure. Representative high resolution spectra of the N (1s), S (2p), O (1s) and C (1s) regions of a 10-C methyl-terminated SAM are shown in Figure 3.3.

The XPS spectra of the S (2p) region of the SAM are shown in Figure 3.3A. The raw data has been fitted by a pair of spin-orbit doublets with the same FWHM, branching area ratio of 2 ($2p_{3/2}$:$2p_{1/2}$), and standard spin-orbit splitting of 1.2 eV.[34,43,44] After 4×10^3 L of NO_3 exposure, the doublets shift to a higher binding energy (166.7 eV), indicating that the native Au-S bonds have been mostly oxidized after reactions of the methyl-terminated SAM with NO_3.[45] The high resolution XPS spectra of the N (1s) regions for the SAM surface before and after NO_3 exposure are shown in Figure 3.3B. The N (1s) spectrum of the surface-bound product after reactions was fit to a peak centered at 405.1 eV. Similar peaks at nearly the same binding energies have been observed in several previous studies and assigned to physisorbed NO_2 (405.6 eV).[37,38]

As the sulfur atoms are oxidized and nitrogen-containing species adsorbed on the surface upon NO_3 exposure, signal corresponding to the binding energy for O (1s) electrons also emerges in the high resolution XPS spectra (see Figure 3.3C). As expected, the methyl-terminated monolayer shows no signal above noise for the O (1s) transition before exposure. After 4000 L of NO_3 exposure, a peak positioned at 530.4 eV is likely due to the formation of oxidized sulfur species or adsorbed NO_2 on the surface.[46] Further, the desorption of the entire methylene chains in the 10-C H_3C-SAM can also be elucidated by the high resolution XPS spectra in the C (1s) region (see Figure 3.3 D). The peak centered at 284.4 eV and 287.2 eV is coincident with binding energy

of the C (1s) electron in methylenes and carbon atoms bound to sulfur atoms (C-S).[43,47,48] After NO_3 exposure, the peak intensity at 284.5 eV significantly decreased, indicating that, in agreement with RAIRS data, oxidation of NO_3 with the SAM results in methylene chains desorbed from the surface. In addition, the weak band positioned at 287.9 eV suggests the emergence of a C=O species on the surface and is likely due to the oxidation by NO_3.[45]

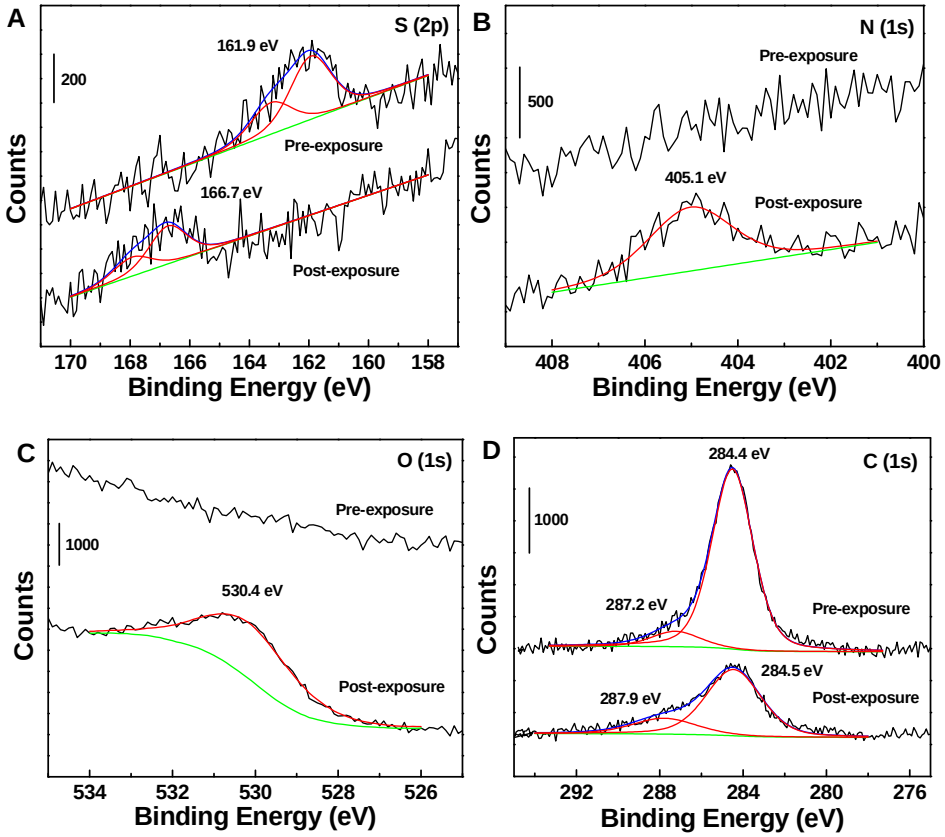

Figure 3.3. High resolution X-ray photoelectron spectra of the S (2p), O (1s), N (1s), and C (1s) regions of an 10-C CH_3-terminated SAM before and after 4000 L of NO_3 exposure, which indicates the oxidation of sulfur groups attached to the Au surface.

For the case of NO_3 impinging onto an 18-C H_3C-SAM, high resolution spectra of the S (2p), O (1s) regions are shown in Figure 3.4. Similar to what has been done in Figure 3.3A, the raw data (Figure 3.4A) is fitted to a pairs of S ($2p_{3/2,1/2}$) (S ($2p_{3/2}$) peak at 161.8 eV). After 7×10^3 L of NO_3 exposure, similar doublets are observed with nearly the same peak intensity, indicating

that the native thiolate species has been mostly preserved. In addition, unlike what we observed in Figure 3.3A, no peak appears in the range of 167-168 eV for oxidized sulfur species,[45] which reveals that Au-S bonds have been preserved during the NO_3 exposure and that reactions, if any, occur primarily at the hydrocarbon chains. Such preservation of unoxidized sulfur species can also be elucidated by the high resolution spectra in the O (1s) region, as shown in Figure 3.4B. No observable peak can be seen above noise after NO_3 exposure, suggesting that, consistent with findings in IR, very few amount of the monolayer has been oxidized upon collisions of NO_3 with the 18-C H_3C-SAM.

Although results from RAIRS and XPS show little evidence about oxidation of the entire hydrocarbon chain by NO_3, the features in RAIRS that show the decrease in intensities of CH_2 stretching modes indicate removal of these modes, which could be due to hydrogen abstraction from methylene groups.[49] Following abstraction, the formed alkyl radicals may initiate subsequent reactions, such as addition of NO_3/NO_2 or even reaction with neighboring radicals to crosslink. The likely dominant mechanism of hydrogen abstraction for reactions of CH_3-SAMs with NO_3 motivated the study involving a hydroxyl-functionalized surface that will be discussed in Chapter 4 and 5.

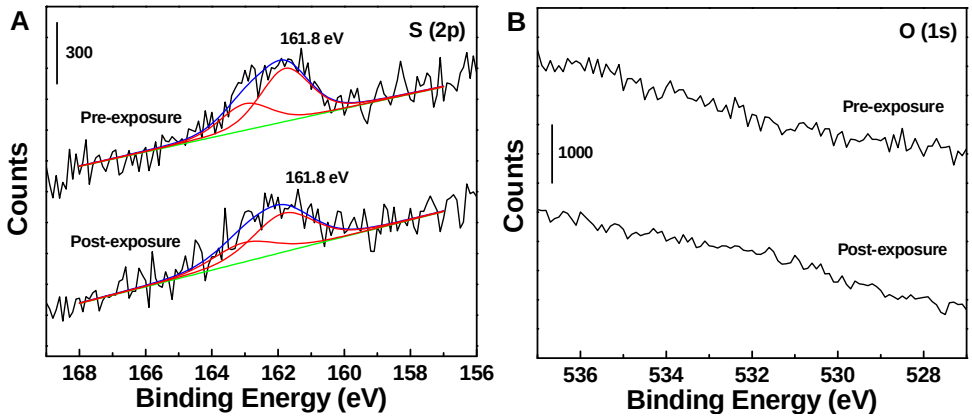

Figure 3.4. High resolution X-ray photoelectron spectra of the S (2p) and O (1s) regions of an 18-C methyl-terminated SAM before and after 7000 L of NO_3 exposure, which indicates the preservation of concentration and oxidation state of sulfur groups attached to the Au surface.

3.3.2 Reactions of NO_3 with Vinyl-terminated SAMs

The reaction dynamics and kinetics that govern the interactions between NO_3 and vinyl-terminated self-assembled monolayers have been investigated by tracking interfacial bond formation and rupture with infrared spectroscopy. The SAMs provide a well-characterized model surface with the double bond positioned precisely at the gas-surface interface. Upon NO_3 collision with the SAM, the molecules could either react with the terminal vinyl groups or simply desorb into vacuum. For those molecules that react, the probability for reactions, γ = number of reaction/number of collisions, was determined from the kinetics for vinyl group decomposition and new product formation during exposure to a constant flux of nitrate radicals. The kinetics of bond rupture and formation were tracked with *in situ* reflection-absorption infrared spectroscopy while the reaction products were analyzed with RAIRS and XPS.

3.3.2.1 Initial H_2C=CH-SAM Characterization by RAIRS

The model hydrocarbon surface chosen for this work was an 18C vinyl-terminated SAM. The reasons for selecting a long-chain SAM were threefold: (i) the thermodynamic stability of SAMs increases with the length of the chains, (ii) long-chain (n>10) SAMs are more ordered than short-chain SAMs, and (iii) oxidation of S attached to Au does not occur on the time scale of our measurements for the long-chain vinyl-terminated SAM (illustrated in Section 3.3.1). Further, the C=C stretch of the vinyl group has a strong transition dipole moment that facilitates detailed infrared spectroscopic studies of this mode as it transforms from reactant into product.

Infrared spectra, recorded prior to NO_3 exposure, revealed that the long-chain vinyl-terminated alkanethiols formed well-ordered monolayers on the gold substrates employed in these studies. Figure 3.5 shows the reflection-absorption infrared spectrum of an 18C vinyl-terminated SAM on a polycrystalline gold substrate. The most intense peaks at 2918 and 2849 cm^{-1} are due to the asymmetric ($\nu_a(CH_2)$) and symmetric ($\nu_s(CH_2)$) stretching modes of CH_2 groups along the backbone of the chains. Both the position and the width of the two peaks suggest that the chains reside in a crystalline-like environment.[22,25] An extensive discussion of RAIRS characterization for SAMs can be found in references [41] and [42]. In addition to the methylene stretching modes, six of the bands associated with the terminal vinyl group appear in the spectrum of Figure 2. The bands at 3084 and 2984 cm^{-1} are attributed to the asymmetric ($\nu_a(=CH_2)$) and symmetric CH_2 ($\nu_s(=CH_2)$) stretching modes of the $=CH_2$ group.[50] The four other spectral features at 3008, 1644, 994 and 914 cm^{-1} are due to the β C-H stretch of $-HC=CH_2$ ($\nu(H-C=CH_2)$), the C=C stretch ($\nu(C=C)$), the C=C out-of-plane deformation ($C=C_{oop\ def}$), and the $=CH_2$ out-of-plane deformation ($\omega(=CH_2)$), respectively.[51,52] The wavenumbers and corresponding mode assignments for the RAIR spectrum are provided in Table 3.1. The consistency of the features in this characteristic spectrum with

previous studies suggests an average area of 21.4 Å^2 per molecule adsorbed on the gold substrate, which corresponds to a surface density of 4.7×10^{14} molecules cm^{-2}.[20,25]

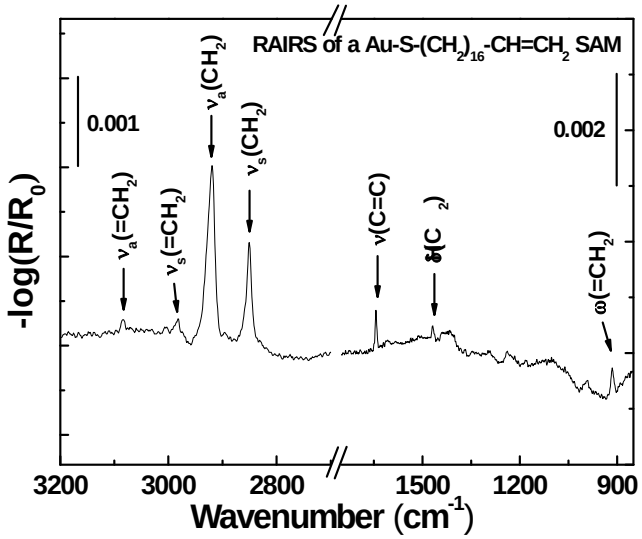

Figure 3.5. Reflection-absorption infrared spectrum of a H_2C=CH-SAM on Au formed from an 18C vinyl-terminated alkenethiol fabricated through solution immersion. The four most intense IR active modes are highlighted as $\nu_a(CH_2)$, $\nu_s(CH_2)$, ν(C=C), and $\omega(=CH_2)$.

Table 3.1. RAIR spectroscopic band positions and vibrational mode assignments for an 18C vinyl-terminated SAM on Au and the vinyl-terminated SAM after NO_3 exposure.

Vibrational Modes	Wavenumber (cm^{-1})		References
	Pre Exposure	Post Exposure	
$\nu_a(=CH_2)$	3084	-	50-52
ν(H-C=CH_2)	3008	-	50-52
$\nu_s(=CH_2)$	2984	-	50-52
$\nu_a(CH_2)$	2918	2919	30, 33
$\nu_s(CH_2)$	2849	2850	30, 33
$\nu_a(-ONO_2)$	-	1649	34, 56, 57, 60, 61
ν(C=C)	1644	-	50-52
$\nu_s(-ONO_2)$	-	1280	34, 56, 57, 60, 61
$C=C_{oop\ def}$	994	-	50-52
$\omega(=CH_2)$	914	-	50-52
$\delta(-ONO_2)$	-	857	34, 56, 57, 60, 61

3.3.2.2 IR Characterization of H_2C=CH-SAMs during NO_3 exposure

Oxidation of the H_2C=CH-SAM by NO_3 was monitored *in situ* by RAIRS. Figure 3.6A shows a subset of RAIR difference spectra for the 18C vinyl-terminated SAM during NO_3 exposure. Following the initial characterization, the vinyl-terminated SAM was exposed to a continuous source of NO_3/NO_2 gas. In this experiment, the original SAM was used as the background such that negative features in the spectra indicate the removal of modes from the surface and positive bands reveal an increase in absorbance or the development of new modes. The initial spectrum in Figure 3.6A (the lower-most spectrum) is the difference spectrum of the monolayer before exposure. From the bottom toward the top of this figure, the exposure of the monolayer to NO_3 increases by 2×10^2 L (1 L = 10^{-6} Torr·s) per scan with a total exposure of 5×10^3 L of NO_3. Control experiments performed by exposing an 18C vinyl-terminated SAM to an effusive room-temperature flux of N_2O_5 or pure NO_2 displayed little-to-no evidence, as shown in Figure 3.6.

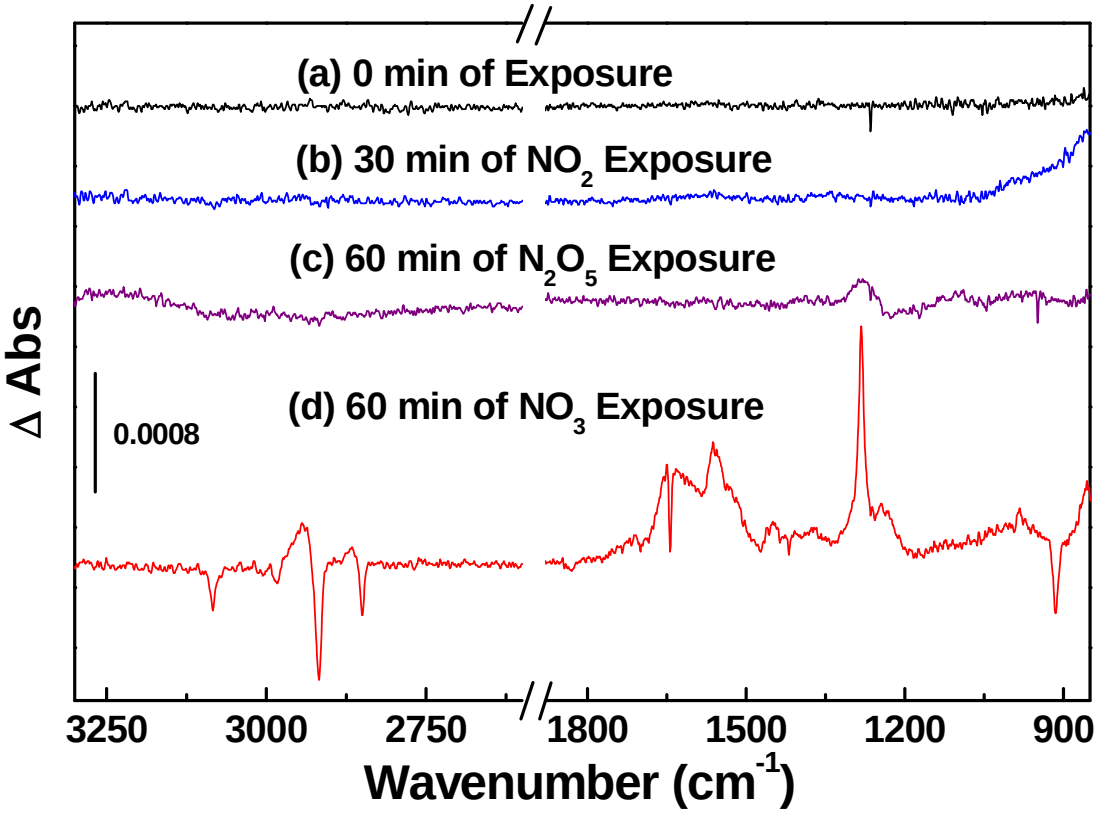

Figure 3.6. Reflection-absorption infrared difference spectra of an 18C vinyl-terminated SAM exposed to NO_2 (spectrum (b)), N_2O_5 (spectrum (c)), and NO_3 (spectrum (d)). The spectrum shown on top (spectrum (a)) is that of the SAM prior to NO_3 exposure using the CH_2=CH-SAM as the background.

In addition, results from previous section (Section 3.3.1) show that the exposure of an 18C CH_3-SAM to the NO_3-rich source resulted in only minor changes in the difference IR spectra. For exposure of the H_2C=CH-SAM to the NO_3-rich gas source, three notable changes in the RAIR difference spectra are readily observed: (*i*) all of the bands associated with the double bond decrease in intensity, (*ii*) new modes emerge at 1649 cm^{-1}, 1555 cm^{-1}, 1280 cm^{-1} and 857 cm^{-1}, and (*iii*) the peaks associated with the methylene backbone of the SAM broaden and decrease in intensity by ~10%. As discussed below, these spectral changes are attributed to reactions of NO_3 at the vinyl group. The identities of key products in this reaction are determined through spectral assignments of the IR modes and analysis of electron binding energies (XPS).

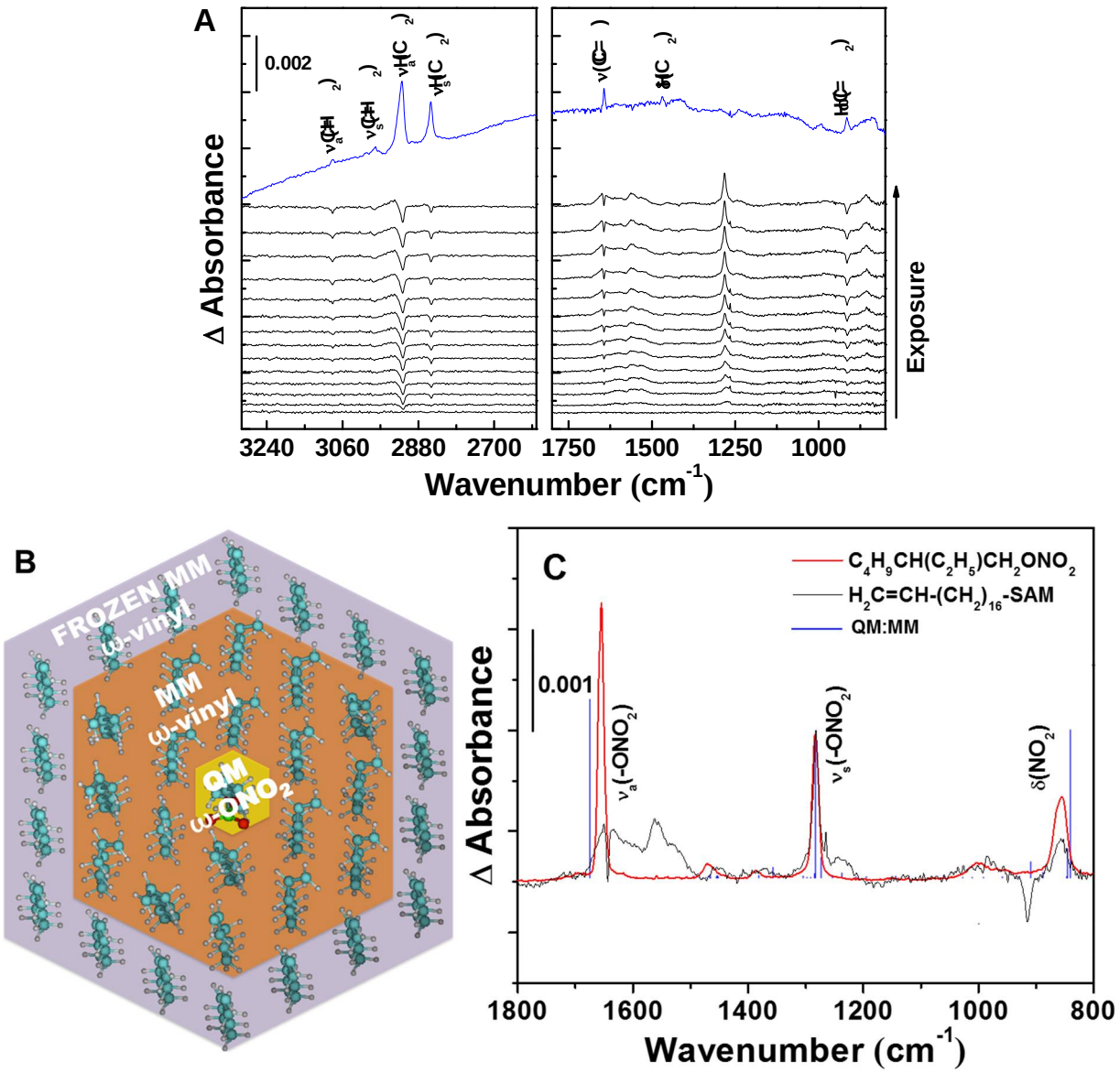

Figure 3.7. (A) Reflection-absorption infrared difference spectra of an 18C vinyl-terminated SAM exposed to NO_3. The spectrum shown on top in blue is that of the SAM prior to NO_3 exposure using a clean Au sample as the background. Upon NO_3 exposure, the spectra in black show that modes associated with the C=C moiety decrease and new modes emerge. The background for this scan is the original pre-exposure spectrum (blue), with the exposure increasing by 2×10^2 L per spectrum. (B) Schematic of the model SAM used in the QM:MM calculations of this work. (C) RAIR spectra of a 2-ethylhexyl nitrate surface (red), an 18C vinyl-terminated SAM after 5000 L of NO_3 exposure (black), and theoretical QM:MM frequencies (blue) of the central ω-ONO_2 radical chain.

As mentioned above, commensurate with a decrease in the absorbance for the modes associated with the C=C group, positive features emerge in the spectra at 1649 cm^{-1}, 1555 cm^{-1},

1280 cm^{-1}, and 857 cm^{-1}. Previous infrared spectroscopic studies of the vibrational modes of nitro groups in aromatic and aliphatic nitro organics showed an asymmetric stretch of NO_2 near 1555 cm^{-1}, which suggests that the peak shown in Figure 3.6 at this frequency is most likely the asymmetric NO_2 stretch of nitro compounds.[53,54] Other mode assignments were aided by the creation of a reference sample composed of a thin film of 2-ethylhexyl nitrate ($C_4H_9CH(C_2H_6)CH_2ONO_2$) on gold. The RAIR spectrum for this thin film is displayed in Figure 3.6C (red line). For comparison, an infrared spectrum for an 18C vinyl-terminated SAM after 5000 L of NO_3 exposure (with the original SAM as the background) is also exhibited in Figure 3.7C (black line). The coincidence of peaks at 1649 cm^{-1}, 1280 cm^{-1} and 857 cm^{-1} for the two spectra suggests that organic nitrates similar to those in 2-ethylhexyl nitrate are created during exposure of the H_2C=CH-SAM to NO_3. This result corroborates previous results obtained during studies of NO_3 reactions with unsaturated alcohols, which reported the appearance of infrared bands at 1678 cm^{-1}, 1285 cm^{-1} and 842 cm^{-1} in FTIR.[55] Other investigations into reactions between NO_3 and an 11C vinyl-terminated SAM also showed evidence for product formation that yielded spectral signatures similar to those displayed in Figure 3.7.[18]

To further aid the interpretation of the IR peaks that emerge during exposure, a series of electronic structure calculations were performed by our collaborators in the Troya group (Robert C. Chapleski). For these calculations, a SAM model was constructed consisting of a central ω-ONO_2 octyl radical chain surrounded by 36 8C vinyl-terminated chains arranged as they are on the self-assembled monolayer utilized in the experiment (hexagonal arrangement with each chain occupying 21.4 $Å^2$ surface area). Because fully *ab initio* calculations of this SAM model are prohibitive, a multilevel quantum mechanics/molecular mechanics (QM:MM) approach was used. In this QM:MM approach, the central, ω-ONO_2 alkyl radical, chain was optimized at the B3LYP/6-

31G* level, and the rest of the SAM was computed at the MM level with the universal force field (UFF).[56] To test the reliability of the model, calculations were repeated using a modified AMBER force field[57] for the MM region. Finally, deleterious edge effects in the SAM model were prevented by fixing the outermost boundary of ω-vinyl chains and all the α carbons during the geometry optimization. Figure 3.7B shows the construction and optimization strategy of this QM:MM system and the blue trace in Figure 3.7C represents the vibrational spectrum of the central radical chain. The very close agreement between the theoretically calculated vibrational spectrum for the nitrate terminus of the SAM model and the experimental IR spectrum verifies that the most likely assignments for the key peaks during NO_3 reactions with the H_2C=CH-SAM are the asymmetric and symmetric NO_2 stretches and the NO_2 scissoring of organic nitrates.

Table 3.2 lists the vibrational frequencies relevant to the experiments in this work. Interestingly, as the table shows, the largest difference between gas-phase and SAM models in the electronic structure calculations is only 10 cm^{-1} at the same level of theory. The fact that the ω-ONO_2 vibrational modes differ only modestly between the gas-phase and the SAM model indicates that embedding a nitrate alkyl chain in a SAM has very little effect on the nitrate vibrational frequencies.

Table 3.2. Experimental ω-ONO_2 octadecyl SAM and theoretical gas-phase and SAM ω-ONO_2 octyl chain vibrational frequencies (cm^{-1})

Methods	**δ(-ONO_2)**	**ν_s(-ONO_2)**	**ν_a(-ONO_2)**
Experiment	857	1280	1649
B3LYP/6-31G* (gas-phase)	831	1275	1673
MP2/6-31G* (gas-phase)	825	1234	1750
Multilevel SAM (B3LYP/6-31G*:UFF)	841	1283	1673
Multilevel SAM (B3LYP/6-31G*:Amber)	834	1277	1673

Beyond the spectral changes observed in the low wavenumber region (1800-800 cm^{-1}) and the decrease in the intensity of stretching modes associated with the double bonds at high wavenumbers (>3000 cm^{-1}), the only changes observed in the difference spectra (above the detection limit of the spectrometer, which we estimate to be 2% of a ML) are the decrease in intensities, the broadening, and the blue shift of bands assigned to the asymmetric and symmetric stretching modes of the CH_2 groups along the backbone of the chains. Typically, the frequency of the asymmetric and symmetric CH_2 stretching modes falls at 2918 cm^{-1} and 2849 cm^{-1}, respectively, in tightly packed well-ordered monolayers.[22] Relatively disordered organic films exhibit stretching modes at much higher vibrational energy.[33] Thus, the blue shift of these two modes for methylene chains observed in Figure 3.7A indicates that the well-ordered SAM becomes increasingly disordered as the terminal groups react with impinging NO_3. In addition, as the local environment becomes less homogeneous, the substantial broadening of the two bands was observed. Therefore, the addition of a bulky nitrate group to the end of the alkane chain likely leads to disordering of the originally well-ordered SAM, which could result in the broadening of the peaks assigned to the methylene stretching modes. In addition, the decrease in the absorptivity for the features assigned to C-H stretches along the methylene backbone might be due to hydrogen abstraction to form HNO_3, which has been reported in previous studies of NO_3 reactions with organics.[6,19,58] However, any HNO_3 (g) that may have been produced was below the limit of detection of our quadruple mass spectrometer.

3.3.2.3 XPS Characterization

While infrared spectroscopy provides insight into the vibrational motions of adsorbed products, the elemental composition of the adsorbates can be effectively analyzed with XPS. Elemental analysis was performed prior to and after reactions of the vinyl-terminated SAM with

NO_3. Representative high resolution spectra of the N (1s), S (2p), O (1s) and C (1s) regions of an 18C vinyl-terminated SAM are shown in Figure 3.8.

The high resolution XPS data collected in the N (1s) region of the SAM surface before and after NO_3 exposure are shown in Figure 3.8A. The N (1s) spectrum of the surface-bound product after reactions was fit best by a model containing three components with equal full-width-at-half-maximum (FWHM) values. The best fit required a FWHM value of 1.8 eV which is quite similar to the values found in a number of XPS studies of nitrates adsorbed at different metal surfaces.[37,38,59-61] The agreement of the binding energy at 406.9 eV in the N (1s) region in this work with that from previous XPS studies on nitrate adsorbates further demonstrates the formation of an organic nitrate group during reactions between the vinyl-terminated SAM and NO_3. Two additional and much weaker peaks are present in the spectrum centered at 405.5 eV and 408.8 eV. Similar peaks at nearly the same binding energies have been observed in several previous studies and assigned to physisorbed NO_2 (405.6 eV) or NO_3^- adsorbates (408.1 eV).[37,38] A summary of the binding energies compared to literature values is provided in Table 3.3.[37,38,59-61] It should be noted that the organic nitrates were found to be highly unstable when exposed to X-rays and the intensity of the signal at the N (1s) binding energy decayed rapidly with exposure. Subsequent experiments have also shown that the surface-bound product decomposes upon visible-light exposure, a topic that will be explored in future studies.

As the vinyl groups are converted to nitrate-containing products, a signal corresponding to the binding energy for O (1s) electrons also emerges in the high resolution XPS spectra (see Figure 3.8C). As expected, the vinyl-terminated monolayer shows no signal above the noise for the O (1s) transition before exposure. After 5000 L of NO_3 exposure, a peak positioned at 531.6 eV is consistent with that observed for $AgNO_3$ at 532.2 eV, and for adsorbed nitrates on a silver surface

at 531.6 eV.[59] Interestingly, the FWHM of the O (1s) peak used for fitting here is larger than that used to fit the same region in previous studies of surface-adsorbed nitrates,[38,59-61] indicative of a more diverse chemical environment for oxygen that may arise from nitro- as well as nitrate-containing surface-bound products.

Table 3.3. Comparison of binding energies for N (1s) transitions for several nitrogen-compounds

Species	**Binding Energy (eV)**	
	N (1s)	
	This Work[a]	**Literature Reference**[b]
-ONO_2	406.9	407.3, 407.2, 405.7 Baltrusaitis et al., Vovk et al., Zemlyanov et al.
NO_3^-		407.5 Rosseler et al.
$AgNO_3$		406.2 Zemlyanov et al.
$NaNO_3$		407.4 Baltrusaitis et al.
NO_2, NO_3	405.5, 408.8	405.9, 409.5, 405.4, 407.6 Baltrusaitis et al., Rosseler et al., Ammann et al.

[a] Calibrated to the Au ($4f_{7/2}$) peak at 83.8 eV. [b] Baltrusaitis et al. C (1s) at 285.0 eV; Vovkc et al. calibration not specified; Zemlyanov et al. and Rosseler et al. Au ($4f_{7/2}$) at 84.0 eV; Ammann et al. O (1s) of gas-phase water at 539.7 eV

The N (1s) spectra revealed that oxidation of the vinyl-terminated SAM by NO_3 resulted in the formation of nitrate compounds. However, in addition to the vinyl terminus, the Au-S bond is susceptible to oxidation, which would complicate interpretation of the IR results. Fortunately, XPS spectra of the S (2p) electrons before and after NO_3 exposure show that concentration and oxidation state of sulfur are unaffected by the impinging gas. The XPS data (Figure 3.8B) has been fitted to a composite (blue line) of two pairs of S ($2p_{3/2,1/2}$) with the same FWHM, branching area ratio of 2 ($2p_{3/2}$:$2p_{1/2}$), and standard spin-orbit splitting of 1.2 eV (the S ($2p_{3/2}$) peak at 161.9 eV and an irradiation-induced sulfur species S ($2p_{3/2}$) peak at 163.8 eV).[34,43,44] After 5000 L of NO_3

exposure, similar doublets are observed with nearly the same peak intensity,[45] which reveals that few, if any, Au-S bonds have been oxidized during the NO_3 exposure. Thus, reactions for this study appear to be isolated to the vinyl groups at the chain terminus. The preservation of the SAM is also evidenced by the high resolution XPS spectra in the C (1s) region (see Figure 3.8D). The peaks centered at 284.5 eV and 286.7 eV are coincident with the binding energy of the C (1s) electron in regular methylene groups and in the carbon atoms bound to sulfur.[43,47,48] After NO_3 exposure, the peak intensity at 284.4 eV was preserved, indicating that, in agreement with RAIRS data, few methylene chains desorbed from the surface upon reaction. In addition, the shoulder positioned at 287.0 eV suggests the emergence of a C-O or C=O species on the surface and is likely related to the carbon adjacent to the nitrate group that forms during oxidation of the double bond to form a $C\text{-}ONO_2$ group.[38,45,62]

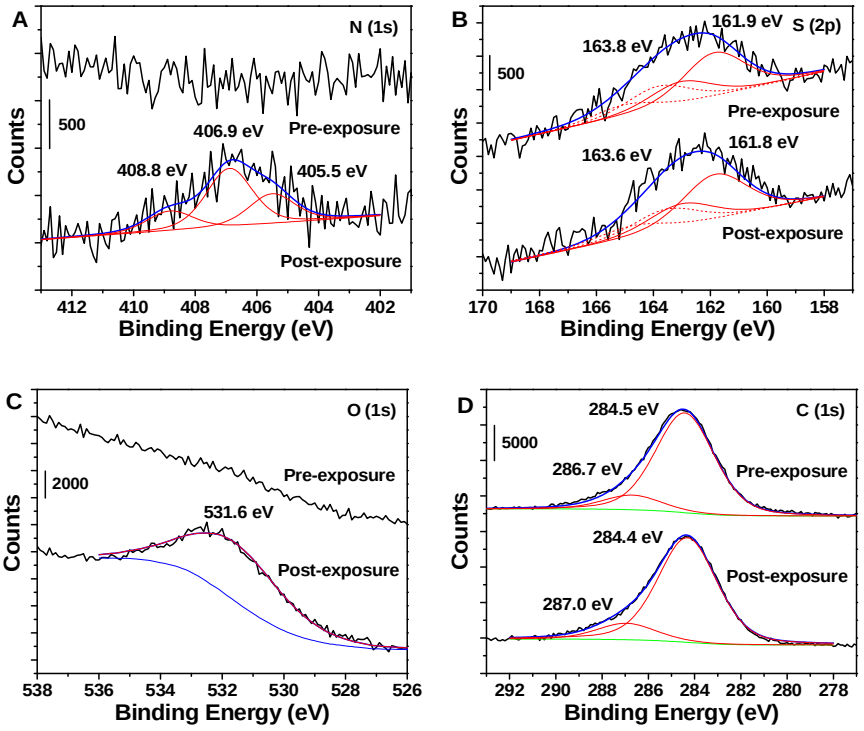

Figure 3.8. High resolution X-ray photoelectron spectra of the N (1s), S (2p), O (1s), and C (1s) regions of an 18C vinyl-terminated SAM before and after 5000 L of NO_3 exposure, which indicates the formation of organic nitrates and preservation of concentration and oxidation state of sulfur groups attached to the Au surface.

3.3.2.4 Reaction Rate, Probability and Proposed Mechanism

The preceding results provide evidence for the formation of an organo-nitrate species during the collisions of NO_3 on the vinyl-terminated SAM. The overall reactivity of NO_3 with the vinyl-terminated SAM is characterized by the reaction probability, which can be determined from the reaction rates.[18,31,63] The integrated intensities of the infrared bands assigned to the C=C mode at 1644 cm^{-1} and the asymmetric NO_2 stretch of organic nitrates at 1280 cm^{-1} are shown as a function of time during NO_3 exposure in Figure 3.9A and 3.9B. The lines through the data show that the rate of change for these IR features track pseudo-first-order kinetics, which follows a single exponential trend characterized by the rate constants $k_{obs} = (1.4 \pm 0.3) \times 10^{-3}$ s^{-1} and $k_{obs}' = (1.3 \pm 0.2) \times 10^{-3}$ s^{-1} according to the following equations:

$$A_{1644}(t) = (A_{1644})_0 \exp(-k_{obs}\, t) \quad (3.1)$$

$$A_{1280}(t) = (A_{1644})_0 [1 - \exp(-k_{obs}'\, t)] \quad (3.2)$$

where $A_{1644}(t)$ is the absorbance of the C=C group, $(A_{1644})_0$ is the initial absorbance of the same group before exposure to NO_3, $A_{1280}(t)$ is the absorbance of the asymmetric NO_2 stretch of organic nitrates at 1280 cm^{-1}, and t is the exposure time. The similarity of the two rate constants demonstrates a strong correlation between consumption of the double bonds and production of surface-bound nitrates.

The overall reaction probability, reflected by the rate of change in the IR intensity of the vinyl group, decreases exponentially with time as surface sites are consumed. The reaction probability for NO_3 impinging on the vinyl-terminated SAM depends on the rate constant, the surface coverage of reactive sites and the flux of NO_3. The initial reaction probability, γ_0, was determined by Equation (3.3)[64]

$$\gamma_0 = 4\theta_{max} k_{obs} / (\langle v \rangle [NO_3]_g) \quad (3.3)$$

where $\langle v \rangle$ is the mean molecular velocity of gas-phase NO_3, $[NO_3]_g$ is the gas-phase NO_3 concentration adjacent to the surface, and θ_{max} is the initial surface coverage of the carbon-carbon double bonds. The initial reaction probability for NO_3 collision with the 18C vinyl-terminated SAM is $\gamma_0 = (2.3 \pm 0.5) \times 10^{-3}$. That is, we find that approximately two reactions occur in every ~1000 collisions between NO_3 and the carbon-carbon double bonds.

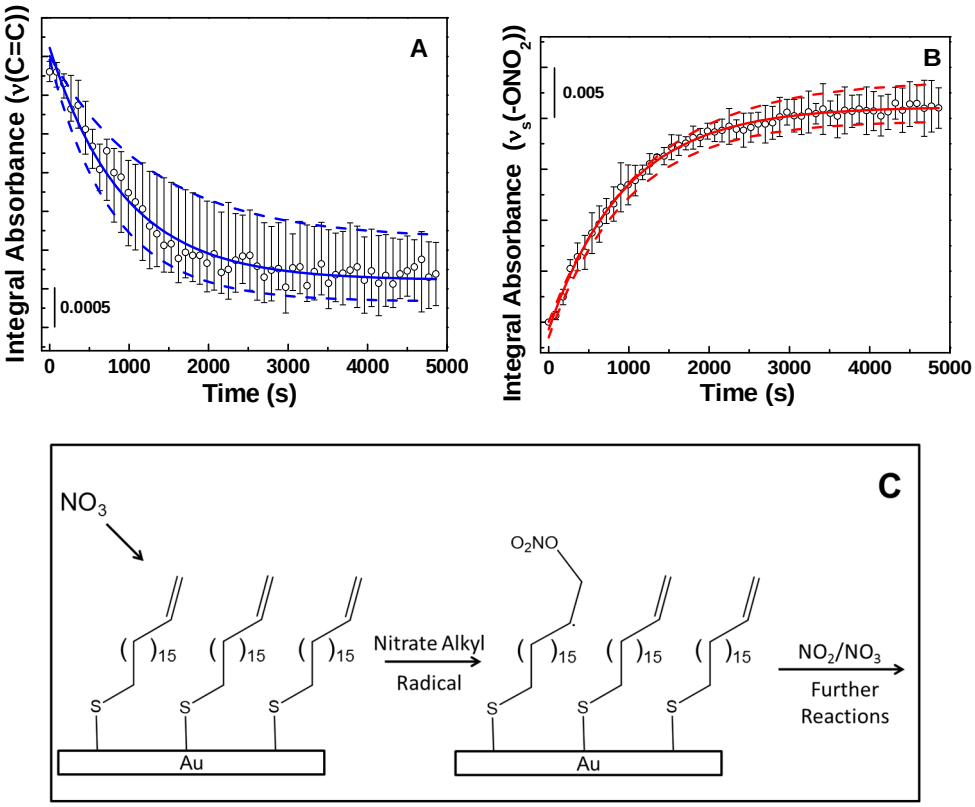

Figure 3.9. (A) Integral absorbance for ν(C=C) (at 1644 cm^{-1}) and (B) $\nu_a(-ONO_2)$ (at 1280 cm^{-1}) versus time during NO_3 exposure. The fitting curves follow the first-order kinetics. (C) A scheme of the possible mechanistic pathways showing the addition of NO_3 to the carbon-carbon double bond and the formation of an alkyl nitrate radical.

The initial reaction probability for NO_3 on the vinyl-terminated SAM is an order of magnitude smaller than the uptake coefficient for NO_3 on unsaturated fatty acid particles, as reported by Zhao et al.[31] Similarly, higher reaction probabilities have been measured for NO_3 on

alkenoic acids in a cylindrical flow reactor by Gross et al.[18] In addition, Bertram et al. reported a reaction probability of 3.4×10^{-2} for NO_3 exposure to an 11C vinyl-terminated SAM.[18] These previous studies differ from the work presented here in two important ways. First, in the previous work, the NO_3 consumption rate (rather than the rate of product formation) during the reaction was employed to determine the reaction probability. Secondly, the work by Bertram et al. was conducted in the presence of O_2 (rather than a clean vacuum environment). O_2 may play a role in the overall chemistry by oxidizing the alkyl radical to produce a nitroxy peroxyl radical that would undergo additional reactions with NO_3.[18] Thus, comparisons between the reaction rate reported here and those in the previous studies by Bertram et al. suggest that background gases play a critical role in the overall chemistry under real-word conditions.

During the heterogeneous oxidation of the vinyl-terminated SAM by NO_3 studied here, we observed that all of the bands associated with the double bond decreased in intensity at identical rates and concurrently with the emergence of new modes at 1649 cm^{-1}, 1280 cm^{-1} and 857 cm^{-1}, which are attributed to the formation of organo-nitrate moieties. The new features observed in RAIRS are consistent with the emergence of N (1s) and O (1s) electrons in the high-resolution XPS energy distributions. These results suggest that the reaction mechanism is one of addition to the vinyl group, such as: $NO_3\cdot + H_2C{=}CH\text{-}(CH_2)_{16}SAu \rightarrow O_2NO\text{-}CH_2\text{-}\cdot CH\text{-}(CH_2)_{16}SAu$. The addition likely occurs in such a way as to generate a radical in the subterminal C atom of the SAM, which is thermodynamically more favorable than its generation on the less substituted terminal C atom, as shown in Figure 3.9C. In addition, the peaks associated with the methylene backbone of the SAM broadened and decreased slightly in intensity, which could be due to many related processes. Specifically, propagation or reaction of the alkyl radicals would likely alter the

configuration of the SAM and reorientation of the methylene backbone may occur if additional impinging NO_3 or NO_2 adds to the alkyl radical.

The experimental results suggest that NO_3 adds exclusively to the terminal vinyl group and we have little evidence for the hydrogen abstraction reaction, $NO_3\cdot + H_2C{=}CH\text{-}(CH_2)_{16}SAu \rightarrow \cdot CH{=}CH\text{-}(CH_2)_{16}SAu + HNO_3$, which would be inconsistent with the type of first-order kinetics observed. This result is contrary to previous studies which highlight the important role that abstraction plays in nitrate-hydrocarbon chemistry.[6,19,28,58] To gain further insight into this result, our collaborators in the Troya group have conducted high-level electronic structure calculations of both the addition and the hydrogen abstraction reaction channels for NO_3 collision with vinyl groups by using propene as a model substrate. CCSD(T)/aug-cc-pVDZ single-point calculations employing B3LYP/6-31G* geometries indicate that the $NO_3\cdot + H_2C{=}CH\text{-}CH_3 \rightarrow \cdot CH{=}CH\text{-}CH_3 + HNO_3$ hydrogen abstraction reaction is endothermic by 8.3 kcal/mol and has a barrier of 9.9 kcal/mol. Under the thermal conditions of the experiment, only a negligible fraction of NO_3 molecules possess enough energy above the hydrogen abstraction barrier. This result provides a thermodynamic justification for the lack of apparent hydrogen abstraction reactions in the collisions of NO_3 with the vinyl-terminated SAMs examined in this work. Regarding the addition reaction, $NO_3\cdot + H_2C{=}CH\text{-}CH_3 \rightarrow O_2NO\text{-}CH_2\text{-}\cdot CH\text{-}CH_3$, electronic structure calculations at the same level (CCSD(T)/aug-cc-pVDZ//B3LYP/6-31G*) indicate this reaction is exothermic by 19.1 kcal/mol. However, the B3LYP/6-31G* calculations failed to locate a transition state. Consequently, the region of the potential energy surface (PES) that connects reagents with the transition state was characterized by scanning the C-O bond that is formed during the reaction from the addition minimum to the reagents' asymptote. The rest of coordinates were fully relaxed during the scan. Figure 3.10 shows that (as anticipated from the inability to locate a transition state

using conventional methods) the B3LYP/6-31G* method predicts a continuously downhill reaction path (black line). Single-point energies with the B3LYP/6-31G* geometries using other density functionals with larger basis sets also corroborate this observation, as illustrated in Figure 3.10. In addition, while using the B3LYP/6-31G* method to scan geometries directly, we utilized CCSD(T)/aug-cc-pVDZ at selected points during the scan to provide a higher-level description of the reaction path (blue line). As with the rest of the methods used in this work, CCSD(T)/aug-cc-pVDZ also predicts the absence of a barrier for the addition reaction. These calculations clearly indicate that addition is kinetically more favored than abstraction, which requires surmounting a significant barrier.

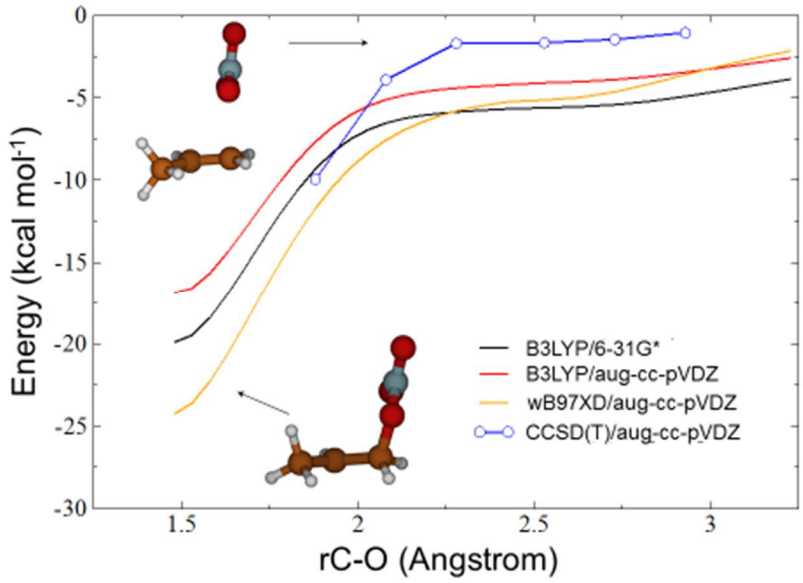

Figure 3.10. Potential-energy surface scan of the C-O coordinate for the addition reaction of NO_3 to propene. All calculations have been carried out with B3LYP/6-31G* geometries. Energies have not been zero-point corrected.

The initial reaction probability reported here, $\gamma_0 = (2.3 \pm 0.5) \times 10^{-3}$, is approximately two orders of magnitude higher than that for the reaction of ozone with long-chain vinyl-terminated SAMs (studied in the same laboratory).[51] One of the factors that might contribute to the origin of this difference in reactivity is that the energetic requirements for ozone addition might be larger

than those of nitrate addition. To illuminate this point, we have calculated the barrier for O_3 addition to propene at the same CCSD(T)/aug-cc-pVDZ//B3LYP/631-G* level that with which we characterized the NO_3 addition reaction. These calculations show that the barrier for ozone addition is below the reagents' asymptote (−1.9 kcal/mol, including zero-point correction). This result, which implies that both nitrate and ozone addition to propene are barrierless, does not explain the two-orders-of-magnitude difference in the measured reaction probabilities.

A difficulty in using these calculated barriers to explain differences in reactivity is that they correspond to gas-phase models, in which the minimum energy approach of NO_3 or O_3 to the double bond is not impaired by neighboring molecules. Along the minimum energy path, the NO_3 molecules approach perpendicularly to the double bond, so that the forming C-O bond is perpendicular to the double bond in the NO_3 addition (see insets of Figure 3.10). For ozone addition, the two forming C-O bonds are perpendicular to the double bond to form a cyclic primary ozonide.[65] Molecular dynamic simulations show that in a vinyl-SAM, the terminal double bond has a distribution of orientations at ambient conditions in which the double bond is rarely, if at all, perpendicular to the incoming NO_3 and O_3 molecules. Instead, the double bond tends to lie predominantly more parallel to the surface normal, implying that the perpendicular transition state obtained in the gas-phase calculations is not readily accessible in the first collision of the gases with the surfaces under our experimental conditions. Instead, reactions are likely caused by NO_3 and O_3 molecules trapped on the surface that encounter thermally fluctuating double bonds in geometries appropriate for reaction. Since the addition of NO_3 to the terminal double bond requires the formation of a perpendicular O-C bond with only the terminal C atom of the vinyl group, but O_3 addition requires the simultaneous formation of two O-C bonds with the terminal and the subterminal C atoms of the double bond, the probability of thermally sampling the transition state

region for nitrate addition may be far more likely than for ozone addition. These differences in the relative accessibility of the reaction coordinate are likely responsible for the larger interfacial reaction probability for nitrate radical observed in our experiments. This result could be a general phenomenon that extends to other organic surfaces and may play a role in the overall shorter lifetime of atmospheric NO_3 relative to O_3.

3.4 Summary

Reactions between NO_3 and model organic surfaces have been investigated by employing UHV-based techniques. Two methyl-terminated SAMs serve as well-characterized surfaces functionalized by saturated hydrocarbons. Results from RAIRS the reactivity of NO_3 with methyl-terminated SAMs increases with the decrease of the order of SAMs, which suggests that the oxidation mainly takes place along the methylene backbones at defect sites of the surface. In addition, elemental analysis performed by XPS suggest that, during the NO_3 exposure, the gas molecules likely attack defect sites and ultimately oxidize the sulfur atoms for relatively disordered SAMs but only react with a small amount of the methylene groups for ordered SAMs.

While the well-ordered methyl-terminated SAM shows low reactivity upon NO_3 exposure, the exploration of the oxidation of surface vinyl groups by NO_3 reveals insight into three key aspects of this reaction. First, surface vinyl groups are consumed at the same rate as organic nitrate formation, suggesting that the consumption of vinyl groups is primarily responsible for the formation of organic nitrates. Second, the initial reaction probability, $(2.3 \pm 0.5) \times 10^{-3}$, is approximately two orders of magnitude higher than that for the reaction of ozone with the same SAM, which is likely due to the accessibility of the transition state for nitrate addition. The reaction mechanism was elucidated from a combination of IR measurements of the reaction in UHV, XPS analysis of the surface, and electronic structure calculations. The reaction begins by initial addition

of NO_3 to the carbon-carbon double bonds to form an alkyl nitrate radical that may undergo subsequent reactions, such as NO_2 addition. Even under long exposure time, there is little indication of sulfur oxidation, suggesting that the reactions were limited to the terminal double bond. Together, these insights may influence the development of more accurate theoretical models to understand the detailed kinetics and dynamics of NO_3 reactions with atmospheric organics for predicting the fate of NO_3 in the environment. Ultimately, future work exploring reactions of mixed SAMs that contain polar functional groups may help us to understand the importance of interfacial functionality in determining the fate of gas-surface collisions involving NO_3 radicals on secondary organic aerosols in the atmosphere.

REFERENCES

(1) Noxon, J. F.; Norton, R. B.; Marovich, E., NO_3 in the Troposphere. *Geophys. Res. Lett.* **1980,** *7* (2), 125-128.

(2) Winer, A. M.; Atkinson, R.; Pitts, J. N., Gaseous Nitrate Radical - Possible Nighttime Atmospheric Sink for Biogenic Organic-Compounds. *Science* **1984,** *224* (4645), 156-159.

(3) Platt, U.; LeBras, G.; Poulet, G.; Burrows, J. P.; Moortgat, G., Peroxy Radicals from Night-Time Reaction of NO_3 with Organic Compounds. *Nature* **1990,** *348* (6297), 147-149.

(4) Eberhard, J.; Howard, C. J., Rate Coefficients for the Reactions of Some C_3 to C_5 Hydrocarbon Peroxy Radicals with NO. *J. Phys. Chem. A* **1997,** *101*, 3360-3366.

(5) Asaf, D.; Tas, E.; Pedersen, D.; Peleg, M.; Luria, M., Long-Term Measurements of NO_3 Radical at a Semiarid Urban Site: 2. Seasonal Trends and Loss Mechanisms. *Environ. Sci. Technol.* **2010,** *44* (15), 5901-5907.

(6) Kerdouci, J.; Picquet-Varrault, B.; Durand-Jolibois, R.; Gaimoz, C.; Doussin, J.-F., An Experimental Study of the Gas-Phase Reactions of NO_3 Radicals with a Series of Unsaturated Aldehydes: Trans-2-Hexenal, Trans-2-Heptenal, and Trans-2-Octenal. *J. Phys. Chem. A* **2012,** *116* (41), 10135-10142.

(7) Gai, Y.; Wang, W.; Ge, M.; Kjaergaard, H. G.; Jørgensen, S.; Du, L., Methyl Chavicol Reactions with Ozone, OH and NO_3 Radicals: Rate Constants and Gas-Phase Products. *Atmos. Environ.* **2013,** *77* (0), 696-702.

(8) Atkinson, R.; Aschmann, S. M.; Winer, A. M.; Pitts, J. N., Kinetics and Atmospheric Implications of the Gas-Phase Reactions of Nitrate Radicals with a Series of Monoterpenes and Related Organics at 294 ± 2 K. *Environ. Sci. Technol.* **1985,** *19* (2), 159-163.

(9) Barnes, I.; Bastian, V.; Becker, K. H.; Tong, Z., Kinetics and Products of the Reactions of Nitrate Radical with Monoalkenes, Dialkenes, and Monoterpenes. *J. Phys. Chem.* **1990,** *94* (6), 2413-2419.

(10) Atkinson, R.; Plum, C. N.; Carter, W. P. L.; Winer, A. M.; Pitts, J. N., Rate Constants for the Gas-Phase Reactions of Nitrate Radicals with a Series of Organics in Air at 298 ± 1 K. *J. Phys. Chem.* **1984,** *88* (6), 1210-1215.

(11) Aschmann, S. M.; Atkinson, R., Effect of Structure on the Rate Constants for Reaction of NO_3 Radicals with a Series of Linear and Branched C_5–C_7 1-Alkenes at 296 ± 2 K. *J. Phys. Chem. A* **2011,** *115* (8), 1358-1363.

(12) Salgado, M.; Gallego-Iniesta, M.; Martín, M.; Tapia, A.; Cabañas, B., Night-Time Atmospheric Chemistry of Methacrylates. *Environ. Sci. Pollut. R.* **2011,** *18* (6), 940-948.

(13) Wang, K.; Ge, M. F.; Wang, W. G., Kinetics of the Gas-Phase Reactions of 5-Hexen-2-One with OH and NO_3 Radicals and O_3. *Chem. Phys. Lett.* **2010,** *490* (1-3), 29-33.

(14) Zhao, Z. J.; Husainy, S.; Smith, G. D., Kinetics Studies of the Gas-Phase Reactions of NO_3 Radicals with Series of 1-Alkenes, Dienes, Cycloalkenes, Alkenols, and Alkenals *J. Phys. Chem. A* **2011,** *115*, 12161-12172.

(15) D. King, M.; E. Canosa-Mas, C.; P. Wayne, R., Frontier Molecular Orbital Correlations for Predicting Rate Constants between Alkenes and the Tropospheric Oxidants NO_3, OH and O_3. *Phys. Chem. Chem. Phys.* **1999,** *1* (9), 2231-2238.

(16) Tapia, A.; Villanueva, F.; Salgado, M. S.; Cabañas, B.; Martínez, E.; Martín, P., Atmospheric Degradation of 3-Methylfuran: Kinetic and Products Study. *Atmos. Chem. Phys.* **2011,** *11* (7), 3227-3241.

(17) Goeschen, U. W. a. C., Oxidative Damage of Thymidines by the Atmospheric Free-Radical Oxidant No_3. *Aust. J. Chem.* **2011,** *64* (6), 833-842.

(18) Gross, S.; Iannone, R.; Xiao, S.; Bertram, A. K., Reactive Uptake Studies of NO_3 and N_2O_5 on Alkenoic Acid, Alkanoate, and Polyalcohol Substrates to Probe Nighttime Aerosol Chemistry. *Phys. Chem. Chem. Phys.* **2009,** *11*, 7792-7803.

(19) Knopf, D. A.; Mak, J.; Gross, S.; Bertram, A. K., Does Atmospheric Processing of Saturated Hydrocarbon Surfaces by NO_3 Lead to Volatilization? *Geophys. Res. Lett.* **2006,** *33* (17), L17816.

(20) Love, J. C.; Estroff, L. A.; Kriebel, J. K.; Nuzzo, R. G.; Whitesides, G. M., Self-Assembled Monolayers of Thiolates on Metals as a Form of Nanotechnology. *Chem. Rev.* **2005,** *105* (4), 1103-1170.

(21) Gates, B. D.; Xu, Q.; Stewart, M.; Ryan, D.; Willson, C. G.; Whitesides, G. M., New Approaches to Nanofabrication: Molding, Printing, and Other Techniques. *Chem. Rev.* **2005,** *105* (4), 1171-1196.

(22) Nuzzo, R. G.; Zegarski, B. R.; Dubois, L. H., Fundamental Studies of the Chemisorption of Organosulfur Compounds on Gold(111). Implications for Molecular Self-Assembly on Gold Surfaces. *J. Am. Chem. Soc.* **1987,** *109* (3), 733-740.

(23) Widrig, C. A.; Alves, C. A.; Porter, M. D., Scanning Tunneling Microscopy of Ethanethiolate and N-Octadecanethiolate Monolayers Spontaneously Absorbed at Gold Surfaces. *J. Am. Chem. Soc.* **1991,** *113* (8), 2805-2810.
(24) Ulman, A.; Eilers, J. E.; Tillman, N., Packing and Molecular Orientation of Alkanethiol Monolayers on Gold Surfaces. *Langmuir* **1989,** *5* (5), 1147-1152.
(25) Dubois, L. H.; Nuzzo, R. G., Synthesis, Structure, and Properties of Model Organic-Surfaces. *Annu. Rev. Phys. Chem.* **1992,** *43*, 437-463.
(26) Moise, T.; Talukdar, R. K.; Frost, G. J.; Fox, R. W.; Rudich, Y., Reactive Uptake of NO_3 by Liquid and Frozen Organics. *J. Geophys. Res.* **2002,** *107* (D2), 4014.
(27) Skov, H.; Benter, T.; Schindler, R. N.; Hjorth, J.; Restelli, G., Epoxide Formation in the Reactions of the Nitrate Radical with 2,3-Dimethyl-2-Butene, Cis-2-Butene and Trans-2-Butene and Isoprene. *Atmos. Environ.* **1994,** *28* (9), 1583-1592.
(28) Finlayson-Pitts, B. J.; Pitts, J. N., *Chemistry of the Upper and Lower Atmosphere: Theory, Experiments, and Applications*. Academic Press: San Diego, CA, 2000.
(29) Hjorth, J.; Lohse, C.; Nielsen, C. J.; Skov, H.; Restelli, G., Products and Mechanisms of the Gas-Phase Reactions between Nitrate Radical and a Series of Alkenes. *J. Phys. Chem.* **1990,** *94* (19), 7494-7500.
(30) Shiraiwa, M.; Poschl, U.; Knopf, D. A., Multiphase Chamical Kinetics of No_3 Radicals Reacting with Organic Aerosol Components from Biomass Burning. *Environ. Sci. Technol.* **2012,** *46*, 6630-6636.
(31) Zhao, Z. J.; Husainy, S.; Stoudemayer, C. T.; Smith, G. D., Reactive Uptake of NO_3 Radicals by Unsaturated Fatty Acid Particles. *Phys. Chem. Chem. Phys.* **2011,** *13*, 17809-17817.
(32) Heintz, F.; Platt, U.; Flentje, H.; Dubois, R., Long-Term Observation of Nitrate Radicals at the Tor Station, Kap Arkona (Rügen). *J. Geophys. Res.* **1996,** *101* (D17), 22891-22910.
(33) DeMore, W. B.; Sander, S. P.; Golden, D.; Hampson, R.; Kurylo, M. J.; Howard, C.; Ravishankara, A.; Kolb, C.; Molina, M., *Chemical Kinetics and Photochemical Data for Use in Stratospheric Modeling*. JPL Pub.: 1994.
(34) Gorham, J.; Smith, B.; Fairbrother, D. H., Modification of Alkanethiolate Self-Assembled Monolayers by Atomic Hydrogen: Influence of Alkyl Chain Length. *J. Phys. Chem. C* **2007,** *111*, 374-382.
(35) Vegh, J., The Analytical Form of the Shirley-Type Background. *J. Electron Spectrosc. Relat. Phenom.* **1988,** *46*, 411-417.
(36) Vegh, J., The Shirley-Equivalent Electron Inelastic Scattering Cross-Section Function. *Surf. Sci.* **2004,** *563*, 183-190.
(37) Baltrusaitis, J.; Jayaweera, P. M.; Grassian, V. H., Xps Study of Nitrogen Dioxide Adsorption on Metal Oxide Particle Surfaces under Different Environmental Conditions. *Phys. Chem. Chem. Phys.* **2009,** *11*, 8295-8305.
(38) Rosseler, O.; Sleiman, M.; Montesinos, V. N.; Shavorskiy, A.; Keller, V.; Keller, N.; Litter, M. I.; Bluhm, H.; Salmeron, M.; Destaillats, H., Chemistry of NO_x on TiO_2 Surfaces Studied by Ambient Pressure Xps: Products, Effect of Uv Irradiation, Water, and Coadsorbed K^+. *J. Phys. Chem. Lett.* **2013,** *4*, 536-541.
(39) Adamson, A. W.; Gast, A. P., Physical Chemistry of Surfaces. **1967**.
(40) NIST Chemistry WebBook: 2011.

(41) Snyder, R. G.; Strauss, H. L.; Elliger, C. A., Carbon-Hydrogen Stretching Modes and the Structure of N-Alkyl Chains. 1. Long, Disordered Chains. *J. Phys. Chem.* **1982,** *86*, 5145-5150.
(42) Greenler, R. G., Infrared Study of Adsorbed Molecules on Metal Surfaces by Reflection Techniques. *J. Chem. Phys.* **1966,** *44* (1), 310-315.
(43) Heister, K.; Zharnikov, M.; Grunze, M., Characterization of X-Ray Induced Damage in Alkanethiolate Monolayers by High-Resolution Photoelectron Spectroscopy. *Langmuir* **2001,** *17*, 8-11.
(44) Wagner, A. J.; Carlo, S. R.; Vecitis, C.; Fairbrother, D. H., Effect of X-Ray Irradiation on the Chemical and Physical Properties of a Semifluorinated Self-Assembled Monolayer. *Langmuir* **2002,** *18*, 1542-1549.
(45) Torres, J.; Perry, C. C.; Bransfield, S. J.; Fairbrother, D. H., Radical Reactions with Organic Thin Films: Chemical Interaction of Atomic Oxygen with an X-Ray Modified Self-Assembled Monolayer. *J. Phys. Chem. B* **2002,** *106*, 6265-6272.
(46) Castner, D. G., X-Ray Photoelectron Spectroscopy Sulfur 2p Study of Organic Thiol and Disulfide Binding Interactions with Gold Surfaces. *Langmuir* **1996,** *12*, 5083-5086.
(47) Wagner, A. J.; Carlo, S. R.; Vecitis, C. D.; Fairbrother, H., *Langmuir* **2002,** *18*, 1542-1549.
(48) Vogt, A. D.; Han, T.; Beebe, T. P., *Langmuir* **1997,** *13*, 3397-3403.
(49) Gross, S.; Bertram, A. K., Products and Kinetics of the Reactions of an Alkane Monolayer and a Terminal Alkene Monolayer with NO_3 Radicals. *J. Geophys. Res.* **2009,** *114* (D2), 1-14.
(50) Duan, L.; Garrett, S. J., Self-Assembled Monolayers of 6-Phenyl-N-Hexanethiol and 6-(P-Vinylphenyl)-N-Hexanethiol on Au(111): An Investigation of Structure, Stability, and Reactivity. *Langmuir* **2001,** *17* (10), 2986-2994.
(51) Lu, J. W.; Fiegland, L. R.; Davis, E. D.; Alexander, W. A.; Wagner, A.; Gandour, R. D.; Morris, J. R., Initial Reaction Probablity and Dynamics of Ozone Collisions with a Vinyl-Terminated Self-Assembled Monolayer. *J. Phys. Chem. C* **2011,** *115*, 25343-25350.
(52) Peanasky, J. S.; McCarley, R. L., Surface-Confined Monomers on Electrode Surfaces. 4. Electrochemical and Spectroscopic Characterization of Undec-10-Ene-1-Thiol Self-Assembled Monolayers on Au. *Langmuir* **1998,** *14* (1), 113-123.
(53) Wandas, M.; Puszko, A., Ir Spectra of 2-Alkylamino- and Alkylnitramino-3- or 5-Nitro-4-Methylpyridine Derivatives. *Chem. Heterocycl. Compd. (N. Y., NY, U. S.)* **2000,** *36* (7), 796-800.
(54) Aubuchon, C. M.; Rector, K. D.; Holmes, W.; Fayer, M. D., Nitro Group Asymmetric Stretching Mode Lifetimes of Molecules Used in Energetic Materials. *Chem. Phys. Lett.* **1999,** *299*, 84-90.
(55) Noda, J.; Hallquist, M.; Langer, S.; Ljungstrom, E., Products from the Gas-Phase Reaction of Some Unsaturated Alcohols with Nitrate Radicals. *Phys. Chem. Chem. Phys.* **2000,** *2*, 2555-2564.
(56) Rappe, A. K.; Casewit, C. J.; Colwell, K. S.; Goddard, W. A.; Skiff, W. M., Uff, a Full Periodic Table Force Field for Molecular Mechanics and Molecular Dynamics Simulations. *J. Am. Chem. Soc.* **1992,** *114* (25), 10024-10035.
(57) Cornell, W. D.; Cieplak, P.; Bayly, C. I.; Gould, I. R.; Merz, K. M.; Ferguson, D. M.; Spellmeyer, D. C.; Fox, T.; Caldwell, J. W.; Kollman, P. A., A Second Generation Force Field for the Simulation of Proteins, Nucleic Acids, and Organic Molecules. *J. Am. Chem. Soc.* **1995,** *117* (19), 5179-5197.

(58) Jee, J.; Tao, F.-M., Reaction Mechanisms and Kinetics for the Oxidations of Dimethyl Sulfide, Dimethyl Disulfide, and Methyl Mercaptan by the Nitrate Radical. *J. Phys. Chem. A* **2006,** *110* (24), 7682-7689.
(59) Zemlyanov, D.; Schlogl, R., Effect of Oxygen on No Adsorption on the Ag(111) Surface: Evidence for a $NO_{3,Ads}$ Species. *Surf. Sci.* **2000,** *470*, L20-L24.
(60) Vovk, E. I.; Turksoy, A.; Bukhtiyarov, V. I.; Ozensoy, E., Interactive Surface Chemistry of CO_2 and NO_2 on Metal Oxide Surfaces: Competition for Catalytic Adsorption Sites and Reactivity. *J. Phys. Chem. C* **2013,** *117*, 7713-7720.
(61) Krepelova, A.; Newberg, J.; Huthwelker, T.; Bluhm, H.; Ammann, M., The Nature of Nitrate at the Ice Surface Studied by Xps and Nexafs. *Phys. Chem. Chem. Phys.* **2010,** *12*, 8870-8880.
(62) Wagner, C. D.; Riggs, W. M.; Davis, L. E.; Moulder, J. F.; Muilenberg, G. E., *Handbook of X-Ray Photoelectron Spectroscopy*. Perkin-Elmer Corporation: 1979.
(63) Xiao, S.; Bertram, A. K., Reactive Uptake Kinetics of NO_3 on Multicomponent and Multiphase Organic Mixtures Containing Unsaturated and Saturated Organics. *Phys. Chem. Chem. Phys.* **2011,** *13* (14), 6628-6636.
(64) Donaldson, D. J.; Mmereki, B. T.; Chaudhuri, S. R.; Handley, S.; Oh, M., Uptake and Reaction of Atmospheric Organic Vapours on Organic Films. *Faraday Disc. Chem. Soc.* **2005,** *130*, 227-239.
(65) Nguyen, T. L.; Park, J.; Lee, K.; Song, K.; Barker, J. R., Mechanism and Kinetics of the Reaction $NO_3 + C_2H_4$. *J. Phys. Chem. A* **2011,** *115*, 4894-4901.

Chapter 4

Hydrogen Abstraction Probability in Collisions of Gas-phase Nitrate Radicals with Surface-bound Hydroxyls

4.1 Introduction

Oxidation of alcohols by NO_3 yields organic nitrates, ketones, and aldehydes, which are precursors of peroxyacyl nitrates (PANs), a component of photochemical smog.[1,2] Furthermore, in the presence of O_2, reactions of alcohols with NO_3 could directly form PANs.[3-5] In addition to producing important environmental organics, reactions between alcohols and NO_3 provide an additional source of O_3, with an ozone generation capacity of up to 17 g of O_3 from 1 g of alcohol oxidized by NO_3.[6] These important aspects of atmospheric chemistry involving NO_3 and alcohols have motivated many laboratory studies into the reaction kinetics and mechanism.[1,6-9]

Previous studies of gas-phase reactions between unsaturated alcohols and NO_3 at ambient pressure showed that carbonyl-containing compounds and organic nitrates were the major products.[1] These products were likely generated from NO_3 oxidation of alkyl radicals, which were formed through either NO_3 addition to carbon-carbon double bonds (C=C) or hydrogen abstraction from methylene groups in the unsaturated alcohols.[1,5] However, whether only one pathway or both mechanisms play a role in the overall reaction has yet to be fully elucidated. Recently, Moreno et al. studied the kinetics of gas-phase reactions between saturated alcohols and NO_3 radicals.[6] The rate coefficients they determined for a series of saturated alcohols reacting with NO_3 were comparable to the rate constants calculated by Aschmann et al. in studies of NO_3 reactions with

varying chain-length 1-alkenes.[6,10] The high gas-phase reactivity of NO_3 with alcohols suggests that NO_3 may also oxidize hydroxyl-functionalized organic particulates found throughout the atmosphere.

Interfacial reactions of NO_3 with alcohol-containing organic particles may alter particulate size, chemical composition, and optical properties.[11] Changes in the properties of the particles may affect the scattering and absorption of light, thereby affecting the balance between incident and outgoing solar radiation.[12] Motivated by the potentially important role of NO_3 heterogeneous chemistry, scientists have explored the fundamental nature of NO_3 reactions on alcohol-containing organic surfaces.[7,8,13] Moise et al. investigated uptake coefficients (the ratio of the number of molecules lost to the total number that collide with a surface) of NO_3 on several types of organic liquids.[13] Interestingly, the uptake coefficient of NO_3 by 1-octanol surface was found to be similar to or even higher than that of NO_3 impinging onto the surface of a liquid alkene.[13] However, in studies of NO_3 impinging on alkenoic acid and polyalcohol substrates by Gross et al., the uptake coefficient of NO_3 was found to be orders of magnitude lower than on alkenoic acid surfaces.[7] Despite the fundamental importance of these reactive uptake measurements, the specific reaction pathways were not resolved in these studies.

As a complement to the previous work in this field, we have employed infrared spectroscopic methods and well-characterized model hydroxylated organic surfaces to investigate the reaction pathways and uptake probability of NO_3 in collisions with HO-functionalized surfaces. Specifically, the work presented below describes an ultrahigh vacuum (UHV) surface science study into the reaction between a well-controlled flux of NO_3 and well-characterized hydroxyl-terminated self-assembled monolayers (SAMs). By tracking the rate of bond rupture and formation

during the gas-surface collision, we have determined the initial reaction probability and identified the likely initial reaction mechanism for this important interfacial oxidation process.

4.2 Experimental

All experiments were performed in an ultra-high vacuum (UHV)-based instrument for the study of the kinetics and dynamics of reactions between nitrate radicals and model organic surfaces. The main chamber, with a base pressure of 10^{-9} Torr, eliminates reactions of background gases (O_2, H_2O etc.) with the surface. The surface-bound molecules were tracked via in situ reflection-absorption infrared spectroscopy (RAIRS).

4.2.1 Preparation of Hydroxyl-terminated Self-Assembled Monolayers

The 16-mercapto-1-hexadecanol used for the work described in this chapter was purchased from Frontier Scientific, Inc. The surface samples were created by immersing pre-cleaned polycrystalline gold substrates in 1 mM ethanol solutions of 16-mercapto-1-hexadecanol. The gold slides composed of 1000 Å of Au deposited on a Cr-coated silica surface were purchased from EMF Corp. and cleaned by soaking them in a piranha solution (7:3 (v:v) ration of sulfuric acid/hydrogen peroxide) for ~ 1 h. Before being placed into the thiol solution, the gold substrates were removed from the piranha solution, rinsed thoroughly with deionized water (Millipore Purification Systems, 18.2 MΩ), and dried with ultra-high purity (UHP) nitrogen. A well-ordered and tightly packed 16-carbon (16-C) hydroxyl-terminated SAM was achieved upon ~48 hours immersion. After being rinsed with ethanol and dried under a stream of UHP N_2, the SAMs were transferred directly into the UHV main chamber through a sample transfer load-lock system.

4.2.2 Nitrate Radical Formation

In the presence of an excess amount of ozone, nitrogen monoxide was oxidized to yield dinitrogen pentoxide (N_2O_5) which was stored in a glass trap submerged in a dry ice/ethanol bath. NO_3 was created by thermal decomposition of N_2O_5 and was dosed directly onto the sample through an all-glass capillary array doser coupled to a N_2O_5 synthesis and storage system which was reported elsewhere.[14] While dosing with the capillary array doser, the high pressure side of the capillary was ~30 Torr, the pressures within the UHV chamber reached ~1×10^{-6} Torr, and the conductance of the capillary array doser was 4.1×10^{-4} cm^3 s^{-1}. The flux of N_2O_5 (2.3×10^{15} molecules s^{-1}) onto the surface was estimated from a calculation based on the kinetic theory of gases. According to the physical dimensions of the doser and the temperature-dependent equilibrium constant for $NO_3 + NO_2 \rightleftharpoons N_2O_5$ ($K_{eq} = 2.7 \times 10^{-27} \times \exp(11000/T)$ cm^3 $molecule^{-1}$),[15,16] the concentration of NO_3 adjacent to the surface was determined to be 2.8×10^{10} molecules cm^{-3}. The calculated flux was consistent with the pressure rise in the vacuum chamber during NO_3 exposure to a clean Au surface.

4.2.3 Reflection-Absorption Infrared Spectroscopy

All experiments were performed in the UHV surface science instrument, which enables *in-situ* measurements of surface-bound species via RAIRS. RAIR spectra were provided by a Bruker IFS 66v/S spectrometer attached to the UHV chamber. Focused IR radiation from a SiC globar was reflected from the gold surface at ~86˚ relative to the surface normal through a differentially pumped KBr window. The reflected radiation was detected by a mid-range (750-4000 cm^{-1}) mercury cadmium telluride (MCT) detector, which was cooled by liquid nitrogen prior to each experiment. Each individual spectrum shown in this manuscript were the average of 100 scans

with a 2 cm^{-1} resolution. A clean Au surface was used as the background unless otherwise declared.

4.3 Results and Discussion

4.3.1 Initial Characterization of a 16-C HO-SAM with RAIRS

Prior to NO_3 exposure, a RAIR spectrum of the 16-C hydroxyl-terminated SAM on a polycrystalline gold substrate was recorded (Figure 4.1). Extensive previous studies have identified the molecular motions associated with each band in this spectrum, which reveal key insights into the monolayer structure.[17-19] Several features in the spectrum show that the long-chain hydroxyl-terminated alkanethiols form a well-ordered monolayer on the gold substrate. First, the most intense bands at 2918 and 2850 cm^{-1} are due to the asymmetric ($\nu_a(CH_2)$) and symmetric ($\nu_s(CH_2)$) stretching modes of CH_2 groups along the backbone of the chains.[20] Both the position and the width of the two peaks suggest that the chains reside in a crystalline-like environment.[20,21] Measurements of film thickness and molecular dynamics simulations found that the film thickness linearly increased with the increasing chain length of the adsorbed thiols from 9 to 21 carbon atoms, which are only seen for all-trans chains.[19] Thus, the crystalline-like packing suggests that the chains are organized in an all-trans configuration. Furthermore, the narrow line width of the 1469 cm^{-1} band, which is attributed to the scissoring deformation of -CH_2- groups in the alkyl chains ($\delta(CH_2)$), is consistent as well with the crystalline-like environment.[18,22] In addition to the stretching and deformation modes of methylene groups, three other bands associated with the terminal hydroxyl group appear in the spectrum of Figure 4.1. The feature at 2878 cm^{-1} is assigned to a C-H stretching mode due to partial disorder at the α-CH_2 adjacent to the -OH group ($\nu(CH_2(OH))$).[17,19,23] The broad band in the range of 3100-3550 cm^{-1} is characteristic of

intermolecular hydrogen bonding between neighboring -OH groups on the topmost surface.[17,21] A very weak feature present ~3650 cm^{-1} is most likely due to non-hydrogen-bonded or weakly-hydrogen-bonded OH vibrational motions (ν(OH)).[21] The bands at 1060 and 1076 cm^{-1} are attributed to the stretching mode of C-O in the terminal -CH_2OH group (ν(CO)).[19]

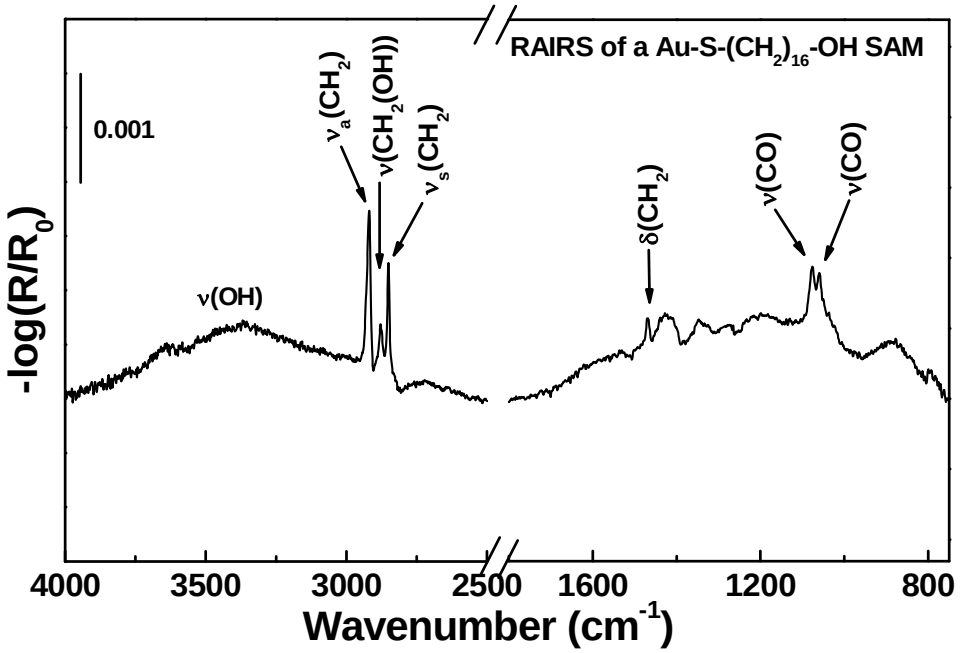

Figure 4.1. Reflection-absorption infrared spectrum of a 16-C hydroxyl-terminated SAM on Au formed from a 16-mercapto-1-hexadecanol fabricated through solution immersion. The five most intense IR active modes are highlighted as $\nu_a(CH_2)$, $\nu_s(CH_2)$, $\nu(CH_2(OH))$, $\delta(CH_2)$, and ν(CO).

The well-resolved splitting of the ν(CO) mode is likely due to the coupling of such stretching frequency to similar C-C stretching frequencies.[17,24,25] In addition, the ν(CO) mode splitting into two components may be due to the presence of the two nonequivalent terminal -CH_2OH units (proton acceptor and donor) in the hydrogen-bonded clusters on the surface.[26] Furthermore, the existence of the two conformers, with the OH group trans and gauche with respect to the methylene group, could also contribute to the splitting of the ν(CO) mode.[27] Studies of vibrational spectroscopy of ethanol molecules by Huisken and co-workers revealed that the

potential energies of trans-trans ethanol dimers (−32.6 kJ/mol) was different from that of gauche-gauche (−28.3 kJ/mol) or trans-gauche (−32.8 kJ/mol) dimers, which may cause the splitting of the CO stretching mode.[26] The consistency of the features in this characteristic spectrum with previous studies suggests a 21.4 $Å^2$ occupation of a single alkenethiol chain adsorbed on the gold substrate, which corresponds to a surface density of 4.7×10^{14} molecules cm^{-2}.[18,19,28]

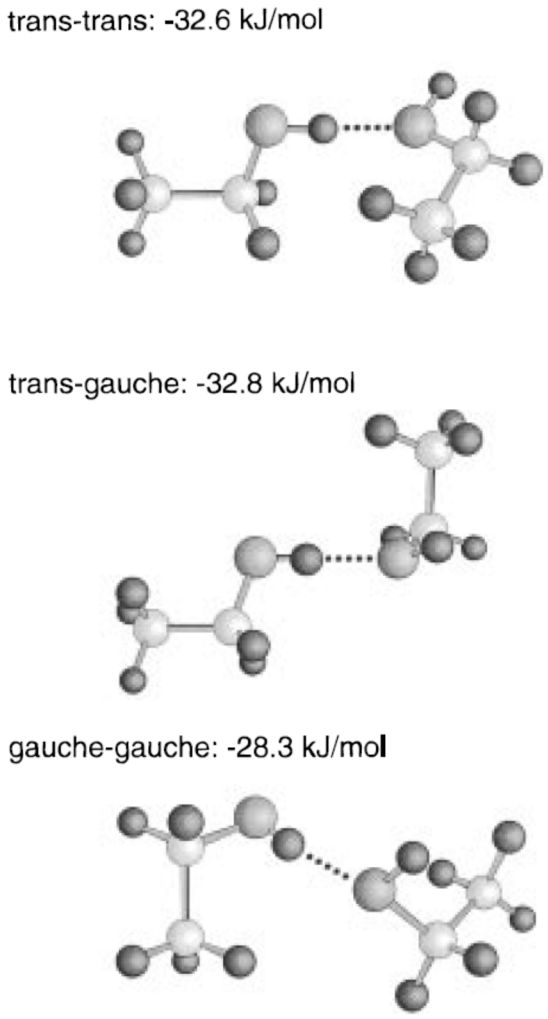

Figure 4.2. A diagram of minimum potential energy configurations of ethanol dimers determined for three different conformer combinations (Reprinted with permission from J. Phys. Chem. A, 1997, 101, 7768-7777. Copyright 1997 American Chemical Society).

4.3.2 IR Characterization of HO-SAM during NO_3 exposure.

Following initial characterization, the 16-C hydroxyl-terminated SAM surface was exposed to a continuous source of incident gases. For studies of the surface chemistry during exposure, the original SAM was used as the background such that negative features in the spectra indicate the removal of groups associated with those modes from the surface and positive bands reveal an increase in absorbance or the development of new modes. To measure the reactivity of NO_2 or N_2O_5, pure NO_2 or room-temperature N_2O_5 (without heating the doser) was introduced into the main chamber. Figure 4.3 shows the difference spectra of the 16-C HO-SAM exposed to NO_2, N_2O_5 and NO_3 in a 1:1 ratio with NO_2 gas. Compared to the features observed in spectrum (d), little change can be seen above noise in spectra (b) and (c), which suggests that the gas-surface reaction is dominated by oxidations of the SAM surface by NO_3.

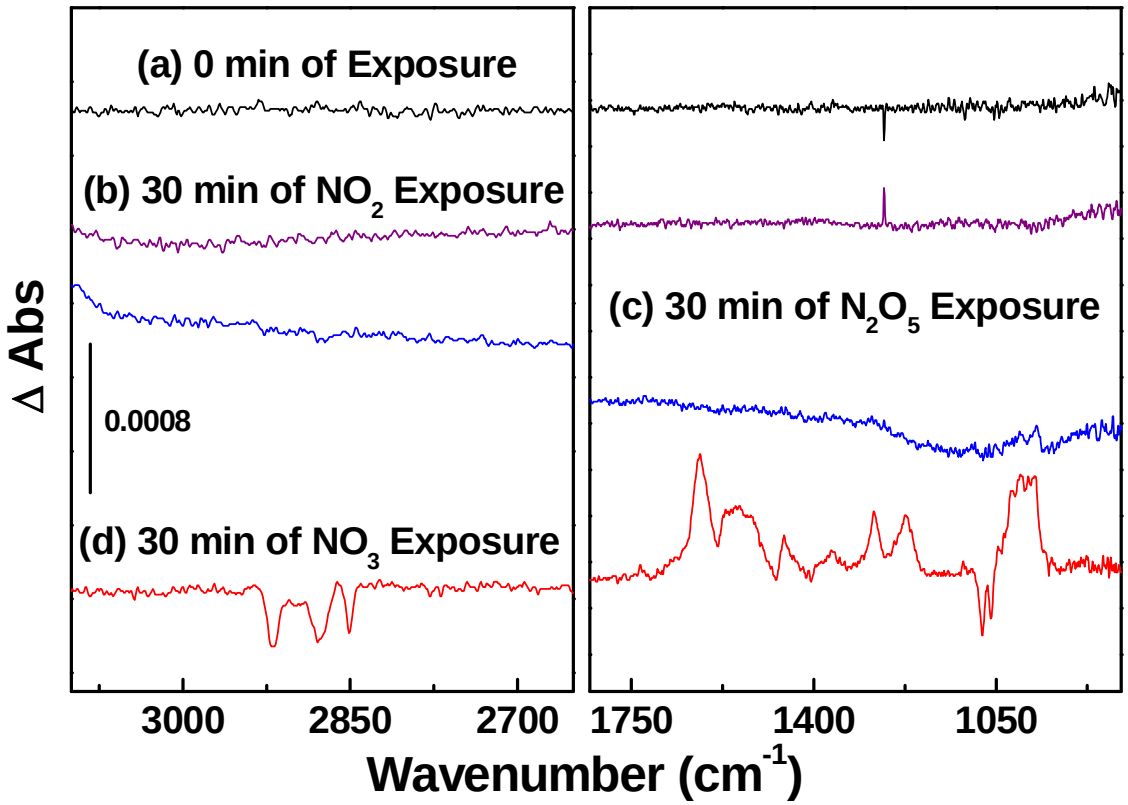

Figure 4.3. Reflection-absorption infrared difference spectra of a 16C HO-SAM exposed to NO_2 (spectrum (b)), N_2O_5 (spectrum (c)), and NO_3 (spectrum (d)). The spectrum shown on top (spectrum (a)) is that of the SAM prior to NO_3 exposure using the HO-SAM as the background.

Figure 4.4 shows the difference RAIR spectra of a freshly-made HO-SAM exposed to NO_3. The initial spectrum in Figure 4.4 (the lower-most spectrum) is the difference spectrum of the monolayer before exposure. The difference spectra clearly show that, at the beginning of reactions (spectrum (b)), the first features observed are the decay in intensity of bands associated with the terminal -CH_2OH groups at 2878 cm^{-1} ($\nu(CH_2(OH))$), 1060 and 1076 cm^{-1} ($\nu(CO)$). As these features decrease in intensity, a broad and intense band appears in the range of 920-1050 cm^{-1}. The emergence of this broad band is likely due to the formation a new C-O bond or due to a shift of the original C-O stretching mode (in the -CH_2OH group) to lower wavenumber. There are several factors that could result in the red shift of $\nu(CO)$. Previous studies found that the differences

between electronegativities of two atoms in a vibratory link played a significant role in predicting properties of bonds and interpreting vibrational spectra.[29] Furthermore, in studies of the relationship between bond force constants and electronegativities of bonded atoms reported by Gordy,[30] the bond-stretching force constant was found to decrease with the product of the electronegativities of two atoms linking a bond.

Previous studies proposed that reactions between NO_3 and saturated organics were likely dominated by hydrogen abstraction from methylene groups and the reaction rate tended to increase with the increasing number of substitution at the $-CH_2-$ group.[8,31,32] In the present work, the reaction between the NO_3 radical and the 16-C HO-terminated SAM is likely initiated by hydrogen abstraction at the terminal groups, $-CH_2OH$. The resultant product would then be the alkyl radical ($AuS(CH_2)_{15}C\cdot HOH/AuS(CH_2)_{15}CH_2O\cdot$), which would readily react with impinging NO_3 or NO_2 to form the organic nitrate ($AuS(CH_2)_{15}(CHONO_2)OH/AuS(CH_2)_{15}CH_2OONO_2$) or the nitro-compound ($AuS(CH_2)_{15}(CHNO_2)OH$).[6,31] For the case of an alkyl radical formation, the electronegativity of the carbon or oxygen atom may increase (the electron affinity increase) with the formation of the alkyl radical ($AuS(CH_2)_{15}C\cdot HOH/AuS(CH_2)_{15}CH_2O\cdot$),[33,34] which would result in the increase of the vibrational force constant of C-O. However, Gordy also found that the force constant was not only correlated with the product of electronegativities but also directly proportional to the bond order.[30] Therefore, it is possible that the formation of the alkyl radical could reduce the bond order enough to more than counterbalance the effects of the greater electronegativity product. And thus, the overall effects could cause the decrease of the force constant, then red shifting the C-O stretching mode in RAIRS. After formation of the alkyl radical, the radical could further react with NO_3 to yield organic nitrates or nitro-compounds. Both of these products would result in a decrease of electronegativity of the carbon or oxygen atom by

effectively replacing the H atom with a more electronegative species (-ONO_2 or -NO_2).[35] This decrease in the electronegativity can be attributed to a reduction in the effective nuclear charge of carbon or oxygen atom on electrons involved in the C-O bond that results from the addition of species with resonance hybrid structure to the terminal group (-NO_2 or -NO_2).[30] Hence, the force constant of the C-O stretching mode may decrease with the product of the electronegativity, resulting in the red shift of that mode in RAIR spectra, as we observed in Figure 4.4. Alternatively, formation of a new C-O bond upon addition of species (-ONO_2 or -NO_2) to the terminal group or intermolecular hydrogen bonding among terminal groups[24,36] could account for the observation of features in the range of 920-1050 cm^{-1}.

Concurrently with changes of features described above, several new bands centered at 1283 cm^{-1}, 1555 cm^{-1}, and 1622 cm^{-1} appear upon 600 L (1 Langmuir (L) = 10^{-6} torr s) exposure, labeled (b) in Figure 4.4. These features have much smaller intensities compared to the broad band in the region of 920-1050 cm^{-1}, which is likely due to the small concentration of products on the surface at the beginning of NO_3 oxidation, a low absorptivity of reaction products, or the parallel orientation of the transition dipole moment for vibrational motions associated with reaction products.[37] The absorbances in the range of 1170-1659 cm^{-1} have very similar vibrational frequencies to those previously assigned to stretching modes of organic nitrates or nitro-containing SAMs,[14] suggesting the addition of NO_2 and NO_3 groups after initial hydrogen abstraction. However, definitive assignments of these features to particular vibrational modes will require future work, possibly involving isotopic labeling experiments and quantum mechanical computations.

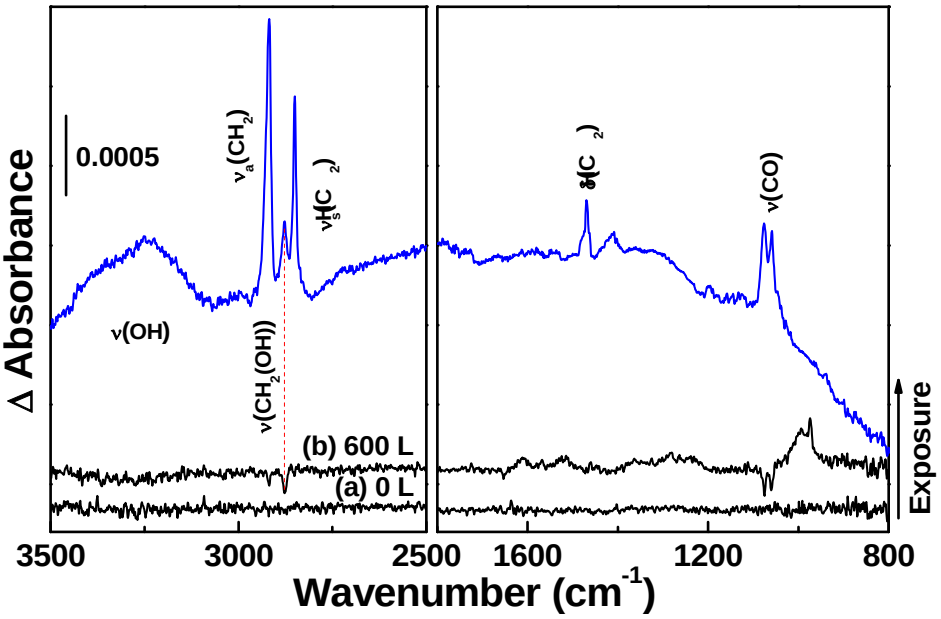

Figure 4.4. Reflection-absorption infrared difference spectra of a 16C hydroxyl-terminated SAM exposed to NO_3. The spectrum shown on top in blue is that of the SAM prior to NO_3 exposure using a clean Au sample as the background. Upon 600 L NO_3 exposure, the spectra in black show that modes associated with the -CH_2OH moiety decrease and new modes emerge. The background for this scan is the original pre-exposure spectrum (blue).

4.3.3 Reaction Rate, Probability of Hydrogen Abstraction

Upon further exposure of NO_3 to the 16-C HO-terminated SAM, all of the bands associated with the terminal hydroxyl groups (-CH_2OH) decay in intensity (Figure 4.5A), indicating consumption of the -CH_2OH groups during NO_3 collision with the organic surface. Furthermore, the well-resolved bands in the range of 920-1050 cm^{-1} become broad, which suggests that the chemical environment of the C-O bond changes with increasing exposure time. Commensurate with a decrease in the absorbance of the modes associated with the -CH_2OH group, positive features in the region of 1170-1659 cm^{-1} increase in intensity. The wavenumbers of these positive bands are consistent with IR features reported previously[1] for organic nitrates (1678 cm^{-1} and 1285 cm^{-1}). In addition, studies of gas-phase reactions of ortho, meta-, and para-cresol with nitrate radicals reported by Olariu et al. showed infrared bands at 1548 cm^{-1}, 1358 cm^{-1}, and 1219 cm^{-1},

which are characteristic of nitrophenol compounds.[9] Therefore, the bands centered at 1222 cm^{-1}, 1283 cm^{-1}, 1555 cm^{-1} and 1622 cm^{-1} in Figure 4.5 are likely due to the formation of organic nitrates and nitro-compounds during NO_3 reaction with the HO-terminated SAM.

Beyond the spectral changes observed in the low wavenumber region (1800-800 cm^{-1}) and the decrease in the intensity of $\nu(CH_2(OH))$ at 2878 cm^{-1}, the only change in the difference spectra (above the detection limit of the spectrometer, which we estimate to be 2% of a ML) is the decrease of bands assigned to the asymmetric and symmetric stretching modes of the CH_2 groups along the backbone of the chains. We speculate that the decrease in the absorptivity of these features at long exposure times is due to hydrogen abstraction from the methylene groups or radical migration along the chain that initiates subsequent reactions, which affect the concentration of methylene groups.

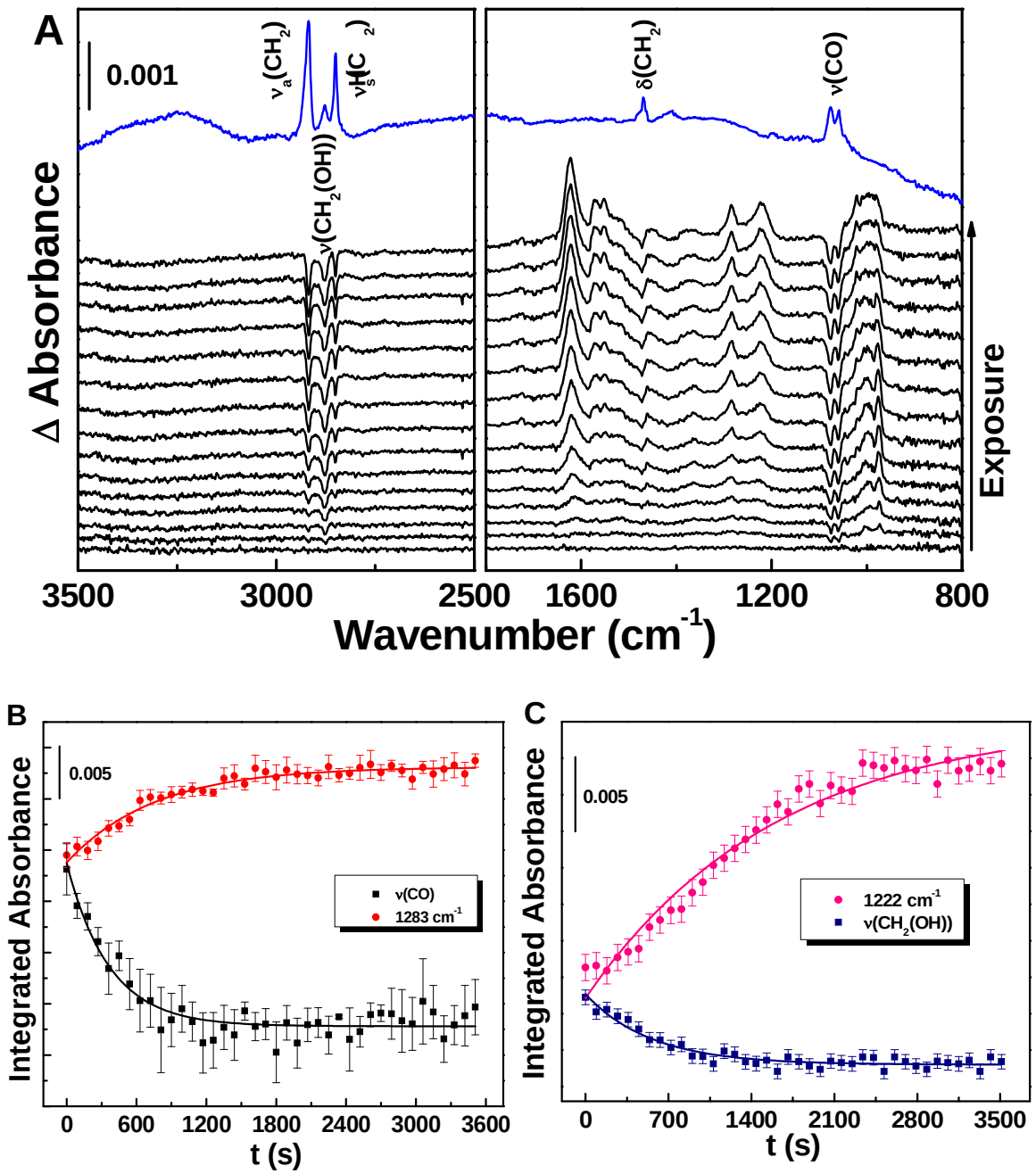

Figure 4.5. (A) Reflection-absorption infrared difference spectra of a 16C hydroxyl-terminated SAM exposed to NO_3. The spectrum shown on top in blue is that of the SAM prior to NO_3 exposure using a clean Au sample as the background. Upon NO_3 exposure, the spectra in black show that modes associated with the -CH_2OH moiety decrease and new modes emerge. The background for this scan is the original pre-exposure spectrum (blue), with the exposure increasing by 3×10^2 L per spectrum. Integrated absorbance of (B) ν(C-O) at 1060 cm^{-1} and 1076 cm^{-1} (black square) and the band at 1283 cm^{-1} (red solid circle) and (C) $\nu(CH_2(OH))$ at 2878 cm^{-1} (blue square) and the band at 1222 cm^{-1} (pink solid circle) versus time during NO_3 exposure. The fitting curves follow the first-order kinetics.

In addition to characterizing the IR spectra during NO_3 collisions with the 16-C HO-terminated SAM, we have studied the rate of consumption of C-O bonds in the terminal -CH_2OH groups and the rate of formation of organic nitrates (absorptivity of the band at 1283 cm^{-1}). Figure 4.5B displays plots of the integrated absorbance of the original ν(CO) band and of the band at 1283 cm^{-1} (ABS_{1283}) as a function of time. The curves through the data show that the rate of change for these bands track pseudo-first-order kinetics, with rate constants of $k_{obs} = (1.9 \pm 0.8) \times 10^{-3}$ s^{-1} (ν(CO)) and $k_{obs}' = (1.1 \pm 0.2) \times 10^{-3}$ s^{-1} (ABS_{1283}) respectively. The rate constants were obtained from fitting in Figure 4.5 according to the following equations:

$$A_{\nu(CO)}(t) = (A_{\nu(CO)})_0 \exp(-k_{obs}\, t) \qquad (4.1)$$

$$A_{1283}(t) = (A_{\nu(CO)})_0 [1 - \exp(-k_{obs}'\, t)] \qquad (4.2)$$

where $A_{\nu(CO)}$ (t) is the absorbance of the C-O group, $(A_{\nu(CO)})_0$ is the initial absorbance of the same group before exposure to NO_3, $A_{1283}(t)$ is the absorbance of the band at 1283 cm^{-1}, and t is the exposure time. The similarity of the two rate constants demonstrates a strong correlation between consumption of the -CH_2OH groups and production of surface-bound nitrates.

Using the same method, the observed rate constants for the consumption of the ν(CH_2(OH)) mode and the band at 1222 cm^{-1} are $(1.6 \pm 0.2) \times 10^{-3}$ s^{-1} and $(0.7 \pm 0.3) \times 10^{-3}$ s^{-1}, respectively (Figure 4.5C). The similarity of the consumption rate of the ν(CH_2(OH)) band to that of the ν(CO) band suggest that the H abstraction by NO_3 primarily occurs at the methylene groups adjacent to the terminal hydroxyls. Other positive bands in the low wavenumber region lacked sufficient resolution for definitive assignments and determination of formation rates for particular functional groups.

The consumption of ν(CO) in the terminal groups may be due to either cleavage of the C-O bond or the shift of the vibrational frequency of ν(CO) resulting from changes in chemical environment. As discussed above, hydrogen abstraction at terminal groups could result in the shift of ν(CO) from high wavenumbers to lower ones. However, no evidence in RAIRS showed the cleavage of C-O bonds. Therefore, the red shift of the stretching mode of C-O bonds is most likely due to H abstraction by NO_3 at the terminal -CH_2OH groups on the surface. The initial reaction probability, γ_0, which is simply the ratio of reactive collisions to total collisions, can be extracted from the rate constant for the consumption of the ν(CO) according to equation (1):

$$\gamma_0 = 4\theta_{max} k_{obs} / (\langle v \rangle [NO_3]_g) \qquad (4.1)$$

where $\langle v \rangle$ is the mean molecular velocity of gas-phase NO_3, $[NO_3]_g$ is the gas-phase NO_3 concentration adjacent to the surface, and θ_{max} is the initial surface coverage of the carbon-carbon double bonds. According to this analysis, the initial reaction probability for NO_3 collision with the 16-C HO-terminated SAM is $\gamma_0 = (6 \pm 1) \times 10^{-3}$. That is, we find that approximately six reactions occur in every ~1000 collisions between NO_3 and the terminal hydroxyl groups.

The current value for the initial reaction probability is about two orders of magnitude lower than the rate at which NO_3 reacts in interfacial encounters with particles composed of aromatic compounds[39] or aromatic alcohols[8] under atmosphere pressure. Similarly, about one order of magnitude higher reaction probabilities, compared with the value for γ_0 reported here, have been measured for NO_3 on alkenoic acids in a cylindrical flow reactor.[7,13] The much higher reactivity of NO_3 with organic compounds in these systems may be due to the presence of multiple functional groups (vinyl groups and hydroxyl groups) that could react with NO_3 as well as the effect of background gases (O_2, H_2O etc.) under atmospheric pressure. In addition, the initial reaction

probability of H abstraction from -CH_2- in an HO-SAM is much higher than that for the reaction of NO_3 with an 18C H_3C-SAM. Although the kinetic data was failed to obtained with the current data for NO_3 collisions with the 18C H_3C-SAM due to the extremely low reactivity (changes can barely observed in the IR spectrum, as shown in Figure 4.6), the upper limit of the initial reaction probability could be estimated through the limit of detection for RAIRS (2% of one monolayer) which is on a scale of 10^{-5}. Therefore, the γ_0 determined in this chapter is at least 2 orders of magnitude than that for H abstraction from methylenes of the 18C H_3C-SAM, which is likely due to a weaker C-H bond of the -CH_2- group adjacent to the terminal hydroxyls.[38] An interesting comparison to the current study is the recent UHV-based experiments reported by Zhang et al.,[14] which show that the initial reaction probability of NO_3 with an 18-C vinyl-terminated SAM is about a factor of three smaller than that value reported here. Because control experiments of NO_3 collision with an 18-C methyl-terminated SAM showed little reaction (see Figure 3.2 in Chapter 3 and Figure 4.6 here), the factor-of-three difference in reactivity is likely due to the effect induced by hydrogen bonding among terminal groups. There may be two ways in which the hydrogen bonding between terminal OH groups enhances chemistry: 1) it opens access to the CH_2 groups adjacent to the hydroxyl terminus; 2) it provides a surface dipole that enhances accommodation and trapping of impinging gases on the surface.[40,41] In a chemical dynamics study of intrasurface hydrogen-bonding effects in gas-surface energy exchange and accommodation, Hase and co-workers showed that the structure of an 11-C HO-SAM surface was relatively disordered with hydrogen-bonding between the hydroxyl groups that forms small clusters of OH groups or chains consisting of a larger number of OH groups.[42] This disordered structure could create hollow sites on the surface so that impinging NO_3 would have high possibility to be trapped on the surface and react with the surface functional group. Furthermore, compared to collisions of Ar atoms with

methyl-terminated SAMs, in collision with HO-terminated SAMs, the Ar atoms access more attractive and repulsive regions of the potential surface and are more strongly bound to the surface.[42] The character of stronger physisorption by HO-terminated SAMs may be a factor that drives a higher reactivity of NO_3 with the 16-C hydroxyl-terminated SAM.

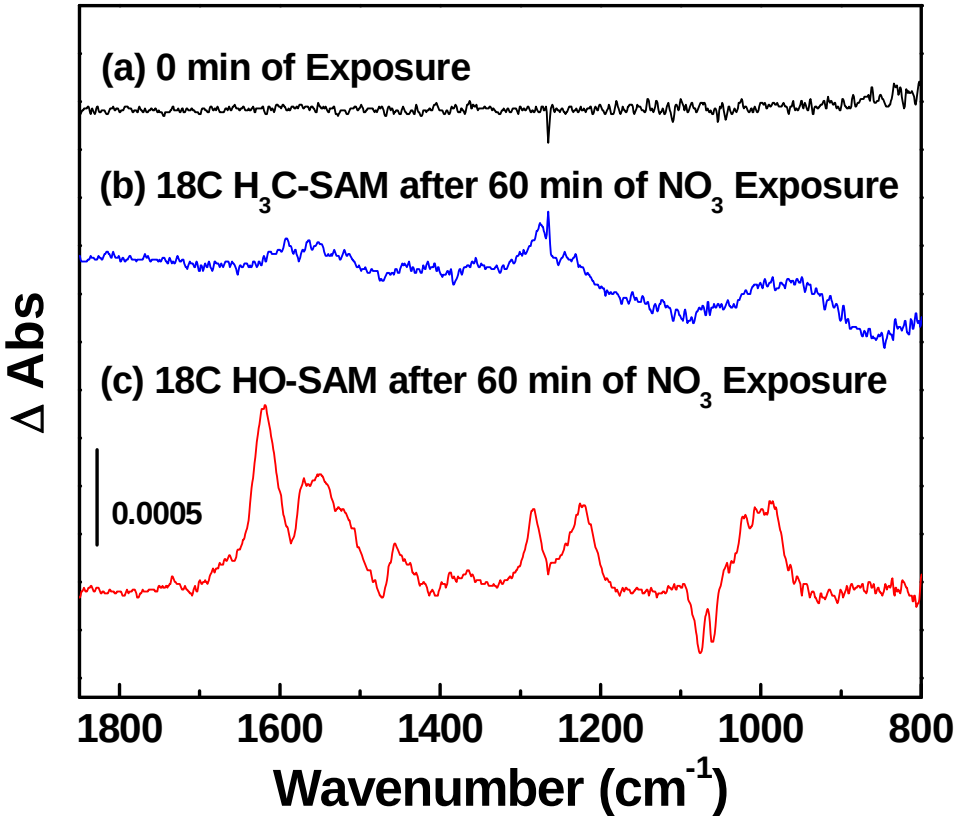

Figure 4.6. Reflection-absorption infrared difference spectra of an 18C H_3C-SAM and a 16C HO-SAM after 60 min of NO_3 exposure. The spectrum shown on top (spectrum (a)) is that of the SAM prior to NO_3 exposure using the original SAM as the background.

4.4 Summary

Overall, the results discussed in this chapter provide fundamental insights into the nighttime oxidation chemistry involving NO_3 and surface-bound alcohols that may ultimately affect their environmental fate. Indeed, there are many factors that play roles in determining the rate and the initial reaction probability of NO_3 collision with the HO-SAM, including the

energetics of the impinging NO_3, the orientation and the momentum of NO_3 molecules, the steric aspects of organic nitrates or nitro-compounds formed on a closely packed SAM surface, and possible structural changes of the surface upon the initial reaction that may alter subsequent interactions between NO_3 and the surface. Although the UHV measurements are not immediately relevant to reactions that take place under atmospheric conditions, they do provide valuable benchmarks for theoretical studies of these reactions, aid in spectral assignments of interfacial nitrogen-containing species, and reveal how NO_3 reacts with organic surfaces under pristine conditions. Such experiments are the first steps in building a comprehensive understanding of the important atmospheric reactions between NO_3 and complex organic surfaces.

REFERENCES

(1) Noda, J.; Hallquist, M.; Langer, S.; Ljungstrom, E., Products from the Gas-Phase Reaction of Some Unsaturated Alcohols with Nitrate Radicals. *Phys. Chem. Chem. Phys.* **2000,** *2*, 2555-2564.

(2) Seinfeld, J. H.; Pandis, S. N., *Atmoshperic Chemistry and Physics*. John Wiley & Sons: New York, NY, 1998.

(3) McCaulley, J. A.; Kelly, N.; Golde, M. F.; Kaufman, F., Kinetic Studies of the Reactions of Atomic Fluorine and Hydroxyl Radical with Methanol. *J. Phys. Chem.* **1989,** *93* (3), 1014-1018.

(4) Atkinson, R., Gas-Phase Tropospheric Chemistry of Volatile Organic Compounds: 1. Alkanes and Alkenes. *J. Phys. Chem. Ref. Data* **1997,** *26*, 215-290.

(5) Finlayson-Pitts, B. J.; Pitts, J. N., *Chemistry of the Upper and Lower Atmosphere: Theory, Experiments, and Applications*. Academic Press: San Diego, CA, 2000.

(6) Moreno, A.; Salgado, M. S.; Martín, M. P.; Martínez, E.; Cabañas, B., Kinetic Study of the Gas Phase Reactions of a Series of Alcohols with the NO_3 Radical. *J. Phys. Chem. A* **2012,** *116* (42), 10383-10389.

(7) Gross, S.; Iannone, R.; Xiao, S.; Bertram, A. K., Reactive Uptake Studies of NO_3 and N_2O_5 on Alkenoic Acid, Alkanoate, and Polyalcohol Substrates to Probe Nighttime Aerosol Chemistry. *Phys. Chem. Chem. Phys.* **2009,** *11*, 7792-7803.

(8) Liu, C.; Zhang, P.; Wang, Y.; Yang, B.; Shu, J., Heterogeneous Reactions of Particulate Methoxyphenols with No3 Radicals: Kinetics, Products, and Mechanisms. *Environ. Sci. Technol.* **2012,** *46* (24), 13262-13269.

(9) Olariu, R. I.; Barnes, I.; Bejan, I.; Arsene, C.; Vione, D.; Klotz, B.; Becker, K. H., Ft-Ir Product Study of the Reactions of NO_3 Radicals with Ortho-, Meta-, and Para-Cresol. *Environ. Sci. Technol.* **2013,** *47* (14), 7729-7738.

(10) Aschmann, S. M.; Atkinson, R., Effect of Structure on the Rate Constants for Reaction of NO_3 Radicals with a Series of Linear and Branched C_5−C_7 1-Alkenes at 296 ± 2 K. *J. Phys. Chem. A* **2011,** *115* (8), 1358-1363.

(11) Ellison, G. B.; Tuck, A. F.; Vaida, V., Atmospheric Processing of Organic Aerosols. *J. Geophys. Res.* **1999,** *104* (D9), 11633-11641.

(12) Lu, J. W.; Flores, J. M.; Lavi, A.; Abo-Riziq, A.; Rudich, Y., Changes in the Optical Properties of Benzo[a]Pyrene-Coated Aerosols Upon Heterogeneous Reactions with NO_2 and NO_3. *Phys. Chem. Chem. Phys.* **2011,** *13* (14), 6484-6492.

(13) Moise, T.; Talukdar, R. K.; Frost, G. J.; Fox, R. W.; Rudich, Y., Reactive Uptake of NO_3 by Liquid and Frozen Organics. *J. Geophys. Res.* **2002,** *107* (D2), 4014.

(14) Zhang, Y.; Chapleski, R. C.; Lu, J. W.; Rockhold, T. H.; Troya, D.; Morris, J. R., Gas-Surface Reactions of Nitrate Radicals with Vinyl-Terminated Self-Assembled Monolayers. *Phys. Chem. Chem. Phys.* **2014,** *16* (31), 16659-16670.

(15) DeMore, W. B.; Sander, S. P.; Golden, D.; Hampson, R.; Kurylo, M. J.; Howard, C.; Ravishankara, A.; Kolb, C.; Molina, M., *Chemical Kinetics and Photochemical Data for Use in Stratospheric Modeling*. JPL Pub.: 1994.

(16) Heintz, F.; Platt, U.; Flentje, H.; Dubois, R., Long-Term Observation of Nitrate Radicals at the Tor Station, Kap Arkona (Rügen). *J. Geophys. Res.* **1996,** *101* (D17), 22891-22910.

(17) Atre, S. V.; Liedberg, B.; Allara, D. L., Chain Length Dependence of the Structure and Wetting Properties in Binary Composition Monolayers of OH- and CH_3-Terminated Alkanethiolates on Gold. *Langmuir* **1995,** *11* (10), 3882-3893.

(18) Dubois, L. H.; Nuzzo, R. G., Synthesis, Structure, and Properties of Model Organic-Surfaces. *Annu. Rev. Phys. Chem.* **1992,** *43*, 437-463.

(19) Nuzzo, R. G.; Dubois, L. H.; Allara, D. L., Fundamental Studies of Microscopic Wetting on Organic Surfaces. 1. Formation and Structural Characterization of a Self-Consistent Series of Polyfunctional Organic Monolayers. *J. Am. Chem. Soc.* **1990,** *112* (2), 558-569.

(20) MacPhail, R. A.; Strauss, H. L.; Snyder, R. G.; Elliger, C. A., Carbon-Hydrogen Stretching Modes and the Structure of N-Alkyl Chains. 2. Long, All-Trans Chains. *J. Phys. Chem.* **1984,** *88* (3), 334-341.

(21) Bertilsson, L.; Liedberg, B., Infrared Study of Thiol Monolayer Assemblies on Gold: Preparation, Characterization, and Functionalization of Mixed Monolayers. *Langmuir* **1993,** *9* (1), 141-149.

(22) Nuzzo, R. G.; Zegarski, B. R.; Dubois, L. H., Fundamental Studies of the Chemisorption of Organosulfur Compounds on Gold(111). Implications for Molecular Self-Assembly on Gold Surfaces. *J. Am. Chem. Soc.* **1987,** *109* (3), 733-740.

(23) Ichimura, A. S.; Lew, W.; Allara, D. L., Tripod Self-Assembled Monolayer on Au(111) Prepared by Reaction of Hydroxyl-Terminated Alkylthiols with Sicl4. *Langmuir* **2008,** *24* (6), 2487-2493.

(24) Stuart, A. V.; Sutherland, G. B. B. M., Effect of Hydrogen Bonding on the Deformation Frequencies of the Hydroxyl Group in Alcohols. *J. Chem. Phys.* **1956,** *24* (3), 559-570.

(25) Socrates, G., *Infrared and Raman Characteristic Group Frequencies: Tables and Charts*. 3 rd ed. ed.; John Wiley & Sons, Inc.: New York, 2001.
(26) Ehbrecht, M.; Huisken, F., Vibrational Spectroscopy of Ethanol Molecules and Complexes Selectively Prepared in the Gas Phase and Adsorbed on Large Argon Clusters. *J. Phys. Chem. A* **1997,** *101* (42), 7768-7777.
(27) Barnes, A. J.; Hallam, H. E., Infra-Red Cryogenic Studies. Part 5.-Ethanol and Ethanol-D Argon Matrices. *Trans. Faraday Soc.* **1970,** *66* (0), 1932-1940.
(28) Love, J. C.; Estroff, L. A.; Kriebel, J. K.; Nuzzo, R. G.; Whitesides, G. M., Self-Assembled Monolayers of Thiolates on Metals as a Form of Nanotechnology. *Chem. Rev.* **2005,** *105* (4), 1103-1170.
(29) Wheland, G. W., *The Theory of Resonance*. John Wiley & Sons, Inc.: New York, 1944.
(30) Gordy, W., A Relation between Bond Force Constants, Bond Orders, Bond Lengths, and the Electronegativities of the Bonded Atoms. *J. Chem. Phys.* **1946,** *14* (5), 305-320.
(31) Harrison, J. C.; Wells, J. R., 2–Butoxyethanol and Benzyl Alcohol Reactions with the Nitrate Radical: Rate Coefficients and Gas-Phase Products. *Int. J. Chem. Kinet.* **2012,** *44* (12), 778-788.
(32) Parker, J. K.; Espada-Jallad, C., Kinetics of the Gas-Phase Reactions of OH and NO_3 Radicals and O_3 with Allyl Alcohol and Allyl Isocyanate. *J. Phys. Chem. A* **2009,** *113* (36), 9814-9824.
(33) Mulliken, R. S., A New Electroaffinity Scale; Together with Data on Valence States and on Valence Ionization Potentials and Electron Affinities. *J. Chem. Phys.* **1934,** *2* (11), 782-793.
(34) Mulliken, R. S., Electronic Structures of Molecules Xi. Electroaffinity, Molecular Orbitals and Dipole Moments. *J. Chem. Phys.* **1935,** *3* (9), 573-585.
(35) Tsu, D. V.; Lucovsky, G.; Davidson, B. N., Effects of the Nearest Neighbors and the Alloy Matrix on SiH Stretching Vibrations in the Amorphous SiO_r:H ($0<r<2$) Alloy System. *Phys. Rev. B* **1989,** *40* (3), 1795-1805.
(36) Jeffrey, G. A., *An Introduction to Hydrogen Bonding*. Oxford University Press: 1997.
(37) Greenler, R. G., Infrared Study of Adsorbed Molecules on Metal Surfaces by Reflection Techniques. *J. Chem. Phys.* **1966,** *44* (1), 310-315.
(38) Haynes, W. M., *Crc Handbook of Chemistry and Physics*. CRC press: 2013.
(39) Zhang, P.; Wang, Y.; Yang, B.; Liu, C.; Shu, J., Heterogeneous Reactions of Particulate Benzo[B]Fluoranthene and Benzo[K]Fluoranthene with NO_3 Radicals. *Chemosphere* **2014,** *99* (0), 34-40.
(40) Alexander, W. A.; Troya, D., Theoretical Study of the Dynamics of Collisions between HCl and ω-Hydroxylated Alkanethiol Self-Assembled Monolayers. *J. Phys. Chem. C* **2011,** *115* (5), 2273-2283.
(41) Levine, R. D., *Molecular Reaction Dynamics*. Cambridge University Press: 2005.
(42) Tasić, U.; Day, B. S.; Yan, T.; Morris, J. R.; Hase, W. L., Chemical Dynamics Study of Intrasurface Hydrogen-Bonding Effects in Gas−Surface Energy Exchange and Accommodation. *J. Phys. Chem. C* **2007,** *112* (2), 476-490.

Chapter 5

Insights into Reaction Mechanisms of Gas-phase Nitrate Radicals with a Hydroxyl-terminated Self-Assembled Monolayer

5.1 Introduction

Interfacial reactions between nitrate radicals (NO_3) and organic particulates are important because changes in the particle components and sizes via these gas-surface reactions affect the balance of pollutants throughout the troposphere (≤ 10-15 km altitude).[1-3] Among all heterogeneous reactions of NO_3 with organics, interfacial reactions between NO_3 and alcohols are of importance due to the following reasons. First, alcohols contribute significantly to the atmospheric emissions of organics during both natural and anthropogenic processes.[4-7] Further, reactions between emitted alcohols and NO_3 affect the transformation of volatile organic compounds (VOCs) in the atmosphere.[8] In addition, the oxygenated products from these reactions could cause health problems such as asthma, allergy, and respiratory irritation.[9] As a result, scientists start to focus on investigations of reaction kinetics of NO_3 with alcohols. Langer et al. measured rate coefficients of reactions between NO_3 and some aliphatic alcohols. From the kinetic data, they found that the rate constant increased with the number of substitutions at the carbon attached to the hydroxyl groups, suggesting that hydrogen abstraction occurs at the C-H bond rather than the O-H bond.[6] In addition, Moreno et al. made similar conclusions based on their kinetic study of the gas-phase reaction of NO_3 with a series of alcohols.[7] By comparing the reactivity of the hydrogen abstraction at a tertiary carbon with that at a secondary or a primary carbon, they observed a higher reactivity of hydrogen abstraction at the C-H bond with more substitutes. Following their studies, Aschmann and co-workers investigated the products of gas-

phase reactions of NO_3 with alcohols, in which they observed the formation of carbonyl compounds in the presence of O_2.[8] But the concentration of these carbonyl compounds decreased with the increase of the concentration of dinitrogen pentoxide (N_2O_5), which they attributed to the reaction of N_2O_5 with alcohols that yielded alkyl nitrates instead of carbonyls. However, Ljungstrom and co-workers found that the reaction rate constants of N_2O_5 with some aliphatic alcohols were 3-4 orders of magnitude lower than that of reactions of NO_3 with the same alcohols, indicating the much less significance of N_2O_5 reaction with alcohols.[6]

To date, most kinetic studies are focusing on reactions between NO_3 and unsaturated alcohols.[5,7-11] For example, Liu et al. determined the uptake coefficients of NO_3 onto the surface of methoxylphenol particulates.[10] The presence of the multi-functional groups (-OH and C=C) in these alcohol particles resulted in the high overall reaction rate that was contributed by reactions of NO_3 with both hydroxyl and vinyl groups. In addition, surfaces utilized so far for the measurement of the uptake coefficient of NO_3 with alcohols are either disordered or poorly characterized surfaces.[10,12] Previous work in Chapter 4 showed that the reaction probability of NO_3 with a HO-terminated self-assembled monolayer (SAM) is $(6 \pm 1) \times 10^{-3}$. However, several fundamental questions remains to be explored, including the reaction mechanisms, reaction barriers, what products formed upon NO_3 collision with the SAM surface, and the stability of the products.

In this chapter, a 16-C DO-SAM was used for the investigation of reaction mechanisms and products upon its interfacial oxidation by NO_3. Reflection-absorption infrared spectroscopy (RAIRS) was implemented to monitor reactions *in situ*. By tracking rates of bond rupture and formation during NO_3 reactions with organic surfaces at different surface temperatures, the reaction barrier was determined according to the Arrhenius equation. In addition to the kinetic

study via RAIRS, X-ray photoelectron spectroscopy (XPS) was employed for elemental analysis to identify the composition of surface-bound molecules prior to and after the gas-surface collisions.

5.2 Experimental

All experiments were performed in an ultrahigh vacuum (UHV) chamber with a base pressure of 10^{-9} Torr. Such low pressure keeps the organic surface clean and eliminates reactions of background gases with the surface. An effusive source of NO_3 radicals was introduced into the UHV chamber through an all-glass capillary array doser. RAIRS was employed to track rates of bond rupture and formation of the organic species on the surface *in situ*. XPS was implemented to analyze elemental composition of surface-bound molecules before and after exposure. A detailed setup of the UHV system can be found elsewhere.[13]

5.2.1 Preparation of Hydroxyl-terminated Self-assembled Monolayers

The 16-mercapto-1-hexadecanol was purchased from Frontier Scientific, Inc. Hydroxyl-terminated SAMs were created using the same method described in Chapter 4. Prior to being transferred to the UHV main chamber through a load-lock system, the gold slides with chemisorbed SAMs were rinsed thoroughly with ethanol and dried under a stream of UHP N_2.

To assist with the investigation of reaction mechanisms, the isotopic effect on the reaction kinetics was studied by employing a 16-C DO-terminated SAM. D-ethanol was purchased from Sigma-Aldrich and used without further purification. The DO-terminated SAM was created by placing a pre-cleaned gold slide in a 1 mM solution of 16-mercapto-1-hexadecanol in D-ethanol. To estimate the ratio of D/H in the SAM, a RAIR spectrum was collected using disordered DO-SAMs. The disordered SAMs were made by spin coating the D-ethanol solution that contains the 16-mercapto-1-hexadecanol and Au particles. Figure 5.1 B shows SEM images of a clean gold

slide and the disordered SAMs (black flakes) on gold particles (white clusters). In addition, the RAIR spectrum of the SAM film is shown in Figure 5.1 A. By comparing the integrated absorbance of ν(O-H) (the broad band in the range of 3150-3500 cm^{-1}, with the integrated value of 0.71) and ν(O-D) (the two bands in the range of 2250-2600 cm^{-1}, with the integrated value of 0.39), the ratio D/H was estimated to be ~1/2, which suggests that ~30% of -OD was present on the SAM surface.

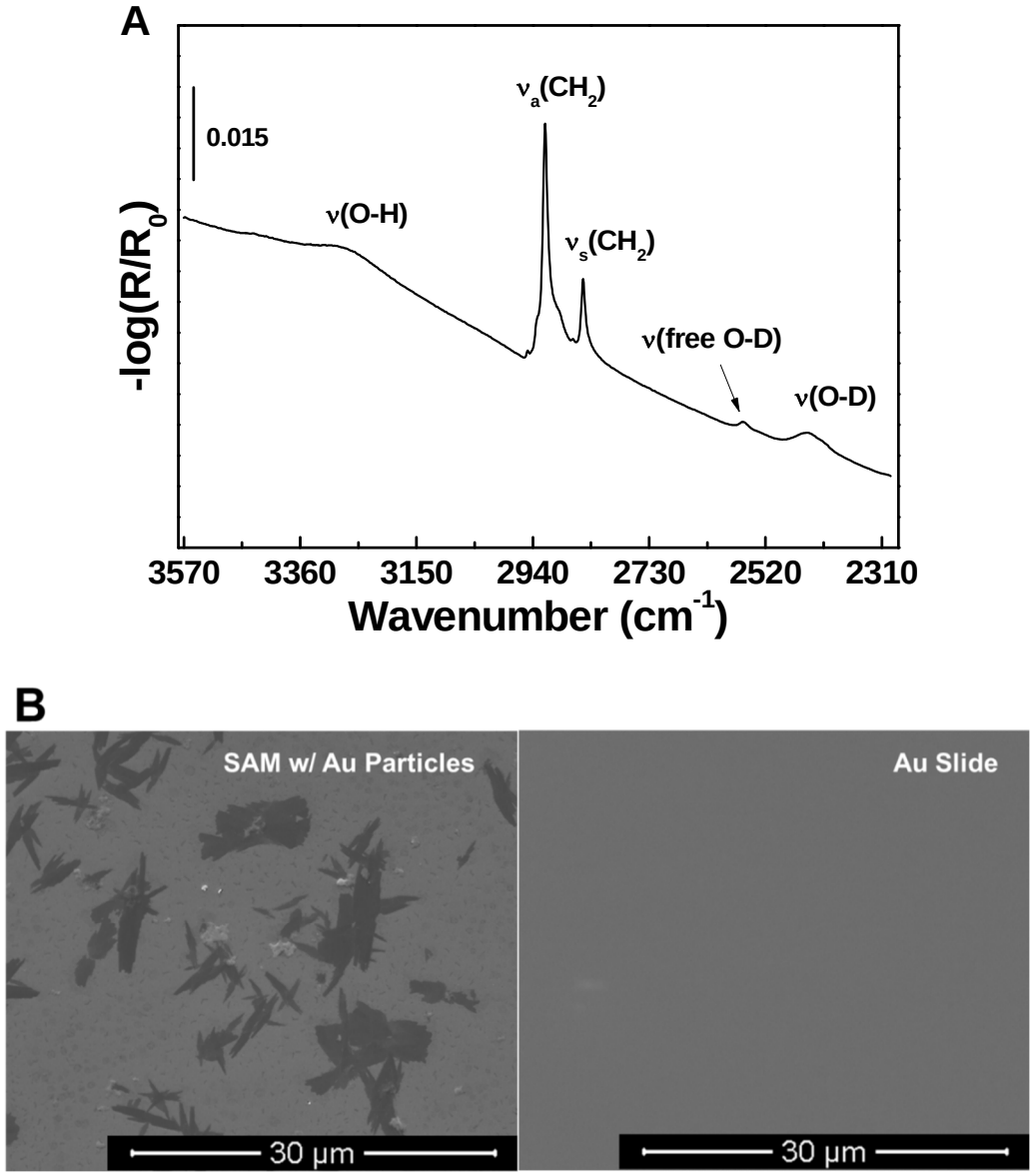

Figure 5.1. (A) Reflection-absorption infrared spectra of the disordered DO-SAMs on Au particles (see text above for details); (B) SEM images of the disordered DO-SAMs on a gold substrate and a clean gold slide.

5.2.2 Generation of Nitrate Radicals

To produce NO_3, nitrogen monoxide (NO, obtained from Sigma-Aldrich) was oxidized by an excess of ozone molecules (O_3). The first step of this process is the formation of NO_2 followed by further oxidation to produce N_2O_5. The gas-phase N_2O_5 was then stored in a sealed glass trap which is submerged into a dry ice/ethanol bath. For exposure experiments, N_2O_5 was volatilized and delivered to the capillary array doser that was heated up to 324 K. NO_3 can be formed through thermal decomposition of N_2O_5 molecules.

5.2.3 Reflection-Absorption Infrared Spectroscopy

Reactions between NO_3 and the SAMs were monitored *in situ* with a Bruker IFS 66v/S spectrometer.[13] Each spectrum was collected by measuring the absorbance of reflected p-polarized IR radiation from a SiC globar at an incident angle of ~86˚ relative to the surface normal. All spectra shown here were taken from the average of 100 scans with 2 cm^{-1} resolution.

5.2.4 X-ray Photoelectron Spectroscopy

Elemental analysis was performed by detecting binding energies of core electrons of the surface-bound elements. A monochromatic radiation (Al Kα 1486.6 eV) was generated from a SPECS XR50 X-ray source operated at 250 W (12.5 kV and 20 mA). Kinetic energies of ejected photoelectrons were measured using a 16.5” hemispherical energy analyzer (SPECS, Phoibos 100) operated at a take-off angle of 90º with respect to the surface. All high-resolution spectra were obtained in the region of interest using the following experimental parameters: pass energy of 50 eV; step size of 0.1 eV and dwell time of 0.1 s. The binding energies for all spectra were referenced to the Au ($4f_{7/2}$) peak at 83.8 eV.[14] The high-resolution spectra were fitted to symmetric curves

that contain a Gaussian/Lorentzian product with 70% Gaussian and 30% Lorentzian character after subtracting a Shirley background accounting for the inelastic scattering of electrons that contributes to the background broadening.[15-18]

5.3 Results and Discussion

The reaction dynamics and mechanism of NO_3 with hydroxyl-terminated SAMs have been investigated by tracking bond rupture and new mode formation at the gas-solid interface using *in situ* reflection-absorption infrared spectroscopy. The isotopic effect (HO-SAM vs. DO-SAM reactions with NO_3) on the rate constants has provided insights into the reaction mechanism. Further, the dependence of the reaction kinetics of NO_3 collision with HO-terminated SAMs on the surface temperature has also been explored to determine the overall reaction barrier. In addition, the reaction products were investigated with x-ray photoelectron spectroscopy.

5.3.1 HO-SAM and DO-SAM Characterization by RAIRS

The NO_3 exposure experiments were performed on a 16-C HO-terminated SAM and a 16-C DO-terminated SAM. Long-chain SAMs are chosen due to two key reasons: i) the order and the thermodynamic stability of SAMs increases with the length of hydrocarbon chains; ii) the oxidation of S attached to Au was not observed on the time scale of our measurements, which suggests that the reaction between NO_3 and the HO-terminated SAMs occurs at the gas-solid interface.

RAIR spectra of the freshly made 16-C HO-terminated and DO-terminated SAMs reveal the formation of well-ordered monolayers on the polycrystalline gold substrates, as shown in Figure 5.2. The most intense bands at 2919 cm^{-1} and 2950 cm^{-1} are assigned to the asymmetric ($\nu_a(CH_2)$) and symmetric stretch ($\nu_s(CH_2)$) of -CH_2- groups along the methylene chains.[19,20] The

position and the band widths suggest the formation of crystalline-like hydrocarbons on the gold surface. In addition, the appearance of the feature at 1469 cm^{-1} due to the scissoring deformation of -CH_2- groups ($\delta(CH_2)$) along the backbone of the chains is consistent with crystalline-like environment.[19] Further, three additional features associated with the terminal hydroxyl groups were observed in RAIRS. The band at 2878 cm^{-1} is attributed to the C-H stretching mode within the terminal -CH_2- adjacent to -OH groups ($\nu(CH_2(OH))$).[21] The doublet bands at 1059 cm^{-1} and 1076 cm^{-1} are assigned to the C-O stretch ($\nu(CO)$).[22] This $\nu(CO)$ mode splitting into two most likely results from the two nonequivalent roles of terminal -CH_2OH units (proton acceptor and donor) in hydrogen bonding,[23,24] coupling of $\nu(CO)$ to C-C stretches with similar vibrational frequencies,[25] or the presence of two conformers associated with the position of -OH groups relative to the adjacent methylene group.[26] Since the C-O stretch of the terminal hydroxyl group shows a strong absorbance in RAIRS, it was used for detailed kinetic analysis.

In the spectra of the HO-SAM and the DO-SAM, the features in the range of 3100 cm^{-1}-3600 cm^{-1} are due to the O-H stretch of the intermolecular hydrogen bonded hydroxyls at the solid-gas interface.[21,27] However, the intensity of the $\nu(OH)$ mode of the DO-SAM is much lower than that of the same mode of the HO-SAM, which suggests that the H atom has been partly exchanged with the D atom. In addition, the appearance of a broad band in the range of 2350-2750 cm^{-1} in the spectrum of DO-SAM is likely due to the O-D stretch of either intermolecular hydrogen bonded or weakly hydrogen-bonded -OD groups.[28,29] Because the surface selection rule dictates that only modes with the transition moment perpendicular to the surface plane can be observed in RAIRS, investigations of the intensity of a particular mode could provide us insights into the orientation of that mode.[30] The low intensity of the broad band ($\nu(OH)$) suggests an almost parallel orientation of the O-H bond relative to the surface.

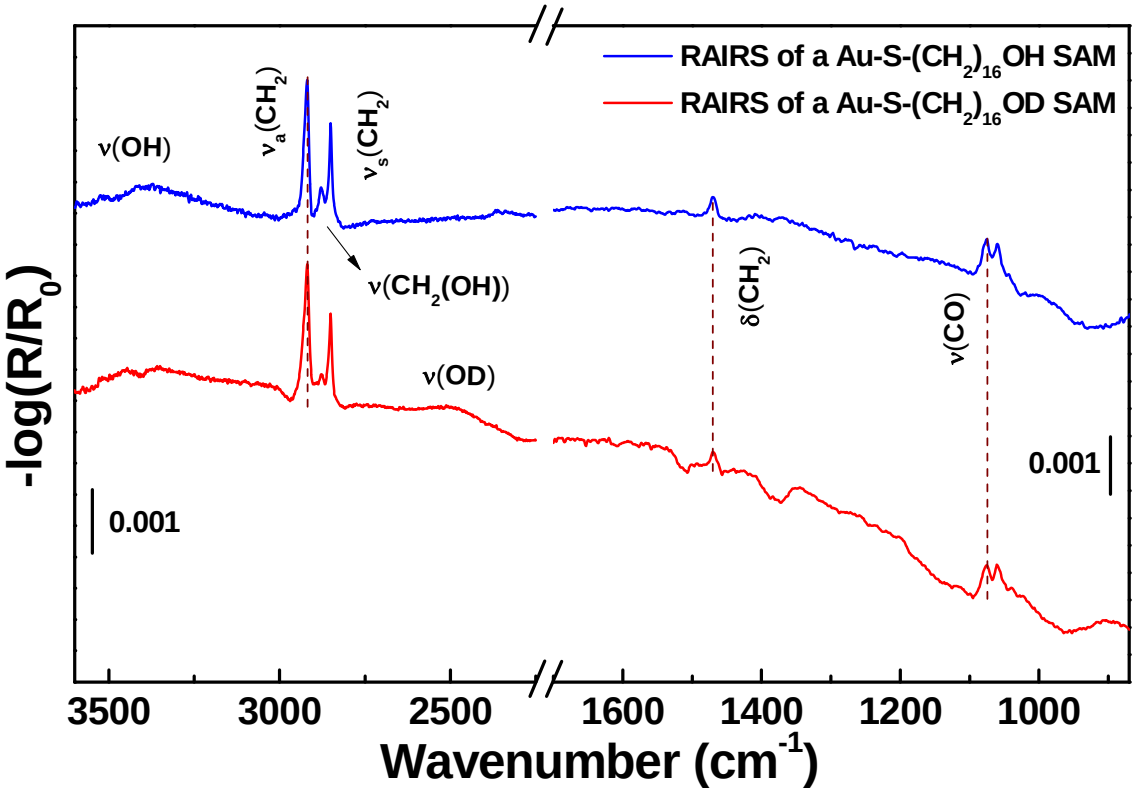

Figure 5.2. Reflection-absorption infrared spectra of a 16-C hydroxyl-terminated (Au-S-$(CH_2)_{16}$OH) SAM and a 16-C deuterated hydroxyl-terminated (Au-S-$(CH_2)_{16}$OD) SAM on Au formed from 16-mercapto-1-hexadecanol fabricated through solution immersion. The five most intense IR active modes are highlighted as $\nu_a(CH_2)$, $\nu_s(CH_2)$, $\nu(CH_2(OH))$ or $\nu(CH_2(OD))$, $\delta(CH_2)$, and $\nu(CO)$.

5.3.2. IR Characterization of DO-SAMs during NO_3 exposure

The reaction of NO_3 with the surface-bound hydroxyl molecules was monitored by RAIRS. The original SAM was used as the background (blue line), such that negative features in Figure 5.3A indicate the removal of bands and positive features reveal the formation of new bands, an increase of absorptivity, or peak shifting. The bottom spectrum in Figure 5.3A is the difference spectrum of the monolayer before exposure to a continuous source of NO_3/NO_2 gas. The exposure of the monolayer to NO_3/NO_2 increases by 70 L in Figure 5.3A with a total exposure of 3000 L. The interfacial reaction has three key effects on the DO-SAM, which are similar to what have been

observed in reactions of NO_3 with a 16-C HO-SAM (Chapter 4). First, all modes associated with the -CH_2OD moieties decrease in intensity ($\nu(CH_2(OH))$ at 2878 cm^{-1}, $\nu(CO)$ at 1059 cm^{-1} and 1076 cm^{-1}), which is likely due to the consumption of these functional groups during the reaction. Concurrently with the changes in band intensities of the original DO-SAM, new modes emerge at 1621 cm^{-1}, 1552 cm^{-1}, 1283 cm^{-1}, 1223 cm^{-1}, and in the range of 930-1048 cm^{-1}. It was reported that the positive features between 1170 cm^{-1} and 1660 cm^{-1} suggest the formation of surface-bound organic nitrates or nitro-containing organics.[5,11,13] In addition, a shift of the original $\nu(CO)$ to a lower wavenumber (a broad band in the region of 930-1048 cm^{-1}) was attributed to the addition of electron withdrawing groups, such as organic nitrates or nitro-containing compounds.[26,31] Furthermore, the bands associated with the methylene chain decrease in intensity, which could be due to the reaction of physisorbed NO_3 with methylenes in the hollow space created by hydrogen bonding among -OD groups of the DO-SAM.[32] The fact that collisions of NO_3 with either the 16-C HO-SAM or the 16-C DO-SAM result in the same IR features during the exposure suggests that the exchange of H and D in the terminal hydroxyl groups has little effect on reaction products.

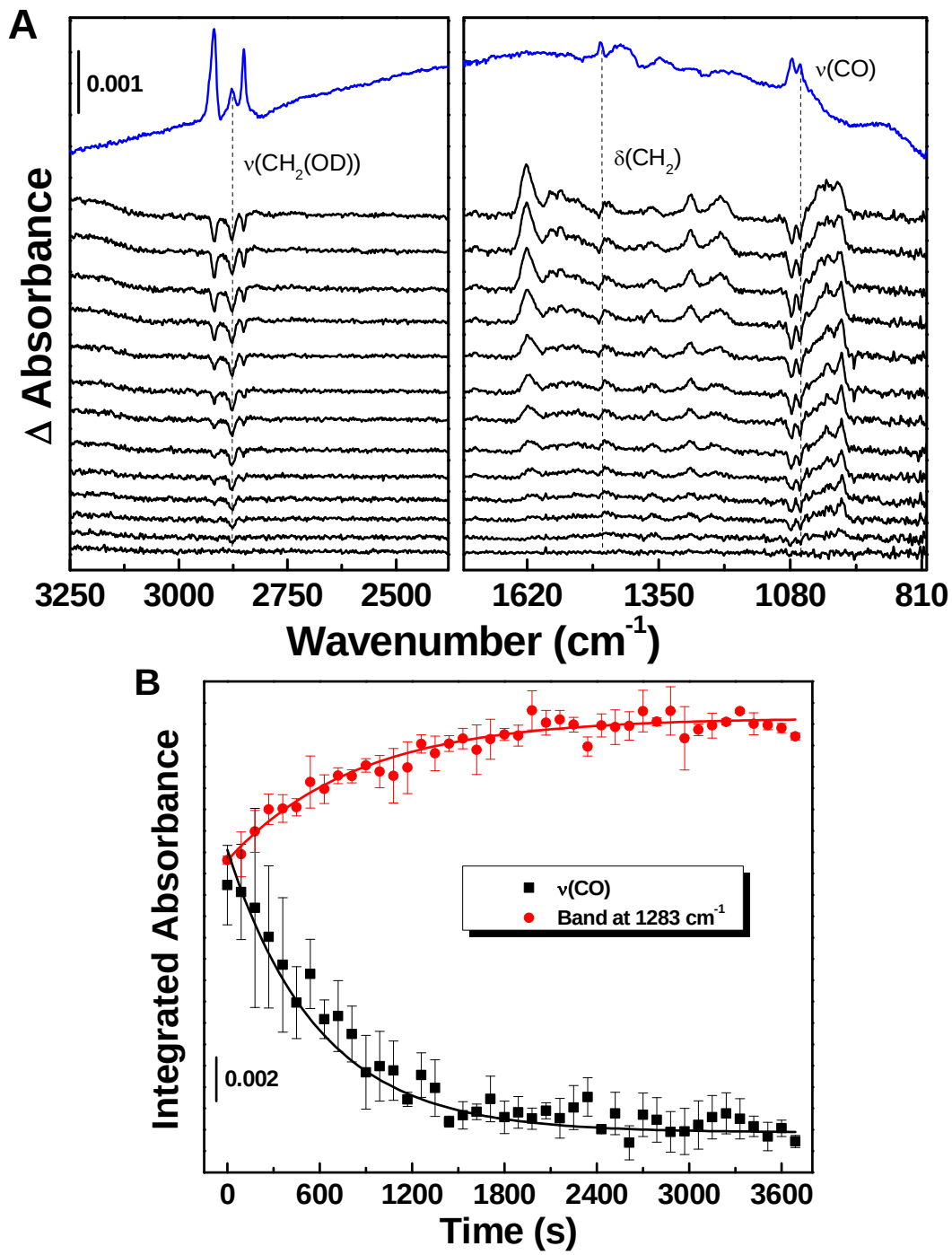

Figure 5.3. (A) Reflection-absorption infrared difference spectra of a 16-C DO-terminated SAM exposed to NO_3. The spectrum shown on top in blue is that of the SAM prior to NO_3 exposure using a clean Au sample as the background. Upon NO_3 exposure, the spectra in black show that modes associated with the $-CH_2OH$ group decrease and new modes emerge. The background for this scan is the original pre-exposure spectrum (blue), with the exposure increasing by 70 L per spectrum. (B) Integrated absorbance for ν(CO) at 1060 cm^{-1} and 1076 cm^{-1} (black solid square) and for the band at 1283 cm^{-1} (red solid circle) versus time during NO_3 exposure. The fitting curves follow the first-order kinetics.

5.3.3 Isotopic Effect on Reaction Kinetics of NO_3 with the Surface Hydroxyl Groups

To explore the effect of the replacement of -OH with -OD in the terminal groups on the reaction kinetics, we plotted integrated intensities of the original C-O band and the band at 1283 cm^{-1} (ν(-ONO_2)) as a function of time, as shown in Figure 5.3B. Both curves show that the rate of the consumption of the C-O band and the formation of the new band at 1283 cm^{-1} follow pseudo-first-order kinetics, with the observed rate constant of $(1.9 \pm 0.5) \times 10^{-3}$ s^{-1} (ν(CO), k_{obs}) and $(1.3 \pm 0.1) \times 10^{-3}$ s^{-1} (ν(-ONO_2), k_{obs}'), respectively. The rate constants were obtained from the model that reproduces the trend of the experimental data, as shown by Equations (5.1) and (5.2):

$$A_{\nu(CO)}(t) = (A_{\nu(CO)})_0 \exp(-k_{obs}\, t) \qquad (5.1)$$

$$A_{1283}(t) = (A_{\nu(CO)})_0 [1 - \exp(-k_{obs}'\, t)] \qquad (5.2)$$

where $A_{\nu(CO)}$ (t) is the absorbance of the C-O band, $(A_{\nu(CO)})_0$ is the initial absorbance of the same band before exposing to NO_3, $A_{1283}(t)$ is the absorbance of the band at 1283 cm^{-1}, and t is the exposure time. The similarity of the two rate constants demonstrates a strong correlation between consumption of the -CH_2OD groups and production of surface-bound nitrates.

When NO_3 is colliding with the DO-SAM surface, it could undergo direct H/D abstraction at the initial collision site (direct H/D abstraction) or yet trapped on the surface before reaction. If we assume that the H/D abstraction by NO_3 occurs at the -OH/-OD terminus and this process is the rate-limiting step, the rate constant, k_H (ν(CO)) or k_H (ν(-ONO_2)), for the reaction of NO_3 with the HO-SAM should be very different from the rate constant, k_D (ν(CO)) or k_D (ν(-ONO_2)), for the reaction of NO_3 with the DO-SAM.[33] This difference mainly arises from the effect on the activation energy induced by changes in the zero-point energy (ZPE) when the reactants are converted to the transition state (TS).[33] Typically, reactions involving O-H bond rupture become ~10 times slower

when O-D bonds are considered if the transition state is linear.[34] While generally the primary kinetic isotopic effects for proton transfers occurring by non-linear TS (k_H/k_D) are on the order of 2.5 - 3.5.[35-37] However, the calculated ratio of the two rate constants, k_H/k_D (ν(CO)) and k_H/k_D (ν(-ONO_2)), is only 1.0 ± 0.6 and 1.2 ± 0.3, respectively, suggesting that hydrogen abstraction from the hydroxyl groups is not the dominant pathway. Nevertheless, in the previous section, we estimated that the amount of -OD was ~30% according to RAIRS, which may account for the value (k_H/k_D) of 1.3 - 1.4 instead of 3 or 10 reported in the literature.[36] Thus, one could hardly make a positive conclusion that the H abstraction occurs at the methylene groups of the terminal -CH_2OH. To propose the reaction mechanism, further investigations such as studies of the kinetic isotopic effect on reactions of NO_3 with -CD_2OH should be considered.

5.3.4 XPS Characterization.

While the reaction kinetics of NO_3 with the HO-SAM was uncovered by investigating vibrational motions of the adsorbed molecules using IR, XPS was utilized as a complementary tool to identify the elemental composition of the adsorbates. Figure 5.4 shows high resolution spectra of the N (1s), O (1s), S (2p), and C (1s) of a 16-C HO-terminated SAM prior to and after NO_3 exposure. The model that fits the high resolution XPS collected in the N (1s) region of the SAM after reactions gives rise to three bands with equal full-width-at-half-maximum (FWHM) values (1.7 eV). The best fit requires a FWHM value of 1.5 eV which is similar to the one obtained in a previous XPS study of cellulose nitrates.[38] In addition, the positions of the two bands at 407.1 eV and 408.3 eV are consistent with the binding energy in the N (1s) region for organic nitrates.[39-41] The band at 405.9 eV is consistent with the binding energy of nitro groups, suggesting the formation of nitro compounds upon NO_3 exposure.[42] As nitrogen-containing products are yielded

during NO_3 collision with the HO-SAM, the intensity of the band in the O (1s) region increases. Prior to NO_3 exposure, a band at 532.3 eV in the O (1s) region has the same binding energy as that of O (1s) electrons in the hydrogen bonded alcohols reported by Madix et al.[43] After 3000 L exposure of NO_3, the band intensity becomes larger, indicating the increase in the amount of O on the surface. Further, the O (1s) binding energy shifts to a lower value after NO_3 exposure, which may be attributed to the breakage of intermolecular hydrogen bonding among the interfacial hydroxyl groups or the formation of less-efficient electron withdrawing moieties ($-ONO_2$).[44]

In addition to the evidence for oxidation provided by the XPS data of N (1s) and O (1s) electrons, S (2p) electrons were also detected to simplify the identification of reaction products since the Au-S bond is susceptible to oxidation as well. Figure 5.4 shows the XPS data in the S (2p) region that has been fitted to a curve composed of a pair of S ($2p_{3/2}$, $2p_{1/2}$) bands with the same FWHM, branching area ratio of 2 ($2p_{3/2}$:$2p_{1/2}$), and standard spin-orbit splitting of 1.2 eV.[45,46] Fortunately, the S (2p) spectra before and after exposure show that the impinging gas has little effect on the concentration and the oxidation state of sulfur. Therefore, the oxidation of the HO-SAM by NO_3 is mainly taking place between the gas and the methylene groups. In addition, the fact that the band intensity at 284 eV was preserved prior to and after NO_3 collision indicated that very few methylene chains was desorbed from the surface.[47,48] The emergence of the band at 286 eV could be due to the escape of C (1s) electrons in the C-O species from the terminal $-CH_2OH$ groups or organic nitrates.[49,50]

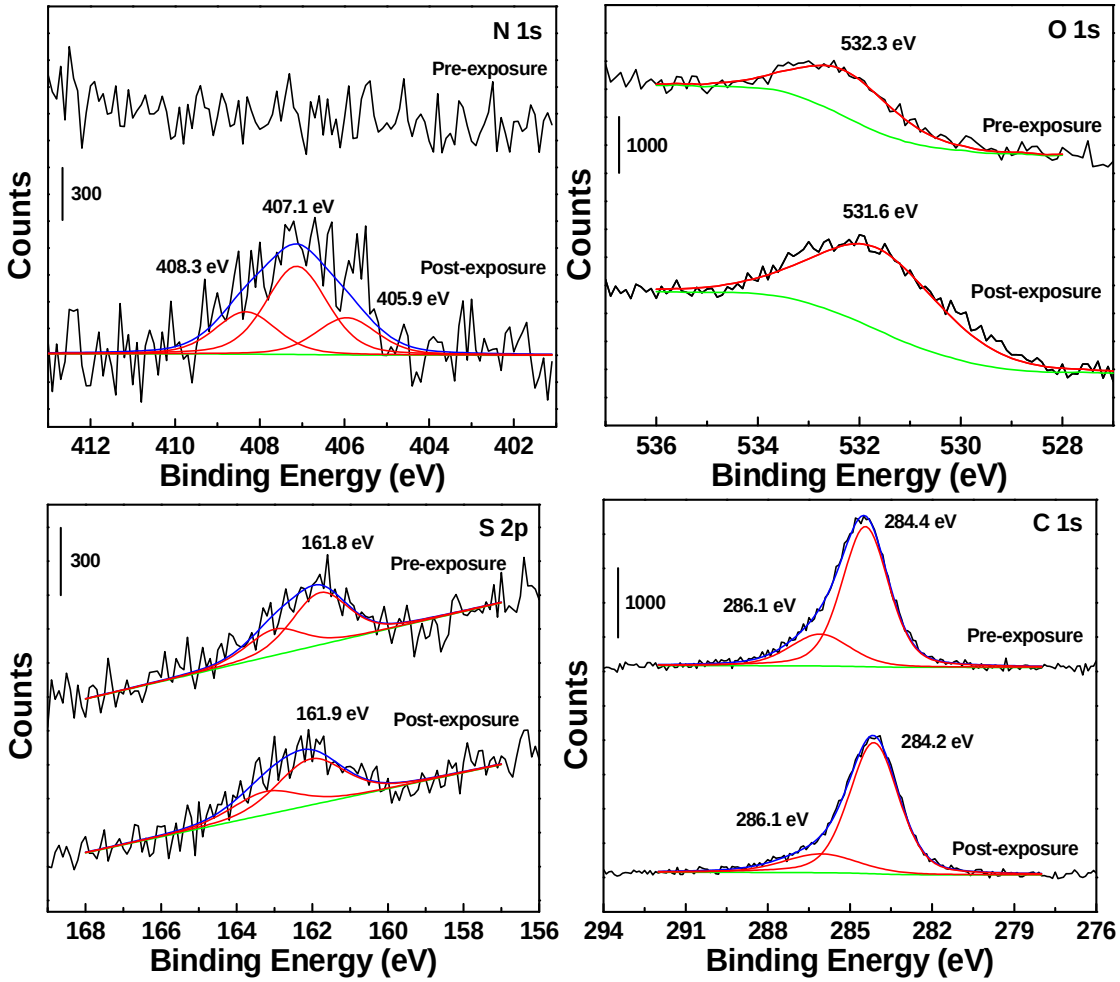

Figure 5.4. High resolution X-ray photoelectron spectra of the N (1s), O (1s), S (2p), and C (1s) regions of a 16-C HO-terminated SAM before and after 3000 L of NO_3 exposure, which indicates the formation of organic nitrates and preservation of concentration and oxidation state of sulfur groups attached to the Au surface.

5.3.5 Reaction Products and the Activation Energy

During the reaction of NO_3 with the 16-C DO-SAM, we learned that all modes associated with the terminal group -CH_2OD decreased in intensity concurrently with the emergence of new modes at 1621 cm^{-1}, 1552 cm^{-1}, 1283 cm^{-1}, 1223 cm^{-1}. These RAIR features provide evidence for the formation of organic nitrates or nitro-containing compounds during the reaction. In

addition, the bands associated with the methylene groups of the hydrocarbon chains decrease in intensity during the NO_3 exposure, which could be due to H abstraction from those methylenes by NO_3 at surface defect sites. Consistent with the observation in IR, XPS data in the preceding section also suggests the presence of organic nitrates on the surface after NO_3 exposure.

The activation energy for the overall reaction was determined by studying the temperature-dependent kinetics. Figure 5.5 shows the plots of integrated intensities of the ν(C-O) mode as a function of time at different surface temperatures (over the range of 89-344 K, Figure 5.5 A) and the corresponding Arrhenius plots (Figure 5.5 B). According to the Arrhenius equation, $k = A \exp[-E_a/(RT)]$,[51] the activation energy can be determined from the slope in Figure 5.5B. The lines models the data using linear least square regression method with R^2 of 0.85 (blue line) and 0.80 (red line). The activation energies, (0.7 ± 0.4) kJ/mol and (0.9 ± 0.3) kJ/mol, were calculated from the slope of the regression equation, which are close to the one for reactions of NO_3 with some unsaturated alcohols reported by Hallquist et al (2.8 ± 2.5 kJ/mol).[4] The activation energy determined in their study results from the contribution of two pathways: hydrogen abstraction and NO_3 addition to the carbon-carbon double bonds.[5] Since the reaction of NO_3 addition to the double bonds is barrierless,[13] a small activation energy for the hydrogen abstraction may be expected. However, much higher activation energy (17.4 ± 6.7 kJ/mol for methanol, 15.1 ± 3.5 kJ/mol for ethanol, and 14.5 ± 8.4 kJ/mol for isopropanol) than that in this work has been reported by Langer et al. for reactions between NO_3 and some aliphatic alcohols.[6] I note that the linear regression (Figure 5.5B) resulted in R^2 values much less than unity, which indicates only a weak linear correlation. The reason for this behavior may be that the pre-factor depends on surface temperature over the range of temperatures employed in this work.[52] The low activation energy of NO_3 reactions with the HO-SAM may be attributed to the weakening of the C-H bond in the terminal

methylene group due to hydrogen bonding among the neighboring -OH moieties.[53] Hydrogen-bond activated or catalyzed chemistry has been reported in many systems.[4,25,26,32,53]

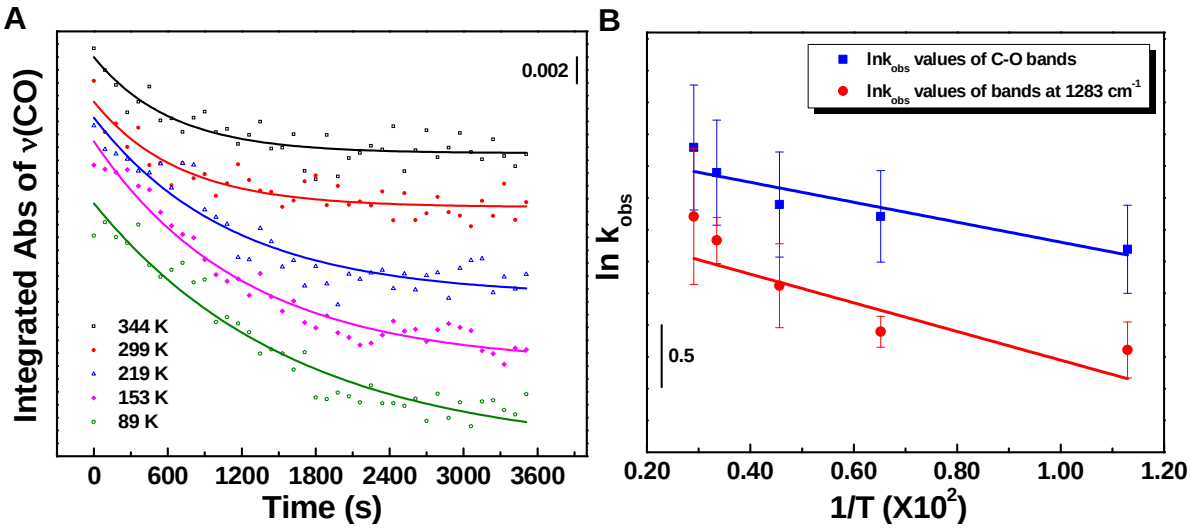

Figure 5.5. (A) Pseudo-first order kinetic plots for the reaction of NO_3 with 16-C HO-SAM at different surface temperatures. (B) Arrhenius plots for the reaction of NO_3 with 16-C HO-SAM in the temperature range of 89-344 K.

5.4 Summary

The investigation of interfacial reaction between NO_3 and a 16-C hydroxyl-terminated SAM provided insights into the reaction mechanism and the energetics for reaction kinetics. The reaction mechanism was elucidated by the combination of UHV-based techniques, including RAIRS and XPS. Although the kinetic isotopic effect failed to give a positive conclusion of hydrogen abstraction at the terminal methylenes, the features in RAIRs suggest the formation of organic nitrates or nitro-containing compounds upon NO_3 reaction with the HO-SAM. In addition, elemental analysis with XPS of the surface prior to and after NO_3 exposure showed the presence of organic nitrates and non-oxidized S atoms and the preservation of hydrocarbon chains on the surface. These features indicate that the oxidation of the HO-SAM by NO_3 radicals primarily

occurs at the gas-solid interface. The activation energy determined from the reaction kinetics at different surface temperature was low, which could be attributed to the weakening of the C-H bond due to hydrogen bonding among the terminal -CH_2OH groups. Together, these key aspects suggest the importance of interfacial hydrogen abstraction from alcohols in the atmosphere. The fact that the reactivity of hydrogen abstraction is comparable to that of NO_3 addition to the carbon-carbon double bonds may assist environmental scientists in understanding the fate and lifetime of certain atmospheric organics in the presence of NO_3 during the nighttime.

REFERNCES

(1) Brown, S. S.; Stutz, J., Nighttime Radical Observations and Chemistry. *Chem. Soc. Rev.* **2012,** *41* (19), 6405-6447.

(2) Finlayson-Pitts, B. J.; Pitts Jr, J. N., *Chemistry of the Upper and Lower Atmosphere: Theory, Experiments, and Applications*. Academic press: 1999.

(3) Prather, K. A.; Hatch, C. D.; Grassian, V. H., Analysis of Atmospheric Aerosols. *Annu. Rev. Anal. Chem.* **2008,** *1* (1), 485-514.

(4) Hallquist, M.; Langer, S.; Ljungström, E.; Wängberg, I., Rates of Reaction between the Nitrate Radical and Some Unsaturated Alcohols. *Int. J. Chem. Kinet.* **1996,** *28* (6), 467-474.

(5) Noda, J.; Hallquist, M.; Langer, S.; Ljungstrom, E., Products from the Gas-Phase Reaction of Some Unsaturated Alcohols with Nitrate Radicals. *Phys. Chem. Chem. Phys.* **2000,** *2*, 2555-2564.

(6) Langer, S.; Ljungstrom, E., Rates of Reaction between the Nitrate Radical and Some Aliphatic Alcohols. *J. Chem. Soc., Faraday Trans.* **1995,** *91* (3), 405-410.

(7) Moreno, A.; Salgado, M. S.; Martín, M. P.; Martínez, E.; Cabañas, B., Kinetic Study of the Gas Phase Reactions of a Series of Alcohols with the NO_3 Radical. *J. Phys. Chem. A* **2012,** *116* (42), 10383-10389.

(8) Chew, A. A.; Atkinson, R.; Aschmann, S. M., Kinetics of the Gas-Phase Reactions of NO_3 Radicals with a Series of Alcohols, Glycol Ethers, Ethers and Chloroalkenes. *J. Chem. Soc., Faraday Trans.* **1998,** *94* (8), 1083-1089.

(9) Harrison, J. C.; Wells, J. R., 2–Butoxyethanol and Benzyl Alcohol Reactions with the Nitrate Radical: Rate Coefficients and Gas-Phase Products. *Int. J. Chem. Kinet.* **2012,** *44* (12), 778-788.
(10) Liu, C.; Zhang, P.; Wang, Y.; Yang, B.; Shu, J., Heterogeneous Reactions of Particulate Methoxyphenols with NO_3 Radicals: Kinetics, Products, and Mechanisms. *Environ. Sci. Technol.* **2012,** *46* (24), 13262-13269.
(11) Olariu, R. I.; Barnes, I.; Bejan, I.; Arsene, C.; Vione, D.; Klotz, B.; Becker, K. H., FT-IR Product Study of the Reactions of NO_3 Radicals with Ortho-, Meta-, and Para-Cresol. *Environ. Sci. Technol.* **2013,** *47* (14), 7729-7738.
(12) Gross, S.; Iannone, R.; Xiao, S.; Bertram, A. K., Reactive Uptake Studies of NO_3 and N_2O_5 on Alkenoic Acid, Alkanoate, and Polyalcohol Substrates to Probe Nighttime Aerosol Chemistry. *Phys. Chem. Chem. Phys.* **2009,** *11*, 7792-7803.
(13) Zhang, Y.; Chapleski, R. C.; Lu, J. W.; Rockhold, T. H.; Troya, D.; Morris, J. R., Gas-Surface Reactions of Nitrate Radicals with Vinyl-Terminated Self-Assembled Monolayers. *Phys. Chem. Chem. Phys.* **2014,** *16* (31), 16659-16670.
(14) Gorham, J.; Smith, B.; Fairbrother, D. H., Modification of Alkanethiolate Self-Assembled Monolayers by Atomic Hydrogen: Influence of Alkyl Chain Length. *J. Phys. Chem. C* **2007,** *111*, 374-382.
(15) Vegh, J., The Analytical Form of the Shirley-Type Background. *J. Electron Spectrosc. Relat. Phenom.* **1988,** *46*, 411-417.
(16) Vegh, J., The Shirley-Equivalent Electron Inelastic Scattering Cross-Section Function. *Surf. Sci.* **2004,** *563*, 183-190.
(17) Baltrusaitis, J.; Jayaweera, P. M.; Grassian, V. H., Xps Study of Nitrogen Dioxide Adsorption on Metal Oxide Particle Surfaces under Different Environmental Conditions. *Phys. Chem. Chem. Phys.* **2009,** *11*, 8295-8305.
(18) Rosseler, O.; Sleiman, M.; Montesinos, V. N.; Shavorskiy, A.; Keller, V.; Keller, N.; Litter, M. I.; Bluhm, H.; Salmeron, M.; Destaillats, H., Chemistry of NO_x on TiO_2 Surfaces Studied by Ambient Pressure XPS: Products, Effect of UV Irradiation, Water, and Coadsorbed K^+. *J. Phys. Chem. Lett.* **2013,** *4*, 536-541.
(19) Love, J. C.; Estroff, L. A.; Kriebel, J. K.; Nuzzo, R. G.; Whitesides, G. M., Self-Assembled Monolayers of Thiolates on Metals as a Form of Nanotechnology. *Chem. Rev.* **2005,** *105* (4), 1103-1170.
(20) Dubois, L. H.; Nuzzo, R. G., Synthesis, Structure, and Properties of Model Organic-Surfaces. *Annu. Rev. Phys. Chem.* **1992,** *43*, 437-463.
(21) Atre, S. V.; Liedberg, B.; Allara, D. L., Chain Length Dependence of the Structure and Wetting Properties in Binary Composition Monolayers of OH- and CH_3-Terminated Alkanethiolates on Gold. *Langmuir* **1995,** *11* (10), 3882-3893.
(22) Bertilsson, L.; Liedberg, B., Infrared Study of Thiol Monolayer Assemblies on Gold: Preparation, Characterization, and Functionalization of Mixed Monolayers. *Langmuir* **1993,** *9* (1), 141-149.
(23) Barnes, A. J.; Hallam, H. E., Infra-Red Cryogenic Studies. Part 5.-Ethanol and Ethanol-D Argon Matrices. *Trans. Faraday Soc.* **1970,** *66* (0), 1932-1940.
(24) Ehbrecht, M.; Huisken, F., Vibrational Spectroscopy of Ethanol Molecules and Complexes Selectively Prepared in the Gas Phase and Adsorbed on Large Argon Clusters. *J. Phys. Chem. A* **1997,** *101* (42), 7768-7777.

(25) Stuart, A. V.; Sutherland, G. B. B. M., Effect of Hydrogen Bonding on the Deformation Frequencies of the Hydroxyl Group in Alcohols. *J. Chem. Phys.* **1956,** *24* (3), 559-570.
(26) Tsu, D. V.; Lucovsky, G.; Davidson, B. N., Effects of the Nearest Neighbors and the Alloy Matrix on SiH Stretching Vibrations in the Amorphous SiO_r:H ($0<r<2$) Alloy System. *Phys. Rev. B* **1989,** *40* (3), 1795-1805.
(27) Nuzzo, R. G.; Dubois, L. H.; Allara, D. L., Fundamental Studies of Microscopic Wetting on Organic Surfaces. 1. Formation and Structural Characterization of a Self-Consistent Series of Polyfunctional Organic Monolayers. *J. Am. Chem. Soc.* **1990,** *112* (2), 558-569.
(28) Weber, G.; Kapphan, S.; Wöhlecke, M., Spectroscopy of the O-H and O-D Stretching Vibrations in $SrTiO_3$ under Applied Electric Field and Uniaxial Stress. *Phys. Rev. B* **1986,** *34* (12), 8406-8417.
(29) Falk, M.; Whalley, E., Infrared Spectra of Methanol and Deuterated Methanols in Gas, Liquid, and Solid Phases. *J. Chem. Phys.* **1961,** *34* (5), 1554-1568.
(30) Greenler, R. G., Infrared Study of Adsorbed Molecules on Metal Surfaces by Reflection Techniques. *J. Chem. Phys.* **1966,** *44* (1), 310-315.
(31) Gordy, W., A Relation between Bond Force Constants, Bond Orders, Bond Lengths, and the Electronegativities of the Bonded Atoms. *J. Chem. Phys.* **1946,** *14* (5), 305-320.
(32) Tasić, U.; Day, B. S.; Yan, T.; Morris, J. R.; Hase, W. L., Chemical Dynamics Study of Intrasurface Hydrogen-Bonding Effects in Gas−Surface Energy Exchange and Accommodation. *J. Phys. Chem. C* **2007,** *112* (2), 476-490.
(33) Westheimer, F. H., The Magnitude of the Primary Kinetic Isotope Effect for Compounds of Hydrogen and Deuterium. *Chem. Rev.* **1961,** *61* (3), 265-273.
(34) Bigeleisen, J.; Wolfsberg, M., Theoretical and Experimental Aspects of Isotope Effects in Chemical Kinetics. In *Adv. Chem. Phys.*, John Wiley & Sons, Inc.: 2007; pp 15-76.
(35) Melander, L. C.; Saunders, W. H., *Reaction Rates of Isotopic Molecules*. John Wiley & Sons: 1980.
(36) Wiberg, K. B., The Deuterium Isotope Effect. *Chem. Rev.* **1955,** *55* (4), 713-743.
(37) Amado, A. M.; Ribeiro-Claro, P. J. A., H/D and D/H Exchange Rates in [Small Alpha]-Cyclodextrin and [Small Alpha]-Cyclodextrin Inclusion Compounds Raman Spectroscopic Study. *J. Chem. Soc., Faraday Trans.* **1997,** *93* (14), 2387-2390.
(38) Beard, B. C., Cellulose Nitrate as a Binding Energy Reference in N(1s) XPS Studies of Nitrogen-Containing Organic Molecules. *Appl. Surf. Sci.* **1990,** *45* (3), 221-227.
(39) Collins, R. J.; Bae, I. T.; Scherson, D. A.; Sukenik, C. N., Photocontrolled Formation of Hydroxyl-Bearing Monolayers and Multilayers. *Langmuir* **1996,** *12* (23), 5509-5511.
(40) Allen, H. C.; Laux, J. M.; Vogt, R.; Finlayson-Pitts, B. J.; Hemminger, J. C., Water-Induced Reorganization of Ultrathin Nitrate Films on NaCl: Implications for the Tropospheric Chemistry of Sea Salt Particles. *J. Phys. Chem.* **1996,** *100* (16), 6371-6375.
(41) Krepelova, A.; Newberg, J.; Huthwelker, T.; Bluhm, H.; Ammann, M., The Nature of Nitrate at the Ice Surface Studied by XPS and NEXAFS. *Phys. Chem. Chem. Phys.* **2010,** *12*, 8870-8880.
(42) Nielsen, J. U.; Esplandiu, M. J.; Kolb, D. M., 4-Nitrothiophenol SAM on Au(111) Investigated by in situ STM, Electrochemistry, and XPS. *Langmuir* **2001,** *17* (11), 3454-3459.
(43) Bowker, M.; Madix, R. J., XPS, UPS and Thermal Desorption Studies of Alcohol Adsorption on Cu(110): II. Higher Alcohols. *Surf. Sci.* **1982,** *116* (3), 549-572.

(44) López, G. P.; Castner, D. G.; Ratner, B. D., XPS O 1s Binding Energies for Polymers Containing Hydroxyl, Ether, Ketone and Ester Groups. *Surf. Interface Anal.* **1991,** *17* (5), 267-272.
(45) Noh, J.; Ito, E.; Nakajima, K.; Kim, J.; Lee, H.; Hara, M., High-Resolution STM and XPS Studies of Thiophene Self-Assembled Monolayers on Au(111). *J. Phys. Chem. B* **2002,** *106* (29), 7139-7141.
(46) Bourg, M.-C.; Badia, A.; Lennox, R. B., Gold−Sulfur Bonding in 2d and 3d Self-Assembled Monolayers: XPS Characterization. *J. Phys. Chem. B* **2000,** *104* (28), 6562-6567.
(47) Pale-Grosdemange, C.; Simon, E. S.; Prime, K. L.; Whitesides, G. M., Formation of Self-Assembled Monolayers by Chemisorption of Derivatives of Oligo(Ethylene Glycol) of Structure $HS(CH_2)_{11}(OCH_2CH_2)_mOH$ on Gold. *J. Am. Chem. Soc.* **1991,** *113* (1), 12-20.
(48) Torres, J.; Perry, C. C.; Bransfield, S. J.; Fairbrother, D. H., Radical Reactions with Organic Thin Films: Chemical Interaction of Atomic Oxygen with an X-Ray Modified Self-Assembled Monolayer. *J. Phys. Chem. B* **2002,** *106*, 6265-6272.
(49) Folkers, J. P.; Laibinis, P. E.; Whitesides, G. M., Self-Assembled Monolayers of Alkanethiols on Gold: Comparisons of Monolayers Containing Mixtures of Short- and Long-Chain Constituents with Methyl and Hydroxymethyl Terminal Groups. *Langmuir* **1992,** *8* (5), 1330-1341.
(50) Bowker, M.; Madix, R. J., XPS, UPS and Thermal Desorption Studies of Alcohol Adsorption on Cu(110): I. Methanol. *Surf. Sci.* **1980,** *95* (1), 190-206.
(51) Laidler, K. J., The Development of the Arrhenius Equation. *J. Chem. Educ.* **1984,** *61* (6), 494.
(52) Espenson, J. H., *Chemical Kinetics and Reaction Mechanisms*. McGraw-Hill: 1981.
(53) Jeffrey, G. A., *An Introduction to Hydrogen Bonding*. Oxford University Press: 1997.

Chapter 6

Molecular Beam Studies of Nitrate Radical Collision with Hydroxyl-Functionalized Organic Thin Films

6.1 Introduction

The nitrate radical (NO_3) is one of several key oxidative gases that accounts for atmospheric chemistry during the nighttime when photochemical reactions are absent.[1,2] NO_3 initially reacts with certain volatile organic compounds through addition or hydrogen abstraction reactions yielding peroxyacetyl nitrate (PAN).[3-6] PAN acts as a reservoir and a transportation medium for NO_2 due to its thermal decomposition to NO_2.[7] In addition, reactions of NO_3 with NO_2 result in the production of dinitrogen pentoxide (N_2O_5), which is an important source of nitric acid in the atmosphere.[8] In addition to gas-phase reactions of NO_3 with VOCs, interfacial reactions between NO_3 and reactive surfaces of organic particles play a critical role in particle growth and transformations in the troposphere. These key aspects have motivated studies of reactions between NO_3 and organics to reveal the role played by organic surfaces during this important environmental process and how these reactions contribute to particle growth and transformations in the atmosphere.[1,9-11]

So far, most researches have been focused on reaction kinetics of NO_3 with unsaturated organic compounds due to a much higher reactivity of NO_3 addition to the carbon-carbon bonds compared with hydrogen abstraction from saturated alkanes. However, the results presented in Chapter 4 indicate that hydrogen abstraction from hydroxyl-functionalized surfaces by NO_3 could also play an important role in the overall atmospheric chemistry. Although hydrogen abstraction at the terminal methylene groups is kinetically more favorable than that at -OH groups for the

effusive NO_3 source (average energy of ~5 kJ/mol), the reaction dynamics may be dependent on incident energy of NO_3 during the collision with the HO-SAMs which will be further examined.

6.1.1 Energy Transfer during Gas-Surface Collisions

The first step in a surface reaction typically involves energy exchange between the impinging molecules and the surface.[12] Previous rate studies of NO_3 reaction with organics assumed unit sticking probability for NO_3 at the surfaces. However, during the collision, instead of reaction, the molecules may simply recoil back into the gas phase. That is, the impinging projectile could be scattered from a surface, so-called impulsive scattering (IS), where the molecules recoil back into gas phase after one or several collisions and transfer only a small fraction of their initial energy to the surface.[13] Alternatively, the incident projectile may be trapped in the attractive potential energy well of the surface, exchange energy with the surface, and thermally accommodate (or stick) prior to reaction or desorption.[14] Owing to the relatively long residence time of the trapped molecules on the surface (on a scale of ~10^{-12} s), they are regarded as having reached thermal equilibrium with the surface (so-called accommodation to the surface).[12] Hase and co-workers explored the energy-transfer dynamics of Ne atoms scattering from CH_3-SAMs and emphasized the importance of the alkyl chains with many surface modes as an energy reservoir.[15] They found that the energy transfer from Ne translation may be enhanced by the presence of a variety of intermolecular conformations of alkyl chains and intramolecular vibrational redistribution (IVR) between surface modes.

As described above, gas-surface interactions can be direct inelastic scattering or “sticking” collisions where the incident molecules have accommodated to the surface.[12] It has been found that reactive scattering behavior is dependent on the composition, structure and temperature of the surface, and the translational energies and the orientation of the colliding molecules with respect

to the surface.[16-18] For example, Lu et al. studied the dynamics of energy exchange and thermal accommodation of CO_2, NO_2, and O_3 on long-chain CH_3-, HO-, and F-SAM (perfluoro CF_3-SAM).[19] They discovered that the extent of energy transfer of these molecules was much larger to the CH_3-SAMs than that to the rigid F-SAMs. Although the HO-SAM is also a rigid surface, the efficiency of energy transfer is approximately the same as the CH_3-SAM surface due to the attractive interactions between the surface and the impinging molecules.[17]

6.1.2. Chemical Transformation upon Gas-Surface Interactions

Energy exchange between the projectile molecules and the surface may result in reconstruction of the surface so that the surface sites become more accessible to the incoming reactive gases.[12] Given sufficient energy, the gas-phase molecules can pass from the physisorption well to the chemical wall (reaction barrier) where new bonds could be formed. Typically, there are two mechanisms that heterogeneous reactions at the gas-surface interface follow, the Langmuir-Hinshelwood (L-H) or the Eley-Rideal (E-R) reaction mechanism.[20,21]

The Langmuir-Hinshelwood mechanism, where the gas-phase reactants are adsorbed and effectively trapped prior to reaction, requires efficient thermal accommodation followed by diffusion along the surface.[22] In a study of atomic $O(^3P)$ scattering from CH_3-SAMs with different chain lengths, Yuan et al. found that the reaction probability depends on the surface temperature and the number of carbons along methylene chains.[18] With decrease of surface temperature, the reaction probability of H abstraction at terminal groups increased for the same chain-length CH_3-SAM due to the increased residence time of $O(^3P)$ on a cold surface. In addition, short-chain SAMs had higher reactivity because of the less-ordered surface that created more reactive sites for H abstraction along methylene chains. The reaction likely followed the L-H pathway since the incident energy of the $O(^3P)$ was less than the reported hydrogen abstraction barriers.[18] Instead of

reacting on the initial collision, gas molecules must accommodate to the surface and gain energy to cross the reaction barrier.

Alternatively, the Eley-Rideal mechanism describes a pathway that involves a direct reaction between the impinging molecules and the surface.[12] There are a few examples of E-R reaction mechanism at the gas-organic surface interface. Lu et al. discovered that the room-temperature reaction of O_3 with a long-chain vinyl-terminated SAM follows the L-H pathway but transitions to an E-R pathway at elevated O_3 translational energies of O_3.[21] Troya investigated the collision dynamics of OH radicals with fluorinated SAMs and found that OH only collides once with the surface before desorbing in most of the trajectories, which exemplifies a direct reaction mechanism.[23] In addition, studies of the dynamics of $O(^3P)$ and atomic F collisions with alkanethiol SAMs by Troya and co-workers found that the high-energy atoms could directly abstract H from hydrocarbons to generate oxygenated surfaces (via an E-R type mechanism).[24,25]

Chapter 4 and Chapter 5 of this thesis showed that the reaction of NO_3 with an HO-SAM is likely initiated by hydrogen abstraction and the initial reaction probability (γ_0) increases with surface temperature. The surface-temperature dependent γ_0 suggests that the reaction likely follows the L-H mechanism. In this Chapter, we exposed a high-energy molecular beam of NO_3 to the HO-SAM in an attempt to explore how the reaction kinetics and mechanism depend on the incident energy.

6.2 Experimental Details

In this Chapter, a series of ultrahigh vacuum (UHV) based molecular-beam scattering experiments were designed to study the reaction probability, energy-transfer dynamics, and reaction mechanisms in collisions of NO_3 on hydroxyl-functionalized surfaces. The instrumental

setup provides the ability to characterize final translational energy distributions of gas-phase molecules desorbed or scattered from the organic surface. A 16-C hydroxyl-terminated self-assembled monolayer (HO-SAM) serves as a well-characterized surface with the hydroxyl groups positioned precisely at the gas-solid interface. Molecular beams of NO_3 provide a source with well-characterized flux and incident energy. The translational energy and mass of the scattered molecules were monitored with pulsed beam time-of-flight (TOF) techniques and quadrupole mass spectroscopy (QMS), respectively, while the surface-bound species were tracked by in situ reflection-absorption infrared spectroscopy (RAIRS). In addition, the wettability of the SAM surfaces before and after reaction was measured by static water contact angle measurements.

6.2.1. Preparation of Hydroxyl-terminated Self-Assembled Monolayers

Hydroxyl-terminated SAMs were created through solution immersion on polycrystalline gold slides that were pre-cleaned (See previous Chapters for detatils). After being rinsed with deionized water (Millipore Purification Systems, 18.2 MΩ) and dried with a stream of ultrahigh purity nitrogen (UHP N_2), the gold substrates were immersed in freshly prepared 1 mM solution of 16-mercapto-1-hexadecanol in pure ethanol for 24-48 h to achieve a well-ordered densely packed monolayer. Prior to being transferred to the UHV main chamber through a load-lock system, the SAMs were rinsed thoroughly with ethanol and dried under a stream of UHP N_2.

6.2.2 Creation of the NO_3 Molecular Beams

The reagents used for NO_3 radical production are nitrogen monoxide (NO), which was obtained from Sigma-Aldrich Inc., and an excess of ozone (O_3) produced from the ozone generator. The first step of the oxidation is the formation of NO_2. Upon further reaction with O_3, NO_2 can be oxidized to produce N_2O_5. The gas-phase N_2O_5 was then stored in a sealed glass trap submerged

into a dry ice/ethanol bath. For molecular beam scattering experiments, 700 torr UHP helium (He) passed over the N_2O_5 trap where the trap temperature was controlled at ~275 K and the partial pressure of N_2O_5 was ~40 torr throughout the experiment. A 0.05 mm diameter nozzle was heated up to ~400 K to thermally dissociate N_2O_5. As a result, ~5% NO_3/He (the mixture of NO_3/NO_2, 1:1 ratio) was created upon supersonic expansion (see Chapter 2) through the nozzle in a triply-differentially pumped source chamber.

6.2.3 Flux of NO_3 beam and Molecular Beam Scattering

The flux (F), defined as the number of beam molecules striking the surface per unit time, is an important parameter for the determination of reaction probability of NO_3 impinging on the model surface.[12] The flux can be derived from the following equation:

$$F = 0.25\, n \langle v \rangle \qquad (6.1)$$

where n is the number density in molecules cm^{-3}, which can be calculated from the NO_3 partial pressure adjacent to the surface; $\langle v \rangle$ is the mean molecular velocity of gas-phase NO_3, in cm s^{-1}, which can be determined from the incident beam energy. The incident beam energy was characterized with an in-line quadrupole mass spectrometer (Residual Gas Analysis, RGA). By determining the flight time ($t_{chopper\text{-}RGA}$) from the chopper to the mass spectrometer ionizer (a known distance l), the incident beam energy was calculated through the simple relationship, $E_i = 1/2\ m\ (l/t_{chopper\text{-}RGA})^2$. For example, the average velocity of the NO_3 molecule in the 77 kJ/mol NO_3/He beam is 1.6×10^5 cm s^{-1}. Throughout the NO_3 exposure experiments, the total pressure in the main chamber was ~10^{-8} torr. Therefore, the corresponding number density of NO_3 was 1.5×10^7 molecule cm^{-3}. The flux of the NO_3 beam was then calculated to be 6×10^{12} molecule cm^{-2} s^{-1}.

For molecular beam scattering experiments, the surface sample was aligned such that the incident angle (θ_i) of the NO_3 beam was 30º relative to the surface normal and the scattered molecules were detected at the final angle (θ_f) of 30º with a doubly-differentially pumped quadrupole mass spectrometer. When the slit of the chopper wheel passed a LED-photodiode pair, a voltage pulse was sent to trigger a multichannel scalar to initiate TOF scans. All TOF data was recorded as a function of time and the spectra were integrated in 10 μs intervals. Because neither stable parent ion $N_2O_5^+$ nor NO_3^+ could be observed via electron impact (EI) ionization of N_2O_5 and the most intense signal is NO_2^+, the mass spectrometer (QMS) signal was monitored at m/z = 46 for NO_2^+,[26] which yields a distribution of scattering NO_3 molecules as a function of the arrival time. Similarly, the high-energy Ar molecular beam was created by seeding 2% pure Ar in a carrier gas (98% pure H_2) and was characterized with the QMS at m/z = 40.

6.2.4 Molecular Beam Scattering Data Analysis

The effect of translational energy on the reaction dynamics in collisions of NO_3 with the model organic surface was explored by measuring the energy exchange and thermal accommodation efficiency for NO_3/He scattering from the HO-SAM. For the first step, to validate the molecular beam system and to gain some information of the structure of the SAM surface prior to and after NO_3 exposure, the TOF spectra and final energy distribution for 108 kJ/mol Ar/H_2 molecular beam scattering from the organic surface was acquired (Figure 6.1). Figure 6.1 (A) represents the raw time-of-flight data for the atoms recoiling from the surface during collisions. The spectrum shows the signal collected in the mass spectrometer for Ar^+ at m/z 40 as a function of time, where t = 0 is the time at which the incident gas molecules strike the surface. The final energy distribution (Figure 6.1 (B)) is derived from the experimental TOF spectra according to

two relationships $E_f = (1/2)\ m_{gas}\ (L/t)^2$ and $P(E_f) \sim t^2N(t)$,[27,28] where E_f is the final translational energy, L is the distance between the surface and the ionizer of the mass spectrometer and t is the arrival time of Ar atoms. The final energy distributions are typically bimodal with two components, trapping desorption and impulsive scattering.[29,30] During the interfacial collisions, the incident atoms or molecules can be trapped in the gas-surface potential energy well. The trapping is followed by simple thermal desorption (evaporation).[12] For such cases, the final energy distribution can be described by a Maxwell-Boltzmann (MB) distribution at the temperature of the surface using the following equation:[19]

$$P_{BC}(E_f) = A\ E_f/(RT_s)^2\ \exp[-E_f/(RT_s)] \qquad (6.2)$$

Where R is the universal gas constant, T_s is the surface temperature, 298 K, and A is the scaling factor determined by a non-linear least-squares fit to the low-energy portion ($E_f < RT_s$) of the overall $P(E_f)$. We refer this low-energy part of the final energy distribution as Boltzmann component (BC) that is likely due to thermal accommodation of gas-phase molecules or atoms on the surface after they dissipate their excess translational energy upon surface collisions.[12] The other component, within the limit of the two scattering channels, is assigned to impulsive scattering (IS), in which the impinging molecules or atoms retain a fraction of their incident energy and arrive at the mass spectrometer at earlier times (blue line in Figure 6.1 (A)) in the TOF distribution.[31] The overall final energy distribution is the sum of the two components, according to Equation (6.3)[19]

$$P(E_f) = \alpha\ P_{BC}(E_f) + (1 - \alpha)\ P_{IS}(E_f) \qquad (6.3)$$

Here, α is a weighting factor analogous to the thermal accommodation coefficient.

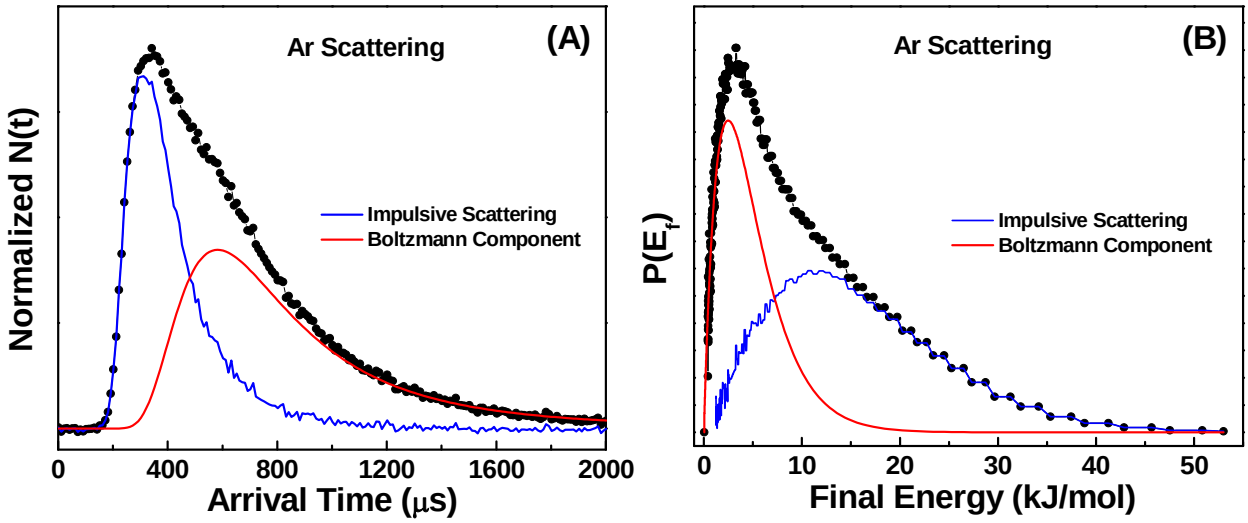

Figure 6.1. (A) TOF distributions and (B) the corresponding final energy distributions for 108 kJ/mol Ar atoms scattering from a 16-C HO-SAM. The red lines in each figure represent the Boltzmann component (BC) at the temperature of the surface (298 K) and the blue lines represent the impulsive scattering (IS) for each data set.

6.2.5 Reflection-Absorption Infrared Spectroscopy Measurements

While the NO_3 beam with a well-characterized incident energy was scattered from the HO-SAM surface, the vibrational motions of surface-bound species were monitored *in situ* via RAIRS. RAIR spectra were provided by a Bruker IFS 66v/S spectrometer attached to the UHV chamber. Focused IR radiation from a SiC globar was reflected from the gold surface at ~86˚ relative to the surface normal through a differentially pumped KBr window. The reflected radiation was detected by a mid-range (750-4000 cm^{-1}) mercury cadmium telluride (MCT) detector, which was cooled by liquid nitrogen prior to each experiment. Each individual spectrum shown in this Chapter was the average of 200 scans with a 2 cm^{-1} resolution. A clean Au surface was used as the background unless otherwise declared.

6.2.6 Water Contact Angle Measurements

Contact angle measurements were performed using an FTA 200 Contact Angle Analyzer (First Ten Angstroms, Portsmouth, VA) with a sessile drop technique. The original HO-SAM and the surface after NO_3 scattering were placed on an adjustable platform and approximately 5 μL of Milli-Q water (Millipore Gradient A10, Esker Laboratories, Virginia Tech) was dropped on the surfaces using a 3 mL 22 gauge syringe. For the contact angle analysis, an image was recorded using a video CCD camera followed by fitting a mathematical expression to the shape of the drop. The contact angle was then calculated through the slope of the tangent to the drop at the liquid-solid-vapor interface (FTA Operator's and Installation Manuals, revision 2.0, May 30, 1997).

6.3 Results and Discussion

The reaction dynamics of NO_3 in collisions with the HO-SAM surface were investigated by employing molecular beam scattering studies. Time-of-flight distributions of the scattered molecules provide insight into gas-surface energy exchange and thermal accommodation efficiency of NO_3 molecules impinging onto the model surface. RAIRS has been used to determine the overall reaction probability by tracking the bond rupture and new bond formation on the surface. Furthermore, by comparing 2% Ar/H_2 scattering before and after NO_3 exposure, the change in surface rigidity upon interfacial reactions has been investigated. In addition, the wettability and the difference in polarity of the surface before and after NO_3 exposure has been explored via water contact angle measurements.

6.3.1 Molecular Beam Scattering of NO_3 and NO_2 gases from a 16-C HO-SAM

Since the generation of NO_3 is always accompanied by the production of NO_2 (thermal decomposition of N_2O_5, see Chapter 2), molecular beam scattering of NO_2 from the HO-SAM surface was also investigated. The TOF and $P(E_f)$ profiles in Figure 6.2 display the arrival times and the final energy distributions for NO_3 (77 kJ/mol) and NO_2 (61 kJ/mol) scattering from the HO-SAM. These distributions show extensive BC fractions (0.68 for NO_3; 0.60 for NO_2) and energy transfer fractions (0.89 for NO_3; 0.82 for NO_2) for both gases scattering from the HO-SAM. Previous studies of NO_2 (70 kJ/mol) scattering showed quite similar energy transfer (0.90) and BC fraction (0.69) to the results of NO_3 scattering described here.[19] The values for the BC fractions, percentage energy transferred, and final average energy for impulsively scattered molecules ($<E_{IS}>$) are summarized in Table 6.1. The extensive energy exchange and thermal accommodation observed for both NO_3 and NO_2 collisions with the HO-SAM result from dissipation of the translational energy of the impinging molecules by the intramolecular vibrational energy redistribution and concerted waving motions of the methylene chains within the monolayer.[15,27] In addition to the available vibrational degrees-of-freedom, the internal energy modes of the projectile can play a role in energy transfer during collisions on organic surfaces.[12]

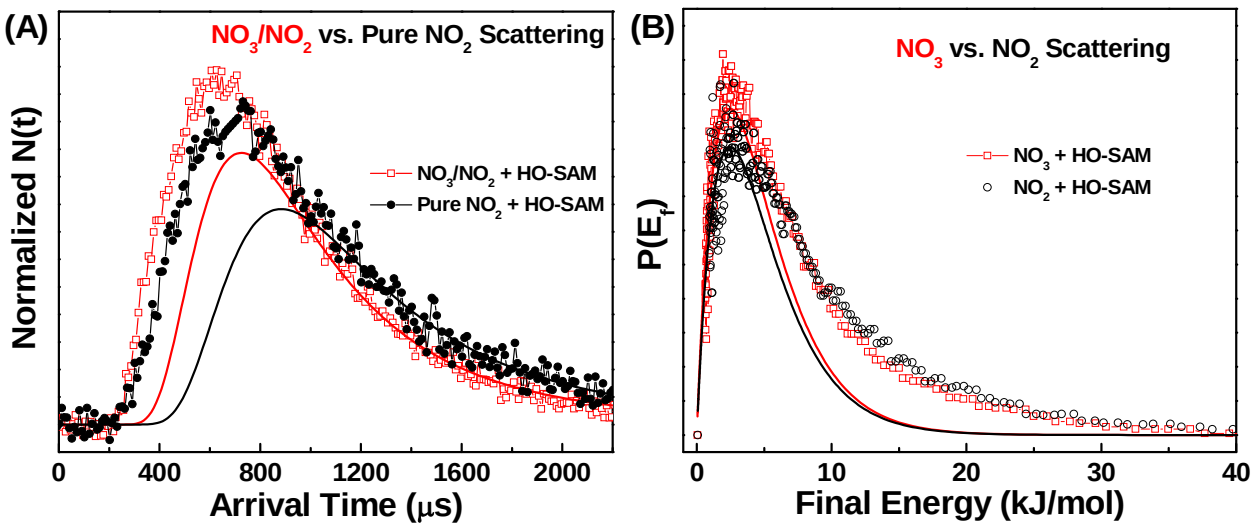

Figure 6.2. (A) Normalized TOF distributions and (B) probability energy distributions for 77 kJ/mol NO_3 and 61 kJ/mol NO_2 scattered from a 16-C HO-SAM. The smooth curves below each distribution are Boltzmann distribution fits (BC) at the temperature of the surface (298 K). Each spectrum was normalized to the same peak area.

With respect to effects of the mass of impinging molecules on the scattering dynamics, it has been found that the BC increases and the IS decreases as the incident gases become heavier.[32] Although NO_3 and NO_2 differ in size, mass, dipole moment, and polarizability (see Table 6.1), the effect of these variances on energy transfer and thermal accommodation efficiency to the HO-SAM appears to be small. Furthermore, as a rigid surface due to the presence of hydrogen-bonding network in the HO-SAM, the monolayer was expected to be a low-efficient energy sink by restricting the low-energy vibrational motions along the hydrocarbon chains.[27,33] However, in a theoretical study of scattering dynamics of HCl from a HO-SAM, Alexander et al. found that the gas-surface attractive interaction by hydrogen bonding due the large dipole of HCl compensates for the influence of surface rigidity and increase the projectile trapped on the surface for extended times.[17] The likely stronger attractions between NO_3/NO_2 and the hydroxyl surface than that between NO_2 and the polar surface may explain a larger energy transfer and thermal accommodation efficiency for NO_3/NO_2 collisions.[34]

Table 6.1. Selected Properties of Gases and Energy Transfer in NO_3 and NO_2 collisions with a HO-SAM.[34,35]

Molecule, E_i	Gas Properties		Energy Transfer and Accommodation		
	Dipole Moment (D)	Polarizability ($Å^3$)	BC fraction	Energy Transfer	$<E_{IS}>$ (kJ/mol)
NO_3, 77 kJ/mol	-	2.60	0.68	0.89	15.4
NO_2, 61 kJ/mol	0	6.04	0.60	0.82	18.6

6.3.2 RAIRS Characterization of HO-SAMs during NO_3 Molecular Beam Scattering

The TOF studies described in Section 6.3.1 do not provide direct insight into the reaction probability and mechanism for NO_3 impinging on the HO-SAM, RAIRS was used as a real-time probe to track the bond breakage and product formation during the NO_3 scattering.

Prior to NO_3 exposure, the RAIR spectrum of a 16-C hydroxyl-terminated SAM on a polycrystalline gold substrate was recorded. Several key features in Figure 6.3 indicate the formation of a well-ordered monolayer on the gold substrate. First, the most intense bands at 2918 and 2850 cm^{-1} are due to the asymmetric ($\nu_a(CH_2)$) and symmetric ($\nu_s(CH_2)$) stretching modes of CH_2 groups along the backbone of the methylene chains.[36] Both the position and the width of the two peaks suggest that the chains reside in a crystalline-like environment.[36,37] The crystalline-like packing of the alkyl chains indicates all-trans conformational sequences since the presence of gauche defects is inconsistent with dense packing.[38] In addition to the stretching modes of methylene groups, two other bands associated with the -CH_2OH terminus emergence in the RAIR spectrum. The weak and broad band at 2878 cm^{-1} is assigned to the C-H stretching mode due to partial disorder at the α-CH_2 adjacent to the -OH group ($\nu(CH_2(OH))$).[38-40] The feature composed of two well-resolved bands at 1061 and 1076 cm^{-1} is attributed to the stretching mode of C-O in

the terminal -CH_2OH group (ν(CO)).[38] The splitting of the feature is likely due to the coupling of C-O stretching mode to similar C-C stretches[39,41,42] and the presence of the two nonequivalent terminal -CH_2OH units (proton acceptor and donor) in the hydrogen-bonded clusters on the surface.[43] Furthermore, the existence of the two conformers associated with the orientation of the OH terminus (trans and gauche with respect to the methylene group) could also contribute to the splitting of the ν(CO) mode.[44] The spectral characteristics are consistent with previous studies, which suggests a 21.4 $Å^2$ occupation of a single alkenethiol chain adsorbed on the gold substrate. Such surface structure and occupation corresponds to a surface density of 4.7×10^{14} molecules cm^{-2}.[38,45,46]

In the molecular beam scattering experiment, the original SAM was used as the background such that negative features in the spectra indicate the removal of modes associated with functional groups and positive bands reveal an increase in absorbance or the development of new modes. The initial spectrum in Figure 6.3 (the lower-most line) is the difference spectrum of the monolayer before exposure. The difference spectra recorded during exposure clearly show that the first features observed are the decay in intensity of the C-O stretching mode associated with the terminal -CH_2OH groups at 1061 and 1076 cm^{-1} (ν(CO)) as well as the appearance of an intense band at 1002 cm^{-1}. The decay of the bands associated with the terminal methylene groups (-CH_2OH) indicates consumption of -CH_2OH during the NO_3 beam scattering from the organic surface. In addition, the emergence of the band in the range of 950-1050 cm^{-1} is likely due to the formation a new C-O bond or a shift of the original C-O stretching mode (in the -CH_2OH moiety) to lower wavenumber. As discussed in Chapter 4, factors that result in the red shift of ν(CO) include the addition of electrowithdrawing groups to the hydroxyl terminus and changes in electronegativities of two atoms in a vibratory link upon NO_3 reactions.[47,48] It has been found that the bond-stretching

force constant decrease with the product of the electronegativities of two atoms linking a bond.[48] For such case, the likely products of reaction between NO_3 and the 16-C HO-terminated SAM are the organic nitrate ($AuS(CH_2)_{15}(CHONO_2)OH$/$AuS(CH_2)_{15}CH_2OONO_2$) or the nitro-compound ($AuS(CH_2)_{15}(CHNO_2)OH$).[49,50] Both products were formed by the replacement of the α H atom (in the $-CH_2OH$ terminus) with a more electronegative species ($-ONO_2$ or $-NO_2$), which may cause a red shift of the CO stretching frequency.[51-53]

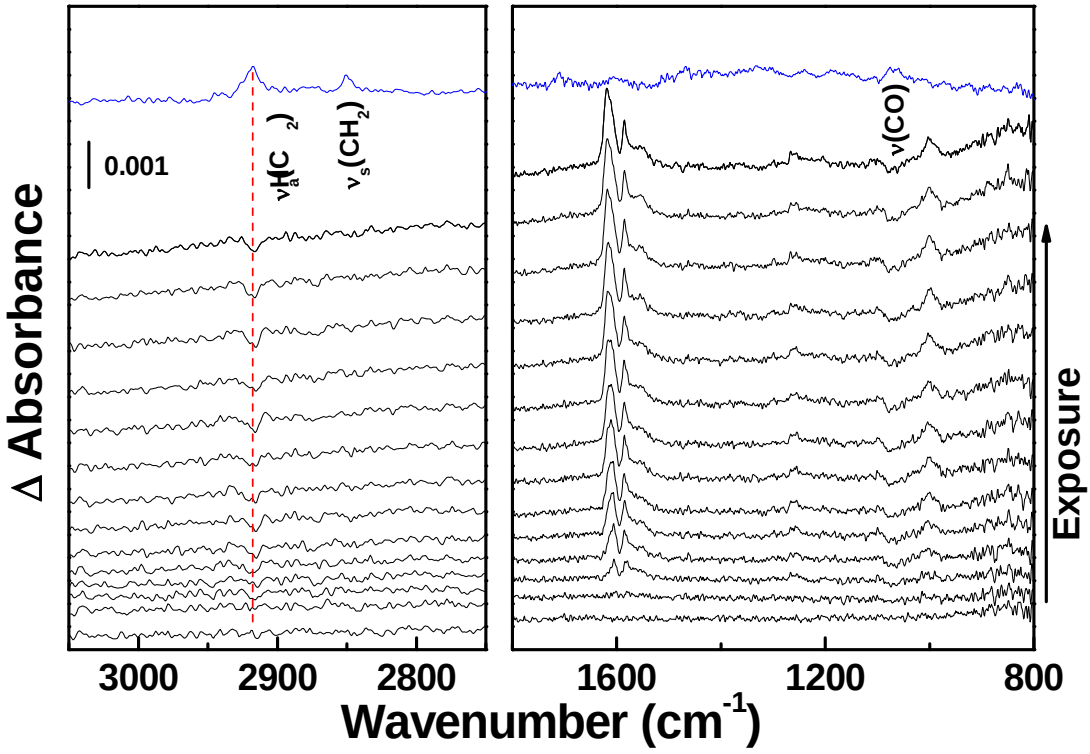

Figure 6.3. Reflection-absorption infrared difference spectra of a 16-C hydroxyl-terminated SAM exposed to NO_3. The spectrum shown on top in blue is that of the SAM prior to NO_3 exposure using a clean Au sample as the background. Upon NO_3 exposure, the spectra in black show that modes associated with the $-CH_2OH$ moiety decrease and new modes emerge. The background for these scans is the original pre-exposure spectrum (blue), with the exposure of the NO_3/He beam increasing by 1 L per spectrum.

In addition to the changes of features described above in RAIRS, several new bands centered at 1260 cm^{-1}, 1558 cm^{-1}, 1585 cm^{-1}, and 1619 cm^{-1} appear and increase in intensity with extended exposure times to the molecular beam. These positive features have very similar

vibrational frequencies to those attributed to stretching modes of organic nitrates yielded from reactions of unsaturated alcohols with nitrate radicals exhibited by Noda et al,[54] suggesting the formation of organic nitrates and nitro-containing compounds during NO_3 collisions on the HO-terminated SAM. However, compared to the bands assigned to vibrational modes of alkyl radical nitrates reported previously by Zhang et al.,[55] the bands emerging in Figure 6.3 are shifted to lower wavenumber. We speculate that the high-energy NO_3 molecules initially abstract a hydrogen atom in the terminal -OH groups. Facile addition of NO_3 onto the oxygen radical may result in the formation of peroxynitrates. Further, the NO_2 molecules, which always accompanies the NO_3 source, continuously impinge on the radical formed by abstraction, leading to the formation of organic nitrates. We observed that the wavenumbers of those bands associated with organic nitrate (shown in Figure 6.3) were lower than the features of RAIRS for alkyl nitrates in previous studies[55] (Chapter 3 and Chapter 4, 1280 cm^{-1} vs. 1260 cm^{-1}). This could be attributed to the formation of peroxynitrates which contain two electronegative oxygen atoms that may weaken the N-O bond by withdrawing electrons from the bond. However, further studies possibly include isotopic labeling experiments and quantum mechanical calculations are required for the definitive assignments of these features.

Concurrent with the spectral changes observed in the low wavenumber region (1800-800 cm^{-1}), the only change in the difference spectra (above the detection limit of the spectrometer, which we estimate to be 2% of a ML) is the decrease of bands associated with the backbone of the chains including $\nu(CH_2(OH))$ at 2878 cm^{-1}, $\nu_a(CH_2)$ at 2918 cm^{-1} and $\nu_s(CH_2)$ at 2850 cm^{-1} (total decrease in intensity is ~20% of the original bands). The decrease in the absorptivity at long exposure times may result from changes in surface concentration of methylene groups due to hydrogen abstraction from $-CH_2-$ by NO_3 molecules. Further, the resultant alkyl radical may react

with impinging NO_3/NO_2 molecules and produce nitrogen-containing products. Beyond the decrease of bands assigned to the symmetric and asymmetric stretch of the CH_2 groups, these bands shift to higher wavenumber and broaden relative to the original ones, which is likely due to the disordering of the methylene chains during the structural changes of the monolayer upon surface reactions (Chapter 4 and 5).

6.3.3 Reaction Probability of NO_3 with the Surface Hydroxyls

While the insight into reaction products of NO_3 collision with the 16-C HO-SAM was provide by in situ RAIRS, the reaction kinetics has been characterized with the rate of consumption of C-O bonds and the rate of formation of organic nitrates (absorptivity of the band at 1585 and 1260 cm^{-1}). Figure 6.4 shows plots of the integrated absorbance for ν(CO) in the $-CH_2OH$ terminus and for the bands at 1585 and 1260 cm^{-1} (ABS_{1585} and ABS_{1260}) as a function of time. The curves, fit to the data according to a non-linear least squares algorithm, show that the rate of change for these bands track pseudo-first-order kinetics, with rate constants of $k_{obs} = 5.4 \times 10^{-3}$ s^{-1} (ν(CO)), $k_{obs} = 5.2 \times 10^{-3}$ s^{-1} (ABS_{1585}), and $k_{obs} = 6.4 \times 10^{-3}$ s^{-1} (ABS_{1260}) respectively. The similarity of these rate constants suggests a strong correlation between consumption of the $-CH_2OH$ groups and yields of surface-bound organic nitrates. The initial reaction probability, γ_0, which is simply the number of collisions that lead to reaction loss divided by that of total collisions, can be determined from the rate constant for the consumption of ν(CO) according to equation (6.4):

$$\gamma_0 = \theta_{max} k_{obs} / F \qquad (6.4)$$

Here, F is the incident flux of gas molecules on the surface, which can be derived from the mean molecular velocity and the concentration of gas-phase NO_3, k_{obs} is the observed rate constant, and θ_{max} is the initial surface coverage of the hydroxyl groups. The initial reaction probability for the

high-energy NO_3 beam (77 kJ/mol) in collisions with the 16-C HO-terminated SAM is γ_0 = 0.4. That is, we find that approximately four reactions occur in every ~10 collisions between the 77 kJ/mol NO_3 beam and the terminal hydroxyl groups, $-CH_2OH$.

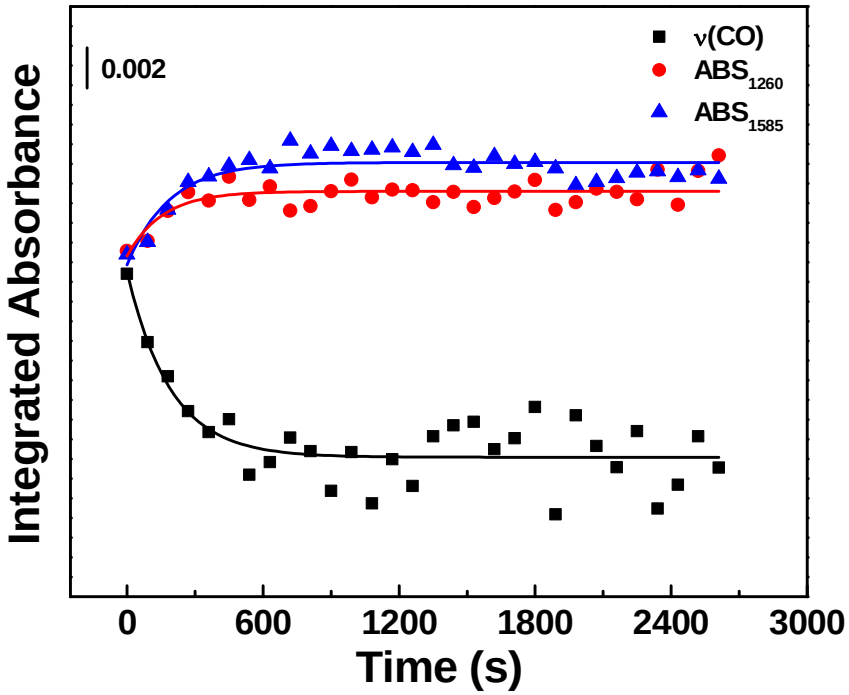

Figure 6.4. Integral absorbance for ν(C-O) at 1060 cm^{-1} and 1076 cm^{-1} (black solid square), the band at 1585 cm^{-1}(blue solid triangle), and the band at 1283 cm^{-1} (red solid circle) versus time during NO_3 exposure. The fitting curves model the results following first-order kinetics. The parameters that provide the best fit are provided in the text.

The initial reaction probability reported here is about two orders of magnitude larger than the rate at which the thermal-energy NO_3 beam (Chapter 4) reacts with the same model organic surface. The much higher reactivity for the high-energy NO_3 beam may be due to a different reaction path for the molecules in the molecular beam or the high-energy NO_3 molecules that may more efficiently surmount any reaction barriers. In addition, the high incident energy NO_3 may penetrate through the monolayer and abstract hydrogen from $-CH_2-$ groups along the hydrocarbon chains or even oxidize the S attached to gold atoms. Sibener and co-workers have previously

demonstrated that such ballistic penetration into alkanethiol SAMs occurs for $O(^3P)$ with translational energy of only 0.11 kJ/mol but larger rare gases required much higher translational energies than those for the NO_3 beam employed here.[15,31]

In Chapter 4, we presented the initial uptake coefficient on a 16 HO-SAM for an effusive beam of NO_3 (average energy of ~5 kJ/mol) through an all-glass capillary doser. The reaction mechanism was proposed to be dominated by hydrogen abstraction at the terminal methylene groups. Here, with the extensive increase of the incident beam energy (77 kJ/mol), the ability of NO_3 molecules penetrating through the rigid hydrogen bonding lattice or diffuse into the hydrocarbon chains through the hollow sites and react may be improved.[17,56]

6.3.4 Stability of Reaction Products and Possible Reaction Mechanism

Figure 6.5 shows RAIR spectra for the 16-C HO-SAM after 90 min of exposure to the high-energy NO_3 beam (spectrum (a)). To examine the stability of reaction products, the sample was left in the UHV main chamber for 250 min after which a new IR spectrum was recorded (spectrum (b)). As discussed above, reactions of NO_3 with the HO-SAM result in the appearance of new bands at 1585 cm^{-1}, 1260 cm^{-1}, and 1002 cm^{-1}, which suggest the formation of organic nitrates following hydrogen abstraction at the terminal -CH_2OH groups.[57] As shown by spectrum (b) in Figure 6.5, the features are mostly preserved after staying in the main chamber for 250 min, which indicates that the organic nitrates are stable for a period of time.

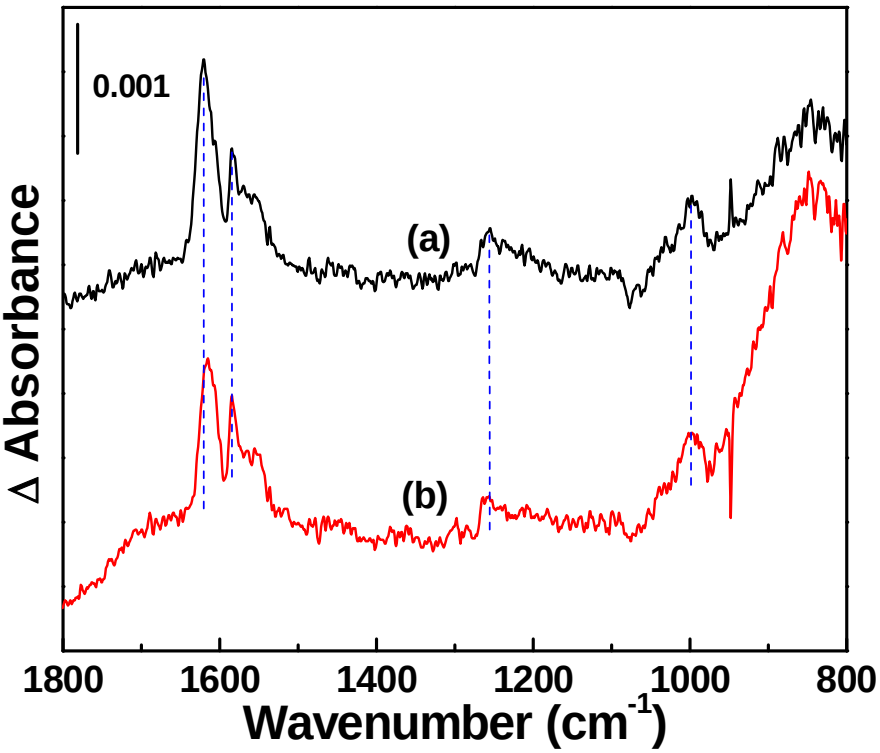

Figure 6.5. Reflection-absorption infrared spectra of a 16-C hydroxyl-terminated (Au-S-$(CH_2)_{16}OH$) SAM on Au (a) after 90 min of NO_3 exposure and (b) sitting in the main chamber for 250 min after NO_3 exposure. The positive IR features are attributed to vibrational modes of organic nitrates or nitro-containing products.

During the heterogeneous oxidation of the HO-SAM by NO_3 presented in this Chapter, we observed that the ν(CO) mode decreased in intensity and shifted to lower wavenumbers, suggesting changes in electronegativity of the two linking atoms (carbon and oxygen). This change in the chemical environment of the two atoms may be due to hydrogen abstraction at the terminal -OH groups upon NO_3 collisions, which is shown by pathway I in Figure 6.6. In addition, several new modes appear (1260 cm^{-1}, 1585 cm^{-1} and 1619 cm^{-1}) and increase in intensity as exposure times extended at identical rate with the decay of the C-O stretch, which is attributed to the formation of organo-nitrate moieties. The terminal nitrates could be formed from the direct addition of impinging NO_3 to the alcohol radical with the unpaired electron on oxygen atom. Alternatively, following the formation of the alcohol radical, NO_2 molecules, accompanied with

the yield of NO_3 from thermal decomposition of N_2O_5, can also add to the oxygen radical to produce organic nitrates. Considering the nature of the terminal nitrate groups, they may hydrogen bond with unreacted neighboring hydrogen atoms and result in the red shift of -ONO_2 asymmetric and symmetric stretches, which is consistent with our observation in RAIRS (as described in Section 6.3.2). Further, the features in the hydrocarbon region (relatively high wavenumbers at 2878 cm^{-1}, 2918 cm^{-1}, and 2850 cm^{-1}) decrease in intensity during the high-energy NO_3 beam scattering from the hydroxyl surface, which may result from the hydrogen abstraction along the methylene chains, as shown by pathway II in Figure 6.6. The high-energy NO_3 molecules may attack the methylene groups by accessing to the hydrocarbon chains at hollow sites due to the formation of hydroxyl clusters by interfacial hydrogen bonding.[17,56] Moreover, the generated alcohol radical could further react with the impinging NO_2 or NO_3 that leads to the production of nitro-containing compounds or organic nitrates, which is consistent with the observations in RAIRS (Section 6.3.2). In addition, according to the assignment of aromatic and aliphatic nitro organics in IR studies,[58] the feature at the shoulder (1558 cm^{-1}) near the 1585 cm^{-1} band may be due to the asymmetric stretch of -NO_2 in nitro-containing compounds.

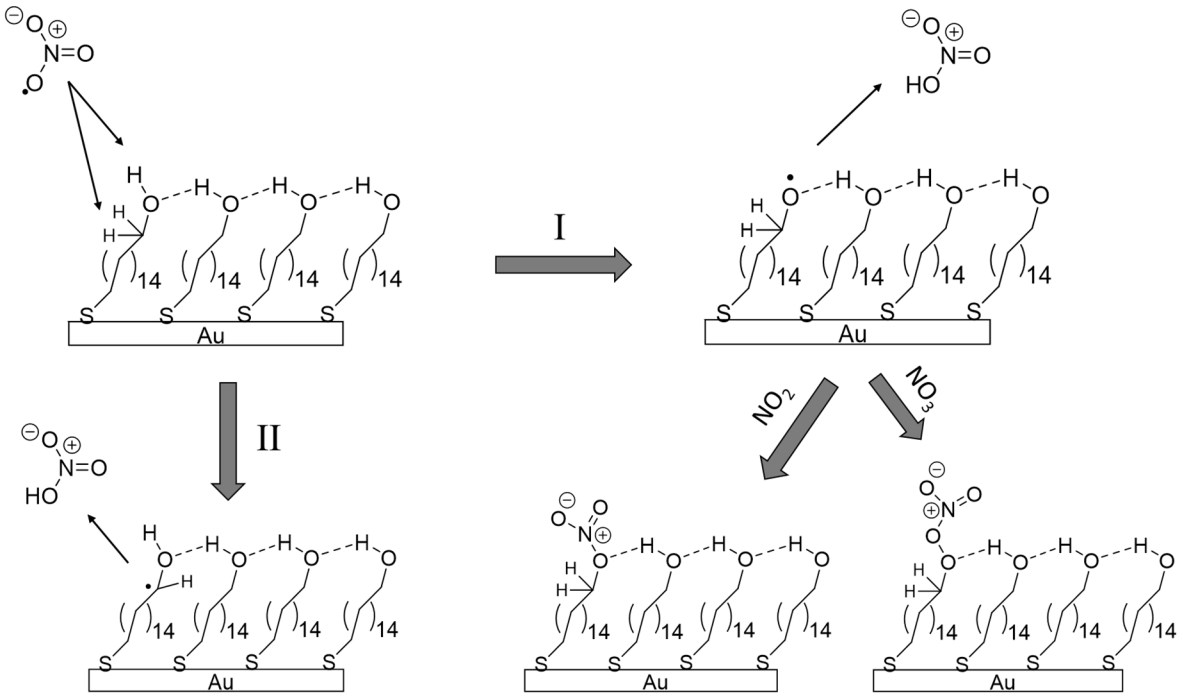

Figure 6.6. A scheme of the possible mechanistic pathways showing the hydrogen abstraction at the terminal -CH_2OH groups by the high-energy NO_3 beam and the formation of nitric acid and organic nitrates.

6.3.5 High-Energy Ar Scattering from the HO-SAM Surface Prior to and After NO_3 Reactions

Atomic Scattering of inert gases (such as He, Ar) are widely used as a probe of changes in the surface structure upon reactive collisions.[16,31,59] Because Ar is atomic and weakly polarizable, studies of Ar scattering from the model organic surface provide insight into collision dynamics in the absence of any strong attractive forces between impinging atoms and the surface. In addition, it has been discovered that the scattering behaviour of rare gas collisions with organic surfaces depends upon specific surface properties including structure, density, mass, and dipole moment.[30,33] Day et al. scattered a high-energy Ar beam (80 kJ/mol) from CH_3-, HO-, COOH-, NH_2-terminated SAMs and found that the atomic beam transferred most energy to CH_3-SAMs and

exchange much less energy with the other ω-functionalized SAMs due to the intramolecular hydrogen bonding.[33] Further, Lu et al. investigated energy transfer efficiency between Ar and CH_3-, HO-, and F-SAMs and discovered that the massive F-SAMs were the least effective at dissipating the translational energy of impinging atoms.[19] Therefore, by scattering high-energy Ar beam from the HO-SAM surface before and after NO_3 reaction, we could gain some key insights into changes in surface properties.

Figure 6.7 shows normalized TOF distributions and corresponding probability energy distributions for 108 kJ/mol Ar scattered from a 16-C HO-SAM surface before (black curves) and after (red curves) NO_3 reaction. The figure exhibits difference in energy transfer efficiency, thermal accommodation fraction (TD fraction), and final average impulsive energy ($<E_{IS}>$) between the original surface and the reacted surface, which signals some changes to the surface properties following reaction.

Previous studies illustrate that the energy transfer efficiency for surfaces in the presence of intramolecular hydrogen bonding is expected to be lower than those in the absence of interfacial hydrogen bonding. Simulations of HO-SAMs indicate that the average distance between oxygen is 2.6 - 3.0 Å,[60] shorter than the 4.9 Å spacing between sulfur atoms bound to the three-fold hollow sites on Au(111),[45] which may restrict low-vibrational modes that are considered to be the primary sink for dissipating the incident translational energy.[15] However, we found that the HO-SAM surface (88.7%) dissipated more energy than the reacted surface with formed organic nitrates at the interface (86.6%). According to the hard cube model, the fraction of energy transferred by the incident translational energy is directly related to the relative mass of gas species to the surface, as illustrated in Equation (6.4):[59]

$$\Delta E/E_i = 4\mu/(\mu+1)^2 \qquad (6.4)$$

Where μ is the ratio of the mass of the projectile (m_g) to the mass of the effective surface (m_s). For the atomic Ar beam scattering from the HO-SAM surface before and reaction, this model qualitatively predicts the scattering behaviour with the interaction between the rare gas atom and the organic surfaces represented by impulsive force of repulsion.[61] The terminus -ONO_2/-$OONO_2$ (as discussed in Section 6.3.4) formed through reactions of the NO_3 beam with the HO-SAM is more massive than the terminal -OH group, resulting in much smaller μ in the hard cube model for Ar atoms scattering from the nitrate surface, and thus smaller energy transfer efficiency. The final IS energy of Ar scattering from the two surfaces in this chapter differs by approximately 4 kJ/mol. It has been shown that the final energy of the impulsive scattering channel for Ar collisions with SAM surfaces demonstrate the relative rigidity of solid surfaces.[31] In our case, due to the formation of large -ONO_2 or -$OONO_2$ groups at the interface that could hinder the gas-surface interactions and facilitate the atoms directly recoiling back to the gas phase, the organic nitrate surface may appear to be more rigid than the HO-SAM. As the energy transfer fraction becomes smaller for Ar/H_2 beam scattering from the nitrate surface, scattered molecules with higher final energy are expected, which is consistent with the observation of increased final IS energy for Ar → nitrate surface.

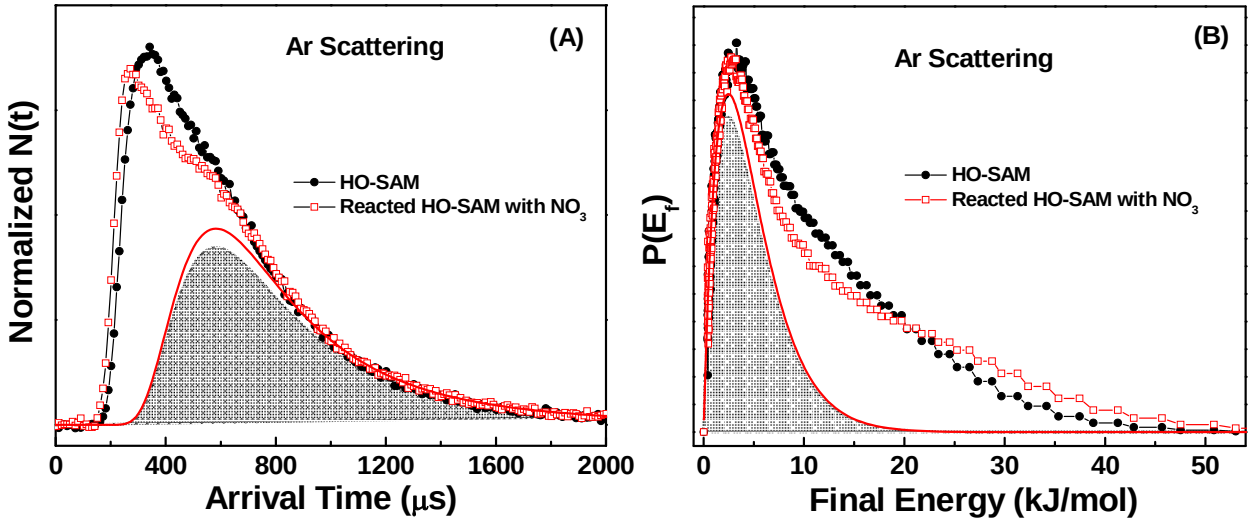

Figure 6.7. (A) Normalized TOF distributions and (B) probability energy distributions for 108 kJ/mol Ar (seeded by H_2) scattered from a 16-C HO-SAM before (black curve and grey area) and after (red curves) NO_3 reactions. The smooth curves below each distribution are Boltzmann distribution fits (BC) at the temperature of the surface (298 K). Each spectrum was normalized to the same peak number density.

Although the HO-SAM is more efficient than the nitrate surface for dissipating the translational energy of the Ar projectile, the TD fraction is smaller for Ar scattering from the HO-SAM surface, as shown in Table 6.2. Morris and co-workers investigated rare gases and polar gas-phase molecules scattering from SAMs with interfacial polar functional groups and found that the extent of gas-surface accommodation efficiency follows the same trend as the "like-dissolves-like" rule for solvent-solute interactions in solution.[31,33,62] The terminal nitrate groups, with more symmetric structure and smaller difference in electronegativity among bonded atoms than that of the -OH terminus, may be less polar, which could give rise to a larger TD fraction.[34] Further, if the Ar → HO-SAM has a deeper attractive well than the Ar → nitrate surface, and if Ar atoms can get closer to the repulsive wall during collisions with the nitrate surface, the accommodation efficiency may be larger for Ar → nitrate surface.[12] However, such speculation needs computational studies about the potential energy surface of Ar approaching the two surfaces.

Table 6.2. Energy Transfer and Accommodation of 108 kJ/mol Ar on HO-SAMs before and after NO_3 Reaction

Monolayer	Percent Energy Transferred, $(E_i - \langle E_f \rangle)/E_i*100\%$	TD fraction	Final IS Energy, $\langle E_{IS} \rangle$, kJ/mol
HO-SAM	88.7%	0.43	16.8
Organic Nitrates	86.6%	0.46	21.1

6.3.6 Wettability of HO-SAMs before and after NO_3 Reactions

Since the process of wetting is accompanied by a change in total surface free energy and this change is related to the molecular structure at the solid-liquid interface, the wettability provides local details of interfacial structure at the angstrom scale.[63] Figure 6.8 exhibits photographs of a water droplet on an HO-SAM and the same surface with organic nitrates formed at the gas-solid interface after NO_3 scattering. The static water contact angle θ_{water} of a 16-C HO-SAM is 30º. After the higher-energy NO_3 beam scattering from the HO-SAM surface, the static water contact angle was measured to be 84º. As a consequence of NO_3 reactions with the surface, the contact angle undergoes significant excursion from hydrophilic toward hydrophobic, indicating decrease in the polarity of functional groups at the interface.[64] The change in the polarity may be due to the formation of $-ONO_2$ or $-OONO_2$ groups after hydrogen abstraction at the $-CH_2OH$ terminus. In addition, the decrease in the polarity is consistent with the increase of TD fraction for atomic Ar beam scattering from the SAM surface after NO_3 reactions (compared to the HO-SAM data, see Section 6.3.5). Further, the change in surface roughness the SAM upon NO_3 reactions with the hydroxyl surface may also affect the water contact angle.[38,45]

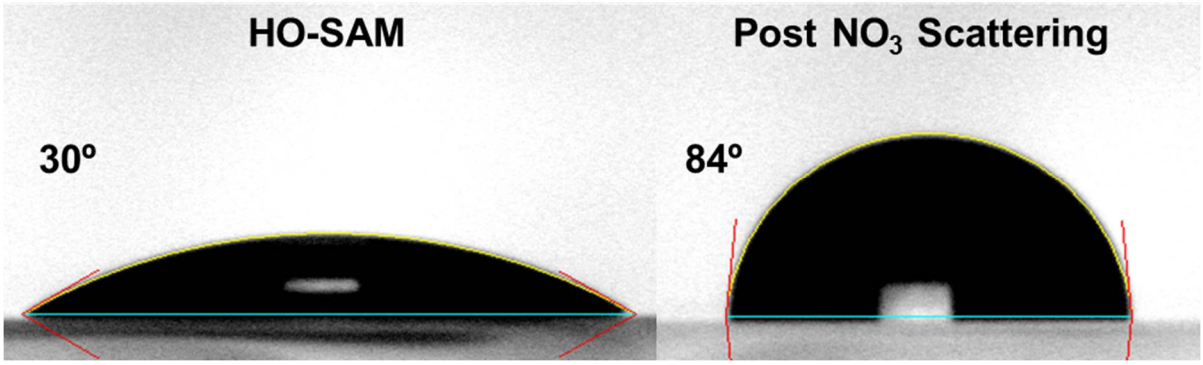

Figure 6.8. Photographs of a water droplet on a HO-SAM (left) and the same surface after NO_3 scattering (right).

6.3.7 Energy Exchange of Ar with HO-SAM affected by Low-Energy NO_3 Collisions

To investigate effects of translational energy of NO_3 on NO_3 → HO-SAM reactions, we create a low-energy beam of NO_3 with pure Ar as the carrier gas (Section 6.2.2). While NO_3/Ar was scattered from a freshly made HO-SAM surface, no change was observed in the RAIR difference spectra after 1 hour of NO_3 exposure. We speculate that the low-energy NO_3 molecules could not directly abstract hydrogen from the terminal -OH groups and the flux of the beam was not high enough to initiate reactions that could be observed in RAIRS.

Nevertheless, the effect induced by the low-energy NO_3 beam on the organic surface was further explored by scattering atomic Ar onto the HO-SAM before and after NO_3 collisions, as shown in Figure 6.9. The TD fraction and energy transfer for Ar scattering from the HO-SAM are 0.43 and 88.5%, which is in agreement with values reported previously for the same system. After NO_3/Ar collisions with the SAM, the TD fraction increased slightly (0.45), suggesting that the HO-SAM was oxidized by the NO_3/Ar beam. However, the changes in TD fraction and the final energy were very small, which could be due to the fact that only a small fraction of the original SAM was oxidized such that the effect on overall gas-surface properties was minimized.

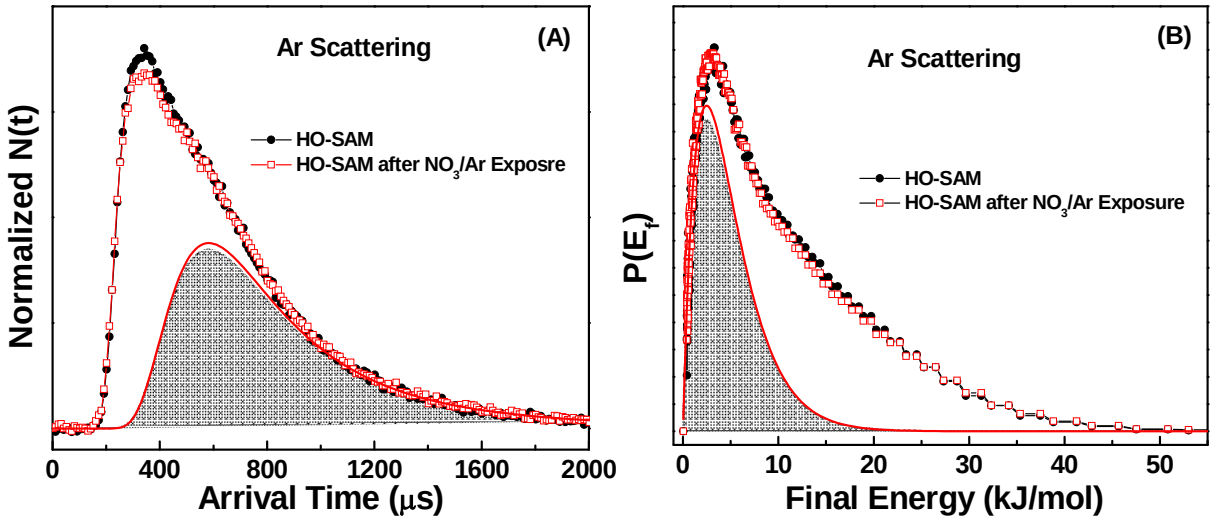

Figure 6.9. (A) Normalized TOF distributions and (B) probability energy distributions for 108 kJ/mol Ar (seeded by H_2) scattered from a 16-C HO-SAM before (black curve and grey area) and after (red curves) NO_3/Ar collisions. The smooth curves below each distribution are Boltzmann distribution fits (BC) at the temperature of the surface (298 K). Each spectrum was normalized to the same peak number density.

6.4 Summary

The dynamics of NO_3 reactions with the 16-C HO-SAM have been investigated by molecular beam scattering methods to probe the effect of NO_3 translational energy on the initial reaction probability. During the gas-surface collision, the NO_3 molecules extensively impart their incident energy to the surface and result in efficient energy transfer. The reaction probability for the 77 kJ/mol NO_3 beam is as high as 0.4, which is orders of magnitude larger than the thermal incident-energy NO_3 collisions with the same surface. The significant increase in the reaction probability is attributed to the promotion in the ability of NO_3 abstracting hydrogen atom at the $-CH_2OH$ terminus or a different reaction path for the elevated-energy molecules in the molecular beam. An interesting comparison would be a UHV study of reaction dynamics of O_3 collisions with a long-chain vinyl-terminated SAM.[21] At similar incident beam energies, the three-order-of-magnitude difference in the reaction probability of NO_3 with the HO-SAM (~0.4) compared to

that of O_3 with the vinyl-terminated SAM ($\sim 10^{-4}$) suggests that, even though NO_3 radicals are only present in the nighttime, interfacial reaction of NO_3 with hydroxyl-functionalized surfaces may play a more prevalent role in the atmosphere than reactions of ozone with unsaturated surfaces.

Following the hydrogen abstraction, excess gas-phase NO_3 or NO_2 molecules could add to the formed radical and generate organic nitrates or peroxynitrates which are stable for a period of time. The formation of interfacial nitrate moieties leads to a less polar, more rigid and massive surface, as evidenced by atomic Ar scattering experiments and water contact angle measurements. It turns out that low-energy NO_3 could not initiate reactions which are observable in RAIRS. Further studies of translational energy dependent reaction probability may be achieved by employing NO_3/Ne beam in molecular scattering experiments.

The scattering studies described in this chapter provide evidence for incident energy dependence of reaction mechanism of NO_3 molecules collisions with a long-chain HO-SAM. For the high energy beam of NO_3 scattering from the HO-SAM, the reaction probability was increased by a huge amount with hydrogen abstraction along the hydrocarbon chains or even at the hydroxyl terminus. In addition, the surface upon reaction became more massive and less polar. These insights may assist theoretical scientist to construct better models for understanding interfacial reactions involving atmospheric NO_3 and organic particulates as well as predicting the fate of those organic particles.

REFERNCES

(1) Disselkamp, R. S.; Carpenter, M. A.; Cowin, J. P.; Berkowitz, C. M.; Chapman, E. G.; Zaveri, R. A.; Laulainen, N. S., Ozone Loss in Soot Aerosols. *J. Geophys. Res. Atmos.* **2000,** *105* (D8), 9767-9771.

(2) Salo, K.; Hallquist, M.; Jonsson, A. M.; Saathoff, H.; Naumann, K. H.; Spindler, C.; Tillmann, R.; Fuchs, H.; Bohn, B.; Rubach, F.; Mentel, T. F.; Muller, L.; Reinnig, M.; Hoffmann, T.; Donahue, N. M., Volatility of Secondary Organic Aerosol During OH Radical Induced Ageing. *Atmos. Chem. Phys.* **2011,** *11* (21), 11055-11067.

(3) Moise, T.; Talukdar, R. K.; Frost, G. J.; Fox, R. W.; Rudich, Y., Reactive Uptake of NO_3 by Liquid and Frozen Organics. *J. Geophys. Res., [Atmos.]* **2002,** *107* (D2), AAC 6-1-AAC 6-9.

(4) Shiraiwa, M.; Poschl, U.; Knopf, D. A., Multiphase Chemical Kinetics of NO_3 Radicals Reacting with Organic Aerosol Components from Biomass Burning. *Environ. Sci. Technol.* **2012,** *46* (12), 6630-6636.

(5) Zhao, Z.; Husainy, S.; Stoudemayer, C. T.; Smith, G. D., Reactive Uptake of NO_3 Radicals by Unsaturated Fatty Acid Particles. *Phys. Chem. Chem. Phys.* **2011,** *13* (39), 17809-17817.

(6) Winer, A. M.; Atkinson, R.; Pitts, J. N., Gaseous Nitrate Radical - Possible Nighttime Atmospheric Sink for Biogenic Organic-Compounds. *Science* **1984,** *224* (4645), 156-159.

(7) Seinfeld, J. H.; Pandis, S. N., *Atmospheric Chemistry and Physics: From Air Pollution to Climate Change*. John Wiley & Sons: 2012.

(8) Wayne, R. P.; Barnes, I.; Biggs, P.; Burrows, J. P.; Canosamas, C. E.; Hjorth, J.; Lebras, G.; Moortgat, G. K.; Perner, D.; Poulet, G.; Restelli, G.; Sidebottom, H., The Nitrate Radical - Physics, Chemistry, and the Atmosphere. *Atmos. Environ. A-Gen.* **1991,** *25* (1), 1-203.

(9) Fry, J. L.; Sackinger, K., Model Investigation of NO_3 Secondary Organic Aerosol (SOA) Source and Heterogeneous Organic Aerosol (OA) Sink in the Western United States. *Atmos. Chem. Phys.* **2012,** *12* (18), 8797-8811.

(10) Che, D. L.; Smith, J. D.; Leone, S. R.; Ahmed, M.; Wilson, K. R., Quantifying the Reactive Uptake of OH by Organic Aerosols in a Continuous Flow Stirred Tank Reactor. *Phys. Chem. Chem. Phys.* **2009,** *11* (36), 7885-7895.

(11) Chu, S. N.; Sands, S.; Tomasik, M. R.; Lee, P. S.; McNeill, V. F., Ozone Oxidation of Surface-Adsorbed Polycyclic Aromatic Hydrocarbons: Role of PAH−Surface Interaction. *J. Am. Chem. Soc.* **2010,** *132* (45), 15968-15975.

(12) Levine, R. D., *Molecular Reaction Dynamics*. Cambridge University Press: 2005.

(13) Saecker, M. E.; Nathanson, G. M., Collisions of Protic and Aprotic Gases with a Perfluorinated Liquid. *J. Chem. Phys.* **1994,** *100* (5), 3999-4005.

(14) King, M. E.; Saecker, M. E.; Nathanson, G. M., The Thermal Roughening of Liquid Surfaces and Its Effect on Gas–Liquid Collisions. *J. Chem. Phys.* **1994,** *101* (3), 2539-2547.

(15) Yan, T.; Isa, N.; Gibson, K. D.; Sibener, S. J.; Hase, W. L., Role of Surface Intramolecular Dynamics in the Efficiency of Energy Transfer in Ne Atom Collisions with a N-Hexylthiolate Self-Assembled Monolayer†. *J. Phys. Chem. A* **2003,** *107* (49), 10600-10607.

(16) SAECKER, M. E.; GOVONI, S. T.; KOWALSKI, D. V.; KING, M. E.; NATHANSON, G. M., Molecular Beam Scattering from Liquid Surfaces. *Science* **1991,** *252* (5011), 1421-1424.
(17) Alexander, W. A.; Troya, D., Theoretical Study of the Dynamics of Collisions between HCl and ω-Hydroxylated Alkanethiol Self-Assembled Monolayers. *J. Phys. Chem. C* **2011,** *115* (5), 2273-2283.
(18) Yuan, H.; Gibson, K. D.; Li, W.; Sibener, S. J., Modification of Alkanethiolate Monolayers by O(^{3}P) Atomic Oxygen: Effect of Chain Length and Surface Temperature. *J. Phys. Chem. B* **2012,** *117* (16), 4381-4389.
(19) Lu, J. W.; Morris, J. R., Gas–Surface Scattering Dynamics of CO_2, NO_2, and O_3 in Collisions with Model Organic Surfaces. *J. Phys. Chem. A* **2011,** *115* (23), 6194-6201.
(20) Weinberg, W.; Rettner, C.; Ashfold, M., Dynamics of Gas Surface Interactions. Royal Society of Chemistry, London: 1991.
(21) Lu, J. W.; Fiegland, L. R.; Davis, E. D.; Alexander, W. A.; Wagner, A.; Gandour, R. D.; Morris, J. R., Initial Reaction Probability and Dynamics of Ozone Collisions with a Vinyl-Terminated Self-Assembled Monolayer. *J. Phys. Chem. C* **2011,** *115* (51), 25343-25350.
(22) Adamson, A. W.; Gast, A. P., Physical Chemistry of Surfaces. **1967**.
(23) Troya, D., Dynamics of Collisions of Hydroxyl Radicals with Fluorinated Self-Assembled Monolayers. *Theor. Chem. Acc.* **2012,** *131* (1), 1-12.
(24) Troya, D.; Schatz, G. C., Theoretical Studies of Hyperthermal O(^{3}P) Collisions with Hydrocarbon Self-Assembled Monolayers. *J. Chem. Phys.* **2004,** *120* (16), 7696-7707.
(25) Layfield, J. P.; Troya, D., Theoretical Study of the Dynamics of F+Alkanethiol Self-Assembled Monolayer Hydrogen-Abstraction Reactions. *J. Chem. Phys.* **2010,** *132* (13), 134307.
(26) Abedi, A.; Cicman, P.; Coupier, B.; Gulejová, B.; Buchanan, G. A.; Marston, G.; Mason, N. J.; Scheier, P.; Märk, T. D., Dissociative Electron Impact Ionization of N_2O_5. *Int. J. Mass Spectrom.* **2004,** *232* (2), 147-150.
(27) Shuler, S. F.; Davis, G. M.; Morris, J. R., Energy Transfer in Rare Gas Collisions with Hydroxyl- and Methyl-Terminated Self-Assembled Monolayers. *J. Chem. Phys.* **2002,** *116* (21), 9147-9150.
(28) Morris, J. R.; Behr, P.; Antman, M. D.; Ringeisen, B. R.; Splan, J.; Nathanson, G. M., Molecular Beam Scattering from Supercooled Sulfuric Acid: Collisions of HCl, HBr, and HNO_3 with 70 Wt D_2SO_4. *J. Phys. Chem. A* **2000,** *104* (29), 6738-6751.
(29) Nathanson, G. M.; Davidovits, P.; Worsnop, D. R.; Kolb, C. E., Dynamics and Kinetics at the Gas−Liquid Interface. *J. Phys. Chem.* **1996,** *100* (31), 13007-13020.
(30) Nathanson, G. M., Molecular Beam Studies of Gas-Liquid Interfaces. *Annu. Rev. Phys. Chem.* **2004,** *55* (1), 231-255.
(31) Lu, J. W.; Day, B. S.; Fiegland, L. R.; Davis, E. D.; Alexander, W. A.; Troya, D.; Morris, J. R., Interfacial Energy Exchange and Reaction Dynamics in Collisions of Gases on Model Organic Surfaces. *Prog. Surf. Sci.* **2012,** *87* (9–12), 221-252.
(32) Alexander, W. A.; Day, B. S.; Moore, H. J.; Lee, T. R.; Morris, J. R.; Troya, D., Experimental and Theoretical Studies of the Effect of Mass on the Dynamics of Gas/Organic-Surface Energy Transfer. *J. Chem. Phys.* **2008,** *128* (1), -.
(33) Day, B. S.; Shuler, S. F.; Ducre, A.; Morris, J. R., The Dynamics of Gas-Surface Energy Exchange in Collisions of Ar Atoms with ω-Functionalized Self-Assembled Monolayers. *J. Chem. Phys.* **2003,** *119* (15), 8084-8096.

(34) Haynes, W. M., *Crc Handbook of Chemistry and Physics*. CRC press: 2013.
(35) Kamboures, M. A.; Raff, J. D.; Miller, Y.; Phillips, L. F.; Finlayson-Pitts, B. J.; Gerber, R. B., Complexes of HNO_3 and NO_3- with NO_2 and N_2O_4, and Their Potential Role in Atmospheric Hono Formation. *Phys. Chem. Chem. Phys.* **2008,** *10* (39), 6019-6032.
(36) MacPhail, R. A.; Strauss, H. L.; Snyder, R. G.; Elliger, C. A., Carbon-Hydrogen Stretching Modes and the Structure of N-Alkyl Chains. 2. Long, All-Trans Chains. *J. Phys. Chem.* **1984,** *88* (3), 334-341.
(37) Bertilsson, L.; Liedberg, B., Infrared Study of Thiol Monolayer Assemblies on Gold: Preparation, Characterization, and Functionalization of Mixed Monolayers. *Langmuir* **1993,** *9* (1), 141-149.
(38) Nuzzo, R. G.; Dubois, L. H.; Allara, D. L., Fundamental Studies of Microscopic Wetting on Organic Surfaces. 1. Formation and Structural Characterization of a Self-Consistent Series of Polyfunctional Organic Monolayers. *J. Am. Chem. Soc.* **1990,** *112* (2), 558-569.
(39) Atre, S. V.; Liedberg, B.; Allara, D. L., Chain Length Dependence of the Structure and Wetting Properties in Binary Composition Monolayers of OH- and CH_3-Terminated Alkanethiolates on Gold. *Langmuir* **1995,** *11* (10), 3882-3893.
(40) Ichimura, A. S.; Lew, W.; Allara, D. L., Tripod Self-Assembled Monolayer on Au(111) Prepared by Reaction of Hydroxyl-Terminated Alkylthiols with $SiCl_4$. *Langmuir* **2008,** *24* (6), 2487-2493.
(41) Stuart, A. V.; Sutherland, G. B. B. M., Effect of Hydrogen Bonding on the Deformation Frequencies of the Hydroxyl Group in Alcohols. *J. Chem. Phys.* **1956,** *24* (3), 559-570.
(42) Socrates, G., *Infrared and Raman Characteristic Group Frequencies: Tables and Charts*. 3 rd ed. ed.; John Wiley & Sons, Inc.: New York, 2001.
(43) Ehbrecht, M.; Huisken, F., Vibrational Spectroscopy of Ethanol Molecules and Complexes Selectively Prepared in the Gas Phase and Adsorbed on Large Argon Clusters. *J. Phys. Chem. A* **1997,** *101* (42), 7768-7777.
(44) Barnes, A. J.; Hallam, H. E., Infra-Red Cryogenic Studies. Part 5.-Ethanol and Ethanol-D Argon Matrices. *Trans. Faraday Soc.* **1970,** *66* (0), 1932-1940.
(45) Love, J. C.; Estroff, L. A.; Kriebel, J. K.; Nuzzo, R. G.; Whitesides, G. M., Self-Assembled Monolayers of Thiolates on Metals as a Form of Nanotechnology. *Chem. Rev.* **2005,** *105* (4), 1103-1170.
(46) Dubois, L. H.; Nuzzo, R. G., Synthesis, Structure, and Properties of Model Organic-Surfaces. *Annu. Rev. Phys. Chem.* **1992,** *43*, 437-463.
(47) Wheland, G. W., *The Theory of Resonance*. John Wiley & Sons, Inc.: New York, 1944.
(48) Gordy, W., A Relation between Bond Force Constants, Bond Orders, Bond Lengths, and the Electronegativities of the Bonded Atoms. *J. Chem. Phys.* **1946,** *14* (5), 305-320.
(49) Harrison, J. C.; Wells, J. R., 2–Butoxyethanol and Benzyl Alcohol Reactions with the Nitrate Radical: Rate Coefficients and Gas-Phase Products. *Int. J. Chem. Kinet.* **2012,** *44* (12), 778-788.
(50) Moreno, A.; Salgado, M. S.; Martín, M. P.; Martínez, E.; Cabañas, B., Kinetic Study of the Gas Phase Reactions of a Series of Alcohols with the NO_3 Radical. *J. Phys. Chem. A* **2012,** *116* (42), 10383-10389.
(51) Tsu, D. V.; Lucovsky, G.; Davidson, B. N., Effects of the Nearest Neighbors and the Alloy Matrix on Sih Stretching Vibrations in the Amorphous SiO_r:H ($0<r<2$) Alloy System. *Phys. Rev. B* **1989,** *40* (3), 1795-1805.

(52) Mulliken, R. S., A New Electroaffinity Scale; Together with Data on Valence States and on Valence Ionization Potentials and Electron Affinities. *J. Chem. Phys.* **1934,** *2* (11), 782-793.
(53) Mulliken, R. S., Electronic Structures of Molecules Xi. Electroaffinity, Molecular Orbitals and Dipole Moments. *J. Chem. Phys.* **1935,** *3* (9), 573-585.
(54) Noda, J.; Hallquist, M.; Langer, S.; Ljungstrom, E., Products from the Gas-Phase Reaction of Some Unsaturated Alcohols with Nitrate Radicals. *Phys. Chem. Chem. Phys.* **2000,** *2*, 2555-2564.
(55) Zhang, Y.; Chapleski, R. C.; Lu, J. W.; Rockhold, T. H.; Troya, D.; Morris, J. R., Gas-Surface Reactions of Nitrate Radicals with Vinyl-Terminated Self-Assembled Monolayers. *Phys. Chem. Chem. Phys.* **2014,** *16* (31), 16659-16670.
(56) Tasić, U.; Day, B. S.; Yan, T.; Morris, J. R.; Hase, W. L., Chemical Dynamics Study of Intrasurface Hydrogen-Bonding Effects in Gas−Surface Energy Exchange and Accommodation. *J. Phys. Chem. C* **2007,** *112* (2), 476-490.
(57) Olariu, R. I.; Barnes, I.; Bejan, I.; Arsene, C.; Vione, D.; Klotz, B.; Becker, K. H., FT-IR Product Study of the Reactions of NO_3 Radicals with Ortho-, Meta-, and Para-Cresol. *Environ. Sci. Technol.* **2013,** *47* (14), 7729-7738.
(58) Jariyasopit, N.; McIntosh, M.; Zimmermann, K.; Arey, J.; Atkinson, R.; Cheong, P. H.-Y.; Carter, R. G.; Yu, T.-W.; Dashwood, R. H.; Massey Simonich, S. L., Novel Nitro-Pah Formation from Heterogeneous Reactions of Pahs with NO_2, NO_3/N_2O_5, and OH Radicals: Prediction, Laboratory Studies, and Mutagenicity. *Environ. Sci. Technol.* **2013,** *48* (1), 412-419.
(59) Harris, J., Notes on the Theory of Atom/Molecule-Surface Scattering. *Phys. Scr.* **1987,** *36* (1), 156.
(60) Sprik, M.; Delamarche, E.; Michel, B.; Roethlisberger, U.; Klein, M. L.; Wolf, H.; Ringsdorf, H., Structure of Hydrophilic Self-Assembled Monolayers: A Combined Scanning Tunneling Microscopy and Computer Simulation Study. *Langmuir* **1994,** *10* (11), 4116-4130.
(61) Logan, R. M.; Stickney, R. E., Simple Classical Model for the Scattering of Gas Atoms from a Solid Surface. *J. Chem. Phys.* **1966,** *44* (1), 195-201.
(62) Bennett, M. E.; Alexander, W. A.; Lu, J. W.; Troya, D.; Morris, J. R., Collisions of Polar and Nonpolar Gases with Hydrogen Bonding and Hydrocarbon Self-Assembled Monolayers. *J. Phys. Chem. C* **2008,** *112* (44), 17272-17280.
(63) Wenzel, R. N., Resistance of Solid Surfaces to Wetting by Water. *Ind. Eng. Chem.* **1936,** *28* (8), 988-994.
(64) Whitesides, G. M.; Laibinis, P. E., Wet Chemical Approaches to the Characterization of Organic Surfaces: Self-Assembled Monolayers, Wetting, and the Physical-Organic Chemistry of the Solid-Liquid Interface. *Langmuir* **1990,** *6* (1), 87-96.

Chapter 7

Summary and Concluding Remarks

7.1 Summary of Results

The main focus of the work described in this dissertation is to develop a fundamental understanding of the kinetics and mechanisms for interfacial reactions between gas-phase NO_3 and model organic surfaces. Heterogeneous reactions between NO_3 and atmospheric organic particles are of importance due to the significant role of NO_3 in environmental chemistry, such as contributing to the formation or degradation of volatile organic compounds, altering the physical or chemical properties of organic particulates, and affecting the balance between incoming and outgoing solar radiation. Therefore, constructing a detailed understanding of the reaction dynamics and pathways will enable scientists to better predict the fate of organic particles in the atmosphere.

In an effort to investigate the fundamental chemistry, self-assembled monolayers (SAMs) were employed due to their ordered nature and high reproducibility. SAMs provide a simple and stable system with the capability of changing the surface functionality. Organic surfaces that have been studied in this research include methyl-, vinyl-, and hydroxyl-terminated SAMs. A customized ultrahigh vacuum (UHV) system, used for its ability to eliminate reactions of background gases with the surface and enable the implementation of surface-sensitive instruments, helped to provide insight into this fundamental chemistry.

The investigations of reactions between NO_3 and methyl-terminated SAMs revealed that gas-phase NO_3 likely reacts with the methylene groups along the backbone of the chains at defect sites of the surface and ultimately oxidizes the sulfur atoms for short chain-length ($C<10$) SAMs.

In addition, results indicated that the reactivity of NO_3 with methyl-terminated SAMs increases with the decrease of the order of the SAMs at the expense of the oxidation of sulfur.

In contrast to the low reactivity of long-chain CH_3-SAMs upon NO_3 exposure, collisions of NO_3 with surface vinyl groups result in reactions with the initial reaction probability of $(2.3 \pm 0.5) \times 10^{-3}$. This reaction probability is about two orders of magnitude higher than that for the reaction of ozone with the same SAM. The increased reaction probability of NO_3 is likely due to the accessibility of the transition state for nitrate addition. Kinetic studies show that surface vinyl groups are consumed at the same rate as organic nitrate formation. Results from XPS analysis and electronic structure calculations indicate that the reaction is initiated by the addition of NO_3 to the carbon-carbon double bonds to form an alkyl nitrate radical that may undergo subsequent reactions, such as NO_2 addition. Even under long exposure times, there is little evidence of sulfur oxidation on the H_2C=CH-SAM, suggesting that the reactions were limited to the C=C terminus.

Studies of reactions between NO_3 and methyl-/vinyl-terminated SAMs provide information about the reactivity of NO_3 towards non-polar saturated/unsaturated surfaces. However, gas-phase studies of reactions between NO_3 and alcohols revealed that the reaction rates were comparable with reaction rates of NO_3 with unsaturated organics. In the meantime, proposed mechanisms reveal a potentially important pathway (other than electrophilic addition), hydrogen abstraction. In order to explore this mechanism, reactions involving NO_3 and surface-bound alcohols were studied employing RAIRS and XPS. The features in RAIRs including the decay in intensity of bands associated with the terminal -CH_2OH groups and the appearance of new bands centered at 1283 cm^{-1}, 1555 cm^{-1}, and 1622 cm^{-1} suggest the formation of organic nitrates or nitro-containing compounds upon NO_3 collision with the HO-SAM. The initial reaction probability for NO_3 collision with a 16-C HO-terminated SAM is determined to be $\gamma_0 = (5.9 \pm 0.6) \times 10^{-3}$. The

initial reaction probability is about a factor of three larger than that of NO_3 with the 18-C vinyl-terminated SAM, which could be due to the increase in the accessibility for NO_3 collisions by hydrogen bonding among the hydroxyl terminus. The reaction mechanism was further elucidated by an isotopic study involving DO-SAMs. Due to the low fraction of D atoms that have been exchanged with H, we failed to make a positive conclusion that the dominant reaction pathway of NO_3 with HO/DO-SAM is the hydrogen abstraction from the methylene groups. Further, results from elemental analysis of the surface prior to and after NO_3 exposure indicate that the oxidation of the HO-SAM by NO_3 radicals is isolated at the gas-solid interface. The activation energy, measured from the reaction kinetics at different surface temperature is low, which may result from the weakening of the C-H bond caused by the terminal hydrogen bonding.

Finally, the dynamics of NO_3 reactions with the 16-C HO-SAM was explored by probing the effect of NO_3 translational energy on the initial reaction probability. The reaction probability, 0.4, for the 77 kJ/mol NO_3 beam is orders of magnitude higher than that of the effusive beam of NO_3 with the same surface. The significant increase in the reaction probability could be due to the efficient energy transfer for NO_3-SAM collisions. As a result, the NO_3 molecules may penetrate through the hydrocarbon chains, which causes the increase in the probability of NO_3 abstracting hydrogen atom from $-CH_2-$ groups along the chain. Following the hydrogen abstraction, excess gas-phase NO_3 or NO_2 molecules could add to the formed alkyl radical and produce organic nitrates or peroxynitrates. Results from atomic Ar scattering experiments and water contact angle measurements suggest that the formation of interfacial nitrates leads to a less polar, more rigid and massive surface.

According to conclusions described above, two major initial pathways for NO_3 oxidizing atmospheric compounds have been considered, hydrogen abstraction at hydrocarbon bond where

the bond is weakened by substitution and NO_3 addition to carbon-carbon double bonds. Subsequent reactions following the formation of the alkyl radical after initial abstraction or addition may involve other atmospheric gases, such as O_2, water vapor. Therefore, the effects of atmospheric background gases and light on reactions between gas-phase NO_3 and SAMs have also been explored (Appendix A). It was discovered that during reactions of NO_3 with the CH_2=CH-SAM, the presence of O_2 may react with the alkyl radical formed upon addition and thus reduce the formation of nitro-containing compounds. However, co-dosing of O_2 to a HO-SAM during NO_3 exposure does not significantly affect the overall reaction. In addition, photolysis of oxidation products, organic nitrates, may play a role in the decomposition of the products, which results in the instability of surface-bound nitrates.

7.2 Atmospheric Implications

Together, all these key insights may serve as valuable benchmarks for the development of more accurate theoretical studies to comprehensively understand reactions between NO_3 and model organic surfaces and ultimately to reveal how NO_3 heterogeneously reacts with organic particles under pristine conditions. The fact that the probability of hydrogen abstraction is comparable to that of NO_3 addition to the C=C bonds may enlighten scientists in estimating lifetime of the atmospheric organics in the presence of nighttime NO_3. The molecular beam scattering studies provide evidence for an incident-energy dependent reaction mechanism for NO_3 impinging onto organic surfaces, which may assist theoretical scientist in the construction of better models for predicting the fate of organic particulates upon exposure to atmospheric NO_3.

7.3 Concluding Remarks and Future Work

SAMs have proven to be useful proxies for studying gas-surface interactions and reactions of atmospheric NO_3 with organic surfaces. The reaction is most likely initiated by either addition of NO_3 to the carbon-carbon double bonds or H abstraction from accessible hydrocarbons, resulting in the formation of alkyl nitrate radicals followed by subsequent reactions with background gases (e.g., NO_2, O_2, and H_2O). Indeed, there are many factors that may have an effect on the reaction kinetics and mechanisms, such as the energetics of the impinging NO_3, the orientation and the momentum of NO_3 molecules, possible changes in structure or functionality of the surface upon the initial reaction, and the relative concentration of present background gases.

First, for reactions of NO_3 with the vinyl SAM, tightly packed CH_2=CH- groups may prevent the majority of impinging molecules from entering the reaction coordinate prior to desorption. In addition, relatively smooth surfaces may limit the number of surface collisions (opportunities to react) prior to desorption. We could therefore create mixed SAMs and explore how monolayer roughness and reactive site accessibility affect the dynamics by intentionally introducing defects into the system. Further, gas-phase studies of NO_3 reaction with alkenes suggested reaction mechanism hallmarked by the direct addition of NO_3 across the double bond to form a five-membered ring, as shown in Figure 7.1. To further explore competing pathways (Figure 7.1) of NO_3 scattering from the H_2C=CH-SAM, scattering experiments could be performed by changing the surface temperature and the beam energy, which may help determine the reaction barriers and reveal if reactivity is limited by accommodation or if NO_3 can add to the double bond on the initial collision.

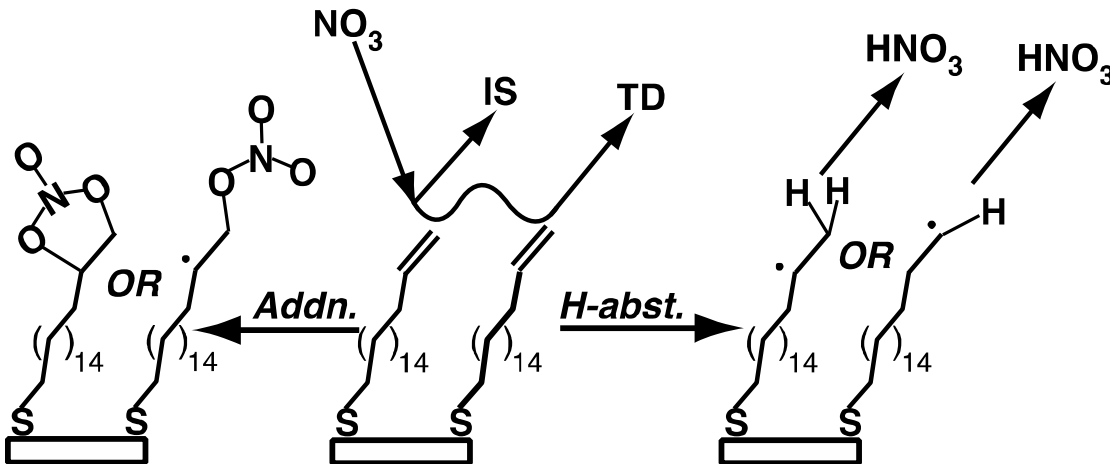

Figure 7.1. Possible NO_3 competing scattering pathways on CH_2=CH-SAMs.

In addition, since results from molecular beam scattering work performed in our lab have shown that interfacial polarity plays a major role in thermal accommodation efficiencies, we could also employ SAMs with various functionality (e.g., aldehydes, acid, amine) to learn how polar groups affect energy exchange and accommodation. Other suggestions for future work include performing the co-dosing experiment in a high-pressure chamber, employing a solar simulator with much lower-wavelength range, and even compute how the trajectory of NO_3 relative to the SAM surface, the vibrational or rotational energy of the incident NO_3 affect the initial reaction pathway.

8. Appendix: Effects of Background Gases and Light on Reactions between NO_3 and Model Organic Surfaces

8.1 Introduction

Since the research into the reaction mechanisms of NO_3 with organic compounds was pioneered by Niki and Morris in 1974,[1] over 150 organic compounds, including alkanes, alkenes, alcohols, and aldehydes, have been explored.[2-4] Atkinson and coworkers investigated rate constants for reactions of NO_3 with several branched and straight-chain alkanes at room temperature.[5] They found that the branched alkanes tended to be more reactive than the straight-chain alkanes toward NO_3, suggesting that the reactions were likely proceeded by hydrogen abstraction and radical formation. Further, in the study of the reaction mechanism of methyl butenol (an organic compound emitted by vegetation) with NO_3 radicals, Fantechi et al. did not observe significant formation of nitric acid (HNO_3) which was an expected product generated from H abstraction.[6] The only detected HNO_3 was from reactions of dinitrogen pentoxide, N_2O_5 (employed to generate laboratory NO_3), with water vapor. As such, they attributed the observed reactivity to another possible pathway, which is the addition of the NO_3 radicals to the carbon-carbon double bonds. Following that work, the reactions of NO_3 with unsaturated alkenes (in both homogeneous and heterogeneous environment) has drawn significant attention.[7-10] Bertram and coworkers explore the reaction kinetics of NO_3 with a well-ordered alkene SAM surface, in which they discovered that the uptake coefficients of NO_3 onto the organic surface were higher than that on liquid or solid organic surfaces reported previously.[11] They attributed this elevation in the uptake coefficients to the increase in the amount of the available double bonds at the interface of the SAM.[11,12] Further, Chew et al. investigated reaction kinetics of NO_3 radicals with a series of alcohols and alkenes and determined rate constants for all organic compounds involved.[13]

Surprisingly, the rate constants of NO_3 reactions with alcohols were found to be similar or even larger (for several alcohol organics) than reactions with alkenes. They proposed the mechanism to be H-atom abstraction at the carbon atom to which the hydroxyl group was attached.

So far, two major initial pathways for NO_3 reaction with atmospheric compounds have been reported, hydrogen abstraction at C-H bond where the bond has been weakened by substitution and NO_3 addition to the carbon-carbon double bonds of unsaturated organic compounds.[14,15] Subsequent reactions following the formation of alkyl radicals after the initial abstraction or addition are of importance for predicting the fate of organic particles in the atmosphere.[15,16] In a study of the temperature dependence on the reaction kinetics of NO_3 with alkanes, Bagley et al. found that the Arrhenius plots for the alkanes were linear at the lower temperatures but showed curvature at higher temperatures, which they attributed to the participation of a sequence of secondary reactions as the temperature elevated.[17] Further, Shu and coworkers examined the products generated from reactions of NO_3 with particle-associated PAHs and identified several products that were likely formed by reactions of ambient O_2 with alkyl radicals.[18] It was proposed that, in the presence of oxygen molecules, the alkyl radical formed after initial oxidation by NO_3 further reacts with O_2 and yield peroxy radicals.[14] The peroxy radical could then trigger a series of atmospheric reactions, including reactions with NO_2 to form dinitrates, reactions with NO to form ketones, and reactions with other peroxy radicals to form new alkyl radicals.[15] The previous four chapters (Chapter 3, 4, 5, and 6) focused on collisions of NO_3 with model organic surfaces in the absence of background gases (e.g. O_2, H_2O, etc.). The research described here provides preliminary insight into the effects of O_2 and water vapor on reactions between nitrate radicals and the model organic surfaces employed in the previous chapters.

As discussed in Chapter 3, 4, and 5, the major products from reactions of NO_3 with model organic surfaces are organic nitrates ($RONO_2$/$ROONO_2$) which are likely the most abundant products from nitration of organic particles in the atmosphere.[14] These organic nitrates are of significant importance in a variety of atmospheric processes, such as acting as a reservoir for NO_x (NO_2 and NO),[16] tropospheric ozone generation,[19] and ambient oxidant formation.[20] Hence, it is crucial to understand their stability and the subsequent chemistry after their formation. Others have reported that the photolysis of organic nitrates through absorption of UV radiation is a significant mechanism for atmospheric loss.[21,22] Roberts and Fajer have measured the absorption cross sections of different alkyl nitrates and found that the magnitude of cross sections increased with the carbon chain length and the degree of substitution.[23] However, the products of photolysis of organic nitrates have not been studied extensively, especially for larger organic nitrates. Here, the investigation of photolysis of reaction products generated from NO_3 collision with model organic surfaces upon green and UV radiation exposure will be described in the following sections.

8.2 Experimental

All experiments were performed in an ultrahigh vacuum (UHV) surface science instrument that enables us to expose model organic surfaces to NO_3 radicals and other atmospheric gases (e.g., O_2, H_2O), study the kinetics during the course of each exposure experiment, and investigate the effect of visible and UV radiation on the reaction products. Two capillary array dosers were employed to provide the effusive sources of NO_3 radicals and O_2 or water gas molecules. The surface-bound species were tracked *in situ* using reflection-absorption infrared spectroscopy (RAIRS), while desorbed products were monitored with a quadrupole mass spectrometer (QMS) during exposure. In addition, to examine the photolysis of reaction products, the NO_3 dosing experiments were followed by green- or UV-LED light exposure. A schematic of the instrument

is shown in Figure 8.1. The vinyl-/hydroxyl-terminated SAMs and NO_3 radicals were prepared in the same way described in Chapter 3, 4 and 5.

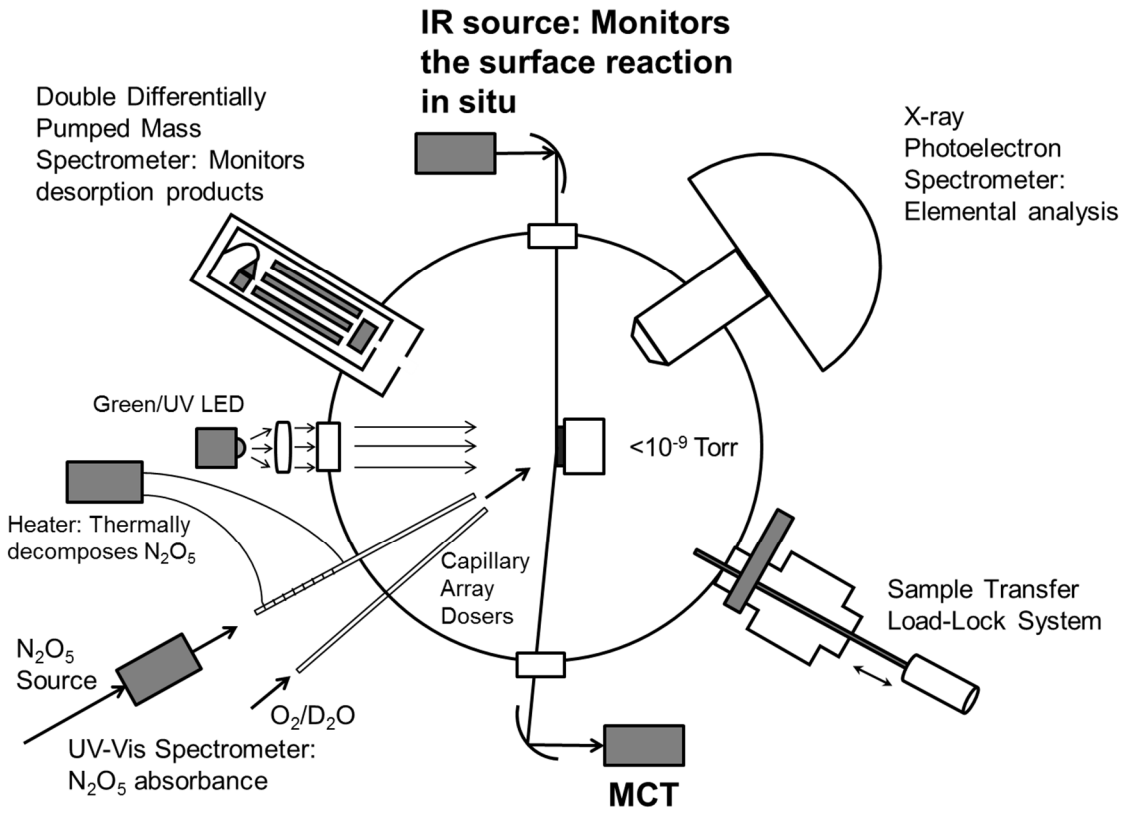

Figure 8.1. A schematic of the UHV system for surface analysis of NO_3 reactions with vinyl- and hydroxyl-terminated SAMs. All pre-exposure data were collected at a base pressure of 10^{-9} torr. N_2O_5 gas molecules were characterized by UV-Vis spectroscopy prior to the thermal decomposition at the doser. In situ RAIRS was used to monitor the NO_3 reactions with the organic surface. Other aspects are described in the text.

8.2.1 Reflection-Absorption Infrared Spectroscopy (RAIRS)

The reactions were monitored *in situ* by a Bruker IFS 66v/S spectrometer and a MCT detector in a glancing angle position.[24] Each spectrum was collected by measuring the absorbance of reflected p-polarized IR radiation from a SiC globar at an incident angle of ~86˚ relative to the surface normal through a differentially pumped KBr window. All spectra shown here were taken from the average of 100 scans with 2 cm^{-1} resolution.

8.2.2 Co-dosing Experiments and Visible/UV Radiation Exposure

Oxygen was obtained from Airgas, Inc and directly used in the co-dosing experiments. Deuterated Water (D_2O) was purchased from Sigma-Aldrich and used without further purification. O_2 or D_2O was introduced into the UHV chamber through a secondary doser installed adjacent to the primary all-glass capillary doser. The green- (533 nm) or UV-LED light (365 nm) was concentrated at the sample via a focusing lens. For the LED exposure experiments, the focusing beam shined on the examined surfaces through a quartz window. The power density of the LED was estimated from the power of the LED (1804 mW for the green-LED and 1200 mW for the UV-LED), the viewing angle of the radiation cone (100° for the green-LED and 115° for the UV-LED), and the distance between the LED source and the sample (4.13 ± 0.95 cm for the green-LED and 3.07 ± 1.33 cm for the UV-LED). The theoretical power densities of the green- and UV-LED are 23.8 ± 1.6 mW cm^{-2} and 16.5 ± 2.1 mW cm^{-2}, respectively.

8.2.3 Water Contact Angle Measurements

Contact angle measurements were performed using an FTA 200 Contact Angle Analyzer (First Ten Angstroms, Portsmouth, VA) with a sessile drop technique. The original HO-SAM or H_2C=CH-SAM and the surfaces after reactions were placed on an adjustable platform. Approximately 5 μL of Milli-Q water (Millipore Gradient A10, Esker Laboratories, Virginia Tech) was then dropped on the surfaces using a 3 mL 22 gauge syringe. For the contact angle analysis, a single frame movie was recorded using a video CCD camera followed by fitting a mathematical expression to the shape of the drop. The contact angle was then calculated through the slope of the tangent to the drop at the liquid-solid-vapor interface (FTA Operator's and Installation Manuals,

revision 2.0, May 30, 1997). For the gold slides employed in this chapter (1 in × 1 in), each water contact angle was averaged from four measurements.

8.3 Results and Discussion

Reaction kinetics of vinyl- and hydroxyl-terminated SAMs with NO_3 radicals in the presence of O_2 or D_2O was investigated by monitoring changes in the vibrational modes associated with the surface-bound functional groups using *in situ* RAIRS. During the dosing experiments, the green-LED or the UV-LED was shining on the surface to explore the effect of photon exposure on NO_3 reactions. Further, photolysis of reaction products was examined post exposure. Finally, the wettability of surfaces after reactions was studied with water contact angle measurements.

8.3.1 RAIR Characterization of H_2C=CH-SAM during NO_3 exposure in the presence of O_2 or D_2O

Similarly to the experiments described in Chapter 3, the 18 C vinyl-terminated SAM was exposed to NO_3 while simultaneously co-dosing with O_2. The spectrum (a) in Figure 8.2 exhibits the RAIR data for the original 18C vinyl-terminated SAM prior to NO_3 and O_2 exposure. Following the initial characterization, the vinyl-terminated SAM was exposed to NO_3 and O_2 gases. In this experiment, the original SAM was used as the background such that negative features in the spectra indicate the removal of modes associated with the carbon-carbon double bonds and positive bands reveal an increase in absorbance or the development of new modes. The spectra (b) and (c) in Figure 8.2 are the difference spectra of the monolayer after exposure of NO_3 and O_2. As discussed in Chapter 3, all bands associated with the double bonds decrease in intensity and the new bands at 1649 cm^{-1}, 1555 cm^{-1}, 1283 cm^{-1}, and 850 cm^{-1} indicate that the reaction between NO_3 and the H_2C=CH-SAM surface results in the formation of organic nitrates and nitro-

containing compounds. While exposing the same surface to NO_3 in the presence of O_2, quite similar features were observed. However, the intensities of bands at 1649 cm^{-1}, 1283 cm^{-1}, and 850 cm^{-1} in spectrum (b) are smaller than that the intensities of the same bands in spectrum (a), which may result from the reduced concentration of NO_3 in the presence of O_2. In addition, the absorbance of the band at 1555 cm^{-1} in spectrum (b) appears to be much smaller than that of the same band in spectrum (c), which is likely due to reactions of alkyl nitrate radicals (formed from addition of NO_3 to the double bonds) with O_2 that prevent the alkyl radical from reacting with NO_2 to yield nitro-containing compounds.[14] Further, a new broad band at ~1000 cm^{-1}, that is likely associated with a C-O stretching mode, suggests the formation of ethers as a result of reactions between O_2 and the alkyl radicals.[16,25]

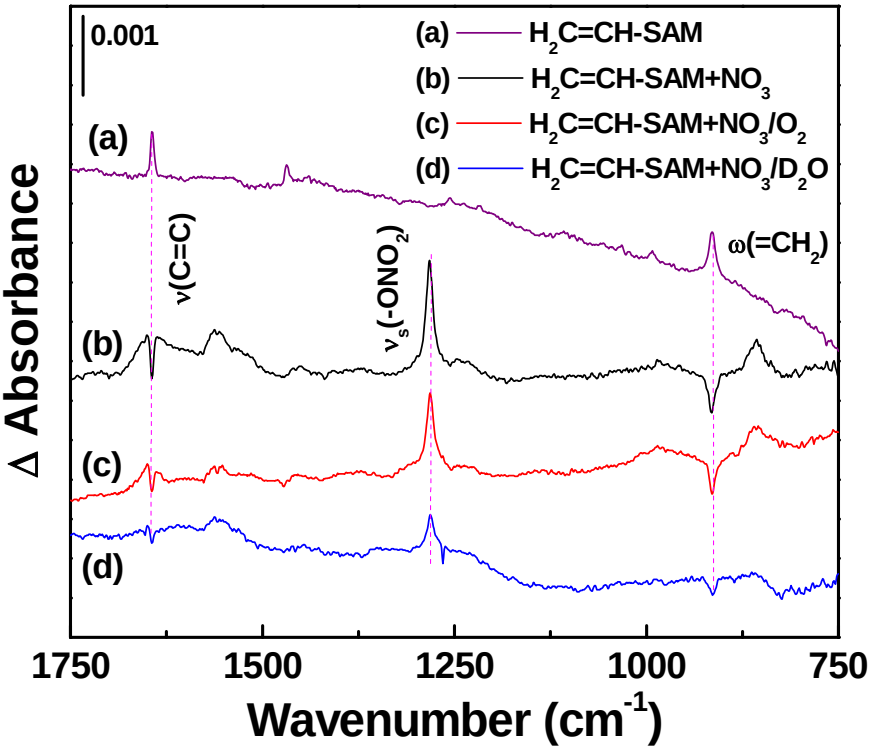

Figure 8.2. Reflection-absorption infrared difference spectra of an 18C vinyl-terminated SAM exposed to NO_3 in the presence of O_2 or D_2O. The spectrum (a) shown on top in purple is that of the SAM prior to NO_3 exposure using a clean Au sample as the background. After the surface exposed to NO_3/O_2 or NO_3/D_2O, the spectra (c) and (d) show that modes associated with the C=C moiety decrease and new modes emerge. The background for this scan is the original pre-exposure spectrum (blue). For comparison, the spectrum (b) shows an 18C vinyl-terminated SAM after 5000 L of NO_3 exposure (black).

When D_2O was co-dosed with NO_3, the features observed in the RAIR spectrum (Figure 8.2 (d)) were similar to that of spectrum (b) which was taken during reactions of the H_2C=CH-SAM with NO_3. In addition, the intensities of the bands (spectrum (d)) at 1649 cm^{-1}, 1555 cm^{-1}, 1283 cm^{-1}, and 850 cm^{-1} are much lower than that of the same bands in spectrum (b), which may result from the reduced reactivity of NO_3 with the SAM in the presence of D_2O. D_2O was expected to affect the NO_3 oxidation by reacting with N_2O_5 and forming nitric acid (HNO_3).[16] As a result, the NO_3 concentration would decrease according to Le Chatelier's principle (NO_3 was produced through thermal decomposition of N_2O_5), which decrease the reaction rate of NO_3 with the SAM surface accordingly. However, the flux of either O_2 or D_2O employed in these experiments is very small compared to their atmospheric abundance. Although the presence of O_2 or D_2O showed little effect on reactions between the surface and NO_3, further studies near atmospheric pressures are needed to more efficiently explore the role of O_2 or water vapor in the oxidation of atmospheric organics by NO_3 radicals.

8.3.2 Reactions of Hydroxyl-terminated SAMs with NO_3 in the presence of O_2 or D_2O

During the reaction of the 16-C HO-SAM with NO_3 in the presence of O_2 or D_2O, we observed the same features in RAIRS (Spectra (b) and (c) in Figure 8.3) as we did during the reaction in the absence of O_2 or D_2O (see Chapter 4): all bands associated with the terminal -CH_2OH groups decrease in intensity and new bands assigned to vibrational modes of organic nitrates emerge. Further, the reaction kinetics of the HO-SAM with NO_3 in the presence of O_2 was obtained from the parameters used for fitting the curve that tracks how the integrated absorbance of the C-O stretching mode changes as a function of the exposure time (Figure 8.4). Similar to the method employed in Chapter 4, the pseudo first-order rate constant for the decay of the C-O band is 1.8×10^{-3} s^{-1}.

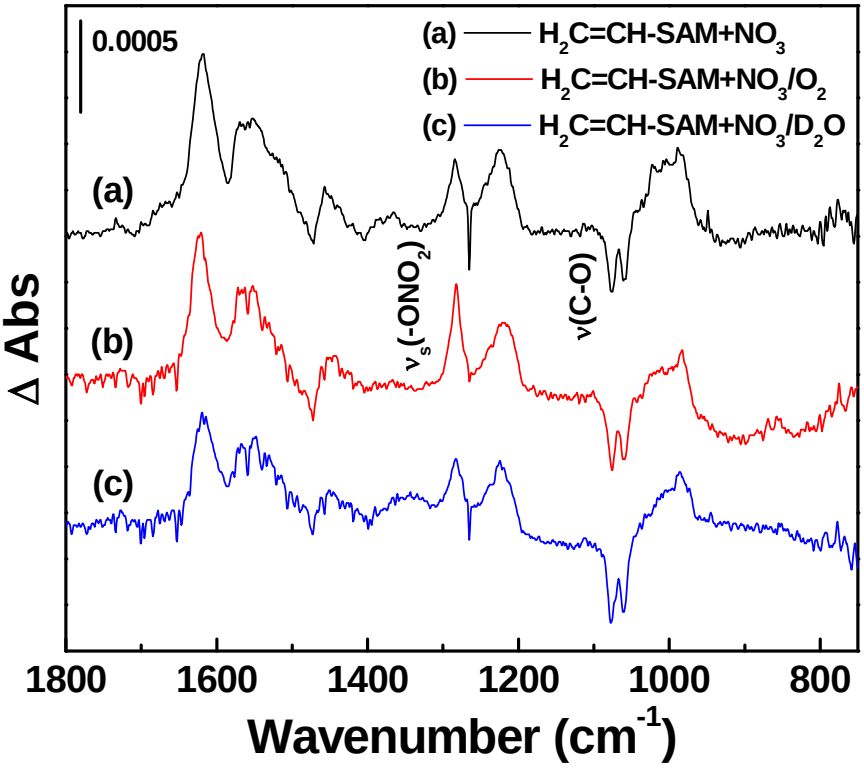

Figure 8.3. Reflection-absorption infrared difference spectra of a 16C HO-SAM exposed to NO_3 in the presence of O_2 or D_2O. The spectrum (a) shown on top in black is that of the SAM upon NO_3 exposure. After the surface exposed to NO_3/O_2 or NO_3/D_2O, the spectra (b) and (c) show that the C-O stretching mode associated with the $-CH_2OH$ groups decreases and new modes emerge. The background for these spectra is the original pre-exposure spectrum (spectrum of the HO-SAM).

Previous studies of gas-phase reactions involving NO_3 and organic compounds suggest that O_2 could react with alkyl radicals (formed upon hydrogen abstraction by NO_3) to yield peroxyl radicals.[26-28] As a result, the product is likely $ROONO_2$ (NO_3 is generated accompanied with NO_2 due to the thermal decomposition of N_2O_5).[14,28] The stretching modes of $-NO_2$ or -CO- in $ROONO_2$ or $RONO_2$ may be too similar to be resolved by our IR spectrometer.[26] As such, isotopic experiments are required to distinguish the IR features assigned to the proposed products. In addition, the role of O_2 or D_2O in the reaction between NO_3 and the HO-SAM may be further explored in the environments near atmospheric pressures.

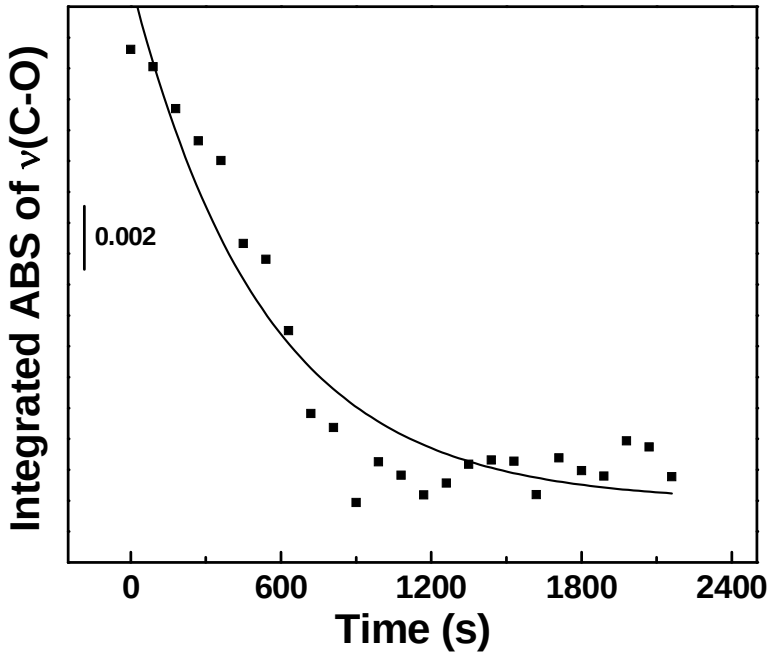

Figure 8.4. Integrated absorbance for ν(CO) at 1060 cm^{-1} and 1076 cm^{-1} versus time during NO_3 and O_2 exposure. The fitting curve follows the first-order kinetics.

8.3.3 The Effect of Light on Reactions of the HO-SAM with NO_3 Radicals

As shown in Figure 8.5 and Figure 8.6, the RAIRS feature in the region of 925-1050 cm^{-1} during NO_3 exposure while shining green- or UV-LED on the HO-SAM surface was decomposed into four Lorentzian peaks, which are centered at 975 cm^{-1}, 987 cm^{-1}, 1005 cm^{-1}, and 1028 cm^{-1} respectively.[25,29] These four bands likely arise from the red shift of the C-O stretching mode of the terminal -CH_2OH groups due to addition of electron-withdrawing groups (-ONO_2 or -NO_2) during NO_3 reactions.[30] The bands at 975 cm^{-1} and 987 cm^{-1} are assigned to the two C-O stretching modes of the -CH(OH)-ONO_2 groups. The vibrational frequency of the C-ONO_2 stretching (975 cm^{-1}) red shifts more than that of the C-OH stretching (987 cm^{-1}) because of the presence of the electron-withdrawing -ONO_2 in the former one.[30,31] In a study of IR spectra of some organic nitrates, Carrington found that the band of the ν(C-O) mode in the -CH_2ONO_2 groups located at ~1030

cm^{-1} in IR.[29] Thus, the band at 1028 cm^{-1} is likely due to the formation of -CH_2-ONO_2 upon addition of NO_2 to the radical generated by hydrogen abstraction at the -CH_2OH terminus. In addition, since the presence of the electron-withdrawing group at the C-O bond would redshift the ν(C-O) mode, the band at 1005 cm^{-1} is assigned to the C-O stretching of the -CH_2-O-ONO_2 group.[30]

Figure 8.5 shows RAIR spectra in the region of 925-1050 cm^{-1} during exposure of the HO-SAM to NO_3 while shining green LED on the surface. Before the LED power was on, the RAIR spectra of the HO-SAM upon NO_3 exposure were shown in Figure 8.5 (A). It can be clearly seen that all four product peaks increase after 20 min NO_3 exposure, suggesting the formation of nitrates due to NO_3 oxidation. Then we shined green LED on the surface to see how the visible light affected the reaction products that were characterized by IR in this region. After 40 min of green LED exposure, three bands at 975 cm^{-1}, 1005 cm^{-1}, and 1028 cm^{-1} decreased in intensity, but the band at 987 cm^{-1} persisted. The significant decrease of the three bands is likely due to photolysis of organic nitrates by the green light while the -CHOH group in the alcohol nitrate does not undergo photodissociation.

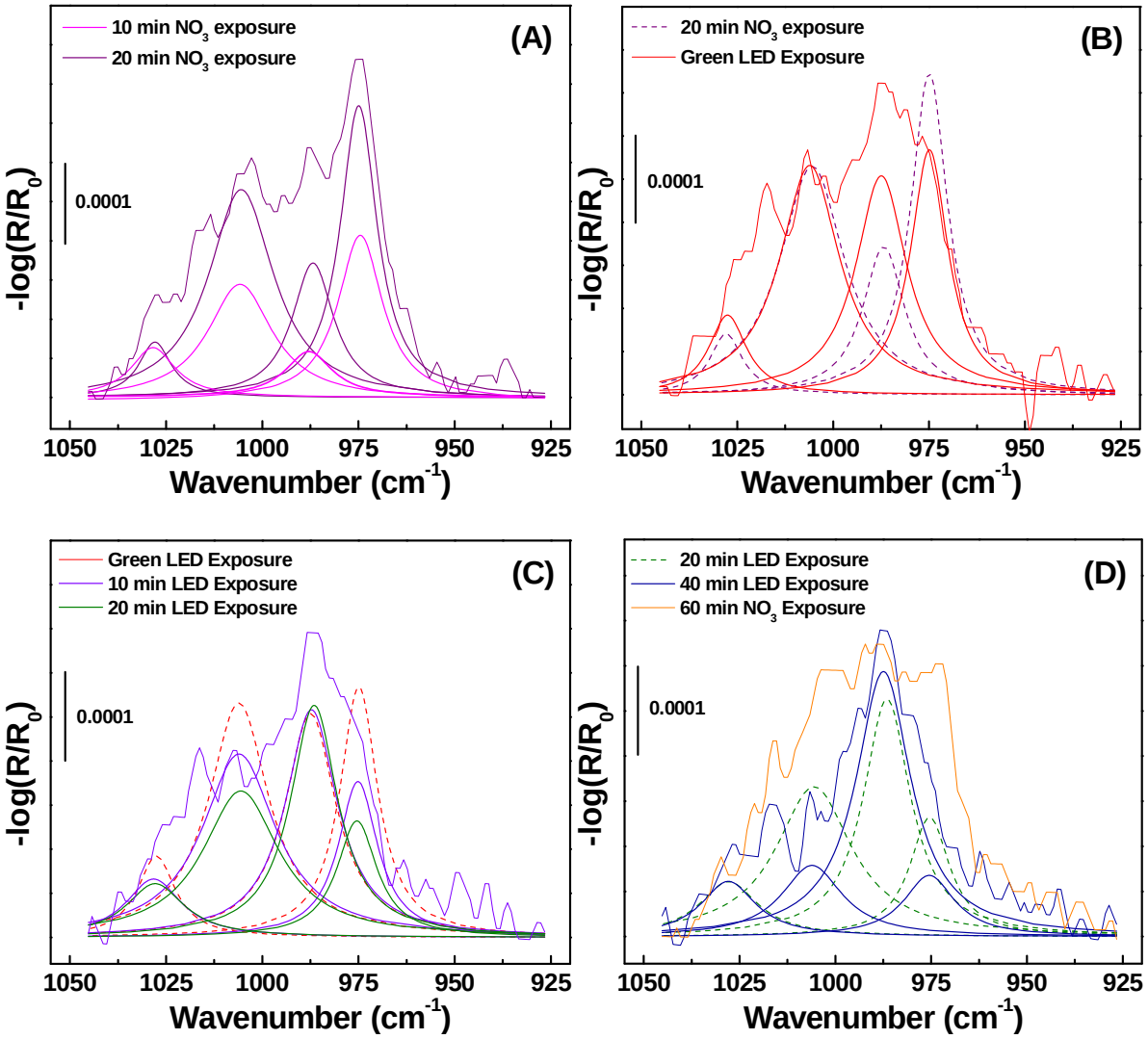

Figure 8.5. RAIR spectra of the HO-SAM in the region of 925-1050 cm^{-1} (A) after 10 min (pink solid lines) and 20 min (purple solid lines) of NO_3 exposure; (B) at the beginning of shining green LED onto to the surface during NO_3 exposure (red solid lines); (C) after 10 min (violet solid lines) and 20 min (green solid lines) of green LED exposure during NO_3 reactions; (D) after 40 min of green LED exposure during NO_3 reactions (blue solid lines) and after 60 min of NO_3 exposure to the HO-SAM in the dark (orange solid line).

Similarly, the UV LED light plays a role in the degradation of organic nitrates generated upon NO_3 exposure. After shining the surface with UV LED for 7 min, all bands assigned to the C-O stretching of the $RONO_2$ or $ROONO_2$ groups decrease in intensity, as shown in Figure 8.6 (C). However, the absorbance of the band at 987 cm^{-1} due to the C-OH stretching does not change

much even after 25 min of UV LED exposure, which may be attributed to the high stability of the alcoholic C-O bond in the presence of UV light. Further, the organic nitrates have been significantly consumed only after 25 min exposure of UV LED. However, it takes 40 min for the green LED to decompose the organic nitrates by a considerable amount. The higher rate of photodissociation of organic nitrates by the UV radiation than photolysis by the green light is consistent with the fact that the absorption cross-section of organic nitrates reaches the maximum slightly below 200 nm but dramatically decreases beyond the UV region (higher than 400 nm).[20]

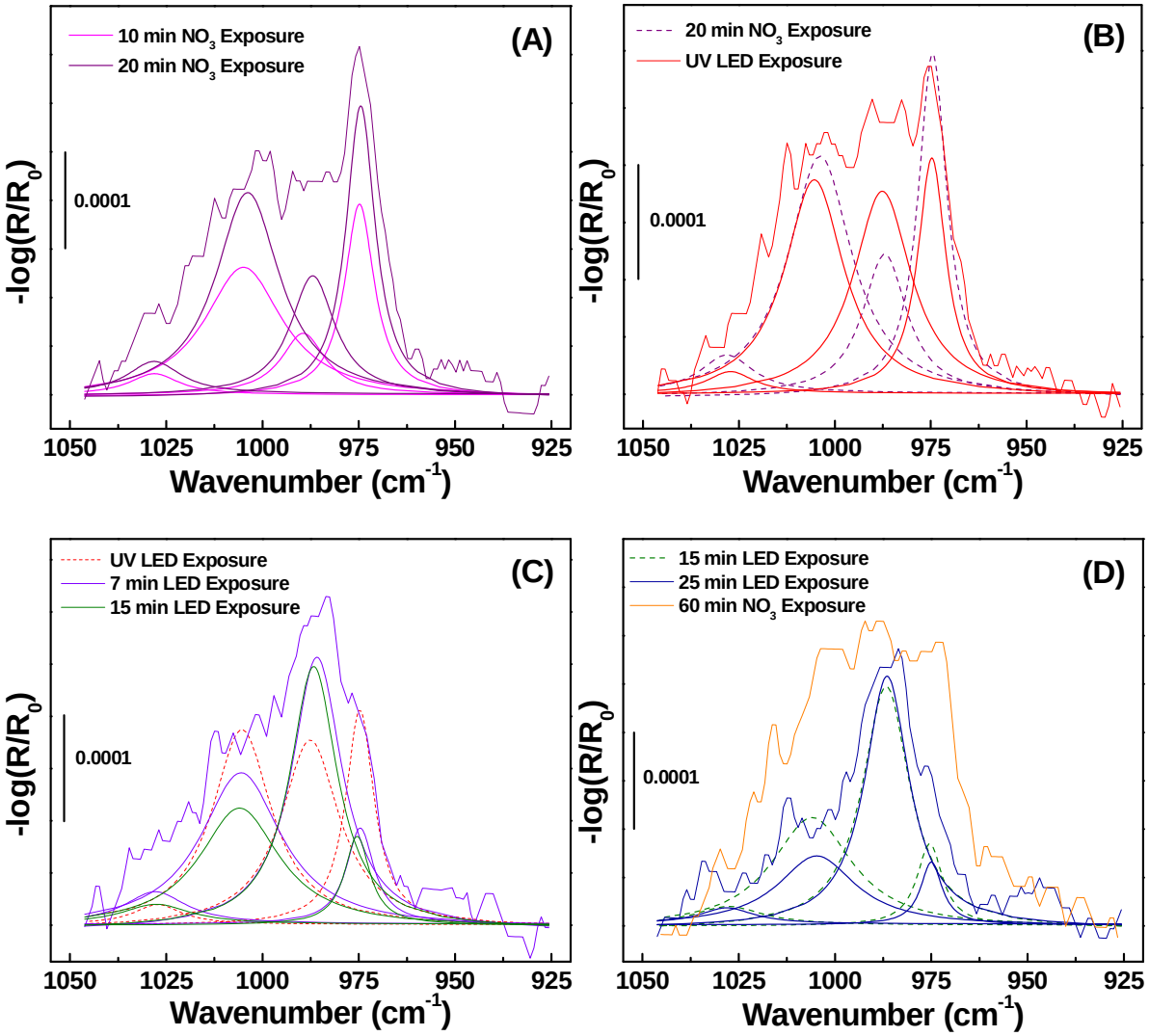

Figure 8.6. RAIR spectra of the HO-SAM in the region of 925-1050 cm^{-1} (A) after 10 min (pink solid lines) and 20 min (purple solid lines) of NO_3 exposure; (B) at the beginning of shining UV LED onto to the surface during NO_3 exposure (red solid lines); (C) after 7 min (violet solid lines) and 15 min (green solid lines) of UV LED exposure during NO_3 reactions; (D) after 25 min of UV LED exposure during NO_3 reactions (blue solid lines) and after 60 min of NO_3 exposure to the HO-SAM in the dark (orange solid line).

8.3.4 Stability of Reaction Products formed from NO_3 collision with the H_2C=CH-SAM and the HO-SAM

Figure 8.7 shows RAIR spectra for an 18-C H_2C=CH-SAM prior to (spectrum a) and after NO_3 exposure (spectrum b). To explore the stability of reaction products, the sample was placed in air for 15 min (spectrum c) and 45 min (spectrum d) before transferring back into the UHV chamber. As shown in Figure 8.7, the emergence of the bands at 1283 cm^{-1} and 850 cm^{-1} suggests the formation of organic nitrates during reactions of NO_3 with the H_2C=CH-SAM.[24] After the sample was placed in air for 45 min, the preservation of the peak intensity at 1280 cm^{-1} and 850 cm^{-1} indicates that the formed organic nitrates are stable in the air for at least 45 min.

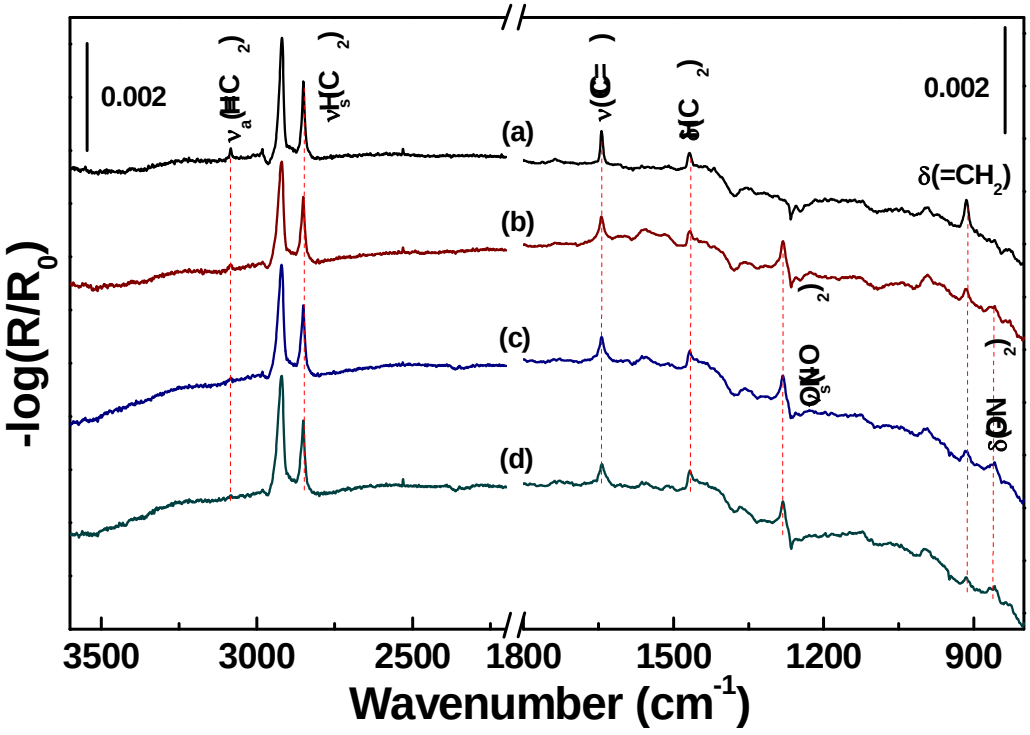

Figure 8.7. Reflection-absorption infrared spectra of an 18-C vinyl-terminated (Au-S-$(CH_2)_{16}CH$=CH_2) SAM on Au (a) before NO_3 exposure, (b) after 1h of NO_3 exposure, (c) sitting in air for 15 min after NO_3 exposure, and (d) sitting in air for 45 min after NO_3 exposure. The most intense IR active modes are highlighted as $\nu_a(CH_2)$, $\nu_s(CH_2)$, ν(C=C), $\delta(CH_2)$, $\delta(=CH_2)$, $\nu_s(-ONO_2)$, and $\delta(-ONO_2)$.

Figure 8.8 shows RAIR spectra for a 16-C HO-SAM prior to (spectrum a) and after NO_3 exposure (spectrum b). To examine the stability of reaction products, the sample was taken out of the UHV chamber, placed in air for some amount of time, and then put back into the chamber for RAIRS collection. During reactions of NO_3 with the HO-SAM, the appearance of the new bands at 1621 cm^{-1}, 1552 cm^{-1}, 1283 cm^{-1}, 1223 cm^{-1} suggests the formation of organic nitrates or nitro-containing compounds. After the sample was placed in the air for 15 min (spectrum c), the preservation of the peak intensity at 1283 cm^{-1} indicates that the organic nitrates are stable in the air.[24] However, the modes at 1552 cm^{-1} and 1223 cm^{-1} decrease significantly in intensity, which suggests the instability of the nitro-containing organics formed on the surface upon NO_3 reaction. The nitro-containing organics may be formed through the reaction, NO_2 + HO-·CH-$(CH_2)_{15}$SAu → HO-$HCNO_2$-$(CH_2)_{15}$SAu, resulting in the formation of a product with -OH and -NO_2 attached to the same carbon atom simultaneously. The higher electron affinity of -OH than that of -NO_2 may weaken the C-N bond, and thus making the nitro group unstable.[30] In addition, the consumption of nitro-containing compounds may lead to the reorientation of the surface-bound organic nitrates. As a result, the transition dipole moment of the ν_a(-ONO_2) mode could be parallel to the surface, which causes the band at 1621 cm^{-1} invisible in RAIRS according to the surface selection rule.[32] Spectrum d in Figure 8.8 shows a small band at ~1720 cm^{-1}, suggesting formation of the carbonyl groups during the exposure of the surface in the atmosphere.[25] Further, the small difference in features between spectrum c and spectrum d reveals that the reaction of the nitrogen-containing products with the atmospheric gases primarily takes place in the first 15 min and the surface-bound organic nitrates are stable for at least 45 min.

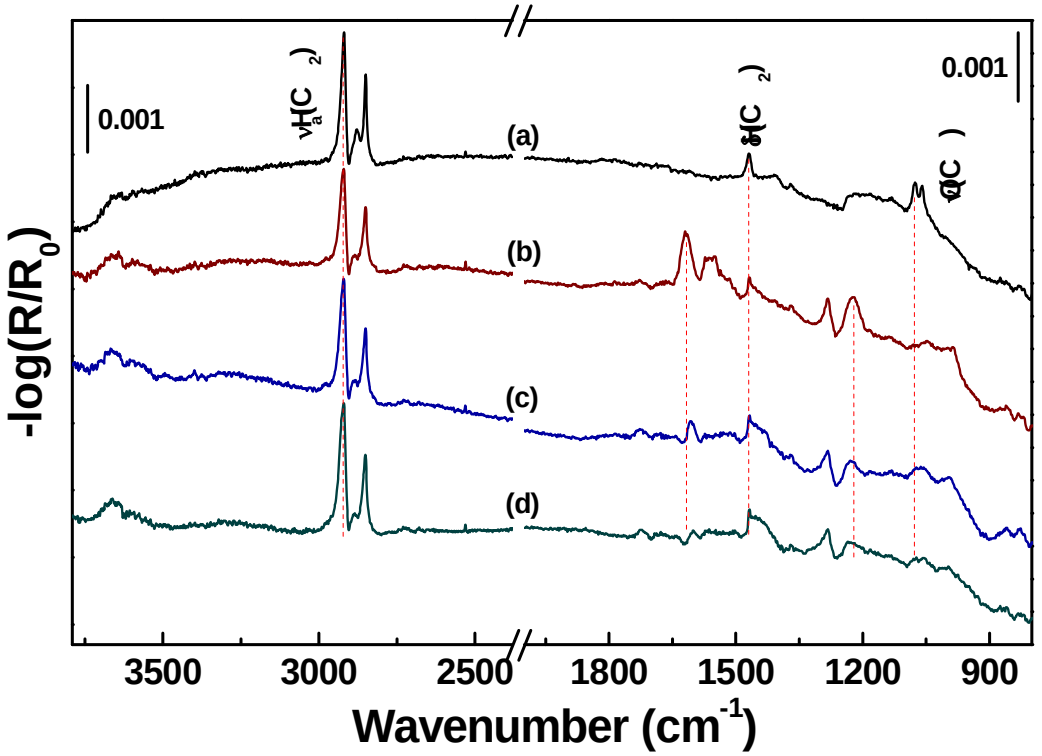

Figure 8.8. Reflection-absorption infrared spectra of a 16-C hydroxyl-terminated (Au-S-$(CH_2)_{16}OH$) SAM on Au (a) before NO_3 exposure, (b) after 1h of NO_3 exposure, (c) sitting in air for 15 min after NO_3 exposure, and (d) sitting in air for 45 min after NO_3 exposure. The most intense IR active modes are highlighted as $\nu_a(CH_2)$, $\delta(CH_2)$, and $\nu(CO)$.

8.3.5 The Effect of Air on the Wettability of the HO-SAM after NO_3 Reactions

The wettability provides local details of interfacial structure at the angstrom scale.[33] Figure 8.9 shows photographs of a water droplet on a HO-SAM (Figure 8.9 (a)), the HO-SAM after NO_3 reaction (Figure 8.9 (b)), the reacted SAM after atmospheric exposure (Figure 8.9 (c)), and the HO-SAM after NO_3 exposure while co-dosing with O_2 (Figure 8.9 (d)). The static water contact angle of a 16-C HO-SAM, θ_{water}, is 30 ± 1°. After the HO-SAM reaction with NO_3, the static water contact angle was measured to be 60 ± 6°, indicating that the gas-solid interface changes from a hydrophilic surface to a more hydrophobic one.[34] The resultant hydrophobic surface demonstrates a decrease in the polarity of functional groups at the interface, which may be due to the change in

the surface roughness.[35] Wenzel found that a rough surface was wetted more rapidly than a smooth surface. The formation of organic nitrate could decrease the amount of hydrogen-bonded clusters (formed by hydrogen bonding among -OH groups of the original HO-SAM) on the surface which may decrease the surface roughness.[36] For further exploration, the surface roughness can be measured with atomic force microscopy (AFM).[37] The reacted surface was then placed in the air for days before measuring the water contact angle (74 ± 4°), as shown in Figure 8.9 (c). The slight increase in θ_{water} compared with that of the reacted SAM (Figure 8.9 (b)) may be due to the adsorption of organic contamination in the atmosphere.

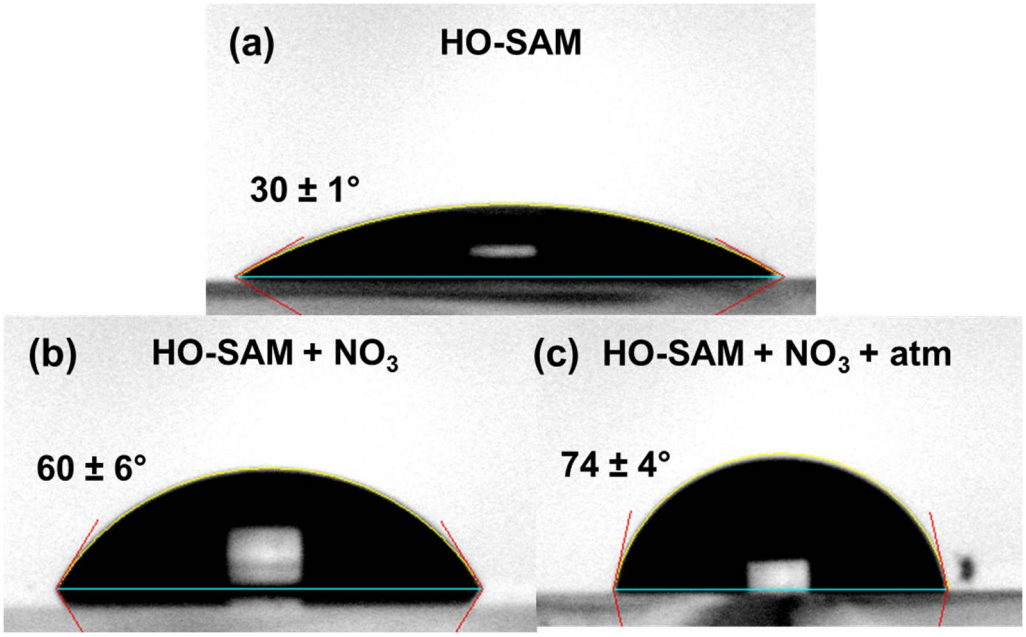

Figure 8.9. Photographs of a water droplet on (a) the HO-SAM, (b) the HO-SAM after NO_3 reactions, and (c) the post-reaction SAM surface after exposing to the atmosphere. The contact angles are averaged over four measurements.

8.4 Summary

The effects of atmospheric background gases and light on reactions between gas-phase NO_3 and model organic surfaces have been explored. It was discovered that during reactions of

NO_3 with the vinyl-terminated SAM, O_2 may react with the alkyl radical (generated from NO_3 addition to the double bonds) and thus reduce the formation of nitro-containing compound. However, the presence of O_2 does not have significant effect on reactions of a hydroxyl-terminated SAM with NO_3. In addition, photolysis of organic nitrates formed upon NO_3 oxidation may play a role in the decomposition of the products. Although the effects of O_2 or light on NO_3-surface reactions need further investigations, such as performing the co-dosing experiment in an environment near atmospheric pressures, employing a solar simulator with much lower wavelengths, the results presented in this Appendix provide benchmarks for future studies of atmospheric reactions involving NO_3 and organic surfaces, including studies of reaction paths of these reactions in the presence of O_2 and solar radiation and the fate of reaction products ($RONO_2$ or $ROONO_2$).

REFERENCES

(1) Morris, E.; Niki, H., Reaction of the Nitrate Radical with Acetaldehyde and Propylene. *J. Phys. Chem.* **1974,** *78* (13), 1337-1338.

(2) Lee, L.; Wooldridge, P.; Nah, T.; Wilson, K.; Cohen, R., Observation of Rates and Products in the Reaction of NO_3 with Submicron Squalane and Squalene Aerosol. *Phys. Chem. Chem. Phys.* **2013,** *15* (3), 882-892.

(3) Jariyasopit, N.; Zimmermann, K.; Schrlau, J.; Arey, J.; Atkinson, R.; Yu, T.-W.; Dashwood, R. H.; Tao, S.; Simonich, S. L. M., Heterogeneous Reactions of Particulate Matter-Bound PAHs and NPAHs with NO_3/N_2O_5, OH Radicals, and O_3 under Simulated Long-Range Atmospheric Transport Conditions: Reactivity and Mutagenicity. *Environ. Sci. Technol.* **2014,** *48* (17), 10155-10164.

(4) D'Anna, B.; Andresen, O.; Gefen, Z.; Nielsen, C. J., Kinetic Study of OH and NO_3 Radical Reactions with 14 Aliphatic Aldehydes. *Phys. Chem. Chem. Phys.* **2001,** *3* (15), 3057-3063.

(5) Aschmann, S. M.; Atkinson, R., Rate Constants for the Reactions of the NO_3 Radical with Alkanes at 296 ± 2 K. *Atmos. Environ.* **1995,** *29* (17), 2311-2316.
(6) Fantechi, G.; Jensen, N. R.; Hjorth, J.; Peeters, J., Mechanistic Studies of the Atmospheric Oxidation of Methyl Butenol by Oh Radicals, Ozone and NO_3 Radicals. *Atmos. Environ.* **1998,** *32* (20), 3547-3556.
(7) Shiraiwa, M.; Poschl, U.; Knopf, D. A., Multiphase Chamical Kinetics of No_3 Radicals Reacting with Organic Aerosol Components from Biomass Burning. *Environ. Sci. Technol.* **2012,** *46*, 6630-6636.
(8) Zhao, Z. J.; Husainy, S.; Stoudemayer, C. T.; Smith, G. D., Reactive Uptake of NO_3 Radicals by Unsaturated Fatty Acid Particles. *Phys. Chem. Chem. Phys.* **2011,** *13*, 17809-17817.
(9) Xiao, S.; Bertram, A. K., Reactive Uptake Kinetics of No_3 on Multicomponent and Multiphase Organic Mixtures Containing Unsaturated and Saturated Organics. *Phys. Chem. Chem. Phys.* **2011,** *13* (14), 6628-6636.
(10) Kwan, A.; Chan, A.; Ng, N.; Kjærgaard, H. G.; Seinfeld, J.; Wennberg, P., Peroxy Radical Chemistry and OH Radical Production During the NO_3-Initiated Oxidation of Isoprene. *Atmos. Chem. Phys.* **2012,** *12* (16), 7499-7515.
(11) Gross, S.; Bertram, A. K., Products and Kinetics of the Reactions of an Alkane Monolayer and a Terminal Alkene Monolayer with NO_3 Radicals. *J. Geophys. Res.* **2009,** *114* (D2), 1-14.
(12) Moise, T.; Talukdar, R. K.; Frost, G. J.; Fox, R. W.; Rudich, Y., Reactive Uptake of NO_3 by Liquid and Frozen Organics. *J. Geophys. Res.* **2002,** *107* (D2), 4014.
(13) Chew, A. A.; Atkinson, R.; Aschmann, S. M., Kinetics of the Gas-Phase Reactions of NO_3 Radicals with a Series of Alcohols, Glycol Ethers, Ethers and Chloroalkenes. *J. Chem. Soc., Faraday Trans.* **1998,** *94* (8), 1083-1089.
(14) Finlayson-Pitts, B. J.; Pitts, J. N., *Chemistry of the Upper and Lower Atmosphere: Theory, Experiments, and Applications*. Academic Press: San Diego, CA, 2000.
(15) Wayne, R. P.; Barnes, I.; Biggs, P.; Burrows, J. P.; Canosamas, C. E.; Hjorth, J.; Lebras, G.; Moortgat, G. K.; Perner, D.; Poulet, G.; Restelli, G.; Sidebottom, H., The Nitrate Radical - Physics, Chemistry, and the Atmosphere. *Atmos. Environ. A-Gen.* **1991,** *25* (1), 1-203.
(16) Seinfeld, J. H.; Pandis, S. N., *Atmospheric Chemistry and Physics: From Air Pollution to Climate Change*. John Wiley & Sons: 2012.
(17) Bagley, J. A.; Canosa-Mas, C.; Little, M. R.; Parr, A. D.; Smith, S. J.; Waygood, S. J.; Wayne, R. P., Temperature Dependence of Reactions of the Nitrate Radical with Alkanes. *J. Chem. Soc., Faraday Trans.* **1990,** *86* (12), 2109-2114.
(18) Zhang, Y.; Yang, B.; Gan, J.; Liu, C.; Shu, X.; Shu, J., Nitration of Particle-Associated PAHs and Their Derivatives (Nitro-, Oxy-, and Hydroxy-PAHs) with NO_3 Radicals. *Atmos. Environ.* **2011,** *45* (15), 2515-2521.
(19) Moreno, A.; Salgado, M. S.; Martín, M. P.; Martínez, E.; Cabañas, B., Kinetic Study of the Gas Phase Reactions of a Series of Alcohols with the NO_3 Radical. *J. Phys. Chem. A* **2012,** *116* (42), 10383-10389.
(20) Roberts, J. M., The Atmospheric Chemistry of Organic Nitrates. *Atmos. Environ. A* **1990,** *24* (2), 243-287.

(21) Csizmadia, V. M.; Houlden, S. A.; Koves, G. J.; Boggs, J. M.; Csizmadia, I. G., Stereochemistry and Ultraviolet Spectra of Simple Nitrate Esters. *J Org. Chem.* **1973,** *38* (13), 2281-2287.
(22) Goodeve, J. W., The Absorption Spectra of Ethyl Nitrate, Ethyl Nitrite, and Nitroethane. *Trans. Faraday Soc.* **1934,** *30* (0), 504-508.
(23) Roberts, J. M.; Fajer, R. W., Uv Absorption Cross Sections of Organic Nitrates of Potential Atmospheric Importance and Estimation of Atmospheric Lifetimes. *Environ. Sci. Technol.* **1989,** *23* (8), 945-951.
(24) Zhang, Y.; Chapleski, R. C.; Lu, J. W.; Rockhold, T. H.; Troya, D.; Morris, J. R., Gas-Surface Reactions of Nitrate Radicals with Vinyl-Terminated Self-Assembled Monolayers. *Phys. Chem. Chem. Phys.* **2014,** *16* (31), 16659-16670.
(25) Socrates, G., *Infrared and Raman Characteristic Group Frequencies: Tables and Charts*. 3 rd ed. ed.; John Wiley & Sons, Inc.: New York, 2001.
(26) Wängberg, I.; Barnes, I.; Becker, K. H., Product and Mechanistic Study of the Reaction of NO_3 Radicals with A-Pinene. *Environ. Sci. Technol.* **1997,** *31* (7), 2130-2135.
(27) Goliff, W. S.; Stockwell, W. R.; Lawson, C. V., The Regional Atmospheric Chemistry Mechanism, Version 2. *Atmos. Environ.* **2013,** *68* (0), 174-185.
(28) Wine, P. H.; Nicovich, J. M., Atmospheric Radical Chemistry. In *Encyclopedia of Radicals in Chemistry, Biology and Materials*, John Wiley & Sons, Ltd: 2012.
(29) Carrington, R. A. G., The Infra-Red Spectra of Some Organic Nitrates. *Spectrochimica Acta* **1960,** *16* (11–12), 1279-1293.
(30) Gordy, W., A Relation between Bond Force Constants, Bond Orders, Bond Lengths, and the Electronegativities of the Bonded Atoms. *J. Chem. Phys.* **1946,** *14* (5), 305-320.
(31) Ehbrecht, M.; Huisken, F., Vibrational Spectroscopy of Ethanol Molecules and Complexes Selectively Prepared in the Gas Phase and Adsorbed on Large Argon Clusters. *J. Phys. Chem. A* **1997,** *101* (42), 7768-7777.
(32) Greenler, R. G., Infrared Study of Adsorbed Molecules on Metal Surfaces by Reflection Techniques. *J. Chem. Phys.* **1966,** *44* (1), 310-315.
(33) Wenzel, R. N., Resistance of Solid Surfaces to Wetting by Water. *Ind. Eng. Chem.* **1936,** *28* (8), 988-994.
(34) Whitesides, G. M.; Laibinis, P. E., Wet Chemical Approaches to the Characterization of Organic Surfaces: Self-Assembled Monolayers, Wetting, and the Physical-Organic Chemistry of the Solid-Liquid Interface. *Langmuir* **1990,** *6* (1), 87-96.
(35) Ashokkumar, S.; Adler-Nissen, J.; Møller, P., Factors Affecting the Wettability of Different Surface Materials with Vegetable Oil at High Temperatures and Its Relation to Cleanability. *Appl. Surf. Sci.* **2012,** *263* (0), 86-94.
(36) Tasić, U.; Day, B. S.; Yan, T.; Morris, J. R.; Hase, W. L., Chemical Dynamics Study of Intrasurface Hydrogen-Bonding Effects in Gas−Surface Energy Exchange and Accommodation. *J. Phys. Chem. C* **2007,** *112* (2), 476-490.
(37) Faucheux, N.; Schweiss, R.; Lützow, K.; Werner, C.; Groth, T., Self-Assembled Monolayers with Different Terminating Groups as Model Substrates for Cell Adhesion Studies. *Biomaterials* **2004,** *25* (14), 2721-2730.